Aeroelastic Modeling of Novel and Flexible Aircraft Configurations: Experimental and Numerical Studies

by

Mario Bras
B.Sc., Instituto Superior Técnico
M.Sc., Instituto Superior Técnico

A Dissertation Submitted in Partial Fulfillment of the
Requirements for the Degree of

DOCTOR OF PHILOSOPHY

in the Department of Mechanical Engineering

Aeroelastic Modeling of Novel and Flexible Aircraft Configurations: Experimental and Numerical Studies

by

Mario Bras
B.Sc., Instituto Superior Técnico
M.Sc., Instituto Superior Técnico

Supervisory Committee

Dr. Afzal Suleman, Co-Supervisor
(Department of Mechanical Engineering)

Dr. Curran Crawford, Co-Supervisor
(Department of Mechanical Engineering)

Dr. Jens Bornemann, Outside Member
(Department of Electrical and Computer Engineering)

ABSTRACT

Novel aircraft configurations are being proposed to meet the demanding environmental goals of the future of aviation. The proposed configurations range from wings with an increased aspect ratio to completely novel designs, such as joined-wing configurations. These configurations show increased aerodynamic efficiency, resulting in overall reduced fuel consumption. These benefits come at a cost of added structural complexity—longer wings require a more careful design of their internal structure, are heavier, and are subject to larger deflections—and unpredictable aeroelastic effects during flight—joined-wing aircraft are prone to buckling of the aft wing and tail boom.

On the one hand, characterizing these novel aircraft configurations in terms of their aeroelastic behavior is of extreme importance if they are to be used in future commercial aircraft designs. Due to the significant cost and risk associated with the testing of full-scale aircraft, reduced-scale flexible unmanned air vehicle (UAV) models are an attractive alternative that can be used to understand the aeroelastic behavior of these designs during flight. On the other hand, current aeroelastic computational codes are relatively new, and their ability to accurately predict the aeroelastic performance of full-scale aircraft requires extensive validation. There is a need for experimental data sets demonstrating in-flight aircraft elastic behavior for tuning such models.

Flexible UAV demonstrators have been developed for the study of active flutter suppression systems, to validate flight dynamics models, identify structural vibration modes and validate design methodologies. However, few studies have focused on developing reduced-scale models to investigate the nonlinear behavior of joined-wing aircraft. Previous work has demonstrated the airworthiness of scaled joined-wing demonstrators through the successful flight of geometrically-scaled remotely piloted vehicles, but the assessment of geometric nonlinearities in flight is yet to be determined.

The main objective of this work was to characterize the aeroelastic behavior of novel aircraft models through the design and testing of flexible linear and nonlinear reduced-scale UAV demonstrators and to explore the development of medium-fidelity tools for the dynamic aeroelastic analysis of such models. To this end, reduced-scale flexible high aspect ratio wing (HARW) and joined-wing aircraft configurations were designed, manufactured, tested, and characterized numerically through aerodynamic, structural, and aeroelastic studies, and experimentally through flight testing. A unified medium-fidelity aeroelastic framework based on an accelerated unsteady panel method and a flexible multibody dynamics formulation based on absolute coordinates was

developed and used to investigate the unsteady aerodynamics of the two aircraft models.

This work illustrates the feasibility of using flexible reduced-scale flight test demonstrators as cost-effective platforms for testing the aeroelastic response of HARW aircraft configurations. It also reinforces the importance of accounting for geometric nonlinearities in the aeroelastic analysis of joined-wing configurations. The developed framework also expands the application range of flexible multibody dynamics based on absolute coordinates in time-domain simulations of large elastic deformations coupled with rigid body motion that arise in next-generation aircraft.

Table of Contents

Supervisory Committee ii

Abstract iii

Table of Contents v

List of Tables ix

List of Figures xii

List of Algorithms xx

List of Code Listings xxi

Acknowledgements xxii

1 Introduction 1

1.1 Background and Motivation 1

1.2 Previous Work 5

1.2.1 Aeroelasticity of High Aspect Ratio Wings and Joined Wing Configurations 5

1.2.2 Development and Testing of Reduced-Scale Aeroelastic Models 8

1.2.3 Aeroelastic Modeling in Multibody Dynamics 15

1.2.4 Nonlinear Aeroelastic Analysis Tools and Methods 18

1.3 Objectives 25

1.4 Research Contributions 25

1.5 Thesis Outline 28

2 Aeroelastic Evaluation of a Flexible High Aspect Ratio Wing UAV: Numerical Simulation and Experimental Flight Validation 30

2.1 Introduction . . . 32
2.2 Flight Test Platform . . . 33
2.2.1 Airframe and Components . . . 34
2.2.2 Flight Control and Sensor Systems . . . 37
2.2.3 Wing Modification . . . 38
2.3 Modeling and Testing . . . 40
2.3.1 Structural Modeling . . . 41
2.3.2 Aerodynamic Modeling . . . 43
2.3.3 Aeroelastic Modeling . . . 44
2.3.4 Bifilar Pendulum Testing . . . 45
2.3.5 Static Load Testing . . . 47
2.3.6 Ground Vibration Testing . . . 48
2.3.7 Wing Displacement Reconstruction . . . 54
2.3.8 Model Updating . . . 56
2.3.9 Pre-Flight Testing . . . 58
2.3.10 Flight Testing . . . 59
2.4 Results and Discussion . . . 65
2.4.1 Wing Aeroelastic Tailoring . . . 65
2.4.2 Mass and Inertia Properties . . . 67
2.4.3 Ground Testing Results . . . 69
2.4.4 Model Update and Comparison . . . 71
2.4.5 Flight-Dynamic Modes . . . 73
2.4.6 Aeroelastic Modes . . . 74
2.4.7 Flight Dynamics . . . 78
2.5 Concluding Remarks . . . 86

3 Numerical and Experimental Characterization of the Nonlinear Aeroelastic Behavior of a Flexible Joined-Wing UAV 88
3.1 Introduction . . . 90
3.2 Flight Test Demonstrator . . . 91
3.2.1 Airframe and Components . . . 94
3.2.2 Electrical and Avionics Systems . . . 96
3.2.3 Ground Control Systems . . . 99
3.3 Modeling and Testing . . . 100
3.3.1 Structural Modeling . . . 101

3.3.2 Aerodynamic Modeling . . . 102
3.3.3 Aeroelastic Modeling . . . 103
3.3.4 Bifilar Pendulum Testing . . . 105
3.3.5 Static Load Testing . . . 106
3.3.6 Ground Vibration Testing . . . 109
3.3.7 Model Updating . . . 112
3.3.8 Pre-Flight Testing . . . 114
3.3.9 Flight Testing . . . 115
3.4 Results and Discussion . . . 117
3.4.1 Mass and Inertia Properties . . . 117
3.4.2 Static Load Testing Results . . . 119
3.4.3 Ground Vibration Testing Results . . . 121
3.4.4 Model Update and Comparison . . . 125
3.4.5 Aerodynamics and Flight Dynamics . . . 127
3.4.6 Aeroelastic Characterization and Preliminary Flight Tests . . . 128
3.5 Concluding Remarks . . . 139

4 A Framework for Medium-Fidelity Nonlinear Aeroelastic Analysis using Absolute Nodal Coordinates and the Fast Multipole Method 140
4.1 Introduction . . . 142
4.2 Aerodynamics . . . 145
4.2.1 Low-Order Panel Method . . . 145
4.2.2 Compressibility Correction . . . 152
4.2.3 Unsteady Wake Convection . . . 152
4.2.4 Trailing Edge Detection . . . 153
4.2.5 Fast Multipole Method . . . 155
4.3 Flexible Multibody Dynamics . . . 162
4.3.1 Corotational Frame Formulation . . . 163
4.3.2 Floating Frame of Reference Formulation . . . 165
4.3.3 Inertial Frame Formulation . . . 166
4.3.4 Beam Element Kinematics . . . 167
4.3.5 Formulation of the Elastic Forces . . . 169
4.3.6 Equations of Motion . . . 171
4.3.7 Definition of the Beam Cross Section . . . 173
4.3.8 Solution of the Multibody Equations . . . 174

4.4 Fluid-Structure Interaction . . . 177
4.4.1 Coupling Strategies . . . 178
4.4.2 Radial Basis Function Interpolation . . . 181
4.5 Framework Overview . . . 184
4.5.1 Mesh Representations . . . 185
4.5.2 Spatial Domain Decomposition . . . 189
4.6 Results and Discussion . . . 190
4.6.1 FMM-Accelerated Aerodynamics of the QT1 and JWSC Configurations . . . 190
4.6.2 Dynamic Aeroelastic Response of the QT1 and JWSC Wings 194
4.7 Concluding Remarks . . . 199

5 Conclusions and Future Work **201**
5.1 Conclusions . . . 201
5.2 Future Work . . . 204
5.2.1 Flight Testing and Data Collection . . . 204
5.2.2 Improvements to Aeroelastic Simulations . . . 205
5.2.3 Progress Towards a Complete Aeroelastic Framework . . . 206

Bibliography **232**

List of Tables

1.1 Overview of currently available commercial, research, and open-source aeroelastic analysis tools. 24

2.1 QT1 aircraft platform specifications. 34
2.2 Geometry of airfoil sections used in the QT1 aircraft platform (percentages of chord). 35
2.3 QT1 payload specifications. 36
2.4 List of design variables used during the NASTRAN model updating process of the flexible QT1 aircraft. 58
2.5 List of parameters logged during a flight test of the flexible QT1 aircraft, organized by sensor source. 62
2.6 Identified bifilar pendulum test (BPT) model parameters of eq. (2.5) from experimental pendulum responses in roll, pitch, and yaw axes, for the assembly composed of the flexible QT1 aircraft and support fixture. 69
2.7 Mass properties of the rigid and flexible QT1 aircraft. C.G. location is measured from the leading edge of the wing root. 69
2.8 Comparison of modal frequencies between a cantilever-wing boundary condition obtained using impact testing (left) and a bungee-suspended-aircraft boundary condition obtained using a shaker (right) for the rigid QT1 aircraft. 70
2.9 Comparison of modal frequencies between a cantilever-wing boundary condition obtained using impact testing (left) and a bungee-suspended-aircraft boundary condition obtained using a shaker (right) for the flexible QT1 aircraft. 71
2.10 Comparison of elastic modal frequencies between experimental modal analysis (EMA) and updated NASTRAN and ASWING models of the flexible QT1 aircraft for a cantilever-wing (left) and a bungee-suspended-aircraft (right) boundary conditions. 72

2.11 Stability and control derivatives of the rigid QT1 aircraft (obtained from NASTRAN, AVL, and a rigid ASWING model), and the flexible QT1 aircraft (obtained from the flexible ASWING model). 73
2.12 Flight-dynamic modes obtained from the AVL model of the rigid QT1 aircraft at airspeeds of 20 and 30 m/s. 74
2.13 Aeroelastic modes of interest obtained from the ASWING model of the flexible QT1 aircraft at airspeeds of 20 and 30 m/s. 76
2.14 Initial conditions for three different flight tests (FT1, FT2 and FT3) of the flexible QT1 aircraft using 3–2–1–1, frequency sweep, and doublet elevator maneuver commands, respectively. 80

3.1 Development of the Joined Wing SensorCraft (JWSC) platform leading up to the flexible 3 m wingspan model that is the subject of this work (adapted from [46]). 92
3.2 JWSC platform specifications. 94
3.3 Summary of ground vibration test (GVT) runs performed on the JWSC. 110
3.4 List of design variables used during the NASTRAN model updating process of the flexible JWSC. 114
3.5 Identified BPT model parameters of eq. (2.5) from experimental pendulum responses in roll, pitch, and yaw axes, for the assembly composed of the flexible JWSC and support fixture. 119
3.6 Mass properties of the flexible JWSC. C.G. location is measured from the fuselage nose. 119
3.7 Modal parameters extracted from impact testing frequency response function (FRF) results of the flexible JWSC with the aft wing removed (left) and aft wing only (right). 123
3.8 Modal parameters extracted from impact testing FRF results with a cantilever-wing boundary condition (left) and shaker testing FRF results with a bungee-suspended-aircraft boundary condition (right) of the flexible fully-assembled JWSC configuration. 125
3.9 Comparison of elastic modal frequencies between impact testing EMA and updated NASTRAN model of the flexible JWSC with aft wing removed (left) and aft wing only (right). 125

3.10 Comparison of elastic modal frequencies between impact testing EMA with a cantilever-wing boundary condition (left), shaker testing EMA with a bungee-suspended-aircraft boundary condition (right), and updated NASTRAN and ASWING models of the flexible fully-assembled JWSC configuration. 126
3.11 Objectives defined in the DOE problem of finding flexible JWSC design candidates. 129
3.12 Constraints used in the DOE problem of finding flexible JWSC design candidates. 130
3.13 Design variables defined in the DOE problem of finding flexible JWSC design candidates. Wing spar properties for two flexible wing designs are also shown. 131
3.14 Stability and control derivatives of the rigid JWSC (obtained from a stiff ASWING model), and the flexible JWSC (obtained from the flexible ASWING model). 133

List of Figures

1.1 Collar's aeroelastic triangle, representing the three aeroelastic forces and their interactions (adapted from [11]). 2
1.2 Friedmann's aeroelastic hexahedron representing the interaction between the three aeroelastic forces, controls, and thermal effects (adapted from [12]). 3
1.3 Overview of recent aeroelastic demonstrators. 11
1.4 Spectrum of fluid mechanics, dynamics, and structural mechanics methodologies for aeroelastic analysis. 19

2.1 Timeline of the different tasks executed in chapter 2. 32
2.2 QT1 aircraft platform 3-view. 33
2.3 Airframe of the QT1 aircraft platform showing wing spars, avionics and payload bays, fuselage frame structure, and internal components. 35
2.4 Avionics bay of the electric variant of the QT1 aircraft platform showing electric motor, electronic speed controller (ESC) and lithium polymer (LiPo) batteries. 36
2.5 Piccolo SL system block diagram. 37
2.6 Payload bay of the QT1 aircraft with Native Instruments data acquisition system (DAQ), automatic flight test unit (AFTU) module and VectorNAV inertial measurement unit (IMU) installed. 38
2.7 Comparison between rigid (top) and flexible (bottom) wing of the QT1 aircraft. 40
2.8 Structural NASTRAN model of the flexible QT1 aircraft with aerodynamic paneling. 41
2.9 Aerodynamic AVL model of the rigid QT1 aircraft. 44
2.10 Aeroelastic ASWING model of the flexible QT1 aircraft. 45
2.11 BPT of the QT1 aircraft in roll, pitch, and yaw axes. 47

2.12 Flexible wing of the QT1 aircraft undergoing a static load test (left) and detail of load application rail and eyebolt used to apply a vertical point load at the joint between rigid and flexible portions of the wing (right). 48
2.13 Impact hammer (left), shaker (center), and 3-axis accelerometer arrangement (right) used during a GVT of the QT1 aircraft. 50
2.14 Impact test points (circled in red) on rigid (left) and flexible (right) aircraft wings. Location of 3-axis accelerometer is shown for the rigid wing only (red arrow on left), while shaker attachment point is shown for the flexible wing only (red arrow on right). 51
2.15 Rigid QT1 aircraft vibration test in a fixed wing setup using impact hammer (left) and a bungee suspension setup using a shaker (right). . 53
2.16 Flexible QT1 aircraft vibration test in a fixed wing setup using an impact hammer (left) and a bungee suspension setup using a shaker (right). 54
2.17 Repeating strain bending bridge pattern applied to the flexible wing of the QT1 aircraft. The pattern is mirrored on the underside of the spar (not shown). 56
2.18 Parametrized NASTRAN model of the flexible QT1 aircraft. 57
2.19 Iron bird test (left) and static thrust test (right) of the QT1 aircraft. 59
2.20 Example of the three different control surface input commands used during flight testing for exciting the aeroelastic modes of the aircraft: 3–2–1–1, frequency sweep and doublet commands. 61
2.21 Ground setup and racetrack pattern used in the QT1 aircraft flight tests. 63
2.22 Pneumatic launch (top) and belly landing (bottom) of the QT1 aircraft. 64
2.23 Root loci of aeroelastic modes of the flexible QT1 aircraft for a sweep of two different wing parameters: spar cross-section thickness (left) and wing tip mass (right). 66
2.24 Comparison of the elastic mode shapes between the rigid (top) and flexible (bottom) QT1 aircraft for cantilever-wing conditions. 67
2.25 Experimental and simulated pendulum angular displacement θ in roll, pitch, and yaw axes, for the assembly formed by the flexible QT1 aircraft and support fixture. 68

2.26 Comparison of spanwise vertical displacement of the flexible QT1 aircraft wing between experimental static load tests and NASTRAN and ASWING static load analyses. Inset shows a detailed view of the displacement at the wing root. 70
2.27 Modal assurance criterion (MAC) analysis comparing elastic mode shapes between EMA and NASTRAN for the rigid QT1 aircraft (left), EMA and NASTRAN for the flexible QT1 aircraft (center), and between updated ASWING and NASTRAN models for the flexible QT1 aircraft (right). 72
2.28 Root loci of flight-dynamic modes for the rigid QT1 aircraft obtained from an AVL and rigid ASWING model (left) and aeroelastic modes for the flexible QT1 aircraft obtained from its ASWING model (right), for airspeeds between 20 and 30 m/s. 75
2.29 Transverse deflection z (left) and twist angle ϑ (right) of the flexible QT1 aircraft wing obtained from ASWING for $1g$ level-flight trim conditions at airspeeds of 16 to 40 m/s. 76
2.30 Comparison of the first out-of-plane wing bending OB1* (top) and short-period SP* (bottom) aeroelastic mode shapes of the flexible QT1 aircraft at different phase angles ϕ. 77
2.31 Root loci of aeroelastic modes for airspeeds between 20 and 80 m/s and flutter onset points obtained from ASWING for the flexible QT1 aircraft 78
2.32 Flight test trajectory of the flexible QT1 aircraft obtained from global positioning system (GPS) data. 79
2.33 Comparison between flight test data and simulated response of the flexible QT1 aircraft to an elevator 3–2–1–1 command, for angle of attack α, true airspeed (TAS), z-acceleration a_z, pitch rate q, pitch angle θ, and elevator deflection δ_e. 81
2.34 Comparison between flight test data and simulated response of the flexible QT1 aircraft to an elevator frequency sweep command, for angle of attack α, TAS, z-acceleration a_z, pitch rate q, pitch angle θ and elevator deflection δ_e. 82
2.35 Comparison between flight test data and simulated response of the flexible QT1 aircraft to an elevator doublet command, for angle of attack α, TAS, z-acceleration a_z, pitch rate q, pitch angle θ and elevator deflection δ_e. 83

2.36 Wing deflection of the flexible QT1 aircraft at different instants of an elevator frequency sweep maneuver. 84
2.37 Comparison of wing tip deflection (left) and spanwise wing deflection at three time instants (right) for flight tests FT1, FT2 and FT3, between reconstructed displacements from in-flight-measured strains and aeroelastic ASWING simulation, for the flexible QT1 aircraft. . . 85

3.1 Timeline of the different tasks executed in chapter 3. 91
3.2 Different-complexity JWSC models leading up to the flexible 3 m wingspan model that is the subject of this work (adapted from [46]). . 93
3.3 JWSC platform 3-view. 93
3.4 Battery and payload bays of the JWSC. 95
3.5 Flexible front and aft wings of the JWSC. 95
3.6 Wiring bay of the JWSC. 97
3.7 Autopilot and modem bays of the JWSC. 98
3.8 Left and right Foxeer Legend 1 fuselage cameras (left and center, respectively), and tail boom Mobius RunCam camera (right) installed on the JWSC. 98
3.9 Aircraft mobile command unit (MCU) (left) and pneumatic launcher (right). 99
3.10 Structural NASTRAN model of the flexible JWSC. 101
3.11 Aerodynamic AVL model of the rigid JWSC. 103
3.12 Aerodynamic ASWING model of the flexible JWSC. 104
3.13 Overview of nonlinear aeroelastic analysis. 105
3.14 BPT of the JWSC in roll, pitch, and yaw axes. 106
3.15 Vinyl markers (left), Creaform fiducial markers (center), and trackball highlight markers (right) placed on the front and aft wings of the JWSC during static load testing. Markers are circled in red. Load anchor points are indicated by red arrows. 107
3.16 JWSC undergoing static load tests. Gravity-only (left) and maximum (right) load cases are shown. 108
3.17 Creaform Go!SCAN 3D portable scanner (left) and 3D printed nose coordinate system (right). 108
3.18 Partial 3D scans of the JWSC during a static load test. 109

3.19 Repeating strain bending bridge pattern applied to the front and aft wings of the flexible JWSC. The pattern is mirrored on the underside of the spars (not shown). 109
3.20 Impact hammer (left), shaker (center), and single-axis accelerometer (right) used during a GVT of the JWSC. 111
3.21 Different methods used to simulate free-free boundary conditions in a GVT of the fully-assembled JWSC. 111
3.22 Parametrized NASTRAN model of the flexible JWSC. 113
3.23 Static thrust test (left), iron bird test (center) and launcher test (right) of the JWSC. 115
3.24 Ground setup and racetrack pattern used in the JWSC flight tests. . 116
3.25 Pneumatic launch (top) and belly landing (bottom) of the rigid JWSC. 116
3.26 Experimental and simulated pendulum angular displacement θ in roll, pitch, and yaw axes, for the assembly formed by the flexible JWSC and support fixture. 118
3.27 Comparison of spanwise vertical displacement of the flexible JWSC front (left) and aft (right) wing between experimental static load tests, NASTRAN linear, NASTRAN nonlinear, and ASWING static load analyses. 120
3.28 Comparison of spanwise twist angle of the flexible JWSC front (left) and aft (right) wing between experimental static load tests, NASTRAN linear, NASTRAN nonlinear, and ASWING static load analyses. . . . 120
3.29 Comparison of spanwise spar maximum strain of the flexible JWSC front (left) and aft (right) wing between experimental static load tests, NASTRAN linear, NASTRAN nonlinear, and ASWING static load analyses. 121
3.30 Elastic modal frequencies for three pre-loaded configurations of the JWSC. 122
3.31 MAC analysis comparing elastic mode shapes of the JWSC between EMA and NASTRAN for aft wing only (left), with aft wing removed (center), and full assembly (right). 126
3.32 Elastic mode shapes of the flexible JWSC for free boundary conditions. 127
3.33 Comparison of JWSC aerodynamics between AVL and ASWING for $1g$ level-flight trim (left) and $2.5g$ pull-up (right) flight conditions. . . 127

3.34 Root loci of flight-dynamic modes for the rigid JWSC obtained from an AVL and rigid ASWING model, for airspeeds between 20 and 30 m/s. 128
3.35 Linear and nonlinear aeroelastic response to a 2.5g pull-up maneuver for two different design candidates of the flexible JWSC. 131
3.36 Comparison of aeroelastic response of the flexible JWSC to a 2.5g pull-up maneuver between the nonlinear NASTRAN-AVL framework and ASWING. 132
3.37 Deformed coupled AVL–NASTRAN (left) and ASWING (right) aeroelastic models of the flexible JWSC. 132
3.38 Root loci of aeroelastic modes for the flexible JWSC obtained from its ASWING model, for airspeeds between 20 and 30 m/s. 134
3.39 Data recorded from the autopilot during a flight test of the rigid JWSC. 135
3.40 Simulated response of the flexible JWSC to an elevator doublet command, for angle of attack α, TAS, x-acceleration a_x, z-acceleration a_z, pitch rate q, and pitch angle θ. 136
3.41 Simulated response of the flexible JWSC to an aileron doublet command, for angle of attack and sideslip α, β, roll, pitch, and yaw rates p, q, r, and roll, pitch, and yaw angles ϕ, θ, ψ. 137
3.42 Aeroelastic ASWING simulation of front wingtip and aft midpoint wing deflection (left) and spanwise wing deflection at three time instants (right) in response to elevator and aileron doublet commands, for the flexible JWSC. 138

4.1 Timeline of the different tasks executed in chapter 4. 144
4.2 Potential flow problem. 146
4.3 Schematic illustration of the Kutta condition at a wing's trailing edge showing the relation between trailing edge upper and lower panel doublet strength and the corresponding wake doublet strength for a steady-state fixed wake (left) and an unsteady convected wake (right). 151
4.4 Example of detected trailing edge (thick solid lines) and automatically generated fixed wake shed from trailing edge segments for the QT1 aircraft. 155
4.5 Schematic illustration of hierarchical spatial decomposition of a two-dimensional mesh (left) into an adaptive quadtree (right). 156

4.6 FMM (left) and direct (right) approaches for solving an N-body interaction problem. 157
4.7 Flexible multibody dynamics system. 163
4.8 Representation of a flexible body using an inertial frame formulation expressed in absolute coordinates (left), a corotational formulation using a local frame for each element (center), and a floating frame formulation using a local frame for each body (right). 164
4.9 Floating frame of reference. 165
4.10 Two-noded fully parametrized beam element. 168
4.11 Physical interpretation of the slope coordinates in the absolute nodal coordinate formulation (ANCF) (adapted from [227]). 169
4.12 General configurations of a continuum body. 170
4.13 Monolithic (left) and partitioned (right) coupling strategies used in fluid-structure interaction. 179
4.14 Different partitioned coupling schemes used in fluid-structure interaction. 181
4.15 Illustration of information transfer from fluid mesh to structural mesh (left), and information transfer from structural mesh to fluid mesh (right). Structural nodes are represented in blue. Fluid nodes and element center points are represented in red. 182
4.16 Flow of information during a weakly-coupled aeroelastic simulation. . 185
4.17 Example of VV, FV, and DCEL mesh representations, showing the different entities stored as part of the mesh implementation. 186
4.18 Representation of a unit sphere using an unstructured mesh (left), its spatial partitioning using an octree (center), and a slice of this partitioning (right). 189
4.19 Representation of the QT1 geometry using an unstructured mesh (left), its spatial partitioning using an octree (center), and a slice of this partitioning (right). 190
4.20 Three-dimensional aerodynamic model of the QT1 aircraft. 191
4.21 Three-dimensional aerodynamic model of the JWSC. 191
4.22 Comparison of QT1 aerodynamics in terms of spanwise lift (left) and drag (right) distributions, between AVL, ASWING, and the developed panel method for a $1g$ level flight condition. 192

4.23 Comparison of JWSC aerodynamics in terms of spanwise lift (left) and drag (right) distributions, between AVL, ASWING, and the developed panel method for a $1g$ level flight condition. 192
4.24 Pressure distribution and wake convection for the QT1 aircraft at the end of an aerodynamic simulation. 193
4.25 Pressure distribution and wake convection for the JWSC at the end of an aerodynamic simulation. 193
4.26 Scaling of the FMM with problem size N. 194
4.27 Aeroelastic wing models the flexible QT1 (left) and JWSC (right) aircraft. 195
4.28 Representation of an impulse load as a normal distribution (left) and evolution of aerodynamic loads transferred to the structure at the start of a simulation (right). 196
4.29 Comparison of aeroelastic response of the flexible QT1 wing to a wingtip impulse command between the developed aeroelastic framework and ASWING at an airspeed of 20 m/s. Unsteady wingtip deflection (left) and steady-state wing deformation (right). 197
4.30 Comparison of aeroelastic response of the flexible JWSC front and aft wings to a wingtip impulse command between the developed aeroelastic framework and ASWING at an airspeed of 20 m/s. Unsteady front wing tip and aft wing midpoint deflection (left) and steady-state front and aft wing deformation (right). 198

List of Algorithms

1 Automatic trailing edge detection for an unstructured surface mesh $\mathcal{T}$ given a threshold angle θ_{te}. 154
2 Domain decomposition phase of the fast multipole method (FMM) . 159
3 Upward evaluation phase of the FMM for kernel $\mathcal{K}$ and source cell tree $\mathcal{S}$. 160
4 Interaction phase of the FMM for kernel $\mathcal{K}$ across source and target cell trees $\mathcal{S}$ and $\mathcal{T}$, respectively. 161
5 Downward evaluation phase of the FMM for kernel $\mathcal{K}$ and target cell tree $\mathcal{T}$. 162

List of Code Listings

4.1 Example vertex data structure used in a VV mesh representation. . . 186
4.2 Example vertex and face data structures used in a FV mesh representation. 187
4.3 Example half-edge, vertex, edge, and face data structures used in a DCEL mesh representation. 188

ACKNOWLEDGEMENTS

When I embarked on this journey, I didn't imagine life would turn out the way it did. Many changes have happened in my life in the last few years, and completion of this work would not have been possible without the support, encouragement, and patience of many people.

I would like to extend my heartfelt thanks to Dr. Afzal Suleman for this opportunity. I am grateful for his guidance and support throughout this work, for the chance to work on exciting projects, for the freedom he afforded me to grow, personally and professionally, to explore different research topics, freedom to teach and engage with fascinating students and talented individuals, and for the undeniable continuous trust in my work. I am also grateful to Dr. Curran Crawford for all the insightful discussions during these years.

I want to thank all present and past personnel from the Center for Aerospace Research at the University of Victoria for their support throughout this work. I will do my best to acknowledge everyone here. I am thankful to Dr. Jenner Richards, Stephen Warwick, Willem Brussow, Peter Sherk, John Cockcrof, Ben Gawley, Patrick Heaney, and John Rafaelli for the manufacturing, systems integration, and flight test support during the execution of the project. I am also thankful for all the assistance from Nuno Mocho and José Carregado for the ground vibration testing they performed. This work would not have been possible without their support.

This thesis research was partially supported by the NSERC CRD grant no CRDPJ 500925-16 in collaboration with Bombardier. The support and discussions during our regular meetings provided by Sid Banerjee and Graham Potter at Bombardier on the development of the computational framework were invaluable for the success of the project.

I also extend my acknowledgments to other industry collaborators involved in this work. The experimental data obtained for the joined-wing and the high-aspect-ratio wing projects were used to validate the computational framework. From EMBRAER S.A., Achilles Olympio Mello, Allan Pereira, Álvaro Oliva, António Bernardo, Fernando Moreira, João Marra, Marcos Pedras, and Polliana Martins. From Boeing, Dr. Frode Engelsen, Dr. Rajesh Talwar, and Dr. Manny Urci.

Last but not least, I would like to thank all my family and friends who have, directly or indirectly, one way or another, given me support and encouragement during all these years.

In memory of my grandfather.

Chapter 1

Introduction

1.1 Background and Motivation

Aircraft transport systems have seen an increasing demand for safer and greener technologies and reduced development and operational costs in the short and long term. These changes have called for a paradigm shift in aircraft design. Improving global operational aircraft efficiency is the most promising approach to meet these objectives. Different methods are being investigated to make these improvements, including new composite materials, better propulsion with improved engine efficiencies, new hybrid-electric propulsion, and enhanced aerodynamics.

Environmental factors, including noise, air pollution, and climate change, play an important role in the growth of civil aviation [1]. From 1999 to 2018, the number of passengers carried by airlines has increased from approximately 1.67 billion to 4.23 billion, and this number is expected to increase to roughly 8.2 billion worldwide by 2037. In the year 2000, an estimated 677 Mton of carbon dioxide are estimated to have been emitted by the aviation sector alone [2]. Aerodynamic efficiency is another factor contributing to commercial aviation growth and innovation. Fuel consumption represents about 22 % of the direct operating costs for airlines. A drag reduction of only 1 % can represent 1.6 ton of operating weight, or 10 passengers for a large transport aircraft [3].

Weight minimization is an essential aspect of aircraft design now more than ever, leading to more and more flexible aircraft designs. Any flexible structure that is exposed to aerodynamic loads can be considered an aeroelastic system. A typical aircraft structure adapts its shape when subject to external aerodynamic and inertial

loads due to the inherent flexibility of the materials. However, this behavior is usually a consequence of flying the aircraft and is not always desirable. An interest in developing aircraft structures that beneficially explore the structural deflections caused by aerodynamic loads has been increasing in the last few years.

Aeroelasticity is a well-established field focused on studying the interaction between aerodynamic, inertial, and elastic forces [4–10]. The interaction between the three disciplines involved—fluid mechanics, structural dynamics, and structural mechanics—is represented by Collar's aeroelastic triangle [11] of fig. 1.1.

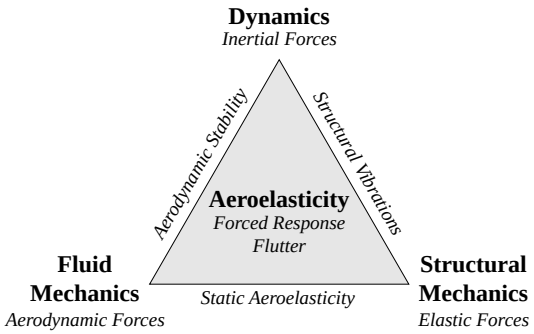

Figure 1.1: Collar's aeroelastic triangle, representing the three aeroelastic forces and their interactions (adapted from [11]).

More recently, Friedmann extended Collar's triangle to include controls and thermal effects [12], as illustrated in fig. 1.2. The upper half of the hexahedron represents aeroservoelasticity—the analysis of the aircraft response due to control input and the investigation of control algorithms (e.g., trim or load alleviation control). The lower half of the hexahedron represents aerothermoelasticity, in which thermal effects are added to the classical aeroelastic model. Aerothermoelasticity is important in the hypersonic flight regime [13].

Aeroelastic phenomena are not limited to aircraft systems. Wind turbine blade structures are designed to have bend-twist coupling to better adapt to the wind flow and to operate more efficiently. Novel energy harvesting systems that use flexible structures and take advantage of aeroelastic effects to generate electric energy from ambient fluid motion are also being developed.

Despite these applications, aeroelasticity is often prejudicial to the performance of an aircraft system. Static and dynamic phenomena that can lead to the destruction of an airframe need to be properly addressed during the system's design. These phenomena can be static (divergence and control reversal) or dynamic (flutter and buffeting). Static divergence occurs when the wing twists due to a steady flow to

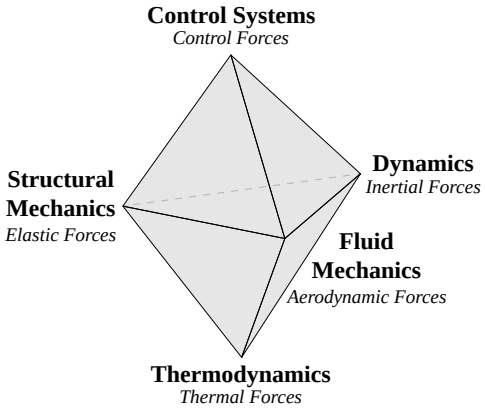

Figure 1.2: Friedmann's aeroelastic hexahedron representing the interaction between the three aeroelastic forces, controls, and thermal effects (adapted from [12]).

a point where the structure fails. Control reversal adversely affects the aircraft's controllability when a wing control surface reverses itself unexpectedly. Flutter is an unstable self-feeding vibration caused by positive feedback between the body's deflection and aerodynamic forces. Aerodynamic forces on an object interact with the structure's natural vibration modes producing a rapid amplified periodic motion leading to structural failure. Buffeting is a high-frequency instability caused by turbulence in the airflow. Different sources of buffeting include airflow separation, shock wave oscillations, nacelles, gusts, or sudden aerodynamic impulses.

Aeroelasticity of stationary wings is considered a mature and well-understood research field [12]. However, aeroelasticity, in general, is still a field in development. Examples of subjects where significant advancement is still taking place are aeroelasticity in the transonic flight regime [14], load alleviation using adaptive structures [15], and inclusion of aeroelasticity in flight mechanics [16].

Computer simulation of the flight of flexible aircraft is not a trivial task [17]. Most models try to capture both disciplines by augmenting the traditional rigid flight mechanics equations with elastic degrees of freedom (DOFs) while assuming decoupled flight mechanics and structural deformation, which is too limiting [16]. Some models, though, have been developed that include coupling effects between flight mechanics and structural deformation. [17].

Instead of a unified approach, aerodynamic and structural models can be implemented separately and coupled with some interaction procedure. This process can yield very accurate results, usually at the cost of high computational times, in the order of days for maneuvers of a few seconds only [18]. Often, a multibody dynamics system

serves as the platform that couples the different disciplines. The inherent strengths of the multibody dynamics approach can be used to reduce the computational time required to simulate coupled aeroelastic flight mechanics maneuvers while retaining model accuracy.

To model an aircraft's aeroelastic flight mechanics behavior, numerical tools that can model the interaction between dynamic aerodynamic loads and structural dynamics are required. A formulation that considers the rigid body motion and the elastic deformations of the structure must be employed. Multibody dynamics was developed to model the interaction between interconnected bodies when subjected to complex loading scenarios while considering inertia forces due to large overall rigid body motion. This approach allows the efficient analysis of the dynamic behavior of systems. Multibody dynamics has a proven track record of successful applications in several engineering fields, including robotics, aerospace engineering, vehicle dynamics, bio-mechanics, and rotor dynamics.

Current aeroelastic computational codes are relatively new, and their ability to accurately predict the aeroelastic performance of full-scale aircraft requires extensive validation. There is a need for experimental data sets demonstrating in-flight aircraft elastic behavior for tuning such models [19]. Reduced-scale models can be used to study these phenomena in wind tunnels. However, a suitable scaling process must be carried out to represent the full-scale models properly. Wind tunnel tests can be costly and accessible only to a small portion of the research community. An attractive alternative is to fly small-scale unmanned air vehicles (UAVs) and test these effects in flight, which can significantly reduce costs and risk. The cost and complexity of UAV demonstrators increase with aircraft size. Therefore, small systems are the preferred choice. Developing these demonstrators can be challenging, as the aircraft needs to be designed to show some degree of aeroelastic instability but simultaneously have the required structural integrity to ensure a safe operation within the range of operational speeds. The design parameters influencing the aeroelastic behavior are stiffness, mass distribution, and the aerodynamic forces defined by the wing planform and airfoil. In addition to the intended aeroelastic instability, the UAV demonstrator must fulfill a flight mission outside the unstable flight regime.

1.2 Previous Work

1.2.1 Aeroelasticity of High Aspect Ratio Wings and Joined Wing Configurations

The interest in high aspect ratio wings (HARWs) has been growing for application in transport aircraft. The wings of current commercial transport aircraft have seen their aspect ratio increase steadily in the past decades. This may be attributed to the reduction in induced drag resulting in greater lift-to-drag ratio and longer flight range [20]. Aerodynamic induced drag can represent 43 % of the overall aerodynamic drag for a large transport aircraft in cruise [21]. On the other hand, these wing designs exhibit higher deflections and higher stress levels at the wing root under normal flight conditions. With the increase of wing structural flexibility, the wing becomes more susceptible to higher deflections at the same operating conditions, which can affect the dynamic behavior, and consequently, the aeroelastic behavior, thus creating instabilities at lower speeds than in a comparable stiffer wing structure. In fact, flap bending, chord bending and torsion modes may couple and result in significant structural nonlinearities and a change in the dynamic behavior of the wing, which generally degrades its aeroelastic behavior [22]. Reported effects include flutter speed reduction [23–25], changing the limit cycle oscillation (LCO) onset [25, 26], modifying the dynamic response [27], high sensibility to gusts [28] and changes in flight dynamic behavior [23, 29, 30].

An important issue regarding the study of highly-flexible aircraft with HARWs is the coupling of structural elastic modes with flight-dynamic modes, which may result in body-freedom flutter (BFF). This phenomenon is not observable in traditional wind tunnel tests [31], since the aircraft is constrained. A solution employing a flexible support is possible and has been proposed [32], but flight tests are recommended over traditional wind tunnel tests for this type of aircraft. Highly-flexible aircraft are susceptible to large deformations that can lead to catastrophic failure, like the NASA Helios prototype, a high-altitude long-endurance (HALE) solar-electric ultra-light flying wing, which crashed after catastrophically breaking up in flight, highlighting the need for more robust tools in the design and operation of such designs [33, 34]. Controlling the wing deformation should prevent Helios-like situations from repeating and has been achieved in the past. Yagil et al. were successful in controlling wing deformations in highly-flexible aircraft by using leading- and trailing-edge control

surfaces [35]. The designed controller proved to significantly reduce the maximum wing deflection experienced by gust disturbances. More recently, Wang et al. have presented a new deformation control concept of HALE aircraft based on moving masses [36, 37]. In their work, they proposed a mass-actuated wing capable of changing its center of mass to control its deformation and the aircraft roll. Their analysis showed that the elastic deformation of the high aspect ratio flexible wing can be effectively controlled by the moving mass to avoid large deformations and that the aircraft rolling moment is improved by using the inherent large span of HALE aircraft.

The ever-growing demand for air transportation and the tendency for a year-on-year increase in greenhouse gas emissions caused by civil aviation is pushing conventional configurations to the limits of their performance [38]. Composite materials have been used to reduce weight and improve the overall aircraft efficiency [39]. Using materials with higher stiffness also allows for the development of higher aspect-ratio wings, promoting a higher lift-to-drag ratio, thus improving efficiency. Even though effective to a certain extent, this approach alone often does not suffice. Departing from conventional designs and searching for a better understanding of new aircraft configurations is paramount to improving aircraft performance.

Research has shown that the joined-wing design can be superior to current conventional aircraft configurations. Wolkovitch [40] points out that the joined-wing configuration can offer greater aerodynamic efficiency and reduced airframe weight compared to conventional aircraft designs. Samuels [41] showed in 1982 that the joined-wing configuration could be 12 % to 22 % lighter than a conventional wing when both are optimized for the same allowable stress. The placement of the inter-wing joint is a design decision that influences the structural integrity and, consequently, the weight of the wings. The Joined Wing SensorCraft (JWSC) has those joints inboard of the wing tips, which generally allows for a lighter structure. Not only are joined-wing structures generally lighter than conventional wing structures, but they also possess higher stiffness since the torsion of the front wing is resisted by the flexure of the aft wing. Rasmussen et al. [42, 43] also concluded that a lightweight joined-wing concept is possible to achieve, although being highly nonlinear.

The internal structure of the joined-wing configuration differs from a conventional wing. When resolving lift into components acting normal and parallel to the airframe, the out-of-plane components tend to bend the wings about a tilted bending axis. This effect is known as the Wolkovitch effect [40] and raises the need for a strengthened upper leading and lower trailing edges.

In relation to the aerodynamic efficiency, wind-tunnel testing conducted by Wolkovitch validated analytical and numerical predictions from Letcher [44] and Kulhman [45] and has proved that the joined-wing produces less induced drag and, in general, reduced transonic and supersonic drag. In addition, this configuration favors the placement of control surfaces at different dihedral angles in the individual wings, allowing for direct lift and side force control.

Another potential benefit this configuration can offer is the ability to incorporate conformal radar antennas in the front and aft wings to provide 360 deg surveillance [46, 47].

Despite all these advantages, some challenges still trouble designers to this day. The structural design of a joined-wing configuration is constrained by the lack of aft wing stability, resulting from the aft wing supporting part of the compression caused by the front wing. This highly nonlinear phenomenon tends to flatten the entire airframe, leading to structural overload due to the loss of the aft wing's ability to react to forward wing loads [46]. With the advent of lightweight, advanced composite materials, wing deflections tend to increase, and the aft wing can be subject to buckling [8]. This potential buckling phenomenon represents a unique and challenging aeroelastic design problem.

Detailed studies by Kroo et al. [48], and Gallman and Kroo [49] showed buckling of the aft wing when the wings were subjected to large deflections. Blair and Canfield [50], and Blair et al. [51] initiated nonlinear exploration on a joined-wing configuration with approximately twice the span of Gallman and Kroo's model. Front wing buckling had been overlooked up to this point. The argument was that the forward and upward wing bending allowed both the aft and front wings to buckle whenever compression was present.

Lin et al. [52] investigated structural instabilities due to the wing-joint moment, shear, and axial reaction loads. The influence of wing-joint fixity on a joined-wing geometry stiffness and strength characteristics was also studied. A rigid joint was found to be the most practical configuration and less likely to promote stiffness instability in the rear wing.

Recent studies by Bhasin et al. [53], Demasi et al. [54, 55], and Cavallaro et al. [56, 57] showed the importance of nonlinear structural analysis to accurately capture large deformations when designing a joined-wing configuration and the snap buckling instability of such configuration. It was further concluded that the flexibility of wings, wing joint connectivity, and anisotropy of the composite materials could significantly

influence the nonlinear structural response.

Cavallaro and Demasi [58] present an in-depth review of the joined-wing configuration studies, challenges, and innovations. Their review mentions the challenges associated with the certification of this configuration and the need for validation of computational models as the major barriers to the development of joined wings.

1.2.2 Development and Testing of Reduced-Scale Aeroelastic Models

Current aeroelastic computational codes are relatively new and their ability to predict the full-scale aeroelastic performance of aircraft requires validation. There is a need for experimental data sets demonstrating the behavior of elastic aircraft in-flight for tuning such models [19]. Reduced-scale models can be used to study these phenomena in wind tunnels. A suitable scaling process must be carried out to achieve a proper representation of the real models. Wind tunnel tests can be quite costly and accessible only to a small portion of the research community. An attractive alternative is to fly small-scale remotely piloted vehicles (RPVs) and test these effects in flight, which can significantly reduce costs and risk. The cost and complexity of UAV demonstrators increase with aircraft size. Therefore, small systems are the preferred choice. Developing these demonstrators can be quite challenging. The aircraft needs to be designed to show some degree of aeroelastic instability but simultaneously have the required structural integrity to ensure a safe operation within the range of operational speeds. The design parameters influencing the aeroelastic behavior are stiffness and mass distribution, as well as the aerodynamic forces defined by the wing planform and airfoil. In addition to the intended aeroelastic instability, the UAV demonstrator must fulfill a standard flight mission outside the unstable flight regime. From this, a complex design task can be concluded with opposing design goals.

Recent work has been done on the development of aeroelastic UAV demonstrators. Hamada and Moreno [59] developed a UAV with a conventional configuration and flexible structural properties in the lifting surfaces to study flutter. They used flight tests to identify the rigid-body dynamics, while the structural dynamics were identified from ground tests. However, the flexible dynamics were not identified in flight, and the wing was relatively stiff, with its first out-of-plane bending mode at 8.47 Hz. Hermanutz and Hornung [60] designed a flutter UAV demonstrator, by formulating a design optimization problem with the goal of obtaining two different

UAV configurations with a minimum flutter speed and minimum flutter frequency, respectively. It was shown that the optimization algorithm converged to configurations with the largest possible wing area for the low-speed flutter demonstrator, higher sweep angles as well as taper ratios, and higher operating speeds for the low-flutter frequency demonstrator. Zúñiga et al. [61] developed aerodynamic and flexible flight dynamics models for a flexible wing UAV platform named EOLO. A flight test campaign was planned and executed to study the interaction between the rigid-body modes and one elastic mode. It was shown that the reconstructed wing deflection and flight path from the measured and estimated states was consistent with the developed flexible model, even though the model was limited to longitudinal dynamics and a single elastic mode. Computational vision and lasers were later used by de Figueiredo et al. [62] to identify the vibration modes of the aircraft. Mieloszyk et al. have used a UAV to validate the design methodology of a multidisciplinary design optimization (MDO) framework, previously developed by the authors, that introduces dynamic stability constraints into the design process [63]. In their work, they compared data acquired from the design and optimization process with flight test data. They were able to confirm the increased stability of the aircraft by comparison of flight parameters, pilot assessments, and in-flight observations. The aerodynamic performance of the aircraft measured during flight also showed good agreement with simulated computational fluid dynamics (CFD) results.

Flexible UAV demonstrators have also been developed for the study of active flutter suppression systems. For flutter UAV demonstrators, having a predefined, unstable aeroelastic condition is one of the main interests in the design of the aircraft. Since the phenomenon of wing flutter is the focus, the wing design and sizing are essential but constrained by operational aspects. Configurations with low flutter speeds are preferred, as they require a smaller operational radius. Examples of such configurations include Huginn, a flying wing research drone developed by Schmidt, with an aspect ratio of 8.57. The vehicle is an example of a low-frequency BFF, as well as a bending-torsion, flutter platform [64, 65]. The vehicle is a 50 % scaled version of the Lockheed Martin/NASA X-56 (MUTT) vehicle [66] and is developed to support research on the dynamics and control of aeroelastic aircraft. Control laws were first developed for stability augmentation and active flutter suppression where it was identified that the critical factors that limited the performance of the feedback system were the bandwidth of the surface actuators and the pitch effectiveness of the body flaps. More recently, Schmidt et al. built and flight tested the same vehicle and

showed that different flutter controllers were able to augment the damping ratio of the targeted first aeroelastic mode below the open-loop flutter speed and some even expand the flutter boundary of the test vehicle [67]. The FLEXOP demonstrator is another example of a flutter UAV demonstrator. The aircraft shows classical wing flutter at low speeds [68–70].

The study of coupled flight dynamics and highly-flexible structural dynamics has been the focus of the work done by Cesnik et al. [71], and Cesnik and Su [72]. In their work, a flexible, high aspect ratio wing-boom-tail type aircraft named X-HALE was developed that showed coupled rigid-elastic body instability and large wing deflections. The aircraft was developed as a test bed for nonlinear aeroelastic flight tests. The models presented significant wing deflections under trim conditions. The unstable motion that couples the rigid-body motion with elastic wing deformations was achieved by controlled excitation of anti-symmetric aileron deflection. Initial flight tests were performed later on by Jones and Cesnik [73], and the expected coupled response was observed during flight. Time-dependent simulations of the aircraft were performed and compared to in-flight measured data. However, due to the poor quality of the data obtained from the initial flight tests, limited conclusions could be made about the correlation between simulation results and flight test data.

Few studies have focused on developing reduced-scale models to investigate the nonlinear behavior of joned-wing aircraft during flight. Such models can significantly reduce costs and risks compared to wind tunnel tests of full-scale aircraft, simultaneously making them accessible to the wider research community.

The studies on reduced-scale JWSC configurations by Richards et al. [19, 74, 75], and Richards [46] is possibly the most comprehensive work in the literature. However, while the airworthiness of these models was evident from the studies, the scaled models were not sufficiently flexible for aeroelastic studies. Zhang et al. [76] have recently performed numerical investigations on the static aeroelastic response of a highly-flexible high aspect ratio joined-wing aircraft. A prototype was developed, but flight-test data was not discussed nor compared with the computational results.

It has been shown that reduced-scale UAV models can be effective at generating high-quality aeroelastic data. Bras et al. [77] conducted aeroelastic studies on a scaled highly-flexible HARW UAV. A rich set of aeroelastic data was captured from a flight test campaign in terms of aircraft dynamics, wing strain, and wing accelerations. An indirect shape reconstruction method based on strains was employed to extract wing displacements from measured strain data [78]. Time-marching aeroelastic simulations

were set up to simulate the conditions of the flight tests. Results from the simulations were compared with flight test data, showing good agreement between the two. The work of Sobron et al. [79], and Raju Kulkarni et al. [80] are good reviews of the current research being done in sub-scale flight testing. An overview of recent work on aeroelastic demonstrators is shown in fig. 1.3.

(a) Helios [33, 34]

(b) X-HALE [71–73]

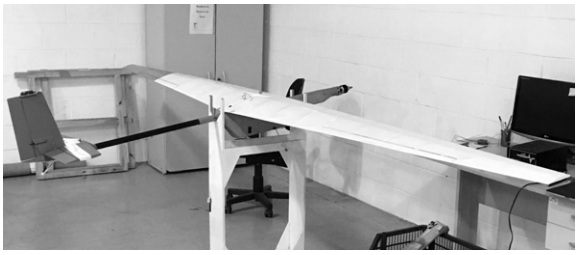

(c) EOLO [61, 62]

(d) FLEXOP [68–70]

(e) X-56 [64–67]

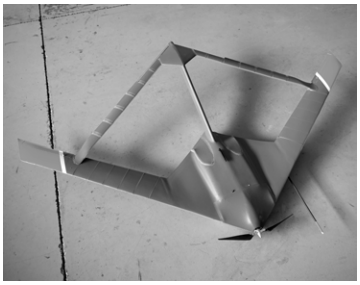

(f) Flexible mini JWSC [46]

Figure 1.3: Overview of recent aeroelastic demonstrators.

The aeroelastic performance of a flexible UAV demonstrator is of prime importance. Therefore, modal testing in the form of ground vibration tests (GVTs), as well as static load testing, are required prior to conducting any flight tests, not only to update the computational models but also to properly characterize the elastic behavior of the scaled model.

GVT, more generally known as experimental modal analysis (EMA), is the experimental measurement of an aircraft's vibration modes, including peak frequencies, damping, and mode shapes. These measurements can be used to prevent adverse dynamic behaviors, such as aeroelastic and aero-servo-elastic instability, in a new or modified aircraft. GVT or EMA can also be used to identify aircraft flutter, structural flaws, and flight-control-dynamics problems. To study the response of a structure, it is necessary to apply a quantifiable input able to produce a measurable excitation of the structure. Two common approaches for this are impact testing and shaker testing,

which involve applying a dynamic force to the structure. Acceleration is typically measured using an accelerometer in these experiments.

Impact testing is the most commonly used technique for exciting a structure. This method involves using an impact hammer with a force-sensing transducer or impedance head. The impact hammer typically has replaceable tips with different geometry and hardness to accommodate different structures and excitation requirements. Simple experiments may require a single impact hammer and one accelerometer. A single DOF can be measured by sampling both the impedance transducer and accelerometer during an impact excitation. The narrow pulse of an impact allows for a broad range of frequencies to be applied to the structure. The more precise the impact, the broader the energy content. This can be controlled by the hardness of the impact tip. In general, the harder the tip, the higher the frequency content. To maintain the validity of the modal experiment, measurements must be kept as linear as possible. Impacts that impart too much energy in one point of the structure can cause nonlinear dynamics to occur. There are several ways to avoid this, including using lighter impacts or softer impact tips at the cost of reducing the frequency range or the signal-to-noise ratio (SNR).

Shakers are sometimes preferred over impact hammers in specific applications because they offer more control over the input excitation at the cost of a more complex experimental setup and planning. For example, they may be more suitable for heavily damped structures. Shakers are typically driven by either electromagnetic or electrohydraulic forces. A shaker setup typically consists of a shaker, stinger, force transducer, response transducer (accelerometer), and test structure. It is important that the shaker is aligned such that it only applies axial forces through the stinger. One way to test for this is through a reciprocity test. Shakers offer flexibility in the types of signals that can be applied to a structure. A wide variety of signals can be used, including deterministic and non-deterministic signals. Deterministic signals include stepped sine and sine chirp signals, while non-deterministic signals include random and burst random noise.

GVTs of aircraft systems are typically performed very late in the development process. Because of the high development costs associated with any aircraft, the goal is to strive for a significantly shorter testing time by increasing the test data's amount and quality. For understanding and performing aeroelastic and dynamic load analysis, the primary inputs are the stiffness, mass, and inertia properties of each aircraft component. GVTs are one of the standard test procedures used in the aircraft

industry and a crucial step in the design process of a new aircraft, as reported by Hernández et al. [81]. Modern solutions for ground vibration testing of large aircraft (for example, the Airbus A330) are reported by Peeters et al. [82]. Böswald et al. [83] present recent advances in ground vibration test and flight vibration test. As reported by Voracek [84], in order to certify an airplane, it is essential to demonstrate its dynamic stability. GVTs determine stiffness distribution, natural frequencies, mode shapes, and damping [85]. They are necessary to make reliable flutter predictions, validate and update the mathematical model of the aircraft dynamics, and for the certification process. One of the main methods to obtain the modal characteristics of an airplane structure is by the use of frequency response functions (FRFs), as reported by Simsiriwong and Sullivan [86]. These functions can be based on the displacement (admittance, compliance, or receptance), velocity (mobility), or acceleration (inertance or accelerance) response of the system.

Static load tests are performed on reduced-scale aircraft models to determine the strength and durability of an aircraft's structure. These tests help engineers understand how an aircraft will perform under various loads, such as those it will encounter during takeoff and landing or a high g flight maneuver, such as a pull-up maneuver. This information is essential for ensuring the safety and reliability of an aircraft structure. Static load tests can also be used to identify potential design flaws and make necessary improvements before a full-scale aircraft is built.

Different methods can be used to measure structural deformation during flight. Strain gauges can be attached to the aircraft's structure to measure the amount of strain on that structure. The strain gauges can be wired to a data acquisition system, which records the strain readings and can transmit them to the ground for analysis. An alternative is to use laser displacement sensors that use lasers to measure the distance between two points on the aircraft's structure. By taking multiple readings at different points on the structure, it is possible to calculate the amount of deformation that has occurred. Another method is photogrammetry that involves taking photographs of the aircraft from multiple angles and using the images to create a three-dimensional model of the aircraft. By comparing this model to a reference model of the aircraft, it is possible to determine the amount of deformation that has occurred.

There are two popular methods for estimating the deformation of aircraft structures using strain data. The first method is known as Ko's displacement theory [87], and it uses a set of equations based on classical beam theory cast in terms of strain to estimate a beam's slope, transverse deflection, and cross-sectional twist angle. This

method was initially developed for highly-flexible aircraft wings, and it was first used in a flight test of NASA's Ikhana UAV [88]. Since then, it has been used on several other HARW aircraft [89–91]. Some changes to the original equations have been suggested to improve the method's performance in real-world conditions [92].

The second method for estimating aircraft structure deformation using strain data is called strain pattern analysis (SPA). It was developed by Gaukroger and Hassal [93], and it uses a set of strain and displacement modes to fit a measured strain pattern and estimate shape. The method relies on identifying strain patterns to recreate the shape of a given structure. The initial application of SPA involved creating mode shapes using static measurements of approximate shapes. Bousman [94] later investigated using numerically-estimated rotor flapwise mode shapes. This method has been considered for various aerospace applications, including identifying structural shapes [95, 96]. Recently, it has also been used in civil applications, such as structural health monitoring applied to bridges [97]. Mode shapes are essential in SPA to estimate the shape of deformed wings during flight. This method has some advantages, such as the ability to be used with a reduced number of measurement points and affordable and small strain measurement equipment. It also has low processing overhead and provides consistent measurements regardless of lighting conditions [78].

These methods for estimating aircraft structure deformation require the use of sensors to measure the strain generated by a beam's deformation. The most common type of sensor is the resistive foil strain gauge [98], which consists of a metallic foil pattern backed or encased in an insulating material. The foil strain gauge works by changing its electrical resistance when deformed.

Another type of sensor is the fiber Bragg grating (FBG) sensor, which was first demonstrated by Hill et al. [99]. FBGs are selective reflector sensors that can reflect specific wavelengths of light while allowing other wavelengths to pass with minimal attenuation. This is achieved using periodic variations in the refractive index of an optical fiber's core. FBG sensors are becoming a popular alternative to traditional strain gauges because of their benefits, such as the ability to daisy-chain multiple sensors on a single fiber, the ability to conduct measurements over long distances, non-conductivity, and resistance to chemicals and radiation.

1.2.3 Aeroelastic Modeling in Multibody Dynamics

Multibody dynamics (MBD) is a convenient method for simulating multi-physics systems composed of rigid and flexible bodies with arbitrary types of nonlinearities dominated by large rigid-body motion [100, 101]. It focuses on modeling the interaction between interconnected bodies when subjected to complex loading cases. This formulation is capable of describing the large overall rigid-body motion of systems, making it possible to efficiently analyze and optimize the dynamic behavior of systems for improved load-carrying capacity or performance behavior.

When analyzing a mechanical system, it becomes essential to model the kinematic coupling between bodies. This modeling can be achieved using algebraic constraint equations [101]. These constraints are used to model idealized joints that allow relative motion between bodies. Constraint equations are, in general, highly nonlinear equations that are functions of both the system configuration and time. The constraint equations can be coupled with the system's equations of motion leading to a set of constrained equations of motion for the entire system. This set of equations contains both algebraic and differential terms. Due to the nonlinearity of both the constraint equations and the overall motion of the system, in general, there is no analytical closed-form solution to the constrained equations of motion, suggesting that efficient numerical solution techniques are required to simulate the system's behavior over time.

Multibody dynamics was originally developed as a general method for analyzing mechanisms made up of rigid bodies. Schiehlen [102] provides a review of foundational work in this field. It was later expanded to include flexible systems, generally following two paradigms: first, by combining linear finite element (FE) modeling with arbitrary rigid-body dynamics described by a floating frame of reference formulation (FFRF); and second, by directly modeling nonlinear finite elements within the multibody formalism using absolute nodal coordinates, sometimes referred to as absolute nodal coordinate formulation (ANCF), as demonstrated by Shabana [103].

The ability to model arbitrary large displacements and rotations, generic force definitions and joints between rigid and flexible bodies are some of the cornerstones of multibody dynamics methods. The equations of motion that arise from a multibody dynamics formulation act as the glue capable of coupling large rigid-body motion with flight mechanics and elastic deformation without the need to develop dedicated monolithic formulations.

Structural models in MBD are typically reduced as much as possible while still accurately reproducing the relevant physics. Compared to typical FE models used for dynamics analysis, models used in multibody dynamics are often quite simple. Geometrically nonlinear finite element models in absolute coordinates, using beam or shell elements in specific cases, are also sometimes used. In the field of aerospace, MBD is particularly useful for preliminary design as it allows for a medium level of complexity in structural modeling. This makes it well-suited for early-stage design work.

Multibody dynamics is a useful tool for combining flight mechanics with the aeroelastic simulation of aircraft. This approach allows for an efficient representation of both elastic motion and arbitrary rotations, making it ideal for multi-physics simulations that include nonlinearities. It allows for direct modeling of structural dynamics, servo-systems, controls, and nonlinearities such as backlash, free-play, friction, and generic nonlinearities all within a single framework.

The aeroelasticity of very flexible aircraft has been studied using nonlinear beam models coupled with aerodynamic formulations ranging from strip theory to unsteady vortex lattice method (UVLM) and CFD [23, 26, 104–106]. However, less focus has been devoted to the use of multibody simulation for the modeling of novel flexible aircraft configurations. Novel aircraft configurations, such as HARW and joined-wing configurations, can exhibit large deformations during a typical flight. In order to simulate both the elastic deformations arising from the flexible wings of these aircraft configurations and the high inertial effects arising from dynamic flight maneuvers, MBD methods are an attractive alternative for studying these coupled dynamic systems.

Multibody dynamics has been used to simulate the maneuvering of flexible fixed-wing aircraft coupled with aerodynamic methods of various levels of fidelity. Spieck et al. [107] presented a multibody simulation-based analysis and simulation framework for studying the maneuvering of free-flying elastic aircraft. The focus was on the challenge of accurately representing aerodynamics in a hybrid multibody system. Scarlett et al. [108] performed aeroelastic simulations of a folding wing combat UAV by integrating finite element modeling, aerodynamic loading, and continuous-time multibody simulation. Simulated wind tunnel tests consisting of changing flight conditions and morphing wing states were performed using their developed framework. The study of the flight mechanics stability of a HALE configuration is an example of the work done by Krüger and Spieck [109, 110] and Krüger [111, 112]. Another

example is the work of Zhao and Ren [113] on the aeroelastic stability analysis and flight control in maneuvers of a UAV-like flexible aircraft.

Cavagna et al. [16] coupled multibody system dynamics with CFD for the aeroelastic analysis of detailed aircraft models performing arbitrary free flight motion. Castellani et al. [114, 115] developed a procedure for the nonlinear static aeroelastic analysis of HARW aircraft subject to geometric nonlinearities based on multibody dynamics employing strip theory for the aerodynamic formulation and compared the results with a nonlinear FE method coupled with a glsdlm for the aerodynamics. They emphasized the importance of considering the follower nature of aerodynamic forces and large displacements and rotations in the structural dynamics. This framework was later applied to a flexible HARW commercial aircraft, and both trim and gust response analyses were performed in order to calculate flight loads [116].

More recently, Li et al. [117] and Joshi et al. [118] presented a three-dimensional partitioned aeroelastic formulation for a flexible multibody system interacting with incompressible turbulent fluid flow. The framework used a corotational formulation, where the displacement of the body is decomposed into a rigid-body rotation and a small strain component. The framework was applied to study the flow across a bat's flexible flapping wing, modeling the bone fingers as beams and the flexible membrane as thin shells in the multibody system along with the joints. Savino et al. [119] coupled a mid-fidelity aerodynamic solver based on the vortex particle method (VPM) for wake modeling to a multibody dynamics code to improve the accuracy of aeroelastic numerical analysis performed on rotary-wing vehicles. The transient roll maneuver of a complete tiltrotor aircraft was simulated. The aerodynamic interactional effects that characterize rotary-wing aircraft were accurately captured with limited computational cost compared to conventional, higher-fidelity CFD tools. Tamer [120] used flexible multibody dynamics to simulate a wing's response to store separation. A highly-compliant wing was used with a rigid body mounted on it to represent an external store. A simulation of the wing response before and after the store separation was performed to show the benefits of the method.

Few studies have focused on modeling aeroelasticity using a multibody dynamics formulation based on absolute coordinates. Most of the work has employed FFRFs, corotational formulations, or geometrically exact beam formulations (GEBFs). The studies of Otsuka and Makihara [121, 122] and Otsuka et al. [123, 124] are perhaps the only ones in the literature where aeroelasticity has been studied using an ANCF. In their work, they employed a multibody dynamics framework based on geometrically

nonlinear ANCF beams to study morphing deployable wings expected to be used for Mars exploration. They simulated the rigid-body rotation of the wing around the kinematic constraints as induced by the aeroelasticity.

1.2.4 Nonlinear Aeroelastic Analysis Tools and Methods

Aeroelasticity is an important consideration in aircraft design, as it refers to the way in which an aircraft's structure and aerodynamics interact with each other. This can affect the aircraft's stability and performance, so it is important for designers to consider aeroelastic effects during the early design phases.

One way that aeroelasticity is incorporated into aircraft design is through the use of computer modeling and simulation. This allows designers to test different design concepts and evaluate their aeroelastic behavior before building physical prototypes. This can help to identify potential problems early on and allow designers to make any necessary changes before proceeding to more costly and time-consuming stages of development.

Another way that aeroelasticity is considered during the design process is through wind tunnel testing, which allows designers to evaluate how an aircraft's structure and aerodynamics interact under different conditions.

The spectrum of analysis tools for aircraft design and simulation ranges from low-fidelity tools with run times of seconds to high-fidelity tools with run times of days or weeks (fig. 1.4). For the preliminary design phases of aircraft, it is of particular importance to choose numerical tools with low computational times to allow for a rapid iterative design.

In terms of aerodynamic modeling, blade element momentum theory (BEMT), lifting line theory (LLT), vortex lattice methods (VLMs), and panel methods are examples of aerodynamic tools widely used in conceptual aircraft design due to their low computational times at the cost of reduced fidelity. They are great tools for running simple analyses on a personal computer. Corrections can be introduced into simple models such as BEMT and VLM to include some steady interactional aerodynamics.

Even though low-fidelity methods are capable of capturing some steady interactional aerodynamics during conceptual design, they fail to predict unsteady phenomena. In the low-to-medium fidelity range of the spectrum, free-wake methods like unsteady lifting line theory (ULLT), UVLM, and unsteady panel methods can predict a limited

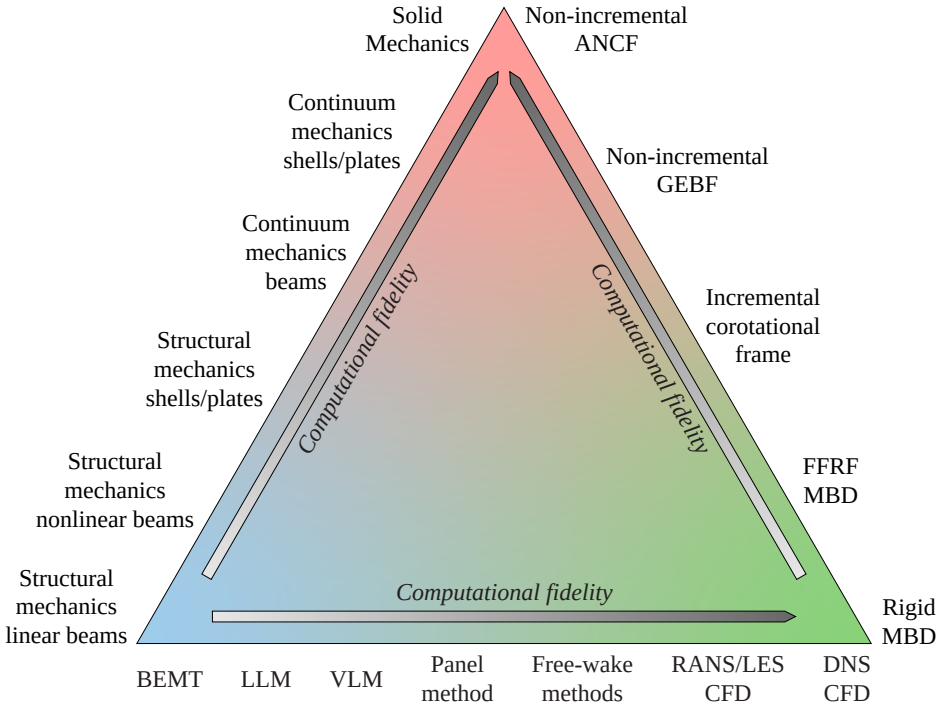

Figure 1.4: Spectrum of fluid mechanics, dynamics, and structural mechanics methodologies for aeroelastic analysis.

range of unsteady interactional aerodynamics.

Free-wake methods have been used in fixed-wing and rotorcraft applications, showing runtimes between tens of minutes to hours on a personal computer. However, the range of applicability of these methods is still limited. In advanced rotorcraft applications, for example, preserving wake connectivity makes free-wake methods numerically unstable when simulating the mixing of wakes and turbulent breakdown, like in mixing two rotor wakes [125]. In the high-fidelity end of the spectrum, mesh-based CFD approaches like unsteady Reynolds-averaged Navier-Stokes (URANS), large eddy simulation (LES), detached eddy simulation (DES), Lattice Boltzmann method (LBM) and direct numerical simulation (DNS) are capable of capturing the full range of interactional aerodynamics.

High-fidelity CFD can help researchers better understand the full range of unsteady aerodynamic interactions of aircraft configurations but generally requires supercomputer resources with runtimes of days or weeks. Its high computational cost precludes CFD from being used in the early stages of design and is reserved for detailed design phases of aircraft.

There appears to be a gap in the medium-to-high fidelity spectrum of aerodynamic

analysis tools available to aircraft designers capable of predicting complex unsteady aerodynamics at a computational cost adequate for conceptual and preliminary design.

Simulating the motion of flexible aircraft systems characterized by high inertia forces and motion discontinuities is sometimes accompanied by computational issues when large displacement finite element formulations are used to simulate the system dynamics. These issues are due to the high nonlinearities in the equations of motion, the coupling of the elastic and reference motions, high inertia forces, and possible motion discontinuities.

Several commercial and research software tools exist for modeling the dynamics of multibody systems. The IFToMM Technical Committee for Multibody Dynamics defines new directions for research and development in multibody system dynamics and presents a list of commercial, no-cost, and free software for multibody dynamics analysis.

Adams is a widely-used commercial software tool by MSC Software, now Hexagon, for modeling the dynamics of mechanical systems including joints and constraints. Adams solves the equations for kinematic, static, quasi-static, and dynamic simulations and offers an advanced visualization of solutions [126].

Simpack is a multibody simulation commercial software for the dynamic analysis of complex mechanical systems. The motion of multibody systems and the computation of coupled forces, accelerations, and stresses in individual parts of the mechanical system can be investigated. Different computation methods can be chosen for the solution of the equations of motion for the mechanical system [127].

Neweul-M^2 is a software package developed in the Institute of Engineering and Computational Mechanics at the University of Stuttgart for the simulation of the dynamic behavior of multibody systems [128]. This software package allows the user to change the solver and formalism properties, but also to implement user-specific extensions.

RecurDyn is a multibody dynamics software combined with a nonlinear finite element formulation. Dynamic motion results including stress analysis, flexible body contacts and nonlinear deformation can be computed in a very efficient way [129]. A control design tool and an intuitive graphical user interface are included.

Robotran is a research software from the Université Catholique de Louvain. Kinematic and dynamic equations are generated symbolically and exported as subroutines written in MATLAB or C and, therefore, can be integrated into any other numerical computation software [130].

MBDyn is an open-source research software package developed at the Politecnico di Milano. It solves initial-value problems in mechanical, aeroelastic, hydraulics and other disciplines. It includes a wide variety of constraints and basic control blocks and can be easily extended for user-specific applications [131].

The previous list of software packages is incomplete and not up-to-date, and a GitHub search reveals that more than seventy repositories containing open-source multibody dynamics simulation software exist today. Of the more than seventy projects found, the most starred ones include Simbody, Project CHRONO, the Robotics Library (RL), PyDy, and others, which appear to be actively maintained.

Simbody is a high-performance, open-source C++ toolkit for science and engineering-quality simulation of articulated mechanisms, including biomechanical structures such as human and animal skeletons, mechanical systems like robots, vehicles, and machines, and anything else that can be described as a set of rigid bodies interconnected by joints, influenced by forces and motions, and restricted by constraints [132].

Project CHRONO, developed in the Simulation-Based Engineering Lab (SBEL) at the University of Wisconsin–Madison, is an open-source multi-physics package used to model and simulate the dynamics of large systems of connected rigid and deformable bodies governed by differential-algebraic equations (DAEs) [133]. It is implemented almost entirely in C++ but provides Python and C# application programming interfaces (APIs). The core functionality of Chrono provides support for the modeling, simulation, and visualization of rigid and flexible multibody systems with additional capabilities offered through optional modules.

The Robotics Library (RL) is an open-source self-contained C++ library for rigid-body kinematics and dynamics, motion planning, and control [134]. It covers spatial vector algebra, multibody systems, hardware abstraction, path planning, collision detection, and visualization. It is being used in research projects and education and is free for commercial applications.

PyDy, short for Python Dynamics, is a workflow that utilizes an array of scientific tools written in the Python programming language to study multibody dynamics and a set of software packages that help automate and enhance the workflow [135]. The core of this toolset is the SymPy mechanics package which generates symbolic equations of motion for complex multibody systems, and PyDy, which extends the SymPy output to the numerical domain for simulation, analysis, and visualization.

Several aeroelastic analysis tools exist today, including both commercial and open-source options, that are used by aerospace engineers to simulate the behavior of aircraft

structures and systems under a variety of conditions, including both steady-state and dynamic load conditions. One of the most commonly used aeroelastic analysis tools is perhaps NASTRAN, a finite element analysis (FEA) software program that was originally developed for NASA in the late 1960s and early 1970s. It is capable of performing static and modal linear structural analysis through the `SOL 101` and `SOL 103` solution sequences, respectively, nonlinear static and transient structural analysis, with the `SOL 106` and `SOL 129` solution sequences, respectively, among others [136].

There are four solution sequences that relate to aeroelasticity in NASTRAN. `SOL 144` solves quasi-steady aeroelastic problems. It can be used to obtain aerodynamic forces and pressures on the aerodynamic elements for different trim conditions. Aerodynamic loads are first calculated using the doublet lattice method (DLM), although other aerodynamic solvers are available within NASTRAN. Spline functions transfer these loads onto the structural model, and a linear FE analysis calculates structural displacements. This solution sequence is also capable of static aeroelastic divergence analysis. NASTRAN also includes `SOL 145` and `SOL 146` to solve aeroelastic flutter problems and dynamic aeroelasticity problems, respectively. Finally, the design sensitivity and optimization solution sequence `SOL 200` can be used for multidisciplinary analysis, and design [137].

ZAERO is a software package that integrates all essential disciplines required for advanced industrial aeroelastic design and analysis. It allows for the analysis of aircraft behavior in different conditions, using high-fidelity modeling of aircraft geometry and accurate interfacing between structural and aerodynamic models. The tool can be used to perform various types of analyses, including flutter, static aeroelasticity, and aeroservoelasticity. It can be applied to subsonic, transonic, supersonic, and hypersonic aircraft. ZAERO integrates quite well with NASTRAN, augmenting the latter's aeroelasticity capabilities. It packages aerodynamic solvers of different fidelity, including `ZONA6`, a higher-order panel formulation for subsonic unsteady aerodynamics, `ZTRAN`, that solves the time-linearized transonic small disturbance equations using an overset field-panel method, `ZONA7`, a panel formulation for supersonic unsteady aerodynamics, and others [138].

Patil and Hodges [29] developed the NATASHA code based on the finite-state airloads models presented by Peters et al. [139], and the geometrically exact intrinsic beam formulations of Hodges [140, 141].

Cavagna et al. [142–144] developed the Next generation Conceptual Aero Structural Sizing (NeoCASS) MATLAB framework, which couples a nonlinear C^0 beam

formulation based on the finite volume concept [145] with an aerodynamic solver based on the VLM.

OpenFAST, formerly known as FAST [146], is a physics-based engineering tool for simulating the coupled dynamic response of wind turbines developed at the National Renewable Energy Lab (NREL). OpenFAST uses a GEBF to model the structural dynamics and an actuator-line-based aerodynamic solver to enable coupled nonlinear aero-hydro-servo-elastic simulation in the time domain. The wake is modeled using quasi-steady BEMT.

Drela developed the ASWING software code [147–149] for the aerodynamic, structural, and control-response analysis of aircraft with flexible wings and fuselages of high to moderate aspect ratio. It is based on geometrically nonlinear beams with approximated rigid-body dynamics. Aerodynamics are modeled using a LLT solver with prescribed coefficients.

Cesnik and Brown [150], Su et al. [151], and Wan and Cesnik [152, 153] used a strain-based beam formulation along with a two-dimensional finite inflow theory [154] in the development of the University of Michigan's Nonlinear Aeroelastic Simulation Toolbox (UM/NAST). The framework was used to develop a highly flexible aircraft flown to validate the code [71–73].

More recently, del Carre et al. [155–157] have developed SHARPy, a nonlinear aeroelastic analysis package developed at Imperial College London. SHARPy is open-source and can be used for the structural, aerodynamic, and aeroelastic analysis of flexible aircraft, flying wings, and wind turbines. The structural model is a geometrically exact composite beam (GECB) and supports multibody features such as hinges, joints, and absolute and relative nodal velocity constraints. The aerodynamic solver is an UVLM. It can simulate an arbitrary number of surfaces together with their interactions. A non-conventional force evaluation scheme is used to support large sideslip angles and obtain an induced drag estimation. Added mass effects can be obtained and introduced into the problem.

A summary of the most relevant aeroelastic modeling and analysis tools currently available is shown in table 1.1.

Name	Structural formulations	Aerodynamic formulations	License	Language	Source code
NASTRAN [136]	Linear FE [137]	Strip theory and DLM [137]	Commercial	FORTRAN	No
ZAERO [138]	Uses NASTRAN	Several [138]	Commercial	FORTRAN	No
NATASHA [29]	GEBF-based [140, 141]	Finite-state airloads [139]	N/A	N/A	No
NeoCASS [142]	Finite volume C^0 beams [145]	VLM	Open-source GPL-2.0	MATLAB	Yes
OpenFAST [146]	GEBF	BEMT-based	Open-source Apache-2.0	FORTRAN	Yes
ASWING [147]	FFRF with geometrically nonlinear beams [148, 149]	LLT-based [148, 149]	Commercial and academic	FORTRAN	Yes, with academic license
UM/NAST [150]	FFRF with strain-based beams [151]	2D finite inflow theory [154]	N/A	N/A	No
SHARPy [157]	GECB	UVLM	Open-source BSD-3-Clause	Python	Yes

Table 1.1: Overview of currently available commercial, research, and open-source aeroelastic analysis tools.

1.3 Objectives

The overall objective of this work was to characterize the aeroelastic behavior of novel aircraft models through the design and testing of flexible linear and nonlinear reduced-scale UAV demonstrators and to explore the development of medium-fidelity tools for the dynamic aeroelastic analysis of such models. This objective created four main challenges:

1. Design of HARW and joined-wing aircraft configurations. This involved developing computational structural, aerodynamic, and aeroelastic models using different industry-standard numerical analysis tools in optimization loops to generate configurations with the correct degree of flexibility for the desired static and dynamic behavior.

2. Manufacturing, testing, and characterization of these aircraft configurations. Manufacturing was a tenuous process that required collaboration with many partners and iteration on many aspects of the design. Characterization was conducted through a series of ground tests and flight tests.

3. Validation of computational models with experimental flight test data. This required an update of all computational models through a modal update process. Time-dependent aeroelastic simulations were set up to simulate the same conditions of the flight tests to help validate the models.

4. Development of a medium-fidelity aeroelastic framework. This yielded an exploratory study on the use of flexible multibody dynamics in conjunction with medium-fidelity fast aerodynamic methods to investigate the dynamic aeroelastic behavior of HARW and joined-wing aircraft configurations. This involved developing a unified computational framework and evaluating its effectiveness through different test cases.

1.4 Research Contributions

This thesis presents work on the development of better tools for the aeroelastic characterization of flexible aircraft. It attempts to accomplish this by developing experimental reduced-scale flexible HARW and joined-wing UAV models, and fully characterizing them using existing computational tools of different levels of fidelity.

First, different aeroelastic models of the aircraft are developed and compared against each other through static and dynamic analyses. Second, the process of development and testing of flexible aircraft vehicles is described. Finally, flight-testing of the vehicles leads to the collection of a rich set of flight-test data, which allows for the validation of computational aeroelastic models.

This work also tries to make a case for better medium-fidelity aeroelastic tools by developing a unified framework for coupling flexible multibody dynamics with an accelerated.

The contributions resulting from the thesis are in the area of airworthiness investigation, aeroelastic characterization, performance evaluation and structural characterization of reduced-scale flexible novel aircraft vehicles, and development of better numerical tools for dynamic aeroelastic modeling.

The following are the main contributions made in this thesis towards a better understanding of coupled nonlinear aeroelastic–flight dynamics effects in flexible aircraft structures and improving numerical analysis tools in the field of aeroelasticity:

1. **In-depth literature survey** on the aeroelasticity of HARW and joined-wing aircraft configurations, development and testing of reduced-scale flexible aircraft models, the use of multibody dynamics for the study of aeroelasticity, and the currently available nonlinear aeroelastic analysis tools and methods.

2. **Aeroelastic analysis of HARW aircraft configurations** through the complete design, numerical modeling, ground and flight testing of a flexible reduced-scale HARW aircraft configuration. This research work was conducted in partnership with EMBRAER S.A. and aimed at studying the dynamic behavior of a reduced-scale UAV designed to be very flexible and exhibit coupling of flight-dynamics and structural modes. A complete study was performed, from sizing, design, ground and flight testing, numerical modeling, and validation of results with flight test data. Preliminary results from this work were presented at IFASD 2017. More recently, a conference paper was submitted to AIAA Scitech 2019, and a journal paper was published in Aerospace Science and Technology:

    - F. Afonso et al. “Validation and Evaluation of a Nonlinear Aeroelastic Framework Using Flight Test Data”. In: *International Forum on Aeroelasticity and Structural Dynamics (IFASD) 2017*. 2017
    - S. Warwick et al. “Measurement of Aeroelastic Wing Deflections Using

Modal Shapes and Strain Pattern Analysis". In: *AIAA Scitech 2019 Forum*. 2019. DOI: 10.2514/6.2019-1116

- M. Bras, S. Warwick, and A. Suleman. "Aeroelastic evaluation of a flexible high aspect ratio wing UAV: Numerical simulation and experimental flight validation". In: *Aerospace Science and Technology* 122 (2022), p. 107400. DOI: 10.1016/j.ast.2022.107400

3. **Investigation of the nonlinear aeroelastic behavior of joined-wing aircraft configurations** through the development and testing of an aeroelastically-tuned joined-wing UAV with flexible front and aft wings. This research work was conducted in partnership with Boeing. The aircraft was a reduced-scale version of Boeing's JWSC and was designed to show geometric nonlinearities under normal flight conditions. This work generated static load and ground vibration test data and preliminary flight test data, which helped validate the aeroelastic models created. This work was submitted for publication in AIAA Journal:

   - M. Bras and A. Suleman. "Numerical and Experimental Characterization of the Nonlinear Aeroelastic Behavior of a Highly-Flexible Joined-Wing UAV". In: *AIAA Journal* (2023). Submitted

4. **Development of a medium-fidelity aeroelastic analysis tool** through a unified framework coupling a flexible multibody dynamics formulation and an accelerated unsteady three-dimensional panel method. An oral publication was given at EngOpt 2018. A journal publication based on this work is currently being prepared for submission:

   - M. Bras, C. Crawford, and A. Suleman. "A Modern Free-Wake Panel Method Using Unstructured Meshes". In: *6th International Conference on Engineering Optimization (EngOpt) 2018*. 2018. Oral presentation
   - Journal publication in preparation

Other contributions of this research in the areas of design, optimization, and integration of UAV systems resulted in two NATO Science and Technology Organization (STO) Lecture Series:

- M. Bras, J. Richards, and A. Suleman. *Unmanned Air Systems*. Tech. rep. STO-LS-AVT-274. NATO, 2018

- M. Bras et al. *Air Platforms Design, Optimization, Propulsion and Flight Control Systems*. Tech. rep. STO-LS-AVT-274. NATO, 2018

Work on the inclusion of viscous effects in three-dimensional panel methods by coupling it with a two-dimensional interactive boundary layer procedure was also performed and resulted in the following oral presentation:

- D. Brandão, M. Bras, and A. Suleman. "Static Aeroelastic Analysis of Flexible Wings Using a 3D Panel Method Including Viscous Flow Effects". In: *63rd Aeronautics Conference (AERO) 2017*. 2017. Oral presentation

Finally, work related to topology optimization of wing box cross-sections applied to HARW aircraft using heuristic methods was also conducted. An oral presentation was given at AERO 2017 and a paper was presented at CANCAM 2017:

- R. Diogo et al. "Topology Optimization of a High Aspect Ratio Wing Box Using an Ant Colony Optimization Algorithm". In: *63rd Aeronautics Conference (AERO) 2017*. 2017. Oral presentation
- M. Bras et al. "Ant Colony Optimization Algorithm Applied to Topology Optimization of Aircraft Structures". In: *26th Canadian Congress of Applied Mechanics (CANCAM) 2017*. 2017

1.5 Thesis Outline

This dissertation consists of three separate but related works that have been published, submitted for publication, or are in the process of being prepared for submission to peer-reviewed academic journals. Each main chapter is self-contained and presents a complete work, including its own introduction, specific objectives, methodology, results, discussion, and conclusions.

Chapter 2 describes the work performed on sizing, design, ground and flight testing, numerical modeling, and validation of a flexible HARW UAV platform. The UAV has a wing aspect ratio of 13, and its wing structure was designed such that it reaches large deformations at low subsonic flight conditions. The flexible aircraft platform allows for validation and evaluation of the aeroelastic behavior and flight dynamics of HARWs. Experimental data consisting of static load tests, ground vibration tests, and flight tests are compared with the results generated from aerodynamic, structural,

and aeroelastic computational models developed in AVL, NASTRAN, and ASWING, respectively.

In chapter 3, the design, sizing, numerical modeling, ground testing, and validation of an aeroelastically-tuned JWSC UAV platform with flexible front and aft wings is presented. The flexible wing airframe was designed to exhibit geometric nonlinearities under normal flight conditions. This flexible aircraft platform can be pushed to high g loading cases that allow for the investigation of its nonlinear aeroelastic behavior, flight dynamics, and validation of computational models. Experimental data consisting of static load tests, ground vibration tests, and preliminary flight tests are compared with the results generated from aerodynamic, structural, and aeroelastic computational models developed in AVL, NASTRAN, and ASWING, respectively.

Chapter 4 presents work on the development of a medium-fidelity aeroelastic tool using an accelerated low-order panel method and a flexible multibody dynamics formulation based on absolute coordinates. The main objective of this work is to propose a versatile framework that can be applied to the time-domain analysis of aeroelastic models based on flexible multibody dynamics and unsteady aerodynamics. The three-dimensional unsteady panel method is accelerated using the fast multipole method (FMM) and is coupled with a flexible multibody dynamics formulation based on absolute coordinates through a weak fluid-structure interaction (FSI) scheme. The transfer of information between solvers is accomplished through radial basis function (RBF) interpolation. The steady-state aerodynamic solution and unsteady aeroelastic response of a flexible HARW and a JWSC UAV models are studied and compared against aerodynamic and aeroelastic models developed in AVL and ASWING, respectively.

In chapter 5, the major developments of the thesis are revisited. Conclusions and remarks are drawn from the findings of the work. An outlook on possible future research directions is given.

Chapter 2

Aeroelastic Evaluation of a Flexible High Aspect Ratio Wing UAV: Numerical Simulation and Experimental Flight Validation

This chapter presents the work performed during a multi-year project developing a flexible-wing HARW UAV, conducted in partnership with EMBRAER S.A. The design, sizing, ground testing, and flight testing of a UAV platform with a flexible wing are discussed in this chapter. The flexible aircraft platform allows for validation and evaluation of the aeroelastic behavior and flight dynamics of HARW aircraft. Experimental data consisting of static load tests, ground vibration tests, and flight tests are compared with the results generated from aerodynamic, structural, and aeroelastic computational models. The work is based on the following publication:

M. Bras, S. Warwick, and A. Suleman. "Aeroelastic evaluation of a flexible high aspect ratio wing UAV: Numerical simulation and experimental flight validation". In: *Aerospace Science and Technology* 122 (2022), p. 107400.
DOI: 10.1016/j.ast.2022.107400

Abstract

Aeroelastic phenomena occur when aerodynamic and structural loads interact in an unstable manner. This is a major concern in the design of modern HARW aircraft, as these structures are more prone to deflection during flight and thus affect flight performance. Studying these effects in full-scale aircraft is prohibitively costly and risky. Scaled flight test demonstrators with flexible wings offer a low-cost and low-risk solution to evaluate the aeroelastic response of HARW aircraft.

In this work, the sizing, design, and testing of an in-house developed flexible-wing UAV is presented. First, the rigid-wing aircraft platform and its performance characteristics are presented, followed by wing modifications to make it flexible. The wing flexibility was designed such that the coupling of flight-dynamic modes and elastic modes is observed in flight. A full numerical characterization of the aircraft was first performed, including structural, aerodynamic, and aeroelastic computational models. Next, ground vibration and static load tests were performed to validate the structural models. Flight tests were conducted to obtain data on aircraft dynamics, and strain measurements along the wing spar. An indirect shape reconstruction method based on strains was employed to extract wing displacements from measured strain data. Flight test data was then compared against simulated aeroelastic results.

It was observed that for the HARW flexible wing aircraft, a degree of coalescence between the aircraft's short period mode and the wing's first out-of-plane bending mode was present. By using different excitation functions applied to the control surfaces, this coalescence was recorded during flight tests, and good agreement with the simulated results was observed. The results obtained are an important step in the study of fluid-control-structure interaction issues in HARW aircraft.

2.1 Introduction

This work is concerned with the complete sizing, design, ground and flight testing, numerical modeling, and validation of a HARW UAV platform with a flexible wing. The UAV is based on an existing rigid wing platform with an aspect ratio of 13, and its wing structure was designed to reach large deformations at low subsonic flight conditions. The flexible aircraft platform allows for validation and evaluation of the aeroelastic behavior and flight dynamics of HARW aircraft. Experimental data consisting of static load tests, ground vibration tests, and flight tests are compared with the results generated from aerodynamic, structural, and aeroelastic computational models developed in AVL, NASTRAN, and ASWING, respectively.

The present chapter is organized as follows: In section 2.2, the reference rigid aircraft platform is described and the modifications required to make the wing flexible are explained. The description of the modeling and testing techniques adopted are the focus of section 2.3. In section 2.4, the results obtained for the HARW aircraft are presented and discussed, including the aeroelastic response of the HARW, ground test results used to validate and update computational structural models, and the comparison of data collected from the flight test campaign with the numerical aeroelastic simulations. Finally, section 2.5 summarizes the findings and conclusions of the study. An overview of the steps taken in this work to aeroelastically characterize a HARW is illustrated in fig. 2.1.

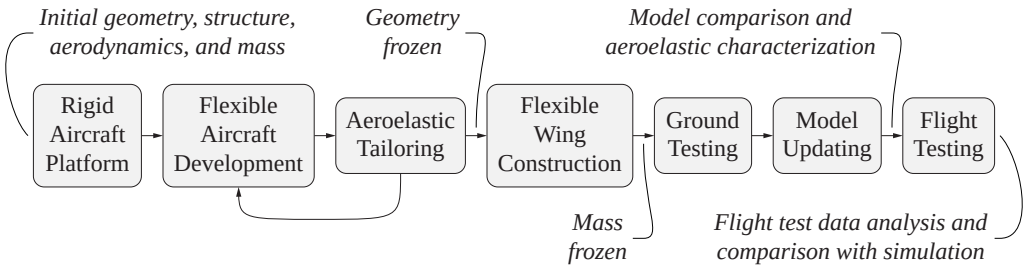

Figure 2.1: Timeline of the different tasks executed in chapter 2.

2.2 Flight Test Platform

The QT1 aircraft research platform is designed and optimized for surveillance and reconnaissance-type applications that require maximum time on station in a loitering pattern. Typically, this mission would include a take-off, climb out at best rate of climb, cruise or dash to station, loiter, cruise back, descent (with provisions for two go-arounds), and then landing. Two variants of the aircraft were designed, one consisting of a gas engine, for longer endurance, and a second one making use of an electric motor, for low-noise, low-vibration missions.

Flexibility of sensor payloads and a large, open fuselage were design drivers in lofting the fuselage outer mold line. Aerodynamic surfaces were modeled using LLT in preliminary sizing stages, empirical relations were used to predict the empty weight fractions based on payload size, fuel load, and wing area, and the propulsion systems were sized using parametric models calibrated from manufacturer data. A 3-view of the final design is shown in fig. 2.2.

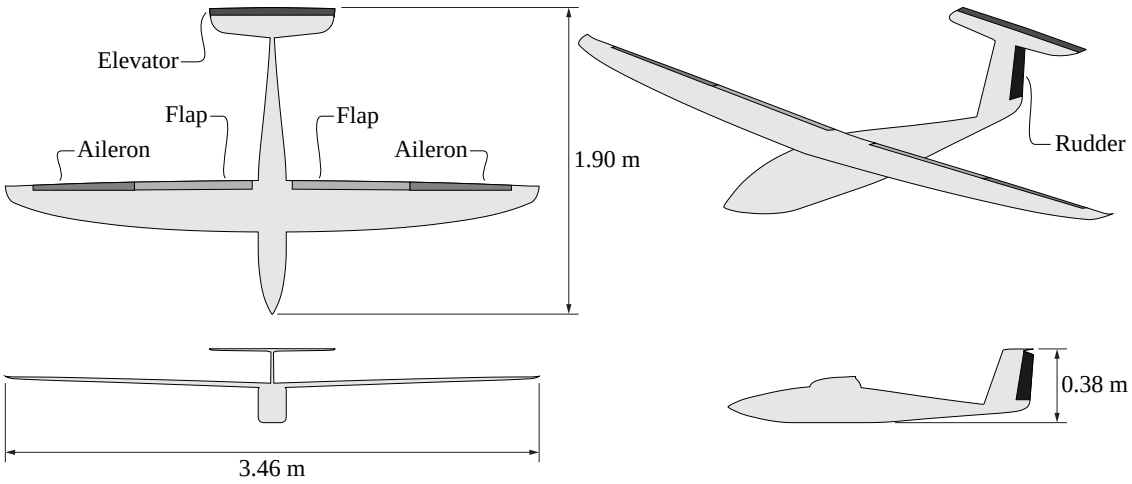

Figure 2.2: QT1 aircraft platform 3-view.

The aerodynamics, propulsion, and structural models of the aircraft were combined into an optimization framework. This framework allowed the automation of the simulation workflow. Constraint evaluations, trade studies, and optimizations were performed on variables ranging from propulsion sizing, wing geometry, airfoil selection, and mission speeds. The output of the optimization was then used to drive the detailed design of the aircraft. The final, as built, specifications of the aircraft are summarized in table 2.1 for both the electric and gas variants.

Parameter	Gas variant	Electric variant
Max. range	500 km	135 km
Max. endurance	more than 4 h	1.6 h
Cruise altitude	600 m AGL	600 m AGL
Ceiling	3000 m	3000 m
Empty mass	13.5 kg	12.8 kg
Max. take-off mass	21 kg	21 kg
Wing loading	170 to 214 N/m^2	163 to 214 N/m^2
Climb angle	11°	13°
Descent angle	−15°	−15°
Stall speed	15 m/s	15 m/s
Cruise speed	24 m/s	24 m/s
Loiter speed	21 m/s	21 m/s
Max. speed	32 m/s	35 m/s

Table 2.1: QT1 aircraft platform specifications.

2.2.1 Airframe and Components

Detailed structural sizing was performed on the optimized model to determine the required composites layup. A carbon fiber sandwich with a foam core was used in the construction of the airframe. FEA was performed using ANSYS with composite layups defined in. Since very few regulations existed at the time of the structural sizing, Federal Aviation Administration (FAA) guidelines for general-class manned aircraft were used to calculate limit loads. Some critical sizing constraints included a limit maneuvering load factor of $-1.5g$ to $3.8g$ ($2.0g$ with flaps deployed) and sizing to withstand vertical gusts of 15 m/s.

The QT1 aircraft platform was designed to have a high aspect ratio wing for sustained, endurance flight, and a T-tail configuration, to decrease the risk of damage to the tail during landing. The main properties of the different airfoil sections for each lifting surface of the aircraft are listed in table 2.2.

The QT1 has flown with a variety of payloads, including gimbaled cameras and data logging systems for collecting flight test data. In this work, the aircraft was configured for a data logging configuration that was used to measure more than 20 channels of strain, 4 accelerometers, inertial measurement unit (IMU) data, and

air data during flight testing to investigate the aeroelastic response of the aircraft. Figure 2.3 shows the QT1 aircraft design, highlighting the two internal wing spars, avionics and payload bays, fuselage frame structure, and internal components.

Lifting surface	**Airfoil**	**Max. thickness**	**Max. camber**
Wing root	SD7037	9.2 % at 26.1 %	2.5 % at 44.7 %
Wing tip	SD7032	10 % at 26.6 %	3.4 % at 45.1 %
Tail	NACA0008	8 % at 30 %	symmetric

Table 2.2: Geometry of airfoil sections used in the QT1 aircraft platform (percentages of chord).

Access to the payload bay is done through the top of the aircraft, as the entire fuselage top and wings are removable, allowing full access to the bay. The final payload volume and weight allowable are listed in table 2.3.

The climb constraints of the aircraft determined the final motor and propeller selection for the electric variant. The electric motor is an E-Flite Power 160 motor paired with a propeller from Rasa. The gas variant uses a Saito FG-30B 4-stroke gasoline engine paired with an APC propeller.

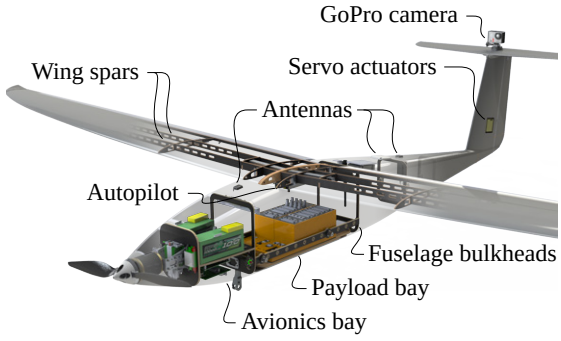

Figure 2.3: Airframe of the QT1 aircraft platform showing wing spars, avionics and payload bays, fuselage frame structure, and internal components.

For the electric configuration, lithium polymer (LiPo) batteries were used due to their ability to supply large burst currents, their high energy densities, and their

relatively low costs. The QT1 requires four battery packs, two in series and two in parallel, in order to achieve its 1.6 h of endurance at maximum take-off weight (MTOW). Each battery pack consists of 6 10 Ah prismatic cells in series, resulting in a final configuration of 12 series and 2 parallel cells. A Castle Creations Phoenix Edge HV 120 electronic speed controller (ESC) is used to control and regulate the speed of the motor. Figure 2.4 shows the QT1 aircraft propulsion system for the electric variant, with batteries installed.

Parameter	**Value**
Length	0.33 m
Width	0.175 m
Height	0.2 m
Volume	11.5 L
Mass	4.5 kg

Table 2.3: QT1 payload specifications.

The servo actuators used to control the different control surfaces were the Volz DA 14-05-60 with rated and peak torques of 6.3 and 30 Ncm, respectively, and a rated speed of $310^\circ\,s^{-1}$.

An in-house-developed ground control station (GCS) was used to provide support for remotely operating the aircraft. The ground station is a full-featured mobile command unit (MCU) housed within a 2013 Mercedes Sprinter van with space to hold a backup pilot, the GCS operator, and the payload specialist.

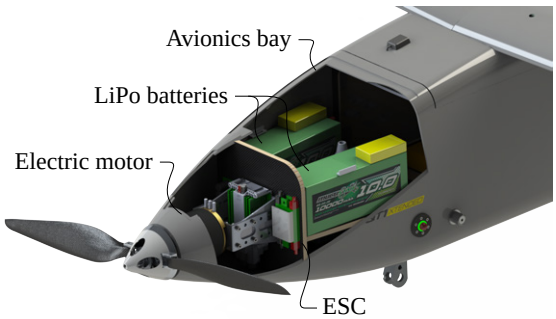

Figure 2.4: Avionics bay of the electric variant of the QT1 aircraft platform showing electric motor, ESC and LiPo batteries.

The aircraft is typically launched from a pneumatic catapult and recovered with a

belly landing. All phases of flight, from launch to landing, can be performed in either manual or fully autonomous mode.

2.2.2 Flight Control and Sensor Systems

The QT1 aircraft platform can be operated with several commercial off-the-shelf autopilots but is primarily operated with the Piccolo family of autopilots developed by CloudCap Technologies.

The Piccolo SL is a near fully self-contained autopilot system, with the only external equipment needed being Pitot and static tubes, and an optional magnetometer. The system includes hardware and software for the avionics, hardware, and software for the ground station, and a flight model development and simulation environment. Piccolo SL has been widely chosen for UAV flight control systems and flight tests have been conducted by several university and industry research programs [158–160]. The basic Piccolo system architecture is shown in fig. 2.5.

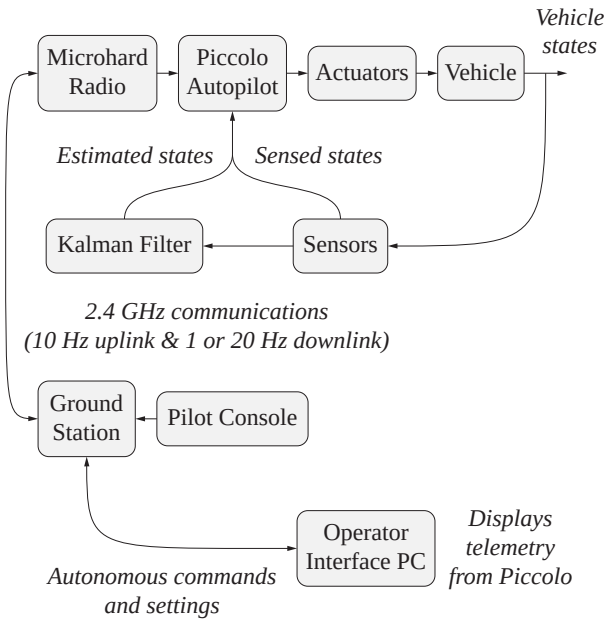

Figure 2.5: Piccolo SL system block diagram.

The system includes a 4 Hz uBlox module global positioning system (GPS) receiver, pressure sensors rated at 192 kts maximum indicated airspeed, and 3-axis gyroscopes rated at $300^\circ\,s^{-1}$. The Piccolo is driven by a 40 MHz core MPC-555 microprocessor. It has fourteen digital I/O lines, three serial ports, and four analog inputs. The digital

I/O lines are used both for payload I/O and servo actuation. A 44-pin connector is used to connect the I/O, serial, analog, and power lines to the autopilot.

An automatic flight test unit (AFTU) hardware module was developed to aid the autopilot in superimposing scripted commands during flight. Accompanying software was developed to allow the pilot to generate commands on the ground and submit them to the onboard unit. The AFTU module was necessary since the Piccolo SL autopilot does not natively support scripted commands other than doublet commands.

A VectorNAV IMU was also used in this work during flight testing to log aircraft accelerations and rates. Figure 2.6 shows the payload bay with two National Instruments data acquisition systems (DAQs), the AFTU module and the VectorNAV IMU installed.

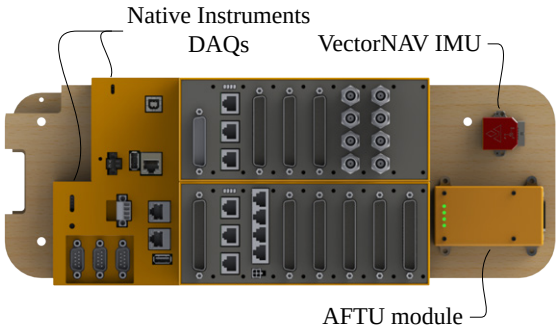

Figure 2.6: Payload bay of the QT1 aircraft with Native Instruments DAQ, AFTU module and VectorNAV IMU installed.

2.2.3 Wing Modification

A significant portion of this work was spent on the modification of the existing rigid wing of the QT1 aircraft in order to make it flexible. The purpose of making the wing flexible was to lower the frequencies of the wing elastic modes and bring them closer to the frequencies of the flight-dynamic modes. The added flexibility must be such that the aircraft's rigid-body motion of should couple with the wing's elastic deformation. In order to achieve this, a parametric optimization process was carried out to determine a set of feasible modifications to the aircraft wing.

Initially, NASTRAN and ASWING models of the rigid aircraft were created. The carbon fiber spars of the rigid aircraft were not good candidates for attaching strain gauges, in addition to being too complex to modify and achieve the desired level of wing flexibility. It was determined that the best course of action would be to replace

the carbon fiber spars of the rigid wing with a single aluminum spar and tailor the cross-section of this spar to give more or less flexibility to the wing. The spars were then replaced by aluminum ones in the models, with an initial reasonable value for the cross-section area. Wing tip mass points and spanwise running masses were also added to the models. These three parameters—wing tip mass, spanwise running masses, and spar cross-section area—formed the space of design variables of the parametric optimization process. Different aerodynamic, aeroelastic, and structural analyses were defined for which constraints were checked during the parametric optimization process. These included: aircraft flying qualities calculated from ASWING flight-dynamic modes; short-period–wing-bending mode proximity from an ASWING aeroelastic analysis; separation of elastic modal frequencies from a NASTRAN modal analysis; maximum static wing deflection and stress for a quasi-steady $3g$ pull-up and launch maneuvers calculated from NASTRAN. The objective of the parametric optimization process was to maximize, to some extent, the coupling between short-period and wing-bending modes while checking the results of these analyses and making sure they were within the set constraints.

In addition to replacing the wing carbon fiber spars with a single aluminum spar, another necessary modification to the wing was to prevent its skin from adding stiffness to the carefully sized aluminum spar. To achieve this, the skin was cut into spanwise sections, which were rigidly connected to the spar at single points along its span. The final design was achieved by applying these modifications to the inner section of the wing while leaving most of the outer section rigid. It was necessary to keep the outer section of the wing relatively rigid in order for control surfaces to be installed (see fig. 2.7). It is possible to see from the figure that the flaps covered most of the inner section of the wing. Because this section was made flexible, the existing flaps had to be removed from the final flexible design. To make up for this, the ailerons, located at the rigid outer section of the wing, had to function as flaperons during take-off and landing.

At the end of the wing modification process, two variants of the QT1 aircraft platform were available: the rigid-wing variant (rigid QT1), used mainly as a baseline platform for testing all the aircraft components; and the flexible-wing variant (flexible QT1), used in this work to investigate the aeroelastic response of the aircraft.

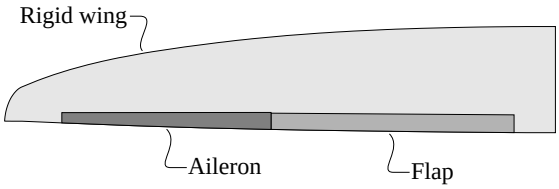

(a) Rigid wing

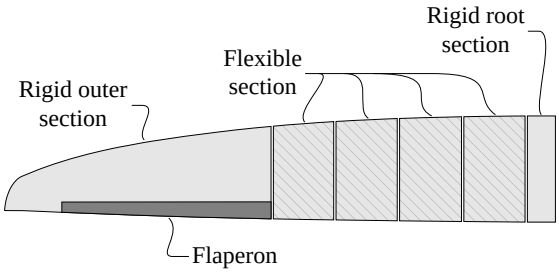

(b) Flexible wing

Figure 2.7: Comparison between rigid (top) and flexible (bottom) wing of the QT1 aircraft.

2.3 Modeling and Testing

The design of the flexible aircraft wing made use of different modeling and analysis tools. Structural, aerodynamic, and aeroelastic models had to be built to assess the performance of the final flexible aircraft. Since some of the used analysis tools were capable of modeling more than one discipline, a comparison between models generated from different tools was possible in some cases. This was essential to guarantee consistency between models. In addition to model comparison, validation with experimental tests was also performed for critical results. This allowed fine-tuning of the computational models and brought them closer to matching the final aircraft as built.

In this section, the tools and methods used to develop structural, aerodynamic, and aeroelastic models of the QT1 aircraft are first presented, followed by the methods used to reconstruct displacements from measured strains. Finally, the procedures and methods used to perform bifilar pendulum, static load, ground vibration, and flight tests are presented.

2.3.1 Structural Modeling

A structural NASTRAN model was developed to study the static elastic behavior of the aircraft wing (fig. 2.8). Static load analyses of the wing were conducted in order to obtain wing deflections for different load cases. Dynamic modal analyses were also performed in order to obtain modal frequencies and shapes for the flexible QT1 aircraft. NASTRAN is a FEA program developed by NASA for the aerospace industry capable of performing static and modal linear structural analysis, through the `SOL 101` and `SOL 103` solution sequences, respectively, nonlinear static and transient structural analysis, with the `SOL 106` and `SOL 129` solution sequences, respectively, among others [136].

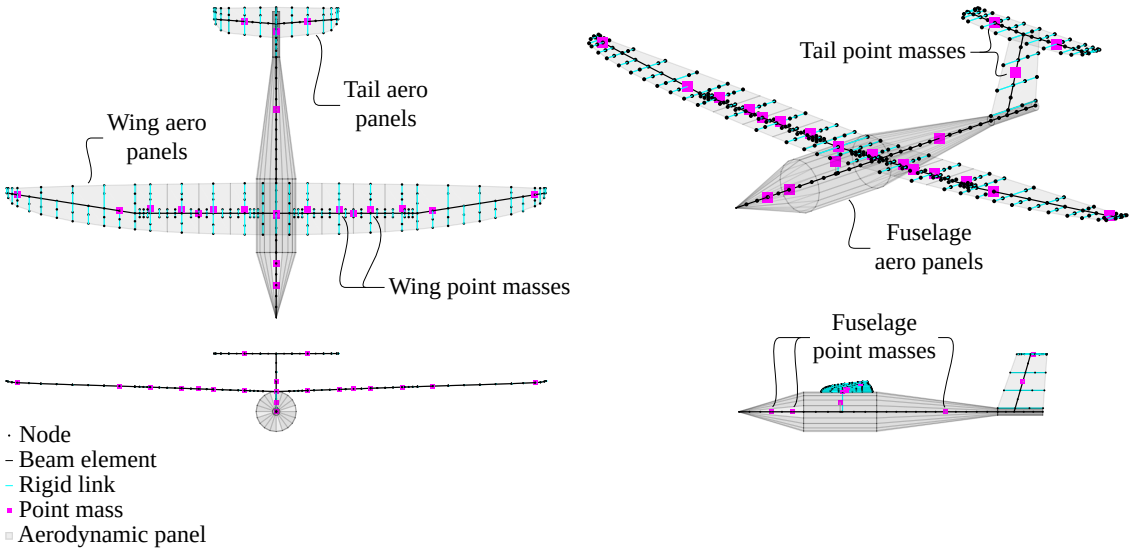

Figure 2.8: Structural NASTRAN model of the flexible QT1 aircraft with aerodynamic paneling.

There are four solution sequences that relate to aeroelasticity in NASTRAN. `SOL 144` solves quasi-steady aeroelastic problems. It can be used to obtain aerodynamic forces and pressures on the aerodynamic elements for different trim conditions. Aerodynamic loads are first calculated using the DLM, although other aerodynamic solvers are available within NASTRAN. Spline functions transfer these loads onto the structural model, and a linear FE analysis calculates structural displacements. In this work, the NASTRAN model was extended with aerodynamic panels, and this solution was used to set up quasi-steady pull-up, launch, and level-flight trim maneuvers. It was also used to extract stability derivatives in level-flight conditions. This solution sequence is also

capable of static aeroelastic divergence analysis, but this was not explored in this work. NASTRAN also includes `SOL 145` and `SOL 146`, to solve aeroelastic flutter problems and dynamic aeroelasticity problems, respectively. Finally, the design sensitivity and optimization solution sequence `SOL 200` can be used for multidisciplinary analysis, and design [137].

A second structural computational model was built using ASWING, developed by Drela at MIT for preliminary aircraft design of flexible aircraft [147]. ASWING can compute the steady and unsteady aeroelastic responses of an aircraft, including stability analyses, simulate flight dynamics that can include disturbances (usually in the form of gust profiles), and predict flutter boundaries. ASWING, like NASTRAN, can be used to study the static and dynamic behavior of an aircraft structure. It is also capable of modeling the aerodynamics of the aircraft and performing aeroelastic analyses. However, unlike NASTRAN, the aeroelastic analyses are nonlinear, and so geometric nonlinearities, as well as the follower nature of aerodynamic forces, are captured. Because of this, it was used throughout this work to study the aeroelastic behavior of the aircraft. ASWING is further described in section 2.3.3.

The structural part of the ASWING model was compared against the NASTRAN model in terms of static deflections of the wing, as well as mode shapes and frequencies of the entire aircraft. Having two structural models of the same aircraft helped in comparing results and further validating experimental tests. To compare the mode shapes of both models, the modal assurance criterion (MAC) was employed. The MAC is a statistical indicator of the correlation between mode shapes that is most sensitive to large differences and relatively insensitive to small differences in the mode shapes. A review of the development and use of the MAC can be found in [161, 162]. The MAC is calculated as the normalized scalar product between two vectors $\mathbf{u}^r$ and $\mathbf{v}^q$ of degrees of freedom of modes r and q from each model, respectively

$$\mathrm{MAC}\left(\mathbf{u}^r, \mathbf{v}^q\right) = \frac{|\mathbf{u}^r \mathbf{v}^q|^2}{\|\mathbf{u}^r\|^2 \|\mathbf{u}^q\|^2} = \frac{\left|\sum_{j=1}^{n} u_j^r v_j^{q*}\right|^2}{\left(\sum_{j=1}^{n} u_j^r u_j^{r*}\right)\left(\sum_{j=1}^{n} v_j^q v_j^{q*}\right)}, \tag{2.1}$$

where n is the number of degrees of freedom of the modal displacement vectors and $\cdot^*$ denotes complex conjugation. In more practical terms, MAC values range from 0 to 1. A value of 1 between two shapes indicates that they are identical, whereas a value of 0 indicates that there are no similarities between the two shapes. Two mode shapes are similar if their MAC value is higher than 0.9, and dissimilar otherwise [163].

2.3.2 Aerodynamic Modeling

The aerodynamic characteristics of the QT1 aircraft were obtained using AVL, a program developed at MIT for the aerodynamic and flight-dynamic analysis of rigid aircraft [164]. It uses a VLM formulation to model lifting surfaces as well as slender bodies, such as fuselages and nacelles. The vortex lattice method is based on potential flow theory, which assumes the flow to be ideal, i.e., incompressible, inviscid, and irrotational. With these assumptions, all viscous drag effects are not accounted for, and only induced drag can be assessed [165]. When all the above assumptions are made, flow can be represented by a velocity potential that satisfies the Laplace equation

$$\nabla^2(\Phi + \Phi_\infty) = 0, \tag{2.2}$$

where Φ is the perturbation velocity potential and Φ_∞ the velocity potential due to the free-stream flow.

The solution to this problem based on VLM is obtained by distributing doublet elementary solutions (or equivalent vortex-ring) on the wing boundaries and applying the Kutta condition on trailing edges. Slender bodies can be modeled by distributing source elementary solutions on their surface. The perturbation velocity potential at any point of the domain is given by

$$\Phi = \frac{1}{4\pi}\int_{S_b+S_w} \mu \mathbf{n}\cdot\nabla\left(\frac{1}{r}\right) dS - \frac{1}{4\pi}\int_{S_b} \sigma\left(\frac{1}{r}\right) dS, \tag{2.3}$$

where μ and σ are doublet and source elementary solutions, respectively, r is the distance of a collocation point to an elementary solution, S_b and S_w are the body and wake surfaces, respectively, and $\mathbf{n}$ is the surface normal. The perturbation potential is discretized, and the vortex distribution is found for a particular wing geometry. Lift and drag coefficients can be calculated from this distribution.

A flight-dynamic analysis is also possible with AVL by linearizing of the aerodynamic model about a flight condition. In addition, aircraft with arbitrary configurations can be modeled. In this work, the aircraft was split into four components: fuselage, wing, vertical tail, and horizontal tail. These components were modeled separately in AVL, and the final assembled model can be seen in fig. 2.9. The discretization of the different lifting surfaces (vortex lattice) can be seen in the figure, as well as the discrete source distribution along the fuselage (slender body).

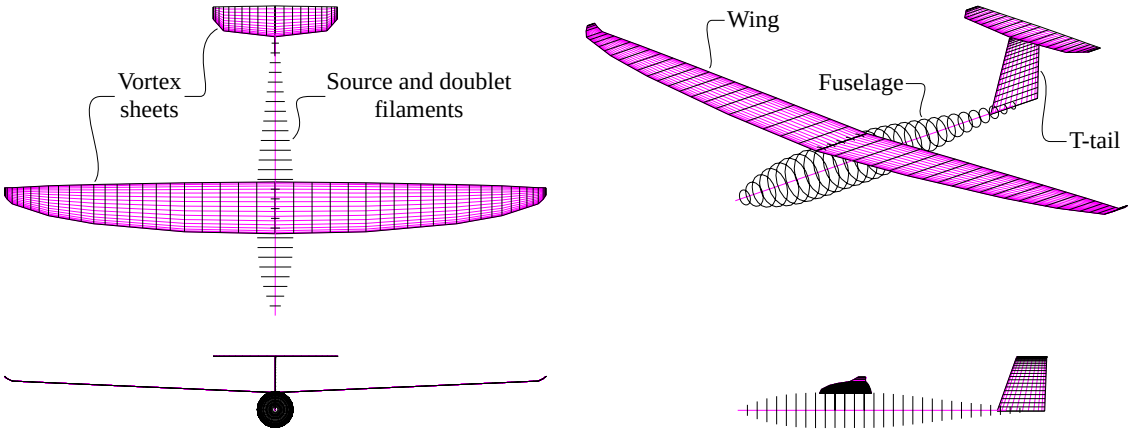

Figure 2.9: Aerodynamic AVL model of the rigid QT1 aircraft.

2.3.3 Aeroelastic Modeling

ASWING was used in this work to study the aeroelastic response of the flexible QT1 aircraft. It incorporates structural (nonlinear beam model using an iterative finite differences solution procedure [166, 167]), aerodynamic (UVLM with compressibility corrections to model lifting surfaces and slender body theory for fuselage bodies), and control (general state-feedback control law) models. ASWING allows for quick nonlinear analyses involving multiple disciplines using low-fidelity models, thus useful for the preliminary design phase of aircraft. Engine models can also be implemented in ASWING, and throttle can be set as a control input. The framework capabilities have been benchmarked with application problems: oscillating beam (good agreement was found when compared to the exact solution) and two-dimensional flutter (flutter speed prediction was close to the exact solution).

ASWING attempts to solve the problem defined by the generalized aeroelastic equations of motion

$$\mathbf{M}\ddot{\mathbf{q}}(t) + \mathbf{C}\dot{\mathbf{q}}(t) + \mathbf{K}\mathbf{q}(t) = \mathbf{F}(t), \tag{2.4}$$

where $\mathbf{q}(t)$ represents the generalized displacement vector, $\mathbf{M}$, $\mathbf{C}$ and $\mathbf{K}$ are the mass, damping, and stiffness matrices, respectively, and $\mathbf{F}(t)$ is the vector of generalized forces.

In addition to nonlinear aeroelastic analysis in time, dynamic response with gusts and modal analysis are also supported. The latter is of particular interest for the analysis of flexible high aspect ratio wings. In these models, the root locus of flight-dynamic modes and structural elastic modes are closer to each other when compared

to a rigid wing model. ASWING outputs the combined root loci of all aeroelastic modes, which can be useful in the identification of body freedom flutter instabilities. This problem was studied by Love et al. [168] using the ASWING framework for a flying HALE aircraft and found the body freedom flutter problem to be critical for low altitude conditions inside the flight envelope. The computational framework formulation is described in two technical reports [148, 149].

The ASWING model of the QT1 aircraft closely follows the NASTRAN FE model, in terms of its geometry and node distribution. Given the aeroelastic capabilities of NASTRAN, the latter model was updated with aerodynamic panels, allowing aeroelastic analyses to be carried out and results compared with those of the ASWING model. Figures 2.8 and 2.10 depict the aeroelastic NASTRAN and ASWING models of the flexible QT1 aircraft, respectively.

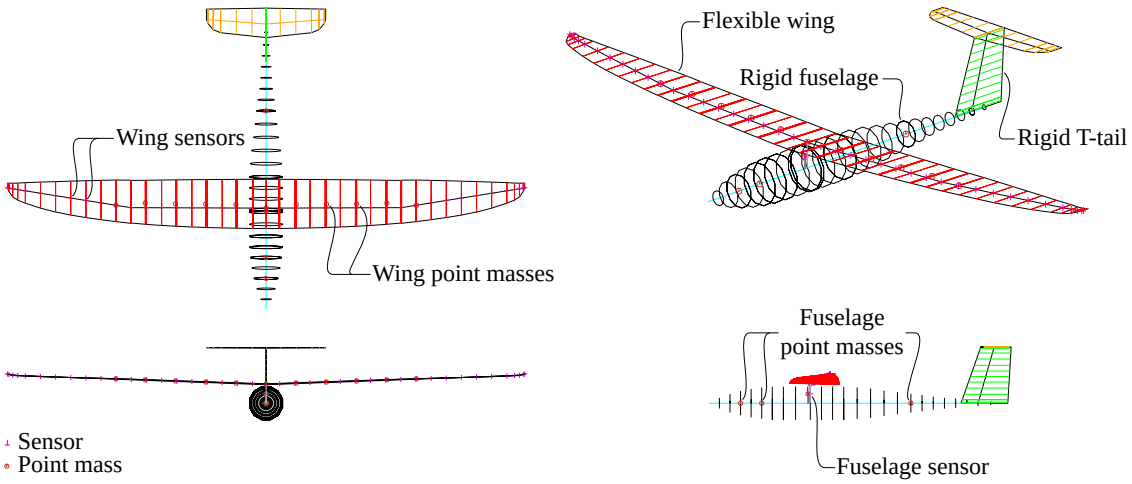

Figure 2.10: Aeroelastic ASWING model of the flexible QT1 aircraft.

2.3.4 Bifilar Pendulum Testing

Bifilar pendulum tests (BPTs) were conducted to determine the moments of inertia of the aircraft. This is a cost-effective way of determining the inertia properties of bodies of complex shapes. In a bifilar vertical-axis torsional pendulum test, an object is hung by two parallel wires that allow it to rotate freely about the vertical axis. The experiment is to measure the moment of inertia for the axis of rotation parallel to the wires. The system is approximated as a compound pendulum, and its natural frequency of free oscillations is estimated [169, 170]. The Lagrangian dynamics of this

system are formulated as

$$I\ddot{\theta} + K_D\dot{\theta}|\dot{\theta}| + C\dot{\theta} + \frac{mgD^2 \sin\theta\cos\theta}{4h\sqrt{1-\left(\frac{D\sin\theta}{2h}\right)^2}} = 0, \tag{2.5}$$

where θ is the rotation angle, m is the object mass, I is the moment of inertia about the axis of rotation, K_D is the aerodynamic damping, C is the viscous damping, D is the distance between wires, and h is the wire length.

This nonlinear differential equation can be simplified by assuming that the angular motion is small, and by omitting damping [171, 172]. This simplification yields the following expression that can be used to estimate the mass moment of inertia about one axis

$$I = \frac{mgD^2}{4h\omega^2}, \tag{2.6}$$

where ω is the frequency of oscillation. This has the advantage of requiring a simple measurement of the frequency of oscillations at the expense of measurement accuracy by neglecting the damping terms.

In this work, the nonlinear model of eq. (2.5) was used for its higher accuracy. Transient experimental data of decaying oscillatory aircraft motion was fit to the model using Simulink, which resulted in the identification of both aerodynamic and viscous damping parameters, K_D and C, respectively.

To obtain the moments of inertia about the three axes, the process was repeated with the aircraft hung at different orientations.

A fixture was designed and constructed to fit around the fuselage of the aircraft and was tied into hard points located on the side of the fuselage. This frame allows eye bolts to be slid in the aluminum extrusion so as to hang the aircraft level in each configuration with the center of mass directly in between the filaments that suspend it. It allows the aircraft to be hung in three orientations, to determine the mass moments of inertia about its body coordinate system. Figure 2.11 shows the aircraft suspended about the yaw, pitch, and roll axes during a BPT.

With the aircraft mounted in the frame and hung from the ceiling, the location of the overall assembly's C.G. was determined. The inertia of the system was measured by setting it into an oscillatory motion by applying an initial angular displacement to the assembly about the vertical axis. This set the assembly into a torsional oscillation which was logged. A VectorNav IMU in conjunction with a National Instruments DAQ was used to record the decaying oscillations during the tests.

The fixture was modeled very accurately, down to all the correct fasteners, in order to estimate its moments of inertia in computer aided design (CAD) software. Alternatively, its moments of inertia could have been determined experimentally, in a similar fashion to the aircraft, but this time only the frame would be suspended. Once the moments of inertia were obtained for the assembly, the moments of inertia for the fixture were subtracted from the result in order to obtain the final moments of inertia of the aircraft.

(a) Roll axis (b) Pitch axis (c) Yaw axis

Figure 2.11: BPT of the QT1 aircraft in roll, pitch, and yaw axes.

2.3.5 Static Load Testing

Static load testing was conducted on the flexible QT1 wing in order to update and validate both the NASTRAN FE model and the structural part of the ASWING model, as well as to aid in the calibration of the wing displacement reconstruction method. Static load tests also provided a pre-load to the already installed strain gauges, which, after preloading, drifted no more than 5 µ following a $2g$ load.

Out-of-plane bending loads were applied to the wing during the tests, and the deflections at different points along the wingspan were recorded. The procedure was repeated while increasing the load magnitude between tests.

A jig was designed to firmly clamp the wing saddle to an optical test table. A rail was attached to a hard point on the wing, located between the rigid and flexible portions of the wing. Eyebolts were threaded to the ceiling and this rail. Turnbuckles were connected between the ceiling eyebolts and fish scales. These were, in turn, attached to a chain that extended and connected to the wing hard points. The

turnbuckles were adjusted between tests to precisely control the applied loads. The baseline shape of the wing was determined by measuring the height of different points of interest on each wing from the test table.

Figure 2.12 shows the flexible wing of the QT1 aircraft undergoing a static load test.

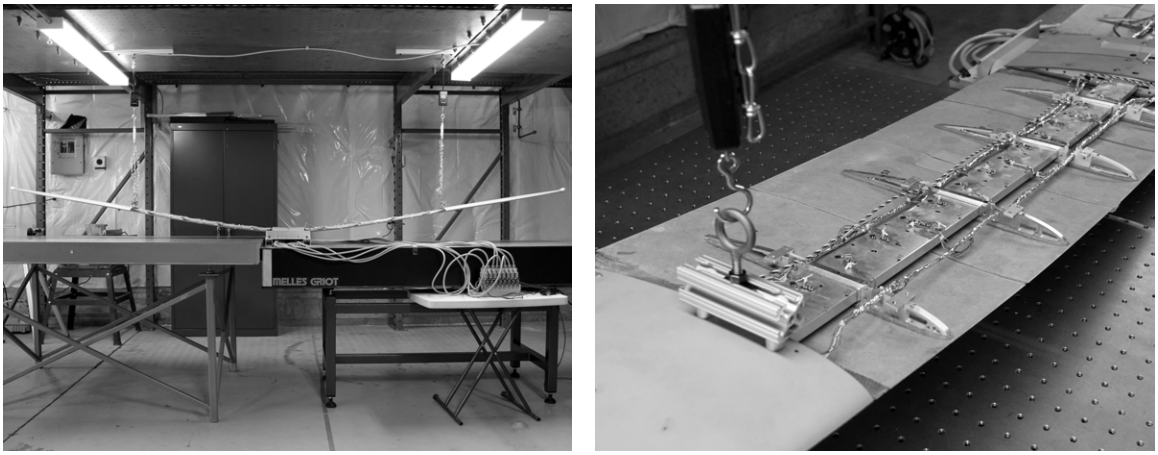

(a) Static load test (b) Load application point

Figure 2.12: Flexible wing of the QT1 aircraft undergoing a static load test (left) and detail of load application rail and eyebolt used to apply a vertical point load at the joint between rigid and flexible portions of the wing (right).

2.3.6 Ground Vibration Testing

EMA is necessary when performing structural analysis of an aircraft as it allows to verify and validate dynamic results obtained numerically through FEA. This is achieved by conducting a GVT campaign and collecting vibration data of the whole aircraft structure to be later used to validate the computational models [173]. For the past decades, the standard way of performing a GVT on a large aircraft has been to use the phase-resonance method, commonly referred to as normal mode testing [174]. This method is very appealing for these applications due to its ability to separate closely spaced modes. Normal mode testing consists of performing a single sine excitation at the natural frequencies of the structure with a shaker system. The modes determined by this method are called critical.

As with any other testing method, there is an interest in developing new GVT techniques that minimize cost. Hence, the main driver of modern ground vibration testing is the reduction of time consumed during testing and analysis, without compromising

the accuracy of the results [82]. State-of-the-art GVT campaigns of large full-scale commercial aircraft can be performed in as short as 9 days per prototype, like the tests conducted by Lubrina et al. on the Airbus A350 XWB [175]. This suggests that careful planning must be done to successfully undertake a GVT campaign. This phase, prior to the testing itself, includes the setup of instruments necessary to measure the quantities of interest. After the actual test is performed, additional attention is required in the post-processing of the acquired data, in order to extract the modal responses of the aircraft.

GVTs were performed on the flexible QT1 aircraft with the objective of validating the FE structural models, in terms of modal frequencies and shapes. Similar tests were also conducted on the rigid QT1 aircraft, and the results served as a baseline for comparing the dynamic properties of the flexible-wing aircraft with those of a rigid-wing with the same geometry.

The tests were done using both impact and shaker excitation of the aircraft structure and the response collected with a set of accelerometers (see fig. 2.13). The hammer was a PCB Piezotronics 086C03 impact hammer, while the shaker was a PCB Piezotronics K2007E01 miniature shaker. Three accelerometers were used in the tests, which were glued together in a 3-axis arrangement. The accelerometers were the PCB Piezotronics 352A24 miniature single-axis piezoelectric accelerometer, with a frequency range of 0.8 Hz to 10 000 Hz ($\pm 5\,\%$).

Even though the structural frequencies of the aircraft are relatively low, the lowest structural frequency encountered was at around 2.7 Hz, which is within the range of frequencies of the accelerometer. Low levels of excitation were used for both impact hammer and shaker testing, in order not to induce operating level excitation. Over-excitation of the structure could make the structure vibrate in a nonlinear manner. The excitation of nonlinear characteristics can distort and render measured data useless for the purpose of modal testing [176].

In order to filter out noise from physical modes when post-processing the GVT results, the modal phase collinearity (MPC) criterion was used. This criterion measures the degree of complexity of a mode shape by evaluating the functional linear relationship between the real and imaginary parts of the modal displacement vector $\mathbf{u}$

$$\mathrm{MPC}\,(\mathbf{u}) = \left(\frac{\lambda_1 - \lambda_2}{\lambda_1 + \lambda_2}\right)^2, \tag{2.7}$$

where $\lambda_{1,2}$ are the eigenvalues of the covariance matrix of the real and imaginary parts

of **u**. For lightly damped structures, physical modes behave as real modes and the MPC value approaches unity. A mode with a low index is either noise or the mode is significantly complex [177].

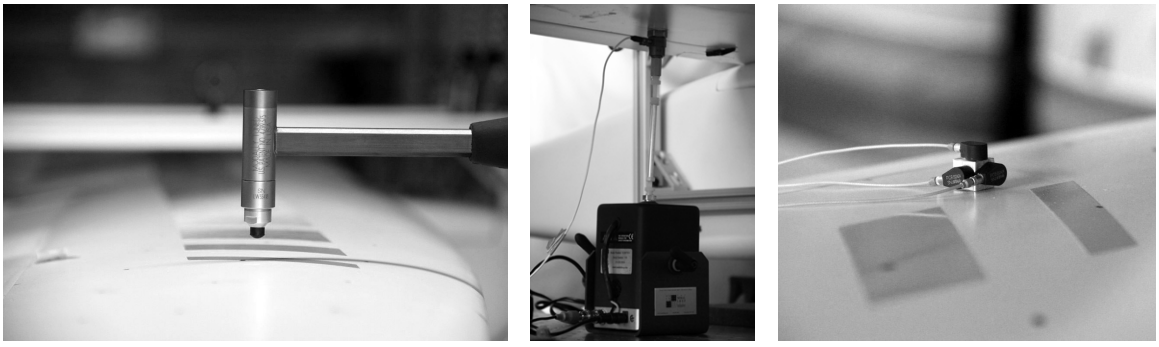

(a) Impact hammer (b) Shaker (c) 3-axis accelerometer

Figure 2.13: Impact hammer (left), shaker (center), and 3-axis accelerometer arrangement (right) used during a GVT of the QT1 aircraft.

Two boundary conditions were used in the tests to allow for more data in the model updating process. The first one was a cantilever-wing boundary condition, where the wing saddle was clamped to a test bench. The second boundary condition was a free-aircraft boundary condition. For the latter, two alternatives were investigated: aircraft fuselage hanging from the ceiling suspended by bungees, and fuselage resting on 100 mm thick polyurethane ester foam. The test stand for all ground vibration testing was done on an optical table with vibration damping to isolate the test equipment from external vibrations.

For each set of wings, over 160 points were measured, including leading-edge points, relevant for in-plane mode measurements. The points correspond to nodes in the FE model that were mapped and marked on the surface and spar of the wings for easier and faster testing (see fig. 2.14).

The main concern when choosing these points is to avoid nodal points. A nodal point of a given mode shows no displacement, and so if a sensor is set to measure the response at a nodal point, the data acquired will not represent the shape at that point, since the FRF for that output will show no peak at the resonance frequency. In the worst-case scenario, spatial aliasing might occur, with the extracted mode shape resembling that of a different mode.

For impact testing, these points correspond to roving impacts. The reference point for the impacts was located at the wing tips, where the 3-axis accelerometer arrange-

ment was placed. For shaker tests, these points correspond to roving accelerometer locations. A single 3-axis accelerometer arrangement was used, which was moved around from point to point between tests. This saved costs but increased the overall testing time. The shaker was kept fixed between tests, and connected to a reference point on the inboard section of the wing. This point was chosen to be far from a modal node point (near an anti-node point) where displacement was expected to be maximum.

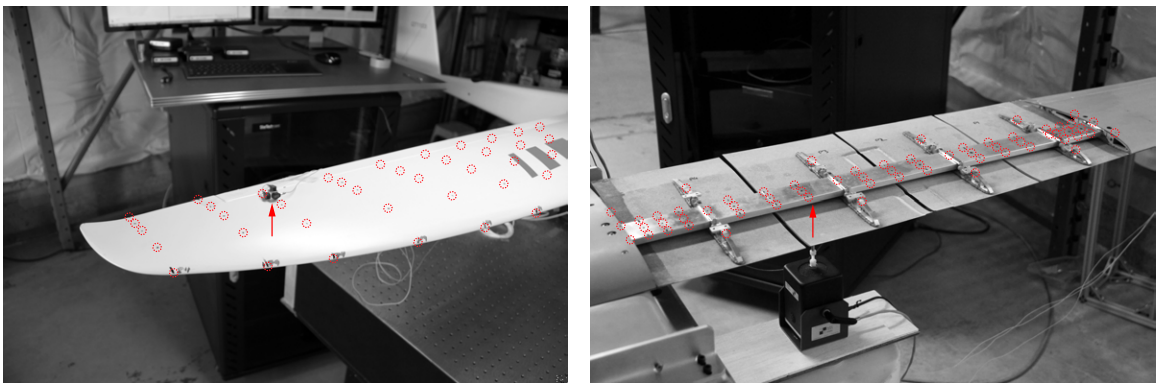

(a) Rigid wing (b) Flexible wing

Figure 2.14: Impact test points (circled in red) on rigid (left) and flexible (right) aircraft wings. Location of 3-axis accelerometer is shown for the rigid wing only (red arrow on left), while shaker attachment point is shown for the flexible wing only (red arrow on right).

The modal parameters of interest—frequencies, damping, and mode shapes—were calculated after curve-fitting the recorded FRFs. A least-squares curve fit was performed on the FRF data, where a first approximation of the resonance frequencies and modal damping values was obtained.

At this stage, one can choose to use local polynomial or global polynomial methods. The former treats one FRF at a time as if the system was described by a single-DOF, while the latter uses multiple FRFs, allowing for multi-reference data. There are other curve-fitting methods, generated by stability criteria, that might be more suitable for specific applications. In this study, the classical polynomial approaches were used in order to obtain fast and reliable results [178].

The response of a GVT can be divided into two groups: response where there is light modal density (the structures that show this are typically called simple structures); and response where there is heavy modal density. In simple structures, the modes are not closely spaced nor heavily damped, and at resonance, a simple structure behaves

predominantly as a single-DOF system, and the modal parameters can be determined relatively easily.

The simplest way of determining the mode shape for a structure is to use quadrature picking [179, 180]. This method is based on the assumption that the coupling between the modes is light. In practice, mechanical structures are often very lightly damped. This implies that the modes are lightly coupled. At any frequency, the magnitude of the frequency response function is the sum of the contributions (at the particular frequency) from all modes. When there is little modal coupling between the modes, the structural response at a modal frequency is completely controlled by that mode, and so quadrature picking can be used to unravel the mode shapes [181].

For single-DOF systems, the frequency response function at resonance is purely imaginary. As a result, the value of the imaginary part of the frequency response function at resonance, for structures with lightly coupled modes, is proportional to the modal displacement. Consequently, by examining the magnitude of the imaginary part of the frequency response function at a number of points on the structure, the relative modal displacement at each point can be found. From these displacements, the mode shapes can be established. The procedure can then be repeated to determine all the required mode shapes.

Due to the structural differences between the rigid and flexible sets of wings, the impact test points had to be marked differently. For the rigid wings, the points were marked on the skin of the wing. This was no issue, as the skin is an integral part of the structure of the wing, and can carry loads and vibrations with it to the internal structure. On the other hand, for the flexible wing case, the points were marked on the spar and ribs instead of points along the skin corresponding to those of the rigid wing. This is because the skin panels on the flexible wing are not structural elements. Even though they are physically attached to a point on the spar, they are not truly a part of it, serving only an aerodynamic purpose.

For testing purposes, only the top panels were removed from the flexible wing panels in order not to considerably change the weight properties of the wing. The location of the measured impact points for both the rigid and flexible wings can be seen in fig. 2.14.

The first boundary condition that was investigated was a rigid connection between the wing saddle and the test stand. When the aircraft is fully assembled, the two wing halves join together and attach to the wing saddle, to form the wing assembly. This wing saddle is then bolted to the fuselage, and this connection becomes fairly rigid.

A rigid aluminum fixture was designed to emulate the portion of the fuselage that the wing saddle bolts onto, and this fixture was bolted to the test stand. The wing saddle was then attached to the fixture. This connection was assumed to be rigid in comparison to the flexibility of the wings. It was also very similar to the boundary condition used in NASTRAN to model the wing fixture.

Two variations of the free-aircraft boundary condition were investigated: bungee suspension and vibration isolation foam. The test done with these boundary conditions differed from the previous boundary conditions in that the whole aircraft was used for testing, as opposed to only the wing assembly. The results from these two configurations were compared as additional assurance for validation.

In fig. 2.15, the QT1 aircraft can be seen with the rigid set of wings installed and ready for shaker and impact testing. Impact testing was performed for the cantilever-wing condition, whereas shaker testing was the chosen technique for the free-aircraft condition.

(a) Fixed wing setup (b) Bungee suspension setup

Figure 2.15: Rigid QT1 aircraft vibration test in a fixed wing setup using impact hammer (left) and a bungee suspension setup using a shaker (right).

Figure 2.16 shows the QT1 aircraft with the flexible set of wings installed and ready for shaker and impact testing. Like the rigid wing case, impact testing was performed for cantilever-wing conditions, and shaker testing was used for free-aircraft conditions.

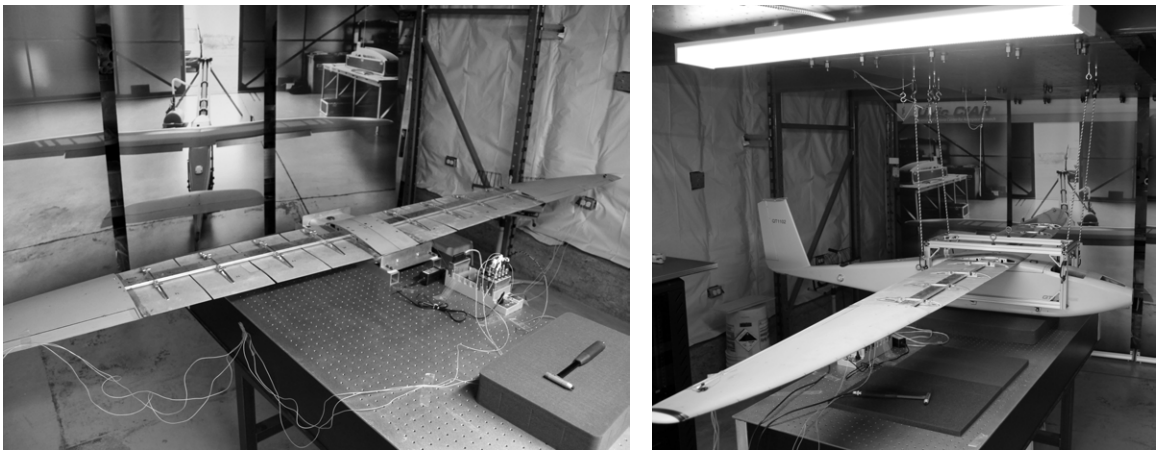

(a) Fixed wing setup (b) Bungee suspension setup

Figure 2.16: Flexible QT1 aircraft vibration test in a fixed wing setup using an impact hammer (left) and a bungee suspension setup using a shaker (right).

2.3.7 Wing Displacement Reconstruction

In order to capture the displacement of the flexible wing during flight, an indirect shape reconstruction method based on SPA was used [78]. The method allows the whole displacement field of the wing to be estimated through the measured strain data at specific locations on the wing. There are two main groups of methods for displacement field reconstruction from strain: the first one is based on the geometry curvature information. Geometry curvature acts as a bridge between structural strain and deformation, through the use of B-spline fitting and curve fitting using polynomial functions [182]; the second uses modal decomposition.

In this work, the second method was employed due to its overall simplicity in requiring only a small set of measurement points and affordability of strain measurement system. In this method, the strain and displacement mode shapes are first calculated from a FE model. Then, a relationship between strain and displacements using the structural elastic mode shapes is used. Finally, the displacement field is reconstructed using several locally measured strains through the developed displacement-strain relationship.

Generally, the displacement $\mathbf{d}$ of a structure can be calculated using the principle of modal superposition as

$$\mathbf{d} = \mathbf{\Phi}_d \mathbf{q}, \tag{2.8}$$

where $\mathbf{d}$ is a vector of N displacement degrees of freedom, $\mathbf{q}$ is a vector of n modal

coordinates and $\mathbf{\Phi}_d$ is a $N \times n$ matrix of displacement mode shapes.

Similarly, strains $\boldsymbol{\varepsilon}$ can be expressed by the strain mode shapes $\mathbf{\Phi}_\varepsilon$ and modal coordinates $\mathbf{q}$ as

$$\boldsymbol{\varepsilon} = \mathbf{\Phi}_\varepsilon \mathbf{q}, \tag{2.9}$$

where $\boldsymbol{\varepsilon}$ is a vector of M strain measurements and $\mathbf{\Phi}_\varepsilon$ is a $M \times n$ matrix.

The approximated modal coordinates $\hat{\mathbf{q}}$ can be obtained by way of least squares as

$$\hat{\mathbf{q}} = \left(\mathbf{\Phi}_\varepsilon^{\mathrm{T}} \mathbf{\Phi}_\varepsilon\right)^{-1} \mathbf{\Phi}_\varepsilon^{\mathrm{T}} \boldsymbol{\varepsilon}. \tag{2.10}$$

Substituting eq. (2.10) in eq. (2.8), the estimated displacement $\hat{\mathbf{d}}$ can be obtained from the measured strain as

$$\hat{\mathbf{d}} = \mathbf{\Phi}_d \left(\mathbf{\Phi}_\varepsilon^{\mathrm{T}} \mathbf{\Phi}_\varepsilon\right)^{-1} \mathbf{\Phi}_\varepsilon^{\mathrm{T}} \boldsymbol{\varepsilon}. \tag{2.11}$$

The estimated displacement $\hat{\mathbf{d}}$ can then be provided by the measured strains $\boldsymbol{\varepsilon}$ through the displacement-strain transformation (DST) relationship

$$\mathrm{DST} = \mathbf{\Phi}_d \left(\mathbf{\Phi}_\varepsilon^{\mathrm{T}} \mathbf{\Phi}_\varepsilon\right)^{-1} \mathbf{\Phi}_\varepsilon^{\mathrm{T}}. \tag{2.12}$$

However, it should be noted that the maximum rank of the DST is equal to M. It is thus important to have a sufficient number of strain measurements to guarantee adequate accuracy. Therefore, the number of strain data points should be greater than or equal to the number of strain mode shapes obtained from the FE model, i.e., $M \geq n$ [183].

It was determined that only 8 strain gauges installed along the wing spar were sufficient for rebuilding strain modal shapes. However, a total of 16 strain gauges were used instead. The additional 8 gauges resulted in improved shape resolution and lowered sensitivity to errors in measurements.

Because the modal strain patterns obtained for the out-of-plane and torsional modes of the spar were almost identical when it was instrumented with evenly spaced strain gauges, all placed in an identical fashion so as to detect both out-of-plane deflections and twist, linear independence of strain patterns was not achieved. In order to develop measured strain patterns that demonstrate linear independence, Tourjansky and Széchényi suggest placing the strain gauge bridges in such a way that no two modes will have the same or similar modal strain patterns [183]. This was achieved by

mounting strain bending bridges on the wing spar with alternating rotational offsets as seen in fig. 2.17. The strain gauge orientations are alternated 90°, resulting in a more uncoupled bend-twist strain pattern.

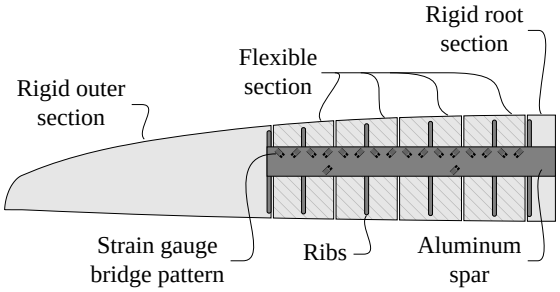

Figure 2.17: Repeating strain bending bridge pattern applied to the flexible wing of the QT1 aircraft. The pattern is mirrored on the underside of the spar (not shown).

2.3.8 Model Updating

Model updating works by modifying the mass, stiffness, and damping parameters of a FE model until an improved agreement between FEA data and experimental test data is achieved. Unlike direct methods, that produce a mathematical model capable of reproducing a given state, the goal of FE model updating is to achieve an improved match between model and experimental test data by making changes to model parameters that correct inaccurate modeling assumptions. Theoretically, an updated FE model can be used to model other loadings, boundary conditions, or configurations, without any additional experimental testing. Such models can be used to predict operational displacements and stresses due to simulated loads.

The structural models of the flexible aircraft had to be updated in order to bring their modal response closer to that of GVTs before any other analyses could be performed or any other results could be analyzed. The structural NASTRAN model was fine-tuned to match experimentally-obtained modal frequencies and mode shapes, as well as static deflections. The updated NASTRAN model properties were then transferred to ASWING for subsequent analysis.

The first step in the update process of the NASTRAN FE model was to manually update the mass distribution of the wing using measured and calculated mass data for all individual components. The second step was to parametrize the NASTRAN model to expose variables for material properties, cross-sectional polar and area moments of

inertia, point mass inertias, and mass distribution of wings. The parts of the model that saw their properties exposed can be seen in fig. 2.18.

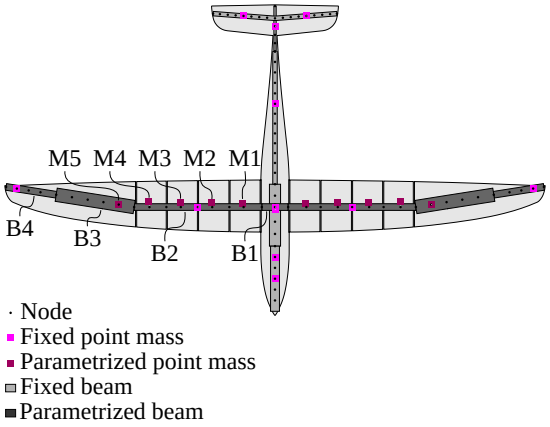

Figure 2.18: Parametrized NASTRAN model of the flexible QT1 aircraft.

Several parameters were used for updating the NASTRAN model, primarily material and beam properties. It was found that Young's modulus E, cross-section area A, torsional stiffness G, bending inertia I, and material density ρ of the wing spar were the parameters that had the most effect on the aircraft modal response. These properties were used to adjust the bending and torsional stiffness of the wing. Table 2.4 lists the parameters exposed for the model.

A gradient-based optimization process was carried out with the objective of matching modal frequencies, mode shapes (using a MAC analysis between experimental and simulated mode shapes), and deflections due to static loading. Two constraints were defined for the optimization problem: mass and spanwise location of the outboard wing C.G. The problem is posed as follows

$$\begin{aligned} \min_{\mathbf{x}} : \quad & |f_i(\mathbf{x}) - \mathcal{F}_i|, -\mathrm{MAC}_i(\mathbf{x}, \mathcal{S}_i), && i = 1, \ldots, 6 \\ & |z_j(\mathbf{x}) - \mathcal{Z}_j|, && j = 1, 2, 3 \\ \text{s.t.} : \quad & m_{\mathrm{B3}} + m_{\mathrm{B4}} + m_{\mathrm{M5}} = \mathcal{M} \\ & \frac{(my)_{\mathrm{B3}} + (my)_{\mathrm{B4}} + (my)_{\mathrm{M5}}}{m_{\mathrm{B3}} + m_{\mathrm{B4}} + m_{\mathrm{M5}}} = \mathcal{Y}, \end{aligned} \tag{2.13}$$

where $\mathbf{x}$ is the vector of design variables defined in table 2.4, f_i and $\mathcal{F}_i$ are the calculated and experimental frequency of the i^{th} mode, respectively, $\mathcal{S}_i$ is the experimentally obtained shape of the i^{th} mode, z_j and $\mathcal{Z}_j$ are the calculated and measured static displacement at point j along the wingspan, respectively, and $\mathcal{M}$ and $\mathcal{Y}$ are the

Location	Variables	Description
		Beam properties
B1	EI, J	Out-of-plane bending stiffness, polar moment of inertia
B2	E	Young's modulus
B3, B4	EI, J, ρ	Out-of-plane bending stiffness, polar moment of inertia, running mass
		Point mass properties
M1–M4	I_y	Moment of inertia about y axis
M5	I_y, y	Moment of inertia about y axis, spanwise location of point mass

Table 2.4: List of design variables used during the NASTRAN model updating process of the flexible QT1 aircraft.

measured mass and spanwise location of the outboard wing C.G., respectively.

To reduce the number of variables required in the optimization routine, some parameters were tuned manually. Several items were modeled or measured individually and added to the model manually, including component mass, moments of inertia, and their C.G. location, which were manually updated in the NASTRAN model to match overall mass and moments of inertia based on experimental BPTs. This required disassembling the wing into constituent components and weighing them. The masses were verified against their CAD equivalent model allowing the update of material density.

2.3.9 Pre-Flight Testing

The aircraft was tested prior to flying to ensure flight readiness of its flight systems. To guarantee a correct integration of all flight systems prior to installing them onto the aircraft, an iron bird test was carried out. The flight control systems and data collection systems were placed on a benchtop, making sure that the distances between the components correspond to the actual vehicle to be built (see fig. 2.19a).

The aircraft propeller was characterized in terms of static thrust generated. To perform this characterization, the aircraft was connected to a load cell using a belt,

and a data acquisition system measured the applied force at different throttle settings, from idle to maximum throttle (see fig. 2.19b).

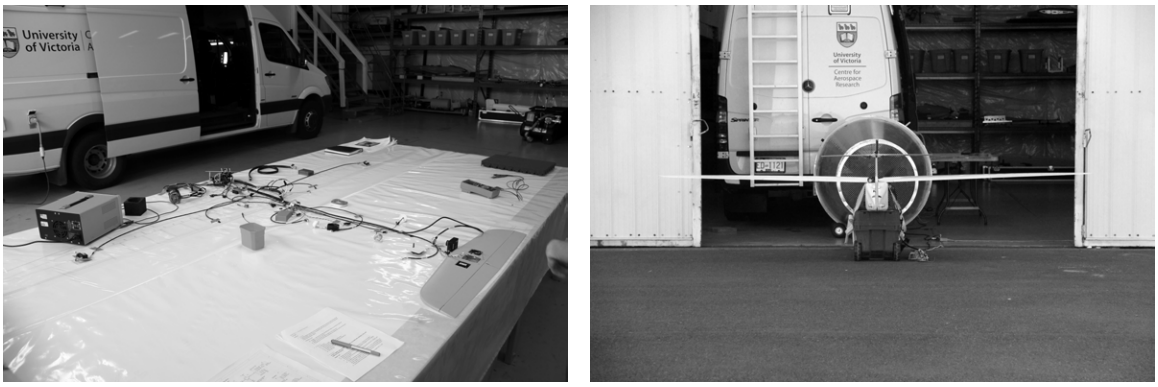

(a) Iron bird test (b) Static thrust test

Figure 2.19: Iron bird test (left) and static thrust test (right) of the QT1 aircraft.

The Piccolo autopilot and ground system allow for software-in-the-loop (SIL) as well as hardware-in-the-loop (HIL) testing to be performed. During SIL testing, autopilot, and aircraft sensor data are both simulated in software and run on the ground station. Virtual flights are simulated, which allows for operator training and early detection of system configuration faults. In HIL testing, the actual autopilot is used but receives artificial sensor information from a simulator running on the ground station over a controller area network (CAN) bus, and it simulates a flight of the aircraft according to these sensor values. The HIL system does not allow for a flexible aircraft to be modeled, and so a dihedral equivalent to the deformed wing shape at $1g$ was applied to the wing for testing the aircraft in HIL. The purpose of the HIL testing was to both approximate acceptable controller gains to start flight testing with, as well as to test AFTU parameters, such as maximum amplitude and test duration.

2.3.10 Flight Testing

The purpose of flight-testing the flexible QT1 aircraft was to capture the aeroelastic behavior of its high aspect ratio flexible wing. The flight tests provide a different insight to those of wind tunnel tests, because the environment is not closed and controlled, as opposed to flight tests, where atmospheric phenomena can happen, such as gusts, and the aircraft dynamics are not constrained.

Flight tests were conducted in order to compare the experimental data obtained from flights with prescribed control surface commands with data from aeroelastic

simulations. In order for the wing flexing dynamics to be identified during flight, they must be apparent in the flight time-history data. This was achieved by means of control surface excitation. Three different types of control surface commands were performed: frequency sweeps, 3–2–1–1, and doublet commands.

Tischler and Remple recommend using a frequency sweep control signal for frequency-response identification as it has a uniform power spectral density across the desired frequency range, resulting in persistent excitation and consistent level of frequency-response coherence [184]. In addition to this, the response time histories are roughly symmetric. However, frequency sweeps are less time efficient than the optimal inputs, such as the 3–2–1–1 input command, resulting in longer record lengths. The frequency sweep function is generated by the equation

$$\delta_{\text{sweep}} = A \sin\left[\theta(t)\right], \tag{2.14}$$

where A is the sweep amplitude and

$$\theta(t) = \int_0^{T_{\text{rec}}} \omega(t) dt. \tag{2.15}$$

The frequency progression is given by

$$\omega = \omega_{\text{min}} + K(\omega_{\text{max}} - \omega_{\text{min}}) \tag{2.16}$$

where ω_{min} and ω_{max} are the starting and ending frequencies of the sweep, respectively, and

$$K = C_2 \left[\exp\left(\frac{C_1 t}{T_{\text{rec}}}\right) - 1\right], \tag{2.17}$$

with $C_1 = 4.0$ and $C_2 = 0.0187$.

The function also has fade-in and fade-out segments, avoiding sharp inputs at the start and end of the sweep.

In a system identification problem, where the dynamic model is constructed based on observed flight test data, this data is typically generated from 3–2–1–1 and frequency sweep maneuver commands. To validate the identified dynamic model, two-sided doublet commands are typically used, which are dissimilar from the identification maneuver commands. This ensures robustness of the identified model for other input forms.

In this work, even though we are not dealing with a system identification problem,

doublet maneuver commands were tested nevertheless. This enriched the amount of flight test data collected and helped further validate the aeroelastic model. Simulated ASWING flights were compared against flight test data generated using 3–2–1–1, frequency sweep and doublet maneuver commands. Examples of these three functions can be seen in fig. 2.20.

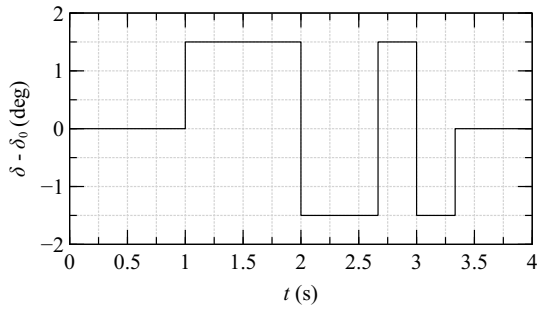

(a) 3–2–1–1

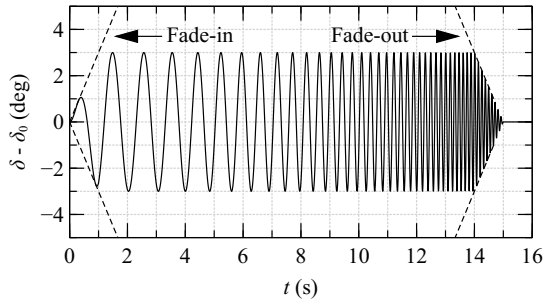

(b) Frequency sweep

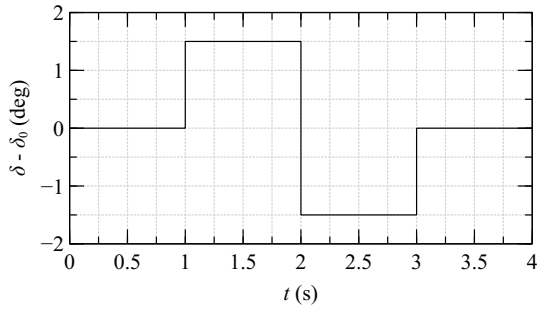

(c) Doublet

Figure 2.20: Example of the three different control surface input commands used during flight testing for exciting the aeroelastic modes of the aircraft: 3–2–1–1, frequency sweep and doublet commands.

The AFTU module was responsible for moving the control surfaces with different

input functions in order to deflect the flexible wing at different frequencies. The time to complete a full AFTU flight test was determined based on the predicted endurance of the flight batteries. A full AFTU flight test includes control surface 3–2–1–1, frequency sweep, and doublet commands in both open and closed loop. The optimal duration for a sweep was determined to be 15 s with the help of HIL testing, based on the size of the flying site and the average airspeed.

Data from different sensors was captured during flight, which was then used to compare the flight test with the simulated aeroelastic response. The list of parameters captured during flight is summarized in table 2.5.

Sensor	**Parameters**	**Description**
Air data boom	α, β, TAS h, p_s, p_t	Angle of attack and sideslip, true airspeed, pressure altitude, static and total pressure
ESC	δ_t	Throttle percentage
Radio receiver	δ_a, δ_e, δ_r MAN/AUTO	Aileron, elevator and rudder deflection angles, autopilot mode
IMU/GPS	ϕ, θ, ψ p, q, r a_x, a_y, a_z X, Y, Z	Roll, pitch and yaw attitude angles, angular rates and acceleration in body axes, GPS coordinates
Strain gauges	$\varepsilon_1, \ldots, \varepsilon_{32}$	Strain measurements along wing spar (16 per semispan)

Table 2.5: List of parameters logged during a flight test of the flexible QT1 aircraft, organized by sensor source.

In order to form limits for constraints in the design of the sensor acquisition system, the first wing torsional elastic mode of the rigid QT1 aircraft was used to form the upper-frequency bandwidth, at around 85 Hz. The minimum frequency of interest to be captured was the short-period mode of the aircraft, at around 1.5 Hz. To be able to capture the frequency phenomena occurring in this bandwidth, sensors capable of measuring over this frequency span and sufficient sample rates needed to be selected. The Nyquist-Shannon theorem states that a sample rate two times that of the frequency to be resolved is the minimum requirement. Tischler and Remple

recommend using a filter bandwidth ω_f of at least five times the desired maximum frequency of interest ω_{max}

$$\omega_f \geq 5\,\omega_{max}.$$

In addition, the sampling frequency ω_s should be at least another factor of five above the filter frequency

$$\omega_s \geq 5\,\omega_f.$$

A low-pass filter was expected to be applied in post-processing to alleviate the aliasing of data from other phenomena with frequencies greater than 85 Hz. With this in mind, the filter bandwidth ω_f was chosen to be 400 Hz, putting the sampling frequency ω_s at 2 kHz for all signals.

The starting ω_{min} and ending ω_{max} frequencies of the frequency sweep were chosen to be 0.8 Hz and 10 Hz, respectively. This was chosen such that the short-period mode of the aircraft was excited during the frequency sweep progression. The servo bandwidth was not stated by the manufacturer, only the rated speed mentioned previously, but it proved to be enough for the actuator to follow the frequency sweep command with no observable lag. This was confirmed by logging both the generated frequency sweep command and the position feedback measured by the servo actuator and comparing the two signals.

In order to reduce the overall project risk, small incremental steps were taken during the flight test campaign. The flight experiments took place in a designated area free of any possible disturbances, and all the flight tests followed a racetrack pattern, shown in fig. 2.21.

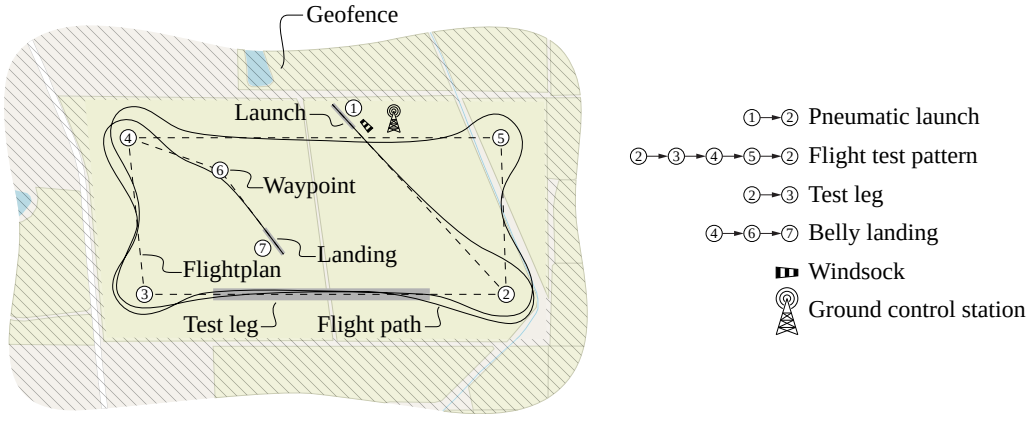

Figure 2.21: Ground setup and racetrack pattern used in the QT1 aircraft flight tests.

To minimize design and construction complexity, the aircraft lacked a dedicated landing gear, so all take-off operations were performed with the help of a pneumatic launcher. The soft grass field also allowed the aircraft to perform belly landings (fig. 2.22).

(a) Pneumatic launch

(b) Belly landing

Figure 2.22: Pneumatic launch (top) and belly landing (bottom) of the QT1 aircraft.

The flight campaign was divided into three phases. The first phase focused on autopilot tuning and crew training using only the rigid set of wings. AFTU testing was also performed. At the end of this phase, flight test procedures were created, and documentation was developed. A total of 18 flights and 20.6 h of flight time were spent on this phase. During the second phase, flights were conducted to ensure the aircraft was trimmed and controllable. Communication and control links were validated, the autonomous flight was tested, and the flight envelope was expanded to test the limits on MTOW and static margin. The aircraft was also flown fully instrumented. This phase required a total of 8 flights and 7.2 h of flight time and still used the rigid set of wings. The third, and last, flight phase was all done using the flexible set of wings. It focused on ensuring the flexible aircraft was trimmed and controllable, and safe to operate. Autopilot gains were re-tuned, the flight envelope was re-tested, and data

collection systems were tested. Finally, at the end of the phase, it was possible to perform data collection flights. This phase saw a total of 20 flights and 13.3h of flight time.

2.4 Results and Discussion

This section includes all the results generated throughout this work. First, the results of the aeroelastic tailoring applied to the wing of the aircraft are presented. Second, the overall mass, C.G. location, and moments of inertia of the aircraft obtained experimentally from bifilar pendulum tests are shown. Following these are the wing displacements obtained from static load tests and dynamic characterization of the aircraft obtained from GVTs. While BPTs and GVTs were carried out for both the rigid and flexible aircraft, static load tests were only performed on the flexible wing.

The results of the model updating process are presented next, followed by a comparison between the updated NASTRAN and ASWING models, and validation against experimental results in terms of wing static deflections, modal frequencies, and mode shapes. The aerodynamics of the aircraft are compared in terms of stability derivatives and flight-dynamic modes. An aeroelastic characterization of the final aircraft in terms of its aeroelastic modes is presented next. Finally, the aircraft flight dynamics and wing deformation obtained from flight test results are presented and compared to an ASWING simulation of the flight.

2.4.1 Wing Aeroelastic Tailoring

The final configuration of the flexible aircraft was chosen by means of parametric studies on the geometry of the spar cross-section as well as the mass and inertia of wing tip mass points.

Figure 2.23a shows the effects of changing the wing spar cross-section thickness on the aeroelastic response of the aircraft, in terms of the root-loci of aeroelastic modes. Looking at the figure, one can see that a decrease in beam thickness decreases the frequency and damping ratio of the aeroelastic mode where the wing's first out-of-plane bending component is predominant (OB1*) while keeping the short-period-dominated mode (SP*) relatively unchanged.

In fig. 2.23b, it is possible to observe the effects of adding wing-tip mass to the aircraft in terms of its aeroelastic modes. As mass is added to the wing tips, the

frequency of mode OB1* decreases, and the mode becomes less damped. On the other hand, the short-period mode has almost no change in its damping ratio and only a slight decrease in its frequency.

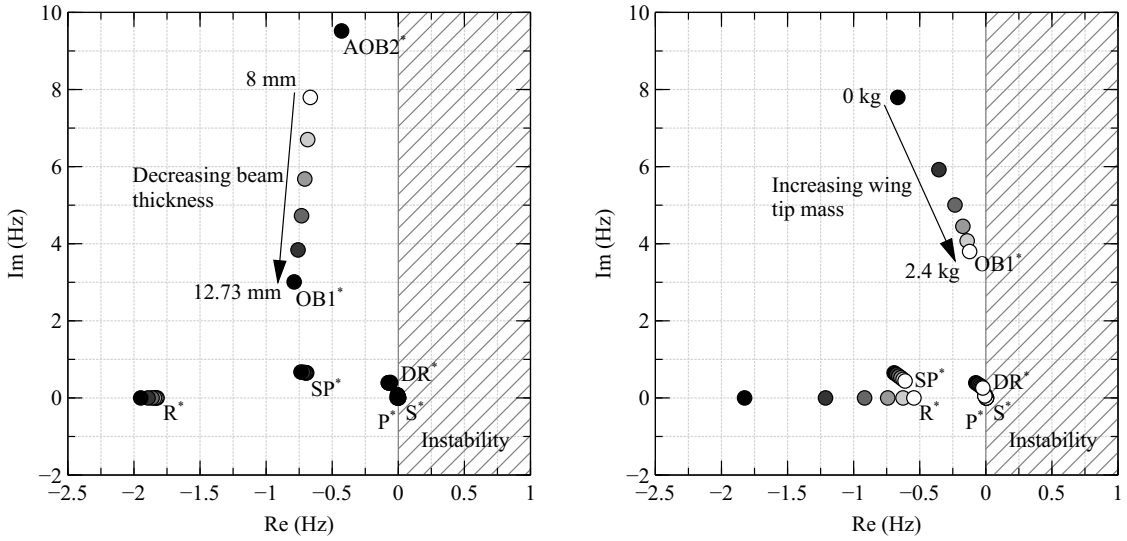

(a) Spar cross-section thickness sweep between 8 and 12.73 mm.

(b) Wing tip mass sweep between 0 and 2.4 kg.

Figure 2.23: Root loci of aeroelastic modes of the flexible QT1 aircraft for a sweep of two different wing parameters: spar cross-section thickness (left) and wing tip mass (right).

Other parametric studies were also performed, mainly a sweep of wing tip inertia values as well as variation of a uniformly-distributed running wing mass. However, it was observed that the variation of wing tip mass inertia, within a feasible range of values, was effective at lowering the frequency of the wing first torsional elastic mode (T1), but was not sufficient to bring it close to any of the flight-dynamic modes. Also, adding a uniformly-distributed running mass to the wing had no effect in reducing the frequency of any of the structurally-dominant aeroelastic modes.

The final flexible wing configuration was chosen to have a custom-extruded hollow rectangular aluminum spar cross-section with a wall thickness of 1.5 mm, 10 mm tall and 50 mm wide, with a running mass of 461.7 g/m, and no mass added to the wing tips. This proved to be a good compromise between weight and flexibility.

A visual comparison between the elastic mode shapes of the rigid and flexible aircraft variants was carried out and is presented in fig. 2.24 for a cantilever-wing condition, with the modes ordered by ascending frequency. Most elastic modes saw a

decrease in their frequency, as expected, and most remained similar in terms of their mode shape. However, one effect of the added wing flexibility that can be seen in the figure is the swapping of some lower-frequency modes between the two models, mainly modes 2 and 3. At first, this was an issue, as the flexible wing's first in-plane bending elastic mode (IB1) had a frequency very close to the first out-of-plane bending elastic mode (OB1), and there was concern that the excitation of the latter mode during flight would also excite in-plane motion of the wing. This is the reason for choosing a high aspect ratio cross-section for the final flexible wing spar. A cross-section with an aspect ratio of 5 ensured a good separation between the two modes in the flexible wing.

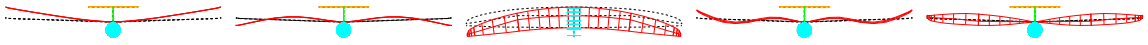

Mode 1 (OB1) Mode 2 (OB2) Mode 3 (IB1) Mode 4 (OB3) Mode 5 (T1)

(a) Elastic mode shapes of rigid aircraft.

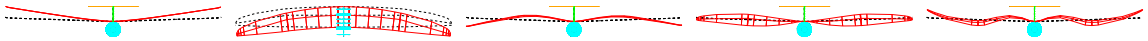

Mode 1 (OB1) Mode 2 (IB1) Mode 3 (OB2) Mode 4 (T1) Mode 5 (OB3)

(b) Elastic mode shapes of flexible aircraft.

Figure 2.24: Comparison of the elastic mode shapes between the rigid (top) and flexible (bottom) QT1 aircraft for cantilever-wing conditions.

2.4.2 Mass and Inertia Properties

The results of the oscillatory BPTs for the flexible aircraft are shown in fig. 2.25, together with simulated results from the model of eq. (2.5). A similar set of results was obtained for the rigid aircraft.

A parameter identification process was carried out in Simulink in order to fit this model to experimental data. The identified parameters were the aerodynamic and viscous damping parameters K_D and C, respectively, the initial angular displacement θ_0, and the moment of inertia I. Their values are listed in table 2.6 for roll, pitch, and yaw axes for the flexible aircraft. A similar parameter identification process was carried out for the rigid aircraft.

The mass and inertia properties of the support fixture were subtracted from those of the assembly in order to determine the aircraft mass and moments of inertia. The values of mass m and moments of inertia about roll, pitch, and yaw axes (I_{xx}, I_{yy}, I_{zz}),

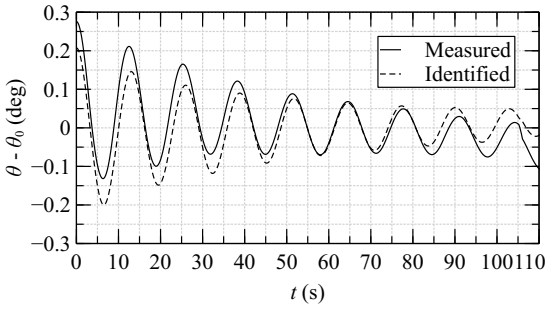

(a) Roll axis

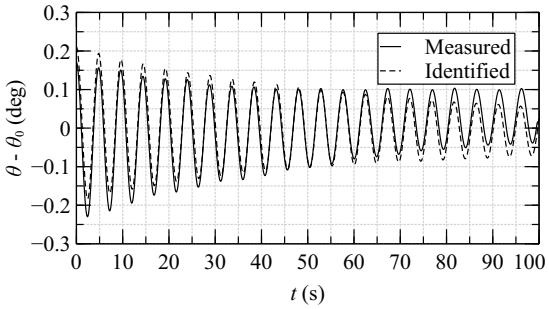

(b) Pitch axis

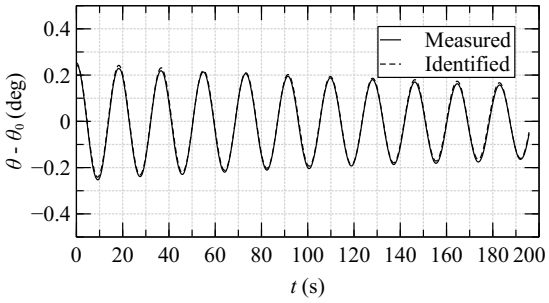

(c) Yaw axis

Figure 2.25: Experimental and simulated pendulum angular displacement θ in roll, pitch, and yaw axes, for the assembly formed by the flexible QT1 aircraft and support fixture.

are summarized in table 2.7 for the rigid and flexible QT1 aircraft, together with the aircraft longitudinal C.G. location x_{cg}.

It is possible to see that the mass of the flexible aircraft was higher than the rigid variant. This was due to all the extra sensors installed on the wing as well as the data collection instrumentation inside the payload bay used for logging flight test data. In addition to this, the flexible set of wings was also structurally heavier than its rigid

Axis	C (kg m^2/s)	K_D (kg m^2/rad)	θ_0 (rad)	I (kg m^2)
Roll	0.049 37	1.7105	0.2214	3.5194
Pitch	0.032 58	0.5094	0.2016	4.1768
Yaw	0.017 66	0.2477	0.2498	7.0618

Table 2.6: Identified BPT model parameters of eq. (2.5) from experimental pendulum responses in roll, pitch, and yaw axes, for the assembly composed of the flexible QT1 aircraft and support fixture.

counterpart. The location of the C.G. was kept at approximately the same location between the two aircraft variants. In terms of inertia, the flexible aircraft saw a small decrease in roll and yaw moments of inertia, while its pitch inertia was kept relatively the same.

Aircraft	m (kg)	x_{cg} (m)	I_{xx} (kg m^2)	I_{yy} (kg m^2)	I_{zz} (kg m^2)
Rigid QT1	15.5	0.125	4.128	3.641	7.404
Flexible QT1	19.8	0.124	3.425	3.864	6.527

Table 2.7: Mass properties of the rigid and flexible QT1 aircraft. C.G. location is measured from the leading edge of the wing root.

2.4.3 Ground Testing Results

During static load tests, out-of-plane point loads were applied at a hard point located between the flexible and rigid portions of the flexible wing of the aircraft. Follower forces were not used and the load was kept always perpendicular to the test table. Five load cases ranging from 16 to 78 N were applied. The same load cases were defined in NASTRAN and ASWING, and the results were compared against the measured points. Figure 2.26 shows a comparison of the spanwise vertical displacement of the flexible wing between static load tests, NASTRAN, and ASWING results.

It is possible to observe that the maximum error of both NASTRAN and ASWING results, relative to the measured displacements, is of 9.02 % and 9.87 %, respectively, and occurs at the wing tip. This not only shows a good agreement between measured

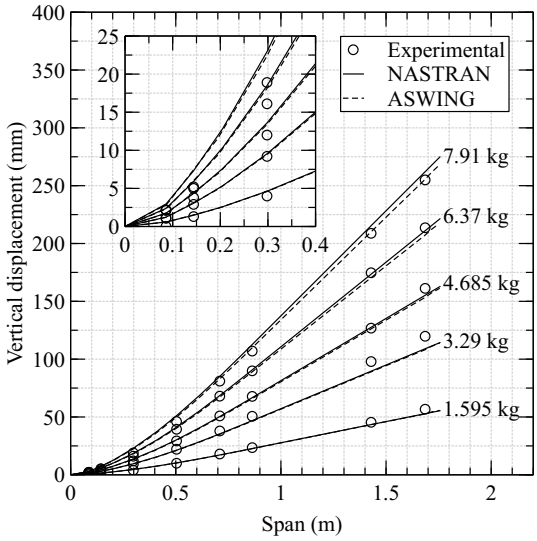

Figure 2.26: Comparison of spanwise vertical displacement of the flexible QT1 aircraft wing between experimental static load tests and NASTRAN and ASWING static load analyses. Inset shows a detailed view of the displacement at the wing root.

and simulated displacements but also a good agreement between NASTRAN and ASWING models.

The GVTs carried out on the QT1 aircraft resulted in a set of identified modal frequencies for the rigid- and flexible-wing variants of the aircraft, and for each boundary condition tested (cantilever-wing and free-aircraft). Table 2.8 lists the modal frequencies, damping ratios, and MPC values for both boundary conditions obtained for the rigid aircraft.

Mode	**Frequency** (Hz)	**Damping** (%)	**MPC**
1 (OB1)	7.31	9.68	0.936
2 (OB2)	36.1	7.02	0.987
3 (IB1)	61.3	4.92	0.041
4 (OB3)	106.0	5.01	0.366
5 (T1)	179.0	3.20	0.650

(a) Cantilever wing

Mode	**Frequency** (Hz)	**Damping** (%)	**MPC**
1 (OB1)	9.30	0.745	0.849
2 (AOB2)	21.6	2.36	0.940
3 (OB2)	37.3	1.20	0.680
4 (IB1)	50.1	1.95	0.951
5 (OB3)	90.3	1.76	0.595

(b) Bungee-suspended aircraft

Table 2.8: Comparison of modal frequencies between a cantilever-wing boundary condition obtained using impact testing (left) and a bungee-suspended-aircraft boundary condition obtained using a shaker (right) for the rigid QT1 aircraft.

In the table, it is possible to see that the MPC of some modes is quite low, especially for the cantilever-wing case, where an impact hammer was used. However, these results are presented here for exposition only and were not used in the update process of the flexible aircraft's NASTRAN model.

In table 2.9, the modal frequencies, damping ratios, and MPC values obtained for the flexible QT1 aircraft with the same two boundary conditions are presented. The first point to notice is that, in this case, there are fewer modes with lower MPC values than those for the rigid aircraft results. The second is that the frequency of the first mode, which happens to correspond to the first out-of-plane bending mode of the wing, is considerably lower for the flexible aircraft case, as expected.

Mode	**Frequency** (Hz)	**Damping** (%)	**MPC**
1 (OB1)	2.671	3.97	0.897
2 (IB1)	12.94	0.689	0.971
3 (OB2)	17.79	1.91	0.999
4 (T1)	37.60	0.983	0.971
5 (OB3)	55.85	1.41	0.964

(a) Cantilever wing

Mode	**Frequency** (Hz)	**Damping** (%)	**MPC**
1 (OB1)	3.04	1.36	0.939
2 (IB1)	12.9	0.689	0.971
3 (OB2)	17.9	0.482	0.994
4 (T1)	37.7	1.2	0.984
5 (OB3)	54.1	0.589	0.973

(b) Bungee-suspended aircraft

Table 2.9: Comparison of modal frequencies between a cantilever-wing boundary condition obtained using impact testing (left) and a bungee-suspended-aircraft boundary condition obtained using a shaker (right) for the flexible QT1 aircraft.

2.4.4 Model Update and Comparison

The results of the model updating process carried out on the NASTRAN model of the flexible QT1 aircraft can be seen in table 2.10 and fig. 2.27b, in terms of elastic modal frequencies and mode shapes, respectively. These are compared to experimentally-obtained results.

It is possible to see from table 2.10 that the final error between the elastic modal frequencies obtained from NASTRAN and experimental tests was small. The MAC analysis also shows good consistency between the two sets of mode shapes (fig. 2.27b).

The updated NASTRAN model properties were transferred to the ASWING model, and comparisons between the two were carried out in terms of elastic modal frequencies

Mode	EMA (Hz)	NASTRAN (Hz)	ASWING (Hz)
1 (OB1)	2.671	2.710	2.715
2 (IB1)	12.94	12.52	12.54
3 (OB2)	17.79	17.15	17.34
4 (T1)	37.60	36.80	39.33
5 (OB3)	55.85	56.95	57.69

(a) Cantilever wing

Mode	EMA (Hz)	NASTRAN (Hz)	ASWING (Hz)
1 (OB1)	3.04	2.919	2.925
2 (IB1)	12.9	13.44	13.48
3 (OB2)	17.9	17.59	17.83
4 (T1)	37.7	36.94	39.45
5 (OB3)	54.1	56.05	58.13

(b) Bungee-suspended aircraft

Table 2.10: Comparison of elastic modal frequencies between EMA and updated NASTRAN and ASWING models of the flexible QT1 aircraft for a cantilever-wing (left) and a bungee-suspended-aircraft (right) boundary conditions.

and mode shapes. The two models were compared for free-aircraft boundary conditions. To perform an elastic modal analysis in ASWING, a zero-speed aeroelastic modal analysis was set up, ensuring that the resultant modes were purely elastic. Figure 2.27c depicts the MAC calculated for the first five elastic modes of both NASTRAN and ASWING models. All diagonal elements of the matrix have a MAC number higher than 0.9, indicating a good correlation between the mode shapes of both models.

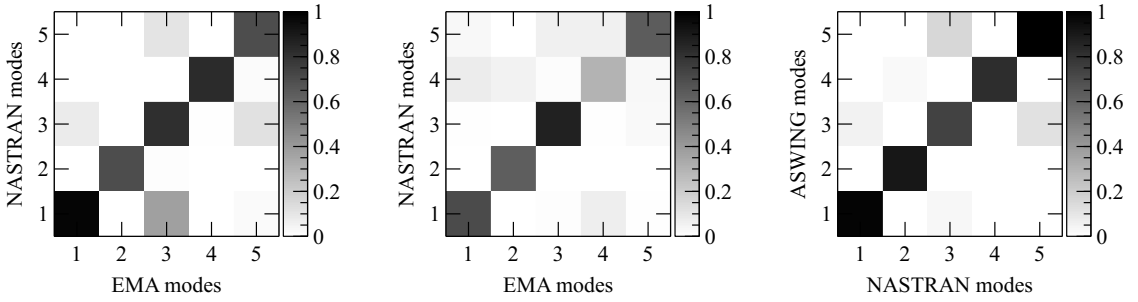

(a) MAC between EMA and NASTRAN rigid aircraft elastic modes.

(b) MAC between EMA and NASTRAN flexible aircraft elastic modes.

(c) MAC between ASWING and NASTRAN flexible aircraft elastic modes.

Figure 2.27: MAC analysis comparing elastic mode shapes between EMA and NASTRAN for the rigid QT1 aircraft (left), EMA and NASTRAN for the flexible QT1 aircraft (center), and between updated ASWING and NASTRAN models for the flexible QT1 aircraft (right).

2.4.5 Flight-Dynamic Modes

The aerodynamics of the baseline (rigid) aircraft were characterized in terms of its stability derivatives and flight-dynamic modes. Stability derivatives were important to properly configure the autopilot for flight. Flight-dynamic modes of the rigid aircraft served as a reference for comparison with the aeroelastic modes obtained after the wing modification process. Table 2.11 lists the stability and control derivatives of the rigid aircraft, obtained from NASTRAN, AVL, and a rigid ASWING model, and the flexible aircraft, obtained from the flexible ASWING model.

Derivative	**Rigid QT1**			**Flexible QT1**
	NASTRAN	**AVL**	**ASWING**	**ASWING**
C_{L_α}	5.868	5.943	6.048	5.966
C_{m_α}	−1.654	−1.806	−2.051	−1.785
C_{Y_β}	−0.294	−0.225	−0.283	−0.391
C_{l_β}	−0.095	−0.109	−0.074	−0.222
C_{n_β}	−0.095	0.058	0.065	0.043
C_{l_p}	−0.610	−0.592	−0.612	−0.617
C_{m_p}	–	–	–	0.005
C_{n_p}	−0.018	−0.070	−0.080	−0.080
C_{l_q}	–	–	–	0.004
C_{m_q}	−28.700	−26.254	−27.879	−26.510
C_{n_q}	–	–	–	−0.001
C_{l_r}	0.017	0.205	0.211	0.220
C_{m_r}	–	–	–	0.022
C_{n_r}	−0.074	−0.052	−0.080	−0.081
$C_{l_{\delta_\mathrm{a}}}$	0.287	0.358	0.301	0.302
$C_{m_{\delta_\mathrm{e}}}$	−1.801	−1.477	−1.766	−1.719
$C_{n_{\delta_\mathrm{r}}}$	−0.068	−0.045	−0.056	−0.056

Table 2.11: Stability and control derivatives of the rigid QT1 aircraft (obtained from NASTRAN, AVL, and a rigid ASWING model), and the flexible QT1 aircraft (obtained from the flexible ASWING model).

All derivatives were obtained at a $1g$ level-flight trim condition. It is possible to observe that although some error is observed for some derivatives, there is an overall good agreement between the models. Between the rigid and flexible models, one can see that there is a reduction in C_{L_α}, C_{m_α} and C_{m_q} with the increase in flexibility. This could be justified by the smaller projected horizontal wing surface area, due to a higher wing deflection required to trim the flexible aircraft in level-flight conditions, resulting in a reduction of the effective wing aspect ratio. In terms of lateral/directional derivatives, there is an increase in C_{Y_β} and C_{l_β}, and a decrease in C_{n_β}, as flexibility increases. The increase in the side force coefficient C_{Y_β} is a consequence of the higher vertical wing surface area component. This appears to decrease the C_{n_β} coefficient (destabilizing), but causes an increase in C_{l_β} (stabilizing), due to a higher wing dihedral. The cross-coupling terms in table 2.11 are zero for the rigid models, but non-zero for the flexible ASWING model.

The flight-dynamic modes for the rigid QT1 aircraft were obtained from its AVL model and are listed in table 2.12. It is possible to see that the three oscillatory flight-dynamic modes (P, DR and SP) lie outside the range of frequencies of the elastic modes of the aircraft (table 2.8).

AVL mode	20 m/s		30 m/s	
	Freq. (Hz)	**Damp.** (%)	**Freq.** (Hz)	**Damp.** (%)
Spiral (S)	–	0.578	–	2.30
Phugoid (P)	0.0669	2.16	0.0651	4.09
Dutch-roll (DR)	0.482	21.1	0.709	27.8
Short-period (SP)	0.799	79.7	1.20	86.1
Roll (R)	–	99.5	–	99.8

Table 2.12: Flight-dynamic modes obtained from the AVL model of the rigid QT1 aircraft at airspeeds of 20 and 30 m/s.

2.4.6 Aeroelastic Modes

The root loci of the flexible aircraft aeroelastic modes can be seen in fig. 2.28b, for a range of airspeeds between 20 and 30 m/s, within the flight envelope of the aircraft. It can be seen in the figure that, as airspeed increases, the first out-of-plane wing bending mode OB1 becomes more damped and its frequency decreases, becoming

closer to that of the short-period mode SP, which in turn increases its frequency with increasing airspeed. The short-period mode does not see a considerable variation of its estimated damping ratio in this range of airspeeds. The same is not true for the roll mode R, where an increase in speed damps out the mode. The remaining aeroelastic modes remain mostly constant in both frequency and damping ratio, for this range of airspeeds.

For comparison, the aerodynamic modes of the rigid aircraft are depicted in fig. 2.28a, for both AVL and ASWING models, for the same range of airspeeds. It is possible to see that: first, there is a good agreement between the aerodynamics of the two models; and second, the short-period SP mode varies differently with airspeed when compared to the flexible aircraft, demonstrating the influence of the nearby OB1 mode in the flexible configuration.

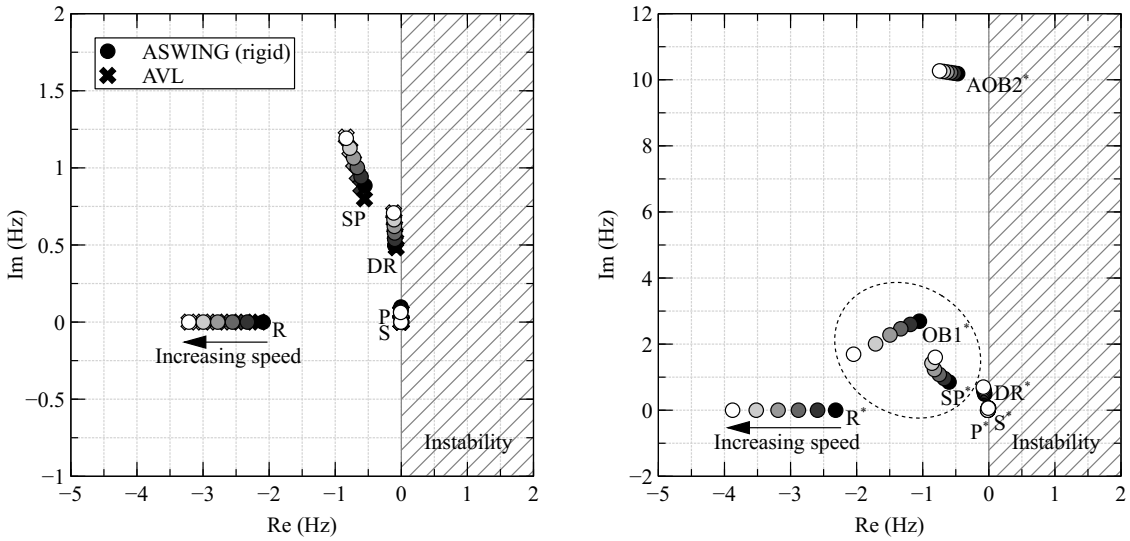

(a) AVL and rigid ASWING flight-dynamic modes for rigid aircraft.

(b) ASWING aeroelastic modes for flexible aircraft.

Figure 2.28: Root loci of flight-dynamic modes for the rigid QT1 aircraft obtained from an AVL and rigid ASWING model (left) and aeroelastic modes for the flexible QT1 aircraft obtained from its ASWING model (right), for airspeeds between 20 and 30 m/s.

The modes in fig. 2.28 were calculated around a $1g$ level-flight trim condition at different airspeeds. The effect of airspeed on wing transverse deflection and twist angle can be seen in fig. 2.29. As speed increases, the aircraft trims in level-flight at lower wing deflections, as expected. The wing twist angle (positive for an upward leading-edge motion) also decreases with increase of speed.

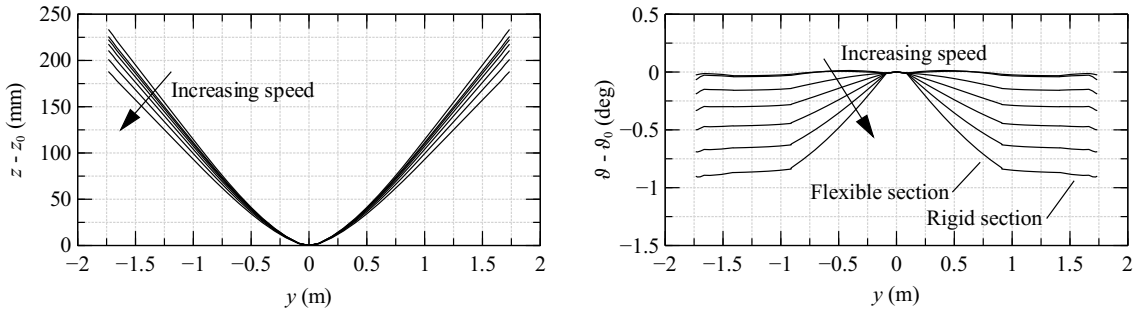

(a) z (b) ϑ

Figure 2.29: Transverse deflection z (left) and twist angle ϑ (right) of the flexible QT1 aircraft wing obtained from ASWING for $1g$ level-flight trim conditions at airspeeds of 16 to 40 m/s.

Table 2.13 lists the frequency and estimated damping ratio of the aeroelastic modes of interest, mainly the phugoid-dominated P*, Dutch-roll-dominated DR*, short-period-dominated SP*, and the first two wing elastic-dominated modes (OB1* and AOB2*), for airspeeds of 20 and 30 m/s. Note that only the wing first out-of-plane symmetric bending aeroelastic mode OB1* reaches a frequency close to those of the flight-dynamic-dominated roots, while the frequency of the mode immediately following this, the wing first out-of-plane anti-symmetric bending aeroelastic mode AOB2*, is already ten times higher than the flight-dynamic-dominated mode with the highest frequency (aeroelastic short-period SP*).

ASWING mode	20 m/s		30 m/s	
	Freq. (Hz)	**Damp.** (%)	**Freq.** (Hz)	**Damp.** (%)
Spiral (S*)	–	4.54	–	8.29
Phugoid (P*)	0.0966	6.35	0.0618	15.2
Dutch-roll (DR*)	0.514	12.7	0.698	11.8
Short-period (SP*)	1.002	46.1	1.568	47.9
Roll (R*)	–	99.5	–	99.8
Wing bending (OB1*)	2.693	83.5	1.694	96.4
Wing bending (AOB2*)	10.185	34.3	10.268	49.8

Table 2.13: Aeroelastic modes of interest obtained from the ASWING model of the flexible QT1 aircraft at airspeeds of 20 and 30 m/s.

The frequency difference between the SP* and OB1* aeroelastic modes is of 1.69 Hz

at 20 m/s and 0.13 Hz at 30 m/s. From the results of table 2.13, it is not clear if the two modes interfere in a constructive or destructive manner. To fully understand the effect of the added flexibility in the coupling of two aeroelastic modes, a MAC analysis was carried out between the aeroelastic OB1* mode and aeroelastic SP* mode of the flexible aircraft. MAC values of 0.257 and 0.817 were obtained for airspeeds of 20 and 30 m/s, respectively. This indicates that, first, the two mode shapes are coupled to a certain degree and, second, that the coupling between mode shapes increases with airspeed. A visual comparison of the coupling effect in terms of mode shapes at different phase angles is shown in fig. 2.30, where it can be seen that there is an added rigid-body motion component to the aeroelastic OB1* mode and an elastic component to the aeroelastic SP* mode.

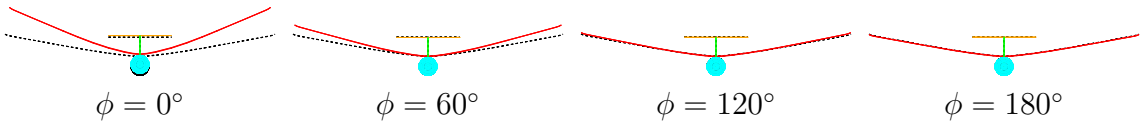

(a) OB1* mode shape

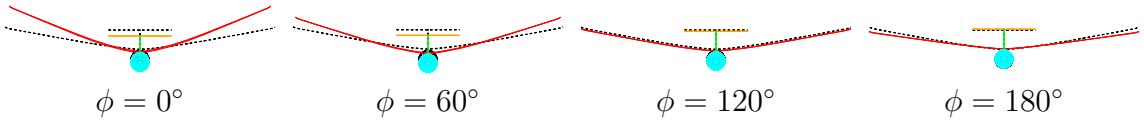

(b) SP* mode shape

Figure 2.30: Comparison of the first out-of-plane wing bending OB1* (top) and short-period SP* (bottom) aeroelastic mode shapes of the flexible QT1 aircraft at different phase angles ϕ.

If we continue to increase the aircraft speed and track the evolution of the aeroelastic roots of fig. 2.30, we can eventually find the speeds at which one or more modes cross the imaginary axis and become unstable. This axis crossing corresponds to a flutter condition and the speed at which it occurs the onset speed of flutter. For the flexible QT1 aircraft, this is shown in fig. 2.31. We can see that there are two branches of roots that lead to flutter instability. If we consider the branch with genesis in the wing first in-plane bending mode (IB1*), as the flight speed increases, the roots initially move further to the left for lower flight speeds. As flight speed continues to increase, this branch loops back around to the right and eventually crosses the imaginary axis. This axis crossing corresponds to a flutter mode involving the first out-of-plane bending and first in-plane bending modes of the wing. A similar phenomenon is visible for the branch with genesis in the wing first torsion mode (T1*), where at low speeds,

the branch moves to the left, but eventually loops back around at higher speeds until it crosses the imaginary axis, corresponding to a flutter mode involving the first out-of-plane bending and first torsion modes of the wing. Both of these crossings occur at a speed of approximately 73 m/s.

Please note the use of a superscript $\cdot^*$ to denote that all modes are aeroelastic in nature and involve coupling with aerodynamics, and hence are not pure in-plane–out-of-plane bending or pure bending-torsion modes.

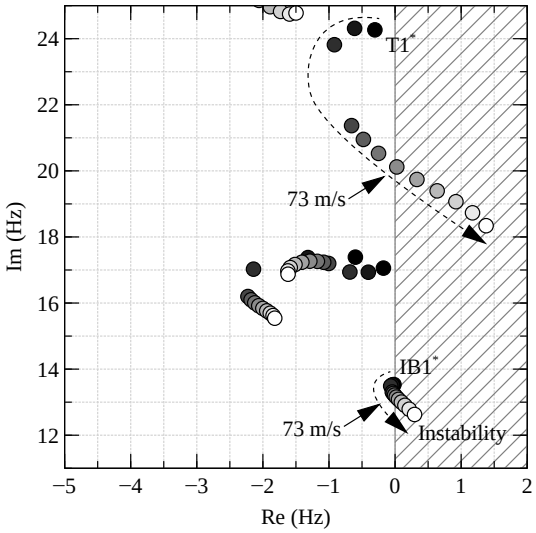

Figure 2.31: Root loci of aeroelastic modes for airspeeds between 20 and 80 m/s and flutter onset points obtained from ASWING for the flexible QT1 aircraft

Regarding the other aeroelastic roots, no crossings are observed in this speed range. While the first out-of-plane bending mode shows some degree of coupling with the short-period mode, as shown before in fig. 2.30, these modes do not result in a flutter condition, and the former eventually damps out completely at higher speeds. This was expected, since the most usual form in which a flutter condition involving rigid-body and elastic DOFs occurs is as a symmetric flutter of a swept wing in which the rigid-body modes, and principally the one in which the aircraft pitches about its C.G., couple with wing flexure. This is referred to as BFF [185].

2.4.7 Flight Dynamics

Three flight tests were selected from the flight test campaign (FT1, FT2, and FT3) and were used to study the flight dynamics of the flexible aircraft and validate the

aeroelastic model. In each of the three flight tests, a different control surface function was used to excite the aircraft dynamics: 3–2–1–1 in FT1, frequency sweep in FT2, and doublet commands in FT3. The flight trajectory of one of the flight tests is shown in fig. 2.32.

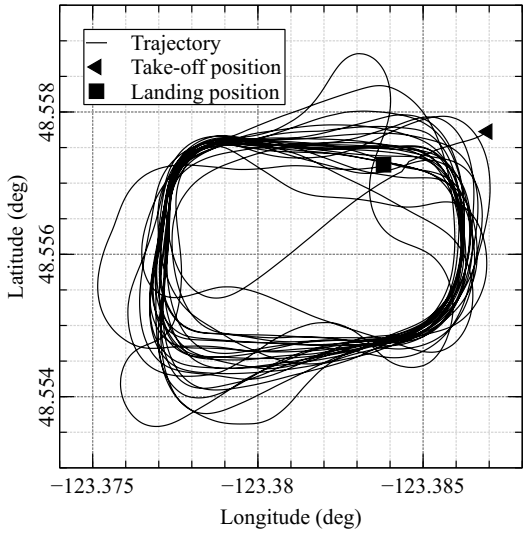

Figure 2.32: Flight test trajectory of the flexible QT1 aircraft obtained from GPS data.

Open-loop time-marching simulations were carried out in ASWING for the flexible aircraft where control surfaces were excited with the 3–2–1–1, frequency sweep, and doublet commands. These simulations were later on compared with flight test data. Initial conditions for the simulation were collected from a snapshot of the flight test data. This included altitude h, true airspeed (TAS), angle of attack α and sideslip β, angular rates (p, q, r), attitude angles (ϕ, θ, ψ), and control surface deflection $(\delta_{\mathrm{a}}, \delta_{\mathrm{e}}, \delta_{\mathrm{r}})$. This snapshot was synchronized with the start of a scripted control surface command. A summary of the initial flight conditions for the three flights is presented in table 2.14.

Correct identification of initial conditions from flight test data proved to be very important in generating good simulation results. These conditions were used to trim the aircraft prior to initiating the time-domain analysis in ASWING. Feedback signals from the servo actuators were used as forcing parameters during the time-marching sequence. Servo feedback signals are a better measure of the actual control surface deflection as they show the true shaft position of a servo actuator, as opposed to the commanded signal, which shows the intended shaft position. This ensured that the same control surface command was used in flight tests and simulations.

Parameter	**FT1** (3–2–1–1)	**FT2** (Freq. sweep)	**FT3** (Doublet)
h_0 (m)	70.0	68.0	67.0
TAS_0 (m/s)	23.6	24.5	22.7
Angle of attack and sideslip (°)			
α_0	5.06	3.99	4.51
β_0	−2.90	−4.15	−4.17
Angular rates (°/s)			
p_0	−7.73	0.849	−7.39
q_0	1.34	1.62	−4.68
r_0	5.647	5.94	5.80
Attitude angles (°)			
ϕ_0	0.144	−2.62	0.670
θ_0	5.66	3.58	−2.97
ψ_0	86.0	−94.2	−82.7
Control surface deflections (°)			
$\delta_{\mathrm{a},0}$	−1.45	−1.38	−1.30
$\delta_{\mathrm{e},0}$	−1.29	−0.936	−0.609
$\delta_{\mathrm{r},0}$	−0.848	−0.846	−0.848

Table 2.14: Initial conditions for three different flight tests (FT1, FT2 and FT3) of the flexible QT1 aircraft using 3–2–1–1, frequency sweep, and doublet elevator maneuver commands, respectively.

The results for the angle of attack, TAS, z-acceleration, pitch rate q, pitch angle θ, and elevator deflection δ_{e} for both experimental data, as logged from the DAQ, and ASWING aeroelastic simulation data, are shown in figs. 2.33 to 2.35, for flight tests FT1, FT2 and FT3, respectively.

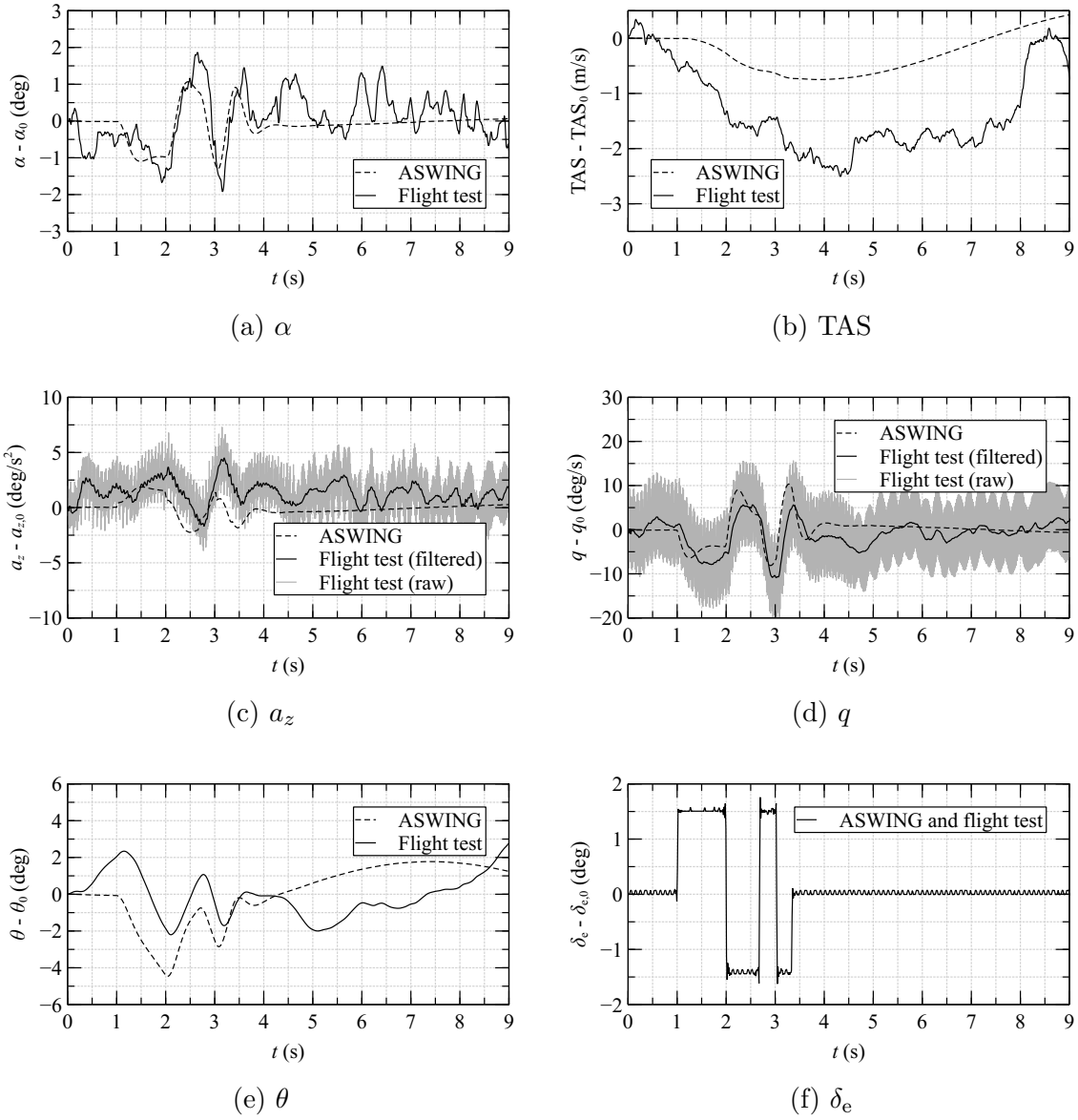

Figure 2.33: Comparison between flight test data and simulated response of the flexible QT1 aircraft to an elevator 3–2–1–1 command, for angle of attack α, TAS, z-acceleration a_z, pitch rate q, pitch angle θ, and elevator deflection δ_{e}.

Several observations can be made about the results. The first observation is that the effect of the 3–2–1–1, frequency sweep, and doublet commands can be noticed in the experimental data. Thus, one can observe the changes in angle of attack, TAS, z-acceleration, pith rate, and pitch angle when the elevator command is prescribed. The second observation is that the ASWING simulated results show good agreement with the experimental results. Not only are the general experimental trends captured, but

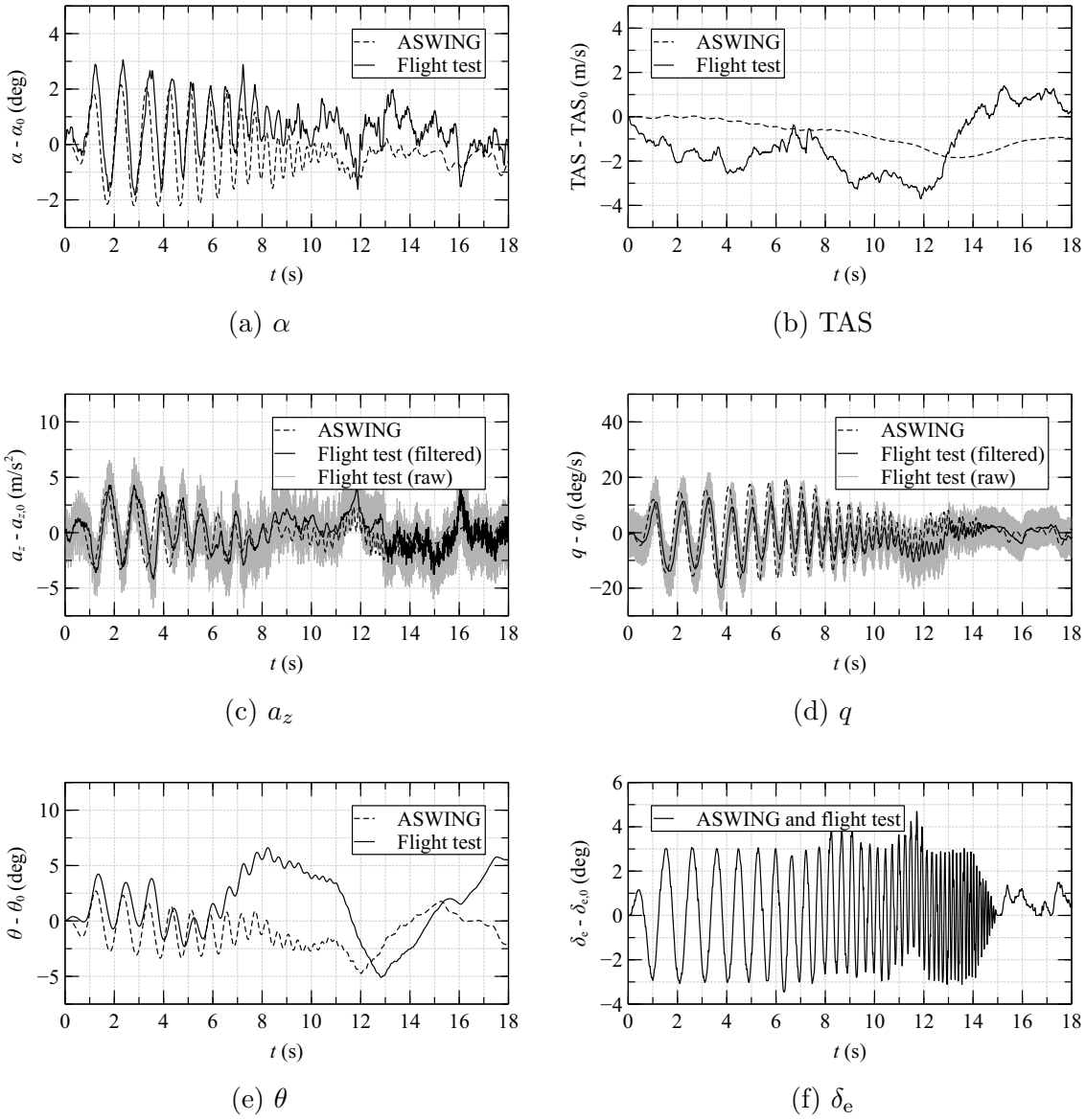

Figure 2.34: Comparison between flight test data and simulated response of the flexible QT1 aircraft to an elevator frequency sweep command, for angle of attack α, TAS, z-acceleration a_z, pitch rate q, pitch angle θ and elevator deflection δ_{e}.

also details such as signal frequency and amplitude variation. However, discrepancies between simulation and flight test data are still present in some cases and are more evident in the TAS and pitch angle results. These discrepancies can be due to several factors. The first is the fact that external disturbances, such as gusts, are not captured in the model. The second comes from a lack of a propulsion model in the simulation. While ASWING allows for propulsion models to be defined, these were not used, since

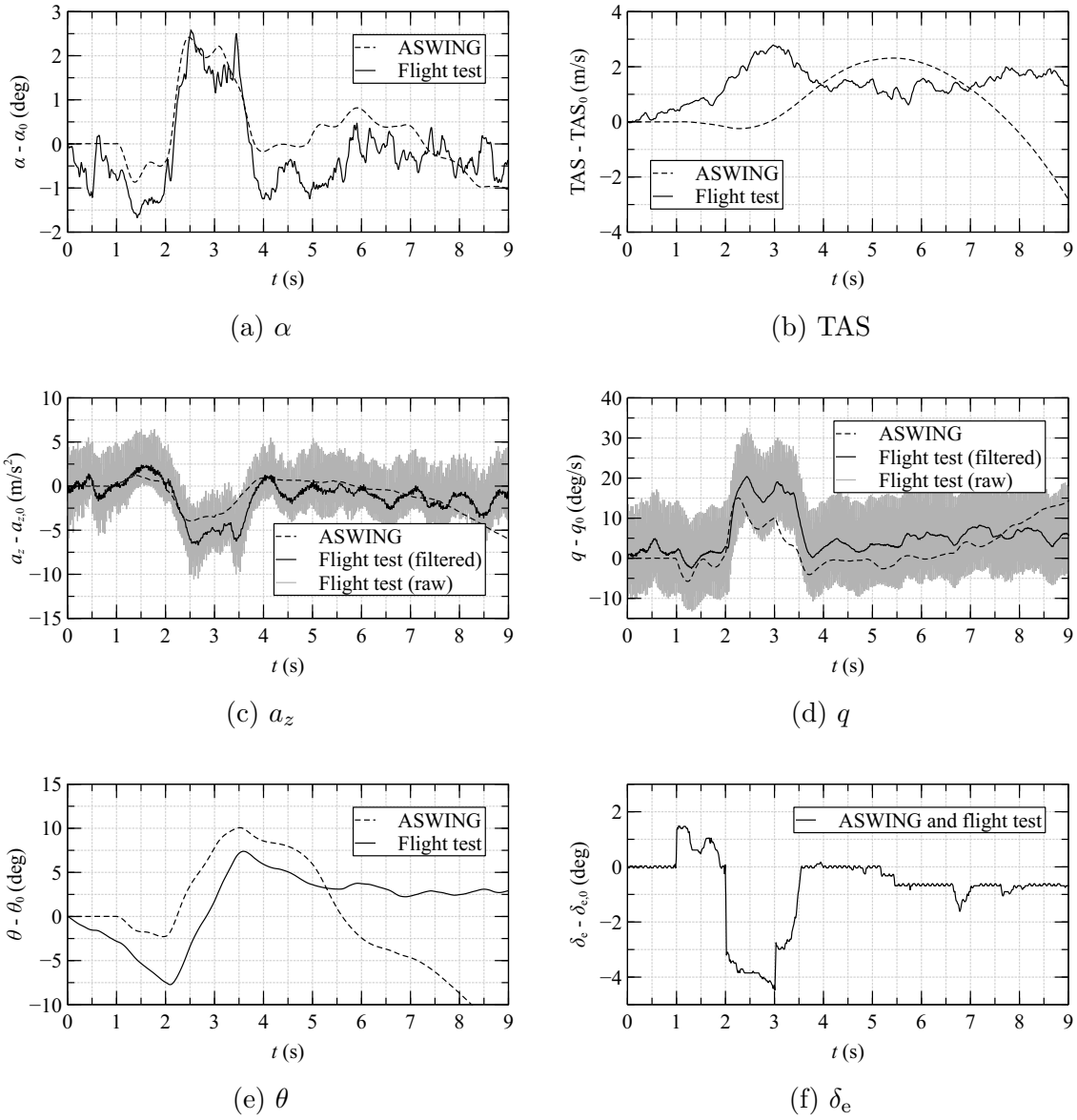

Figure 2.35: Comparison between flight test data and simulated response of the flexible QT1 aircraft to an elevator doublet command, for angle of attack α, TAS, z-acceleration a_z, pitch rate q, pitch angle θ and elevator deflection δ_e.

each maneuver test started with the aircraft leveled and trimmed and was conducted at approximately constant altitude and airspeed. This can help explain the discrepancies in TAS in figs. 2.33b, 2.34b and 2.35b. The third could be that the low-fidelity structural and aerodynamic models used in ASWING (beam-like structure and lifting line method, respectively) could not be accurate enough to model the effects of control surfaces deflection, wing deformation, and drag.

The noise in the raw z-acceleration and pith rate signals observed in figs. 2.33 to 2.35 is most likely high-frequency interference picked up by the DAQ. A low-pass filter was applied in post-processing (filtered signals in the figures), which was able to eliminate any aliasing of data from other phenomena with frequencies greater than 85 Hz, as mentioned before.

Wing deformation was also measured during flight tests and compared against the ASWING simulation. To accomplish this, the SPA method discussed earlier was used to reconstruct the displacement field from the measured strain field along the wing spar. A GoPro camera was also installed on the aircraft tail to capture the wing deflection during flight. Figure 2.36 shows a visual comparison of the flexible wing deflection as captured by the tail camera at different instants of the flight test. Even though the fisheye lens of the camera produces some visual distortion, which ends up amplifying the perceived wing deformation, it is possible to see that the range of motion of the wing during flight is considerable.

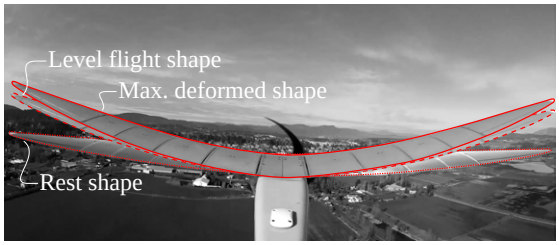

Figure 2.36: Wing deflection of the flexible QT1 aircraft at different instants of an elevator frequency sweep maneuver.

A comparison of the wing tip displacement between flight test data and ASWING simulation data, for flight tests FT1, FT2, and FT3, can be seen in fig. 2.37 on the left. The displacements show a good agreement between experimental and simulated data for all three flight tests. However, for FT2, where an elevator frequency sweep was used as input command, some discrepancies in terms of amplitude can be seen between the two signals. The measured displacement appears to damp out as the frequency of the sweep command increases. This could be explained by structural damping unaccounted for in the ASWING model. Another explanation is that cabling running along the wingspan is free to move by design, in order not to add stiffness to the wing spar, and thus at higher frequencies can damp out wing vibration. Another hypothesis could be due to tail dynamics damping out the wing dynamics. The tail dynamics were not considered in this work due to the fact that its structure is very stiff, just like the fuselage structure, and we would expect its dynamics to become

more apparent at higher frequencies. However, it could still justify the discrepancies observed.

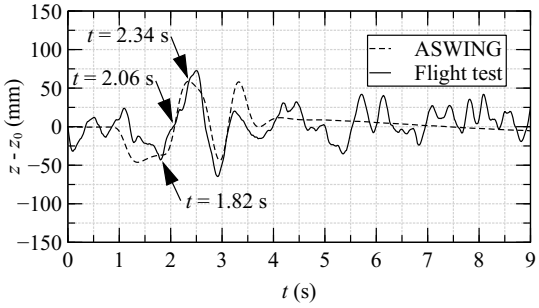

(a) Wing tip deflection for FT1 (3–2–1–1)

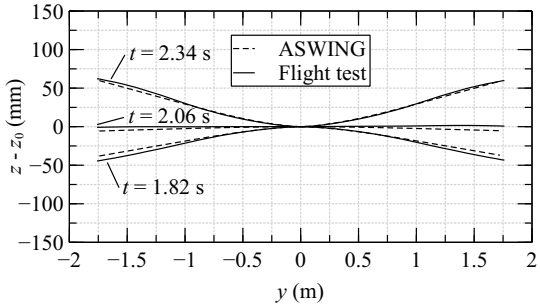

(b) Spanwise wing deflection for FT1 (3–2–1–1)

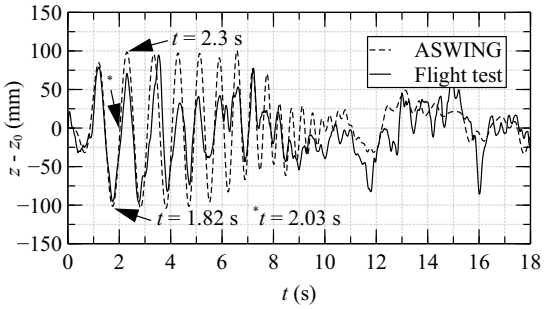

(c) Wing tip deflection for FT2 (frequency sweep)

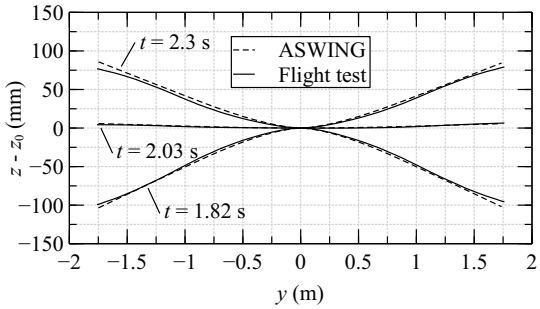

(d) Spanwise wing deflection for FT2 (frequency sweep)

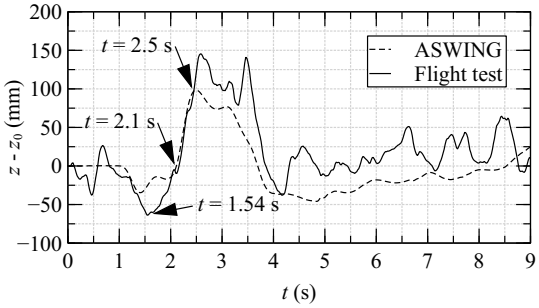

(e) Wing tip deflection for FT3 (doublet)

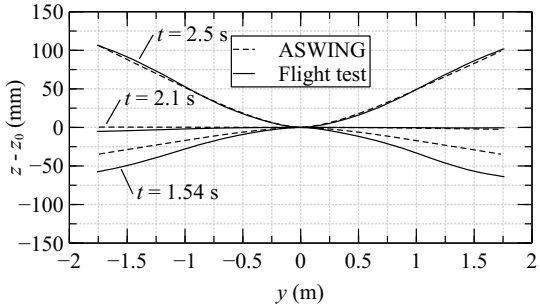

(f) Spanwise wing deflection for FT3 (doublet)

Figure 2.37: Comparison of wing tip deflection (left) and spanwise wing deflection at three time instants (right) for flight tests FT1, FT2 and FT3, between reconstructed displacements from in-flight-measured strains and aeroelastic ASWING simulation, for the flexible QT1 aircraft.

The fuselage–wing and fuselage–tail connections, as well as control surface interfaces, could also be contributing to damp out the wing motion. These connections

were assumed rigid in the models—the components were firmly bolted together and the control surface hinges were relatively stiff—but could be affecting the aircraft dynamics. Nevertheless, the frequency content of the two signals appears to agree well.

It is worth mentioning also that the control surface effectiveness was not studied in this work and could also help justify the differences observed in the results. This would need further investigation and would require either high-fidelity CFD models or system identification techniques in order to update stability and control surface derivatives. This is in fact planned for future work as all the data needed to perform system identification is already collected.

The spanwise wing deflections are compared in fig. 2.37 on the right, at three different time instants of each test. It is possible to observe that the SPA method is able to reconstruct the spanwise wing displacement for the three flight tests and that it agrees well with the predicted displacement from the ASWING time-marching simulation.

2.5 Concluding Remarks

This paper describes the sizing, design, optimization, ground testing, and flight testing of a flexible HARW UAV platform to quantify the coupling between flight-dynamic and elastic modes. Experimental results include static load tests, ground vibration, and flight tests. Aerodynamic, structural, and aeroelastic models were built using AVL, NASTRAN, and ASWING. The static load tests were compared with the NASTRAN and ASWING models with good agreement. GVTs were conducted on two sets of wings, rigid and flexible, with two excitation methods, shaker and impact tests. It was found that higher frequency modes were more difficult to obtain and that impact testing was more versatile than the shaker testing method. Results from GVTs were used in the update of the FE models of the flexible aircraft. Pre-flight ground testing included SIL and HIL simulations in order to approximate acceptable controller gains for flight testing, as well as to test maximum amplitudes and test duration of maneuver tests. A flight test campaign was developed, and data was collected from flight tests where 3–2–1–1, frequency sweep, and doublet maneuvers were carried out.

A comparison between the aeroelastic dynamics from the ASWING model and experimental flight test data was performed for the three different maneuver commands. The time-marching results obtained from the aeroelastic simulation agree well with

the flight test data for all flight tests. The assumptions in initial conditions used to start the simulations in ASWING, as well as the low-fidelity formulations employed in this aeroelastic framework, are two probable causes for some of the differences observed between the experimental and computational results. This work illustrates the feasibility of using scaled flight test demonstrators as a cost-effective platform for testing aeroservoelastic coupling in HARW aircraft designs and the importance of accurately modeling the multiple disciplines (aerodynamics, structures, and controls) involved in aeroservoelastic evaluation of HARW aircraft.

Chapter 3

Numerical and Experimental Characterization of the Nonlinear Aeroelastic Behavior of a Flexible Joined-Wing UAV

The work presented in this chapter discusses the development of a joined-wing UAV with flexible front and aft wings, conducted in partnership with Boeing. The work presents an investigation of the nonlinear aeroelastic behavior of Boeing's JWSC concept. Experimental data consisting of static load tests, ground vibration tests, and preliminary flight tests are compared with numerical aerodynamic, structural, and aeroelastic simulations of the aircraft. This work is based on a paper submitted for publication:

M. Bras and A. Suleman. "Numerical and Experimental Characterization of the Nonlinear Aeroelastic Behavior of a Highly-Flexible Joined-Wing UAV". In: *AIAA Journal* (2023). Submitted

Abstract

Joined-wing aircraft configurations have the potential to improve aerodynamic efficiency, reduce structural weight, and exhibit enhanced sensing capabilities. However, these advantages come at the cost of potential nonlinear aeroelastic behavior. One such design is the Boeing JWSC, a high-altitude long-endurance airborne platform that exhibits elastic buckling resulting from the aft wing supporting, in compression, the forward wing aerodynamic loading.

In an effort to reduce the cost and risk associated with the experimental validation and evaluation of full-scale models, scaled flight test demonstrators with flexible wings are a desirable approach to evaluate the aeroelastic response of joined-wing aircraft. Previous work has demonstrated the airworthiness of scaled joined-wing demonstrators through the successful flight of geometrically-scaled remotely piloted vehicles, but the assessment of geometric nonlinearities in flight is yet to be determined.

In this work, the development and testing of a 3 m-span scaled flexible autonomous JWSC is presented with the objective of validating the nonlinear aeroelastic behavior. Static load tests and ground vibration tests were performed to characterize the vehicle's static and dynamic elastic response and to update the numerical models. These are essential steps for a safe flight test program. Flight testing of a rigid variant of the aircraft was performed to validate flightworthiness. Numerical results of static aeroelastic deformation, lift distribution, stability derivatives, and time-dependent aeroelastic simulations are presented and analyzed in detail and compared with the rigid, linear, and nonlinear structural models. This work provides insights into the importance of considering geometric nonlinearities in the design and analysis of flexible joined-wing aircraft.

3.1 Introduction

To inspire innovation and technology development that addresses the most pressing military capability gaps, the Boeing SensorCraft [186], a multi-disciplinary design challenge, has been under consideration by the United States Air Force Research Laboratory (AFRL) for intelligence, surveillance and reconnaissance (ISR) missions. The goal is to integrate the sensing functionality currently incorporated in several wide-body aircraft into an autonomous airborne sensor capable of 30 h of endurance at 2000 NM range. The SensorCraft is envisioned to fill the role of the next generation HALE ISR platforms and enhance situational battle awareness capabilities [42, 75, 186, 187].

This work presents the design, sizing, numerical modeling, ground testing, and validation of an aeroelastically-tuned JWSC UAV platform with flexible front and aft wings. The flexible wing airframe was designed to exhibit geometric nonlinearities under normal flight conditions. This flexible aircraft platform can be pushed to high g loading cases that allow for the investigation of its nonlinear aeroelastic behavior, flight dynamics, and validation of computational models. Experimental data consisting of static load tests, ground vibration tests, and preliminary flight tests are compared with the results generated from aerodynamic, structural, and aeroelastic computational models developed in AVL, NASTRAN, and ASWING, respectively.

The current work is organized as follows: In section 3.2, the current 3 m-span flexible JWSC platform is described. The modeling and testing techniques adopted are discussed in section 3.3. Section 3.4 presents and discusses the results obtained, including ground test results used to validate and update computational structural models, an aeroelastic characterization of the flexible JWSC, and preliminary data collected from flight tests of a rigid variant of the aircraft. Finally, section 3.5 summarizes the findings and conclusions of the study. Figure 3.1 shows an overview of the research program, including phase 1 leading up to the current work presented in this chapter.

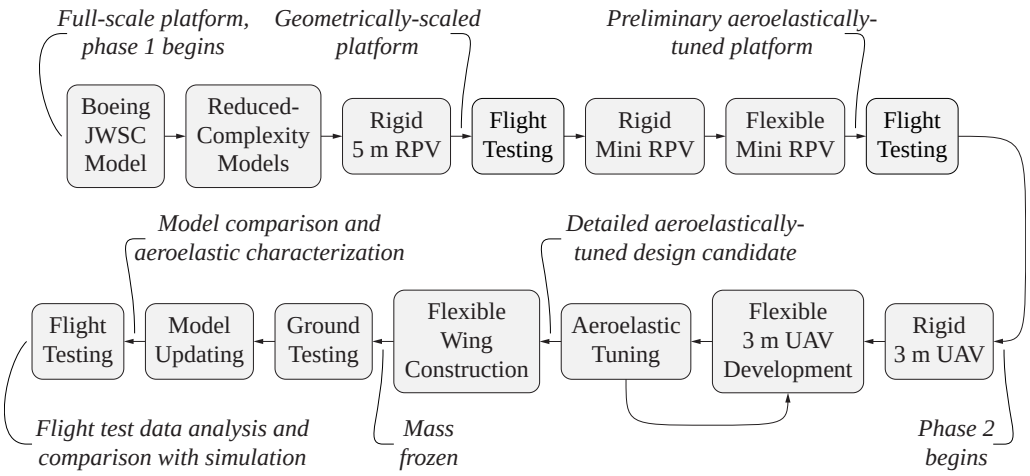

Figure 3.1: Timeline of the different tasks executed in chapter 3.

3.2 Flight Test Demonstrator

The JWSC platform considered in this work is a 3 m wingspan fixed-wing 6.57 % scaled version of the original joined-wing concept proposed by Boeing. The configuration is equipped with electric propellers and is limited to a MTOW of 25 kg. This experimental flight test demonstrator flies primarily in a fully autonomous mode and can be switched into a manual mode as a failsafe. Moreover, previous iterations of this aircraft have already had successful test flights.

Previous iterations of this aircraft have already demonstrated successful test flights [19, 46, 74, 75]. These low-cost models were used to assess fundamental flight dynamics of the JWSC configuration. Over time, these models were improved to the point that they shared the same scaled thrust, mass properties, and outer mold line (OML) of the full-scale aircraft. Initially, two 1.8 m scaled models with electric ducted propellers were constructed and flown before a heavier 5 m JetCat turbine-engine-powered model took flight. Next, a flexible version of the 1.8 m model was built and flown. Wing deflection data was recorded in video, and large deflections of the aft wing were observed. This flexible model was an important step in proving the feasibility of using flexible scaled JWSC models to study the nonlinear buckling effect of the aft wing. Table 3.1 and fig. 3.2 summarize the evolution of the JWSC development.

One of the shortcomings of the 1.8 m scaled model was the difficulty of adequately trimming the aircraft and executing controlled flight maneuvers to accurately see the effects of wing flexibility on the aircraft flight dynamics. The aircraft's low

aerodynamic–inertia force ratio caused the aircraft to move and the aft wing to deflect considerably during small gust encounters.

Name	**MTOW**	**Wingspan (scale)**	**Objective**
Flat plate foamie RC	1 kg	1.68 m (3.68 %)	• first flying model • investigate predicted yaw instability
Twist-corrected foamie RC	2.1 kg	1.85 m (4.05 %)	• correct shortcomings of first foamie • devise take-off and landing strategies • control surface scheduling
Rigid mini RPV	4.6 kg	1.85 m (4.05 %)	• control development • test manufacturing techniques • test plan optimization
Rigid 5 m RPV	92.8 kg	5 m (10.96 %)	• matched mass and inertia • phasing test • development of instrumentation
Redesigned rigid mini RPV	4.6 kg	1.85 m (4.05 %)	• test bed for new pilots • improve weight distribution • modify internal layout • additional payload capacities
Flexible mini RPV	4.6 kg	1.85 m (4.05 %)	• first flexible model with tailored wing spars • demonstrate controllability • collect preliminary wing deformation data
Rigid 3 m UAV	21.6 kg	3 m (6.57 %)	• reconfigurable platform • increased payload mass and volume • characterization through ground testing
Flexible 3 m UAV	21.6 kg	3 m (6.57 %)	• investigation of aeroelastic response • characterization through ground testing • collect detailed wing deformation data

Table 3.1: Development of the JWSC platform leading up to the flexible 3 m wingspan model that is the subject of this work (adapted from [46]).

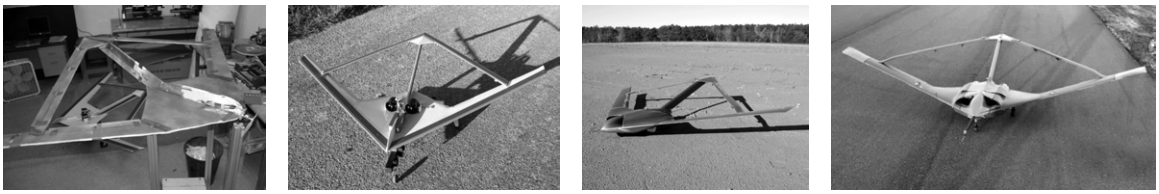

(a) Flat-plate foamie RC (b) Twist-corrected foamie RC (c) Rigid mini RPV (d) Rigid 5 m RPV

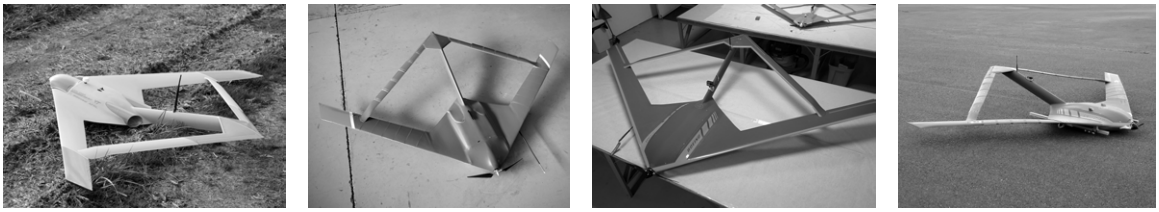

(e) Redesigned rigid mini RPV (f) Flexible mini RPV (g) Rigid 3 m UAV (h) Flexible 3 m UAV

Figure 3.2: Different-complexity JWSC models leading up to the flexible 3 m wingspan model that is the subject of this work (adapted from [46]).

More recently, a new redesigned 3 m JWSC platform has been developed and flown. This platform is heavier and bigger than the 1.8 m model, overcoming the limitations of the smaller model. It is also fitted with a propeller-driven electric motor, making it less complex than the 5 m turbine-engine-powered aircraft. Figure 3.3 shows a 3-view of the final design of the new platform.

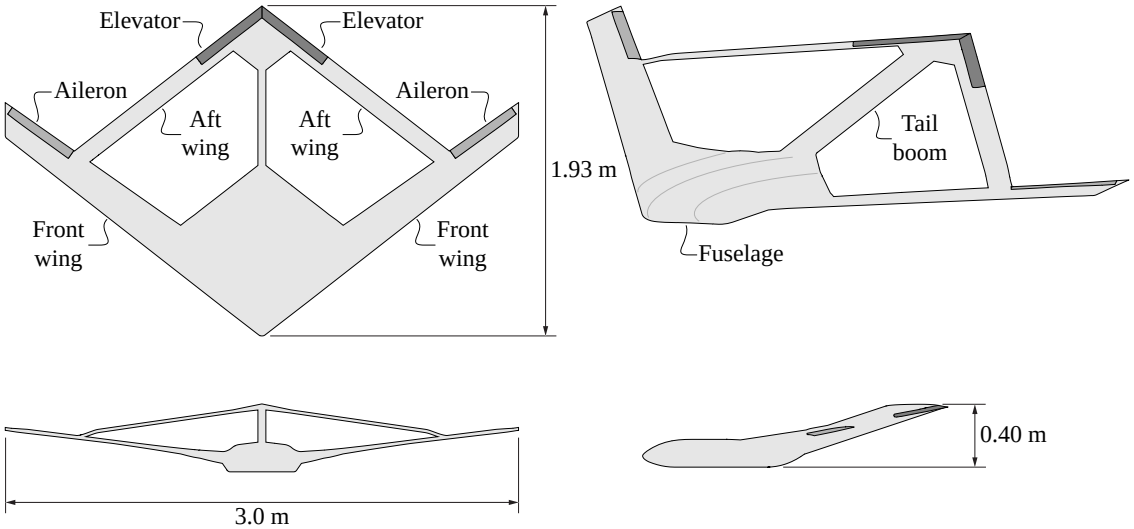

Figure 3.3: JWSC platform 3-view.

This platform served as the basis for developing the flexible 3 m aircraft, which is the focus of this work. It was built with modular fuselage and wing components, allowing the wings to be swapped for flexible ones when needed. The specifications of the 3 m JWSC model are summarized in table 3.2.

Parameter	**Value**
Reference area	0.5 m^2
Wingspan	3 m
MAC	0.242 m
Max. range	164 km
Max. endurance	20 min
Min. altitude	50 m AGL
Max. altitude	150 m AGL
Empty mass	17.6 kg
Max. take-off mass	25 kg
Launch method	Pneumatic launch
Propulsion	Electric puller motor
Stall speed	19 m/s
Cruise speed	28 m/s
Max. speed	38 m/s

Table 3.2: JWSC platform specifications.

3.2.1 Airframe and Components

The airframe is constructed out of carbon/epoxy and fiberglass/epoxy composite materials, with aluminum and carbon/foam/carbon bulkheads, and aluminum ribs.

This aircraft's parts manufacturing methods include 3- and 5-axis milling of bulkheads and ribs, 3D printing of mounting brackets, and layup of fuselage and wing composite skins. The payload bay of the JWSC can carry a maximum of 6.7 kg, with dimensions of 261 mm by 355 mm by 111 mm. Figure 3.4 shows the battery and payload bays of the aircraft. The battery bay holds the propulsion and avionics batteries and provides access to the power management board and electric motor.

The load-bearing structure of the front and aft wings of the flexible JWSC is made of aluminum with a narrow cross-section, allowing them to deform without causing

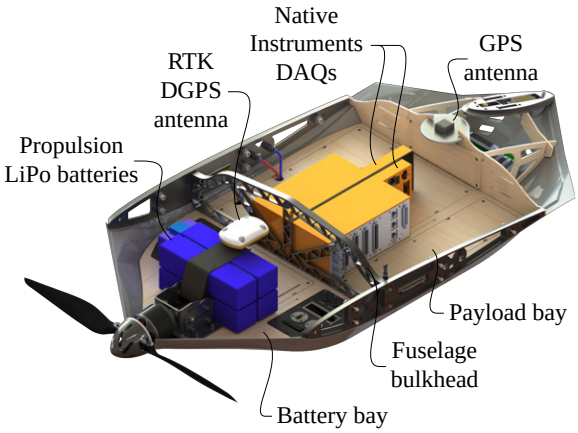

Figure 3.4: Battery and payload bays of the JWSC.

failure. The wings are broken down into a series of aerodynamic panels designed to attach to the wing spars at specific spanwise locations (see fig. 3.5). Each of these aerodynamic panels is attached at only one point to the underlying spar. This minimizes the load transferred from the rigid wing skin to the flexible spars, thus avoiding unwanted added stiffness.

A small gap between panels prevents contact or binding when the aircraft wing bends. The gap is sealed with tape, preventing air from leaking to the wing's top surface. The tape creates a lap joint between two adjacent panels, but it only has adhesive on one edge, allowing it to slide on one side of the gap as the wing flexes.

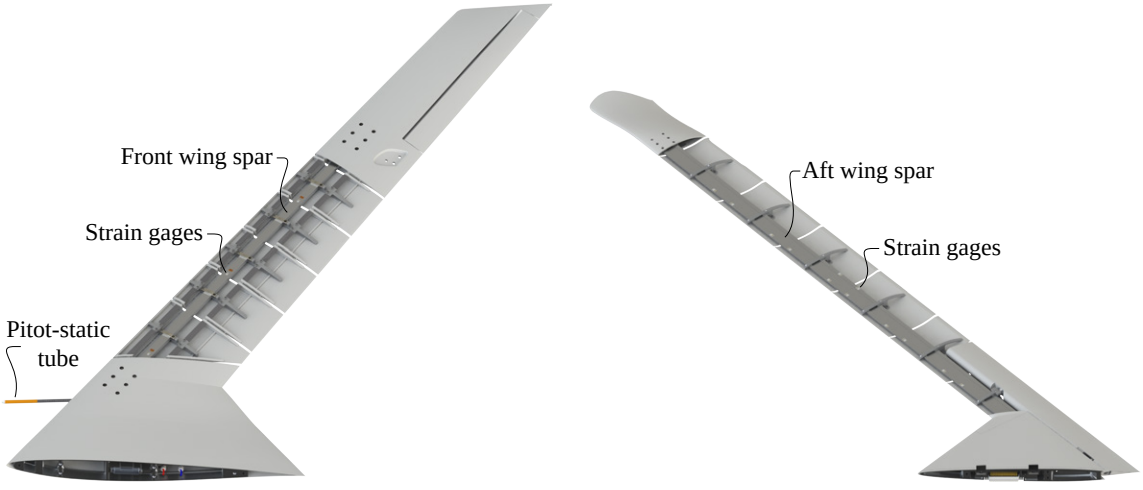

(a) Front wing (b) Aft wing

Figure 3.5: Flexible front and aft wings of the JWSC.

3.2.2 Electrical and Avionics Systems

The design of the JWSC platform is such that different commercial off-the-shelf autopilots can be used but primarily operates with the Piccolo family of autopilots developed by CloudCap Technologies. The autopilot provides the aircraft with stability augmentation, automated navigation, take-off and landing, and payload control capabilities.

The Piccolo family of autopilots supports onboard data logging of telemetry and commands and data logging on the GCS. The autopilot also allows for two layers of control redundancy and provides safety features such as a dead-man switch, electronic fences, and pre-programmed failure protocols. Speed and altitude limits can be programmed to help ensure a safe operation and reduce the operator's likelihood of a hazardous input.

Spatial positioning of the aircraft is achieved with a differential global positioning system (DGPS) real-time kinematic (RTK) positioning solution which achieves a maximum position accuracy of 3 cm. In the event of failure of the positioning system, a backup GPS connected to the autopilot gives a positional accuracy of between 1 m to 3 m.

The Piccolo autopilot provides fly-by-wire stability augmentation, where the pilot provides high-level commands, such as roll, yaw, pitch, and throttle input. The autopilot's inner loops control the surfaces to achieve these desired commands.

Two communication links are capable of controlling the aircraft through the Piccolo autopilot. The primary pilot, located outside the GCS, communicates with the autopilot using a 2.4 GHz transmitter and is responsible for flying the aircraft under direct visual conditions. The Picollo tethered transmitter, located inside the GCS, handles the telemetry link with the autopilot and can serve as the second control link, offering up to 25 km range. In this case, the commands from the controller are passed through a physical connection to the Piccolo ground station and sent to the autopilot via its 900 MHz communications link. A second pilot can fly the aircraft through a camera feed located at the aircraft's tail. The camera feed is transmitted using a 5.8 GHz video downlink.

Suppose the primary pilot encounters communication failure or loss of visual orientation. In that case, the second pilot, tethered to the GCS, could bring the aircraft back to a safe distance and re-acquire the primary control link or ensure the primary pilot regains visual orientation before passing control back.

In case of a complete autopilot failure, the third control layer is a fully manual mode that bypasses the autopilot. In this case, a backup pilot can obtain control during the flight by simply flipping a switch on the radio controlled (RC) transmitter. A downside of this last-resort control layer is a loss of stability augmentation.

The system's design is such that the backup controller can take control of the aircraft at any time, and the switchover is automatic in the event of signal loss with the primary controller.

A total of four 6S LiPo batteries power an E-flite Power 160 Brushless Outrunner motor, with RASA 20×15 folding props controlled by an HV120 ESC. The aircraft is equipped with a safety shunt that must be removed before the motor can be armed.

Underneath the battery bay, there is a wiring bay that houses the power management board and the ESC (fig. 3.6).

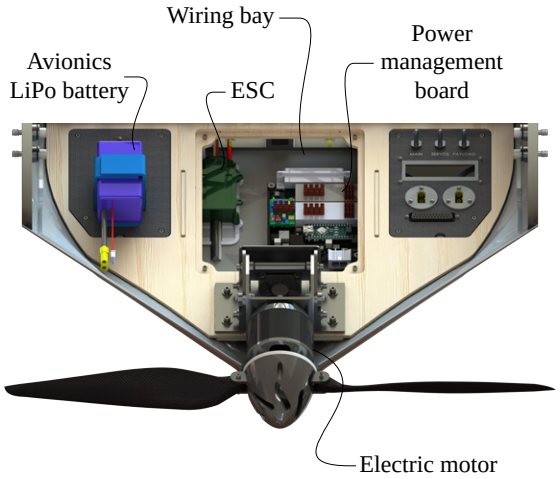

Figure 3.6: Wiring bay of the JWSC.

An AFTU hardware module was developed to aid the autopilot in superimposing scripted commands during flight. Accompanying software was developed to allow the pilot to generate commands on the ground and submit them to the onboard unit. The AFTU module was necessary since the Piccolo autopilot does not natively support scripted commands other than doublet commands.

The autopilot bay is located underneath the payload bay in the aircraft and houses the Piccolo autopilot, a video transmitter, and the AFTU. A junction board and radio modem are located in the adjacent modem bay, as shown in fig. 3.7. The junction board facilitates the integration of any payload system that may need to connect to the aircraft avionics and power sources.

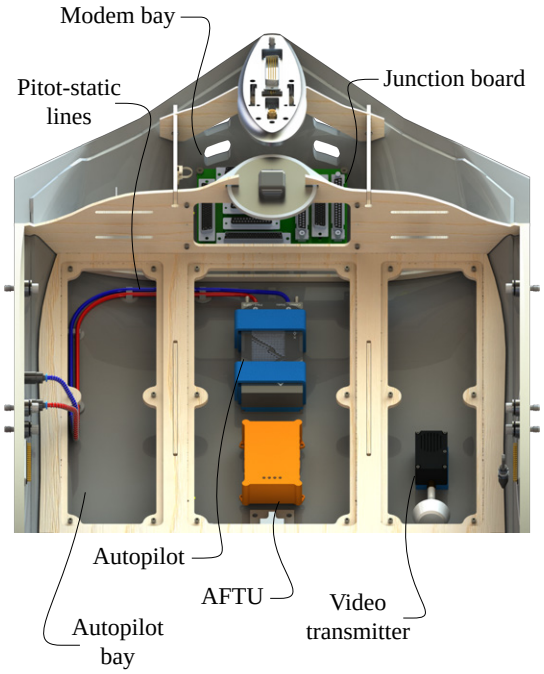

Figure 3.7: Autopilot and modem bays of the JWSC.

There are five cameras installed on the aircraft (see fig. 3.8). The first camera is a Mobius RunCam located in the tail boom and serves to provide first person video (FPV) of the flight. The other four cameras are all Foxeer Legend 1 models. The four cameras, located in blisters that protrude from the fuselage, point towards the aft wings of the aircraft, allowing them to record the wing deformations during flight.

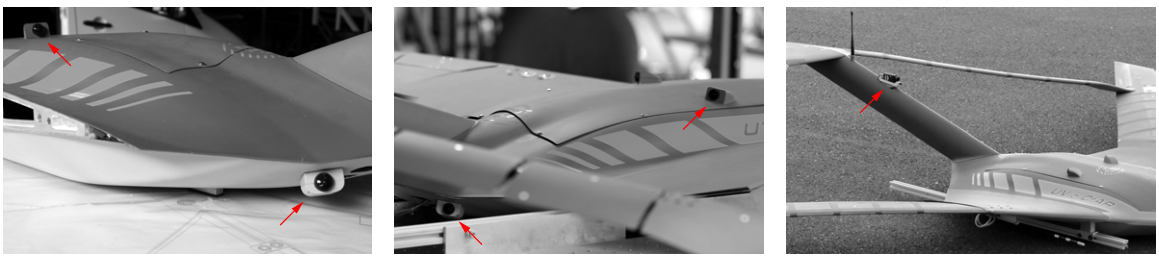

(a) Left fuselage cameras (b) Right fuselage cameras (c) Tail boom camera

Figure 3.8: Left and right Foxeer Legend 1 fuselage cameras (left and center, respectively), and tail boom Mobius RunCam camera (right) installed on the JWSC.

3.2.3 Ground Control Systems

The JWSC platform is used with an in-house-developed mobile GCS, which provides support for remotely operating the aircraft and has several layers of redundancy in communications links, computer resources, and backup power supplies.

The GCS is custom-built on a 2013 Mercedes Sprinter van. The unit consists of three workstations, a backup power/generator, a 45 ft stowable pointing antenna, and a wireless intercom system for communications between pilots and ground support staff (fig. 3.9a).

(a) MCU (b) Pneumatic launcher

Figure 3.9: Aircraft MCU (left) and pneumatic launcher (right).

One computer serves as the primary control station, with the second acting as a payload operator station. The third workstation displays live video feeds from the aircraft.

The aircraft is typically launched from a pneumatic catapult (fig. 3.9b) and recovered with a belly landing. All phases of flight, from launch to landing, can be performed in either manual or fully autonomous mode.

3.3 Modeling and Testing

Validation of the flexible JWSC flight test vehicle used a combination of structural, aerodynamic, and aeroelastic simulations in addition to ground vibration and static load testing. The vehicle also underwent pre-flight checks in the form of static thrust and iron bird testing, as well as SIL and HIL testing.

Predictions of the structural, aerodynamic, and aeroelastic performance of the JWSC used a combination of different-fidelity computational tools.

NASTRAN was used to carry out structural modal and static analyses, which allowed for assessing the structural performance in terms of modal response and static wing deflections.

Aerodynamic analyses were performed using both VLM and LLT through the use of AVL and ASWING, respectively. Aerodynamic lift distribution and stability derivatives were calculated from both models and compared against each other.

Finally, two different-fidelity models were built to characterize the aeroelasticity of the aircraft. The first model was a low-fidelity ASWING aeroelastic model, followed by a higher-fidelity coupled NASTRAN–AVL model. A MATLAB framework built to couple NASTRAN and AVL will be described in more detail later. A comparison of static aeroelastic deflections between the two frameworks showed that both could capture the aft wing's nonlinear buckling phenomenon. ASWING was also used to perform unsteady aeroelastic simulations of the flexible JWSC and study the effect of large wing deformations on the aircraft flight dynamics.

This comparison of different-fidelity computational frameworks was essential to guarantee consistency between models. In addition to model comparison, critical results were also validated against experimental tests, allowing a fine-tuning of computational models to make them match the final aircraft as built.

This section first presents the tools and methods used to develop structural, aerodynamic, and aeroelastic models of the JWSC aircraft. Following are the methods used to measure aft wing displacements during ground and flight testing. Finally, it discusses the experimental procedures used to perform bifilar pendulum, static load, ground vibration, and flight testing.

3.3.1 Structural Modeling

The structural modeling of the JWSC was performed using NASTRAN. The model uses `CBEAM` beam elements, `CQUAD4` quadrilateral shell elements, `CONM1` point masses, and `RBE2` rigid elements. Figure 3.10 depicts the NASTRAN model of the JWSC and the different types of elements used in the model.

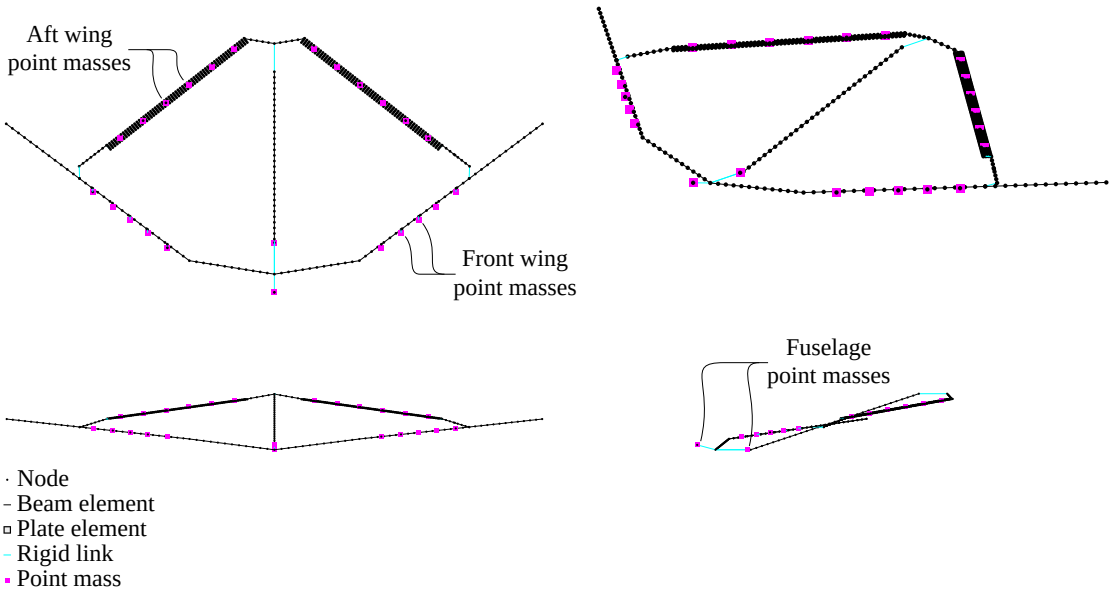

Figure 3.10: Structural NASTRAN model of the flexible JWSC.

In the developed structural model, the connections between different components of the aircraft—fuselage, front wing, aft wing, and tail boom—were assumed to be much stiffer than the components themselves, such that these connections could be modeled with `RBE2` rigid elements. To model the ladder-like geometry of the aft wing spar, `CQUAD4` quadrilateral shell elements were used in the flexible section of the aft wing in order to increase the accuracy of the strain distribution, and the rest of the aft wing used `CBEAM` beam elements. The front wing used `CBEAM` beam elements for the rigid and flexible sections. Rigid elements were also used in the aft wing to connect the flexible portion modeled with shell elements to the one using beam elements.

The model used point mass elements of type `CONM1` to represent the weight of wing ribs and skins and trim the model mass and inertia to match the values determined from bifilar pendulum tests. `CONM1` elements were also helpful when modeling the mass of instrumentation equipment during testing.

All the model's point masses and beam density values were tuned in an iterative

process such that the modal and static responses of the model matched experimental results.

3.3.2 Aerodynamic Modeling

The aircraft aerodynamics was characterized using an AVL model and a rigid ASWING model. The aerodynamic lift distribution was determined at trimmed level-flight and pull-up conditions. Stability derivatives were also calculated from both models. A comparison between rigid and flexible aircraft stability derivatives allowed for an assessment of the effects of reduced rigidity on the stability of the aircraft.

AVL uses a VLM formulation to model lifting surfaces, as well as slender bodies, such as fuselages and nacelles [164]. The vortex lattice method is based on potential flow theory and assumes the flow to be incompressible, inviscid, and irrotational. The flow can be represented by a velocity potential that satisfies the Laplace problem of eq. (2.2) and repeated here for convenience

$$\nabla^2(\Phi + \Phi_\infty) = 0.$$

The solution to this problem based on VLM is obtained by distributing doublet elementary solutions (or equivalent vortex rings) on the wing boundaries and applying the Kutta condition on trailing edges. Slender bodies can be modeled by distributing source elementary solutions on their surface. The perturbation velocity potential at any point of the domain is given by eq. (2.3) and repeated below

$$\Phi = \frac{1}{4\pi}\int_{S_b+S_w} \mu \mathbf{n}\cdot\nabla\left(\frac{1}{r}\right) dS - \frac{1}{4\pi}\int_{S_b} \sigma\left(\frac{1}{r}\right) dS.$$

The discretization of the perturbation potential allows for the computation of the vortex distribution for a particular wing geometry. Lift and drag coefficients can then be calculated from this distribution.

A flight-dynamic analysis is also possible with AVL by linearizing the aerodynamic model about a flight condition. In addition, AVL allows for modeling arbitrary aircraft configurations. The AVL model of the JWSC was composed of three components—front wing, aft wing, and tail boom. Since all these components are lifting surfaces in a joined-wing configuration, the model did not include any fuselage (slender body). The complete AVL model can be seen in fig. 3.11. The figure shows the discretization of the different lifting surfaces (vortex lattice).

The aerodynamics of the ASWING and AVL models were compared for a trimmed level-flight maneuver and a 2.5g pull-up maneuver.

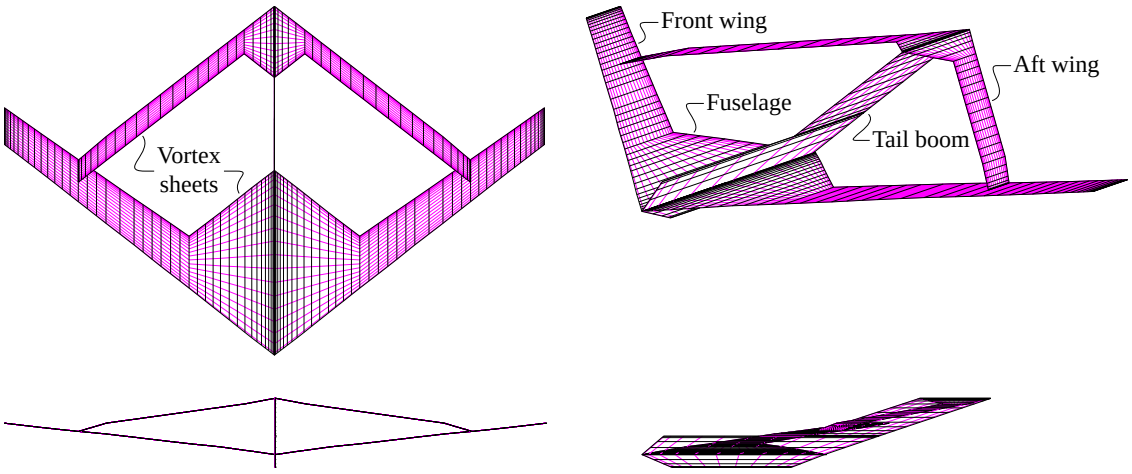

Figure 3.11: Aerodynamic AVL model of the rigid JWSC.

3.3.3 Aeroelastic Modeling

ASWING was used in this work to study the aeroelastic response of the flexible JWSC. It incorporates structural (nonlinear beam model using an iterative finite differences solution procedure [166, 167]), aerodynamic (UVLM with compressibility corrections to model lifting surfaces and slender body theory for fuselage bodies) and control (general state-feedback control law) models. ASWING allows for quick nonlinear analyses involving multiple disciplines using low-fidelity models, thus useful for the preliminary design phase of aircraft. Engine models can also be implemented in ASWING and throttle can be set as a control input.

The framework capabilities have been benchmarked with application problems: oscillating beam (good agreement was found when compared to the exact solution) and two-dimensional flutter (flutter speed prediction was close to the exact solution). ASWING attempts to solve the problem defined by the generalized aeroelastic equations of motion of eq. (2.4) and repeated here for convenience

$$\mathbf{M}\ddot{\mathbf{q}}(t) + \mathbf{C}\dot{\mathbf{q}}(t) + \mathbf{K}\mathbf{q}(t) = \mathbf{F}(t).$$

In addition to nonlinear aeroelastic analysis in time, dynamic response with gusts and modal analysis are also supported. The latter is of particular interest for the

analysis of flexible high aspect ratio wings. In these models, the root locus of flight-dynamic modes and structural elastic modes are closer to each other when compared to a rigid wing model. ASWING outputs the combined root loci of all aeroelastic modes, which can be useful in the identification of body freedom flutter instabilities. This problem was studied by Love et al. [168] using the ASWING framework for a flying HALE aircraft and found the body freedom flutter problem to be critical for low altitude conditions inside the flight envelope. The computational framework formulation is described in two technical reports [148, 149].

The ASWING model of the JWSC closely follows the NASTRAN FE model, in terms of its geometry and node distribution. Figure 3.12 depicts the aeroelastic ASWING model of the flexible JWSC.

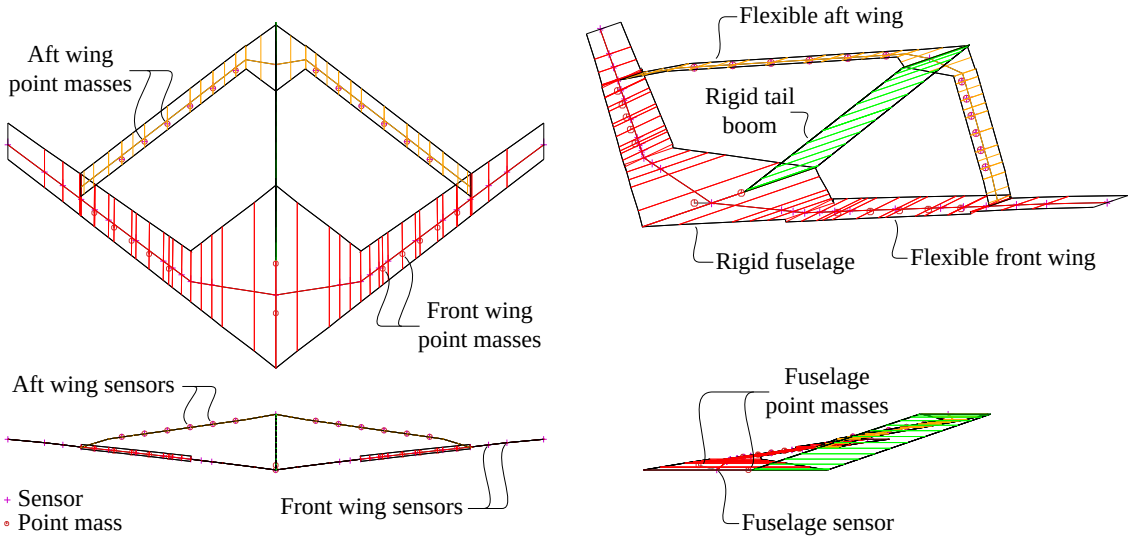

Figure 3.12: Aerodynamic ASWING model of the flexible JWSC.

A coupled AVL–NASTRAN aeroelastic framework was developed to benchmark the ASWING results. This framework allowed for a two-way coupling of the NASTRAN structural solver with the AVL aerodynamic solver. The process is illustrated in fig. 3.13. Ricciardi [188–190] developed a similar framework as part of the SensorCraft investigation, but in their work, a custom VLM solver was used. Howcroft et al. [191] mentions a similar approach but the NASTRAN `SOL 144` aeroelastic module is used to calculate the rigid aerodynamic loads and the structural analysis is performed using the SOL 106 nonlinear structural module.

The process starts with an initial aircraft geometry $\mathcal{T}^{(0)}$ that is passed to AVL for an aerodynamic analysis at specified conditions. This analysis results in stripwise lift,

drag, and moment coefficients C_l, C_d, and C_m, respectively. The forces and moments associated with these coefficients are then calculated and transferred to the structural solver as external loads. A static nonlinear structural analysis (`SOL 400`) is executed in NASTRAN and the vector of spanwise linear and angular displacements $\mathbf{d}$ is recorded. Finally, the aircraft geometry is updated with these displacements, resulting in a new geometry $\mathcal{T}$ that is passed to the aerodynamic solver. The process repeats until the results converge. Convergence is checked by tracking the changes in structural node positions, aerodynamic panel displacements, and aerodynamic loads. The final aircraft geometry $\mathcal{T}^{(*)}$, converged aerodynamic coefficients $C_l^{(*)}$, $C_d^{(*)}$, $C_m^{(*)}$, and structural displacements $\mathbf{d}^{(*)}$ are saved.

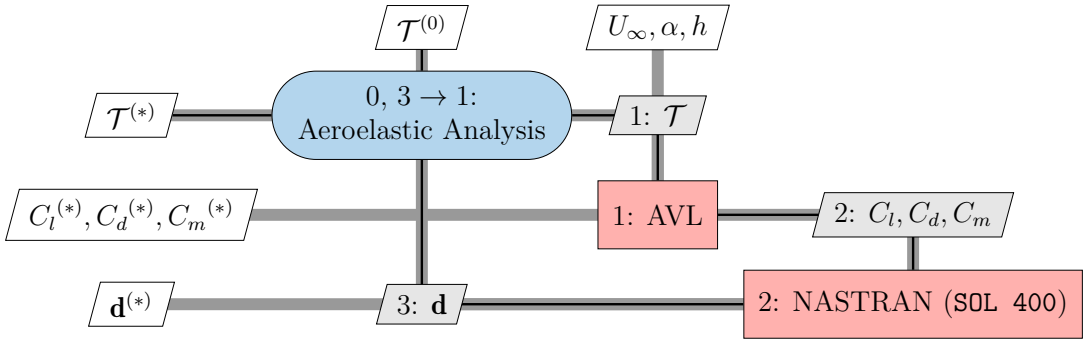

Figure 3.13: Overview of nonlinear aeroelastic analysis.

3.3.4 Bifilar Pendulum Testing

BPTs were performed to determine the inertial properties of the aircraft (both rigid and flexible configurations). BPTs are a cost-effective way of determining the inertia properties of bodies of complex shape. In a bifilar vertical-axis torsional pendulum test, an object hung by two parallel wires is free to rotate about the vertical axis.

The experiment measures the moment of inertia for the axis of rotation parallel to the wires. The system is approximated as a compound pendulum, and its natural frequency of free oscillations is estimated [169, 170]. The Lagrangian dynamics of this system is formulated as in eq. (2.5) and repeated below for convenience

$$I\ddot{\theta} + K_D\dot{\theta}|\dot{\theta}| + C\dot{\theta} + \frac{mgD^2 \sin\theta\cos\theta}{4h\sqrt{1-\left(\frac{D\sin\theta}{2h}\right)^2}} = 0.$$

Transient experimental data of decaying oscillatory aircraft motion was fit to the model using Simulink, which resulted in the identification of both aerodynamic and viscous damping parameters, K_D and C, respectively. The process was repeated with the aircraft hung at different orientations to obtain the moments of inertia about the three axes.

A custom rig was used to hold the aircraft suspended with two parallel wires. These wires are connected to the rig to ensure the rig rests on the chosen oscillating axis. The empty fixture then oscillates in the roll, pitch, and yaw axes, and the resulting data is used to calculate the inertia of the rig. The experiment was repeated with the aircraft inserted into the rig. The system is oscillated in each orientation to determine the overall inertias of the rig and aircraft.

The inertia of the rig was then subtracted to determine the aircraft moments of the aircraft. Since the aircraft will be flying at different weights and C.G. locations, these baseline results will be modified on a per-flight basis to account for added trimming weight and C.G. travel.

Figure 3.14 shows a BPT being performed on the JWSC.

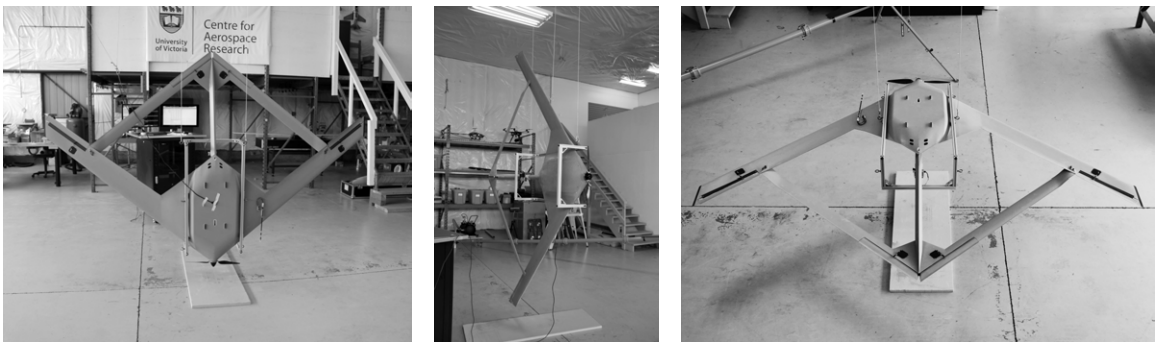

(a) Roll axis (b) Pitch axis (c) Yaw axis

Figure 3.14: BPT of the JWSC in roll, pitch, and yaw axes.

3.3.5 Static Load Testing

A static structural load test of the JWSC was completed to validate the structural design and fabrication and to ensure that the structure was capable of withstanding the predicted aerodynamic loading required to complete all planned flight maneuvers.

The AVL model was used to determine the most adverse aerodynamic loading case and the resulting spanwise load distribution. The aerodynamic load distribution was

approximated by concentrated point loads applied to a point close to the connection between the front and aft wings (see fig. 3.15c).

Anchors were mounted to the aircraft wings close to this point and connected straight to the wing spar, guaranteeing that the load was transferred directly to the spar and not the wing panels. Masking tape with a centerline drawn was used to highlight the wing spar on the wing panels.

Vinyl markers and Creaform fiducial markers were also used to mark points along the wingspan where displacements were to be measured, as shown in figs. 3.15a and 3.15b. Vinyl markers were used with the onboard cameras to track wing displacements during flight, while the fiducial markers were used with a 3D scanner to track wing displacements during static load tests.

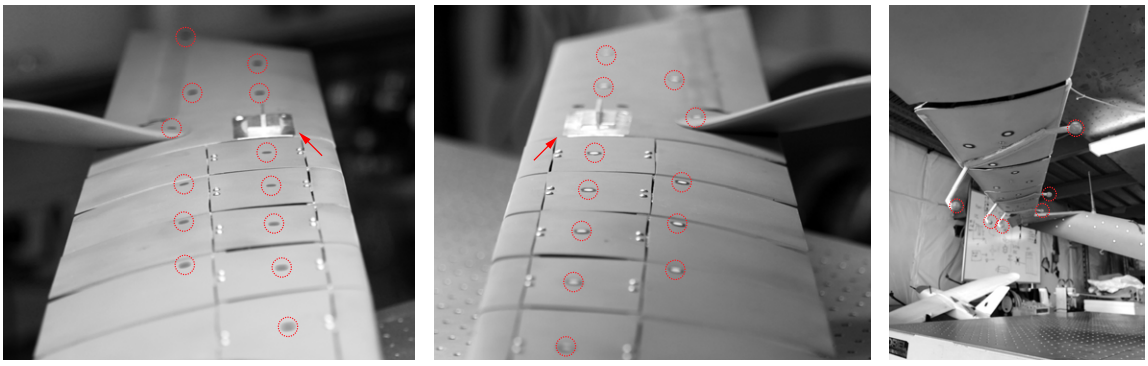

(a) Vinyl markers (b) Creaform fiducial markers (c) Trackball markers

Figure 3.15: Vinyl markers (left), Creaform fiducial markers (center), and trackball highlight markers (right) placed on the front and aft wings of the JWSC during static load testing. Markers are circled in red. Load anchor points are indicated by red arrows.

The first test consisted of the aircraft clamped to an optical table using laser-cut brackets that conform to the fuselage profile. The aircraft was bolted upside down to the ceiling for the second test with no loads applied to the anchor points. The aircraft was kept upside down and fixed to the ceiling for the remaining tests, but sandbags were placed at the anchors previously attached to the wings. With this setup, the direction of the point loads remained vertical, irrespective of the wing's deformation. Each bag's mass was measured before attaching it to the anchor point and was increased for several load steps. Figure 3.16 shows the flexible JWSC undergoing static load tests for two different load cases.

Displacements were measured using a Creaform Go!SCAN 3D portable scanner

(a) Gravity-only load case (b) Maximum load case

Figure 3.16: JWSC undergoing static load tests. Gravity-only (left) and maximum (right) load cases are shown.

(fig. 3.17a). Creaform fiducial markers were placed on the aircraft's front and aft wings, and the position of these points was tracked for every test. A 3D printed coordinate system was attached to the aircraft nose as shown in fig. 3.17b, which served as a fixed reference point for the tracking system.

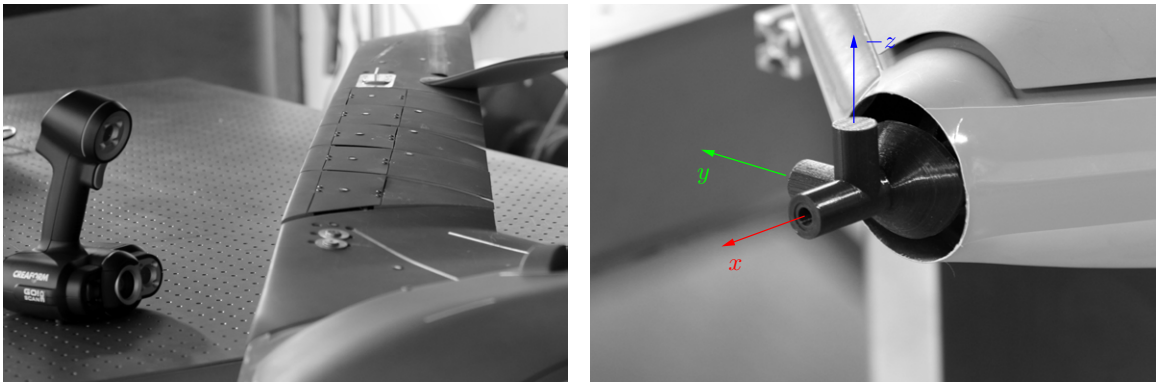

(a) Creaform Go!SCAN 50 3D scanner (b) 3D printed nose coordinate system

Figure 3.17: Creaform Go!SCAN 3D portable scanner (left) and 3D printed nose coordinate system (right).

The position of tracked points was post-processed to determine vertical displacements and twist angles along the span of each wing, which were then compared against NASTRAN and ASWING results. Figure 3.18 shows a series of the partial 3D scans collected during static load tests.

Strain measurements were performed on the flexible aircraft's front and aft wing spars. The spars were instrumented with strain gauges in a half-bridge beam bending configuration for a total of 11 strain measurement points per semi-wing span. Fig-

Figure 3.18: Partial 3D scans of the JWSC during a static load test.

ure 3.19 depicts the location of these points on the front and aft wings of flexible aircraft. The strain gauges are 350 Ω 5 mm-wide gauges and were measured using Native Instruments NI-9237 strain bridge input modules.

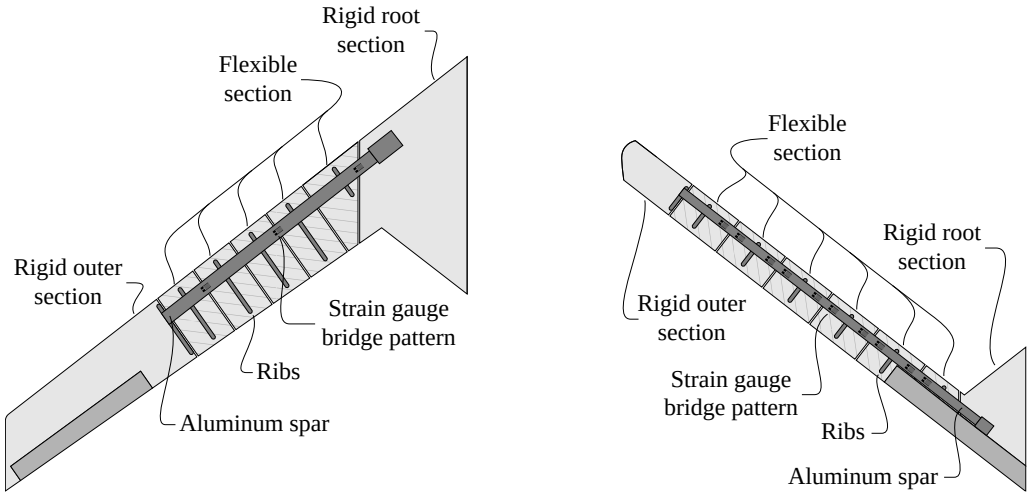

(a) Front wing (b) Aft wing

Figure 3.19: Repeating strain bending bridge pattern applied to the front and aft wings of the flexible JWSC. The pattern is mirrored on the underside of the spars (not shown).

3.3.6 Ground Vibration Testing

GVTs of the JWSC were designed to facilitate the update of the FE model. The tests were performed for two simpler configurations—aft wing removed (C1) and aft wing only (C2)—before testing the full aircraft configuration (C3). This approach allowed the wings to be individually characterized under simpler testing conditions. For instance, with the aft wing removed, the complicated dynamics due to the connection of the aft and front wings vanishes, and the wings are expected to behave like two cantilever beams. The same reasoning applies to the aft wing test.

Once the individual configurations were characterized and the FE model updated, the full aircraft assembly was tested, and the model was updated one more time. Table 3.3 outlines the different tests performed for each configuration and the boundary conditions and test strategies used.

Configuration	**BCs**	**Excitation method**	**Reference type**
Aft wing removed (C1)	Fixed	Roving impact	Single-reference
Aft wing only (C2)	Fixed	Roving impact	Single-reference
Full assembly (C3)	Fixed and free	Roving impact	Single-reference
Full assembly (C3)	Free	Twin-shaker	Multiple-reference

Table 3.3: Summary of GVT runs performed on the JWSC.

The first two configurations (aft wing only and front wing only) were tested by roving impact, using PCB Piezotronics 086C03 impact hammer shown in fig. 3.20a. The hammer has an embedded impedance head to measure the forces applied when exciting the structure. Accelerations were measured using the PCB Piezotronics 352A24 miniature single-axis piezoelectric accelerometer (fig. 3.20c), with a frequency range of 0.8 Hz to 10 000 Hz (±5 %). The aircraft was fixed to a vibration-isolated table with a rig similar to that used for static testing.

The full aircraft assembly was tested by roving impact and shaker testing. Shaker tests were performed to increase the resolution of identified mode shapes from impact tests and identify modes that had been missed from roving impact testing.

Shaker testing allows for a higher signal-to-noise ratio. Longer excitation times promote longer signal decays, making contaminating noise less harmful, even more so when performing averages. The fixed, electronically controlled input allows for more coherent (repeatable) excitation of the structure so that nonlinearities in the system can be identified and their influence can be diminished. This controlled, continuous energy input to the structure was expected to help distinguish the modes.

Multiple input, multiple output (MIMO) shaker testing was performed with a total of 17 PCB Piezotronics 352A24 miniature single-axis accelerometers spread throughout the structure. One miniature PCB Piezotronics K2007E01 electromagnetic shaker was positioned beneath each of the front wings. Unlike the impact hammer, these shakers did not possess embedded impedance heads. PCB Piezotronics 208C01 load cells were used to measure the force input by the shakers. Figure 3.20b depicts the shaker, with

(a) Impact hammer (b) Shaker (c) Single-axis accelerometer

Figure 3.20: Impact hammer (left), shaker (center), and single-axis accelerometer (right) used during a GVT of the JWSC.

its nylon stinger mounted to the load cell. The cells were glued to aluminum tape to prevent damage to the painting.

The shaker tests were performed with simulated free-free boundary conditions that allowed capturing free-free aircraft modes and obtaining better insight into the aircraft dynamics. With the aircraft unconstrained, lower frequencies were expected since the modal density was inferior (the modes were not as close in frequency) compared to the predictions for fixed boundary conditions.

Various methods were tested to recreate free-free boundary conditions as best as possible. Experiments were initially performed with the aircraft resting on foam and air balloons, but the GVT results were unsatisfactory with these methods. Significantly better results were obtained by hanging the aircraft using soft elastic bungee ropes (see fig. 3.21).

(a) Foam (b) Foam and balloons (c) Bungees

Figure 3.21: Different methods used to simulate free-free boundary conditions in a GVT of the fully-assembled JWSC.

A chirp signal was used to drive the shakers. An initial chirp ramp control was

introduced so that the amplitude would grow slowly and steadily at low frequencies, where the shakers do not perform very well. This, along with logarithmic frequency spacing of the chirp signal, promoted better coherence in the low frequencies of the measured FRF. The frequency range used for the chirp was between 2 Hz to 60 Hz.

3.3.7 Model Updating

The structural models of the flexible JWSC were updated in order to bring their modal response closer to that of GVTs before any other analyses could be performed or any other results could be analyzed. The structural NASTRAN model was fine-tuned to match experimentally-obtained modal frequencies and mode shapes, as well as static deflections. The updated NASTRAN model properties were then transferred to ASWING for subsequent analysis.

Model updating works by modifying the mass, stiffness, and damping parameters of a FE model until an improved agreement between FEA data and experimental test data is achieved. Unlike direct methods that produce a mathematical model capable of reproducing a given state, the goal of FE model updating is to achieve an improved match between model and experimental test data by making changes to model parameters that correct inaccurate modeling assumptions.

An updated FE model can be used to model other loadings, boundary conditions, or configurations without additional experimental testing. Such models can be used to predict operational displacements and stresses due to simulated loads. Direct and iterative methods can be used to update a FE model, as described in the review by Sehgal and Kumar [192].

Direct methods compute a closed-form solution for the mass and stiffness matrices using the structural equations of motion and the orthogonality properties of modes. These methods can provide the update in a single step, representing a very computationally-efficient process without the drawback of divergence-related issues. Since these methods reproduce the measured data exactly, measurement noise and spurious modes are reproduced and used in the update process, reducing the accuracy of results if the quality of the experimental data used is poor. These methods can be problematic because the updated system matrices are not symmetric and positive definite, making it significantly more puzzling to understand the system from a physical standpoint.

On the other hand, iterative methods evaluate the mismatch between the experi-

mental and predicted FE response at each step. Material and geometric properties of the elements in the FE model are changed in an iterative process. The main advantage in comparison to direct methods is that iterative methods produce only symmetric and positive definite updated system matrices. However, given their iterative nature, these methods can be computationally inefficient, and the convergence of results is not always guaranteed.

Two main iterative techniques are used in today's commercial software. One is the inverse eigensensitivity method (IESM), proposed by Collins et al. [193]. This technique uses modal data, such as eigenvalues, eigenvectors, and damping ratios, to build the error function. The other is the response function method (RFM), proposed by Lin and Ewins [194] and extended by Lin and Zhu [195] to damped structures, where the measured FRFs are directly used in the model update procedure. The IESM is preferred over RFM in the presence of noise, mainly when a large number of modes is used in the analysis.

In this work, the IESM method was used in FEMTools, a computer-aided engineering (CAE) software that, among other features, allows for FE model updating. In the first step of the update process, the mass distribution of the NASTRAN FE model was manually updated based on measured and calculated mass data for all individual components. The second step was to parametrize the NASTRAN model to expose variables for material properties, cross-sectional moments of inertia, point mass values, and mass distribution of wings (see table 3.4 for a list of the properties exposed). The parts of the model that saw their properties exposed are shown in fig. 3.22.

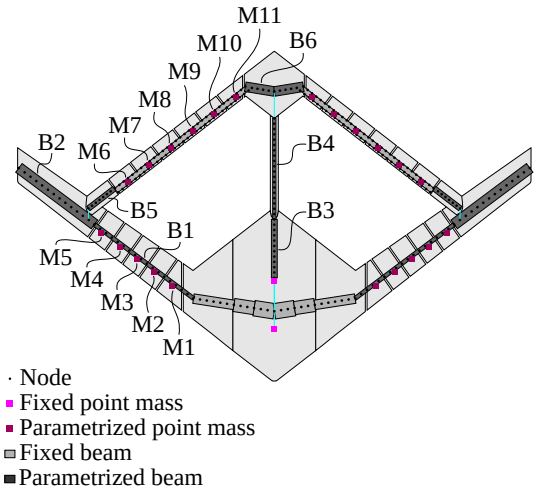

Figure 3.22: Parametrized NASTRAN model of the flexible JWSC.

Finally, the FRFs obtained from GVTs were post-processed through curve fitting, and the resulting experimental modal parameters were used to update the FE models. FEMTools performs sensitivity analysis to calculate each eigenvalue's and eigenvector's derivatives with respect to the selected design parameters. The residual vector is built based on the MAC between FE and experimental mode shapes. Finally, the residual vector is minimized in a least-squares process.

Location	**Variables**	**Description**
B1	I_x, I_y, I_z	Moment of inertia about x, y, and z
B2	A, I_y, I_z, ρ	Cross-sectional area, moment of inertia about y and z, density
B3	E, I_y	Young's modulus, moment of inertia about y
B4	E, A, I_y, ρ	Young's modulus, cross-sectional area, moment of inertia about y, density
B5	E, I_z, ρ	Young's modulus, moment of inertia about z, density
B6	E, I_y	Young's modulus, moment of inertia about y
M1–M11	m	Point mass

Table 3.4: List of design variables used during the NASTRAN model updating process of the flexible JWSC.

3.3.8 Pre-Flight Testing

Static thrust tests were completed to verify the performance of the ESC and installed electric motor (fig. 3.23a). These tests aimed to discover the motor and ESC's operational limits and determine the power draw and thrust output as a function of the throttle percentage.

Radio frequency (RF) testing was performed on the field to check for good connections for communications, GPS, FPV, and signal interference of the integrated aircraft. This test involves validating good signals at 100 m and 200 m distances from four positions around the aircraft to make no loss of signal at any location.

The Piccolo autopilot and ground system allow for SIL as well as HIL testing to be performed. SIL tests served for tuning and validating autopilot gains and settings, training ground crew and pilots prior to each flight test, validating flight test plans

and chosen test maneuvers, and providing simulated data to validate post-processing workflow.

HIL testing was performed to allow the aircraft autopilot to be incorporated into the simulation. The setup electrically stimulates all sensor outputs, allowing for a higher fidelity simulation by more closely replicating in-flight conditions while on the ground. The simulator runs on the ground station, connects to the autopilot over a CAN bus, and simulates the aircraft's flight according to these sensor values.

An iron bird test was carried out to guarantee a correct integration of all flight systems before installing them onto the aircraft. The test consists of connecting the flight control and data collection systems on a benchtop and confirming that all systems operate as expected (see fig. 3.23b).

A pneumatic launcher test was also carried out, which involves outfitting the launcher with a weight comparable to the aircraft MTOW, and the compressor set to a certain pressure (see fig. 3.23c). The weight is then launched, and the motion is recorded to identify the launch speed of the weight. Different pressures and weights were used to characterize the launcher for use with the aircraft.

The balancing of the JWSC is completed with a jig that balances the airframe on two points of the wing. The batteries, which sit at the front of the aircraft, can be moved forward or back to shift the C.G. to the required static margin.

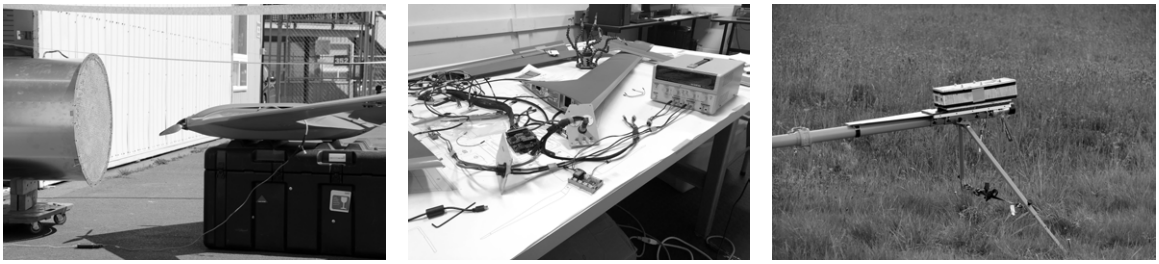

(a) Static thrust test (b) Iron bird test (c) Launcher test

Figure 3.23: Static thrust test (left), iron bird test (center) and launcher test (right) of the JWSC.

3.3.9 Flight Testing

In order to reduce the overall project risk, small incremental steps were taken during the flight test campaign. The flight experiments took place in a designated area free of any possible disturbances and all the flight tests followed a racetrack pattern, shown in fig. 3.24.

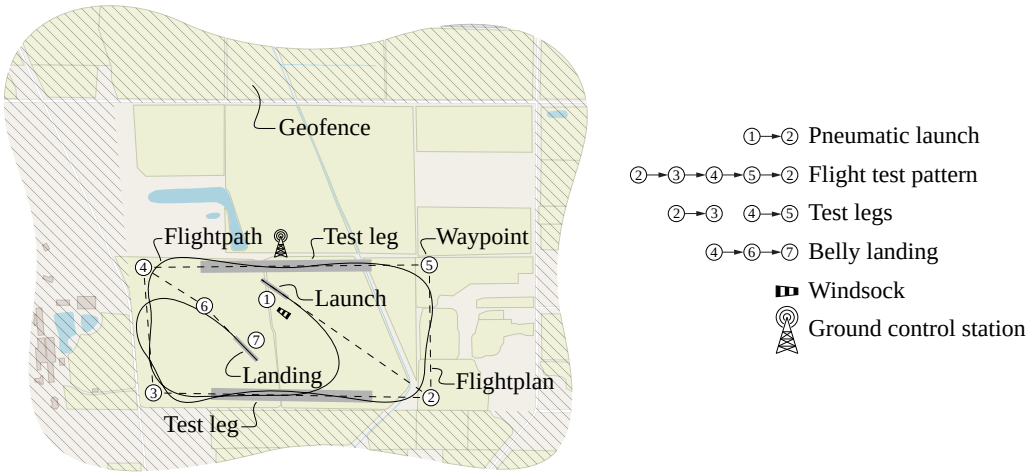

Figure 3.24: Ground setup and racetrack pattern used in the JWSC flight tests.

The expected mission profile for the JWSC is to be pneumatically launched, then climb to an altitude between 50 m and 122 m. The aircraft then proceeds to fly a rectangular racetrack pattern within the designated area. Finally, the aircraft performs a belly landing in the center of the flight field (see fig. 3.25).

(a) Pneumatic launch

(b) Belly landing

Figure 3.25: Pneumatic launch (top) and belly landing (bottom) of the rigid JWSC.

The aircraft was designed to fly with load factors up to $2.5g$, although the planned mission profile is expected to stay below this load limit. Flight maneuver characteristics were determined from flight test data recorded by the autopilot and analyzed with a post-flight data processor.

The aircraft takes off from a pneumatic launcher. The climb rate of the aircraft is 4.9 m/s, taking approximately 25 s to reach cruise altitude and needs a take-off distance of about 700 m to reach cruise altitude. Once at the flight altitude of 150 m, the aircraft has a cruise speed of 26.7 m/s, and has a battery life of 20 m (with safety factor). The landing distance required is at least 670 m, with a descent rate of 2.7 m/s. The aircraft has a minimum turning radius of 91 m (at cruise speed), with a maximum banking angle of 45°.

3.4 Results and Discussion

This section describes the results obtained in this work, starting with the mass and inertia properties of the aircraft in terms of mass, C.G. location, and moments of inertia, obtained experimentally from BPTs. Following are the wing displacements and strains obtained from experimental static load tests and a comparison with structural analyses obtained from NASTRAN and ASWING.

The aircraft dynamic characterization results obtained from GVTs are presented next and are used to update the aircraft structural models. The updated NASTRAN and ASWING models are compared and validated against experimental results in terms of wing static deflections, front and aft wing strains, elastic modal frequencies, and elastic mode shapes.

The aircraft aerodynamics are compared in terms of stability derivatives and flight-dynamic modes. An aeroelastic characterization is also presented in terms of the aircraft's aeroelastic modes.

Finally, the aircraft flight dynamics and wing deformation obtained from flight test simulations using ASWING are presented.

3.4.1 Mass and Inertia Properties

The results of the experimental oscillatory BPTs for the JWSC are shown in fig. 3.26, together with simulated results from the model of eq. (2.5).

The pendulum model solution was fit to the experimental oscillatory data using a

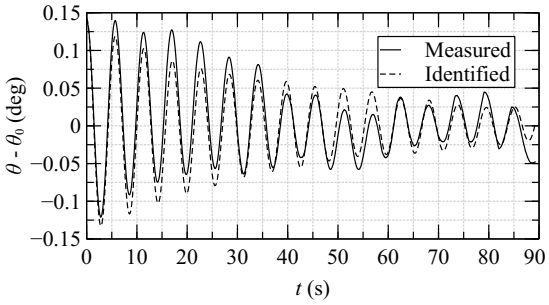

(a) Roll axis

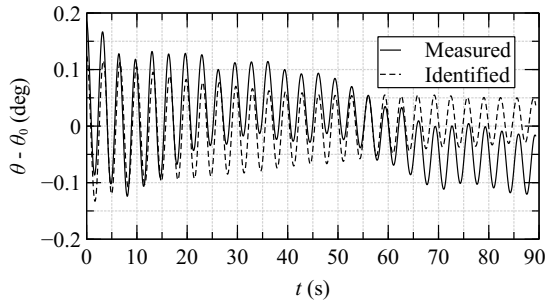

(b) Pitch axis

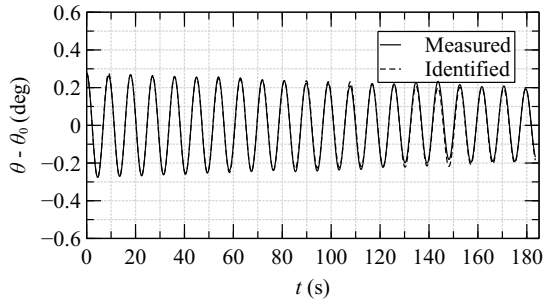

(c) Yaw axis

Figure 3.26: Experimental and simulated pendulum angular displacement θ in roll, pitch, and yaw axes, for the assembly formed by the flexible JWSC and support fixture.

parameter identification process carried out in Simulink. The identified parameters were the aerodynamic and viscous damping parameters K_D and C, respectively, the initial angular displacement θ_0, and the moment of inertia I. Their values are listed in table 3.5 for roll, pitch, and yaw axes.

The mass and inertia properties of the support fixture were subtracted from the assembly to determine the aircraft mass and moments of inertia. The values of mass m

Axis	C (kg m^2/s)	K_D (kg m^2/rad)	θ_0 (rad)	I (kg m^2)
Roll	0.130 46	0.8230	0.141 67	4.3368
Pitch	0.014 88	1.1094	0.131 72	5.1122
Yaw	0.036 40	0.0012	0.277 49	9.3202

Table 3.5: Identified BPT model parameters of eq. (2.5) from experimental pendulum responses in roll, pitch, and yaw axes, for the assembly composed of the flexible JWSC and support fixture.

and moments of inertia about roll, pitch, and yaw axes (I_{xx}, I_{yy}, I_{zz}), are summarized in table 3.6, together with the aircraft longitudinal C.G. location x_{cg}.

m (kg)	x_{cg} (m)	I_{xx} (kg m^2)	I_{yy} (kg m^2)	I_{zz} (kg m^2)
19.65	0.601	4.337	5.112	9.320

Table 3.6: Mass properties of the flexible JWSC. C.G. location is measured from the fuselage nose.

3.4.2 Static Load Testing Results

The flexible JWSC was designed to withstand loads up to a 2.5g pull-up maneuver at flying weight without permanent structural damage. This maneuver set an upper bound for the maximum load to be applied to the aircraft during flight.

Three load cases were considered during static load tests: a gravity-only load case, 5 % of the maximum load, and 100 % of the maximum load defined. These loads were applied at anchor points between the front and aft wings, as described earlier. The same load cases were set up in a linear and a nonlinear NASTRAN static structural analysis as well as an ASWING zero-speed static analysis with the wings anchored at the same locations as the experimental setup. The results were compared against the measured points. Figures 3.27 to 3.29 show a comparison of numerical and experimental results for both the front and aft wings in terms of spanwise vertical displacement, twist angle, and maximum strain.

The linear and nonlinear NASTRAN models, as well as the ASWING model,

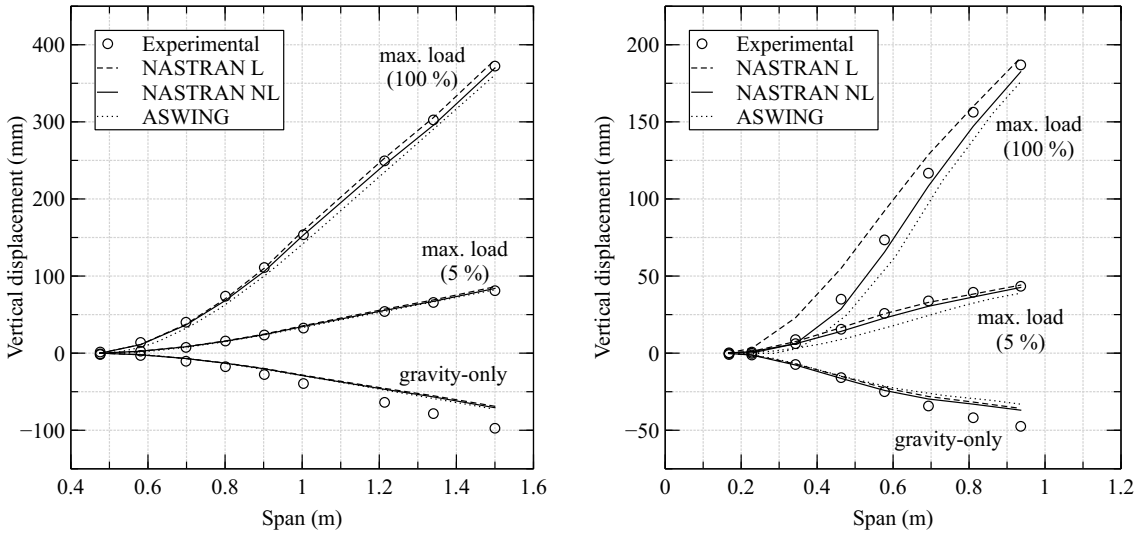

(a) Front wing (b) Aft wing

Figure 3.27: Comparison of spanwise vertical displacement of the flexible JWSC front (left) and aft (right) wing between experimental static load tests, NASTRAN linear, NASTRAN nonlinear, and ASWING static load analyses.

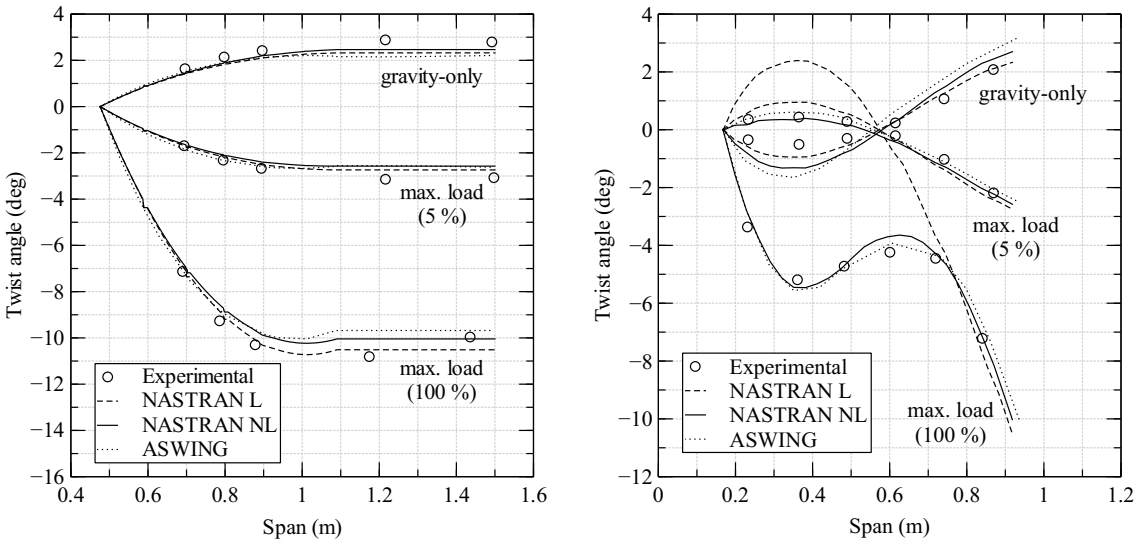

(a) Front wing (b) Aft wing

Figure 3.28: Comparison of spanwise twist angle of the flexible JWSC front (left) and aft (right) wing between experimental static load tests, NASTRAN linear, NASTRAN nonlinear, and ASWING static load analyses.

can predict the front wing's spanwise vertical displacement without much difference between models (fig. 3.27a). However, the three models underestimate the wing

deformation for the gravity-only load case. A similar discrepancy is seen for the aft wing vertical displacement results. Nonlinear effects are more perceptible in the aft wing when the aircraft is loaded at 100 % of the maximum load permissible. The differences between the linear NASTRAN and nonlinear NASTRAN and ASWING results are observable in this case (fig. 3.27b).

The spanwise twist angle results show a similar trend. The front wing does not show considerable nonlinear behavior, and the results from the three models agree with the measured points (fig. 3.28a). In the aft wing, the nonlinear effects are evident when the maximum allowed load is applied (fig. 3.28b).

The strain results in fig. 3.29 also show that the aft wing's nonlinear effects are evident when the aircraft is loaded at 100 % of the maximum load allowed, and the nonlinear NASTRAN model is able to capture these effects.

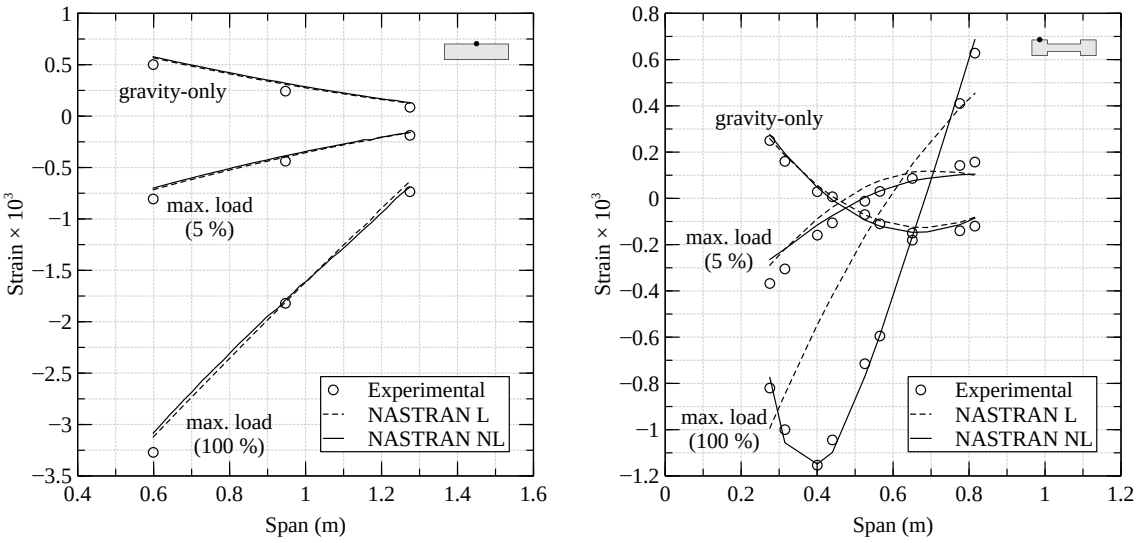

(a) Front wing

(b) Aft wing

Figure 3.29: Comparison of spanwise spar maximum strain of the flexible JWSC front (left) and aft (right) wing between experimental static load tests, NASTRAN linear, NASTRAN nonlinear, and ASWING static load analyses.

3.4.3 Ground Vibration Testing Results

Incremental pre-loads were applied to the aircraft structural model to understand if the nonlinear structural behavior could affect its modal response. NASTRAN's advanced nonlinear solver (`SOL 400`) was used to calculate the elastic modes consecutively. The

modal frequency changes were used to quantify how much the modal response was affected by deformations. Boundary conditions that simulated the static test rig were used for the same load conditions of static load tests.

The results from the modal analysis are shown in fig. 3.30 and suggest that the stiffness nonlinearities induced by pre-loading the structure are not significant at small loads. However, for the maximum load case defined earlier, nonlinear behavior is observed in the static results, both experimentally and computationally, especially in the twist behavior of the aft wing. In this case, the nonlinear behavior is more apparent in the modal response predictions. The frequency shift between the unloaded (gravity-only) and the pre-loaded case at maximum load exceeds 1 Hz in more than half of the modes and shifts between 2 Hz to 7 Hz can be seen at higher frequency modes (modes 23 to 25). However, at higher frequencies (modes 26 to 30), the frequency change drops, which might be due to an interaction of these modes with a buckled aft wing.

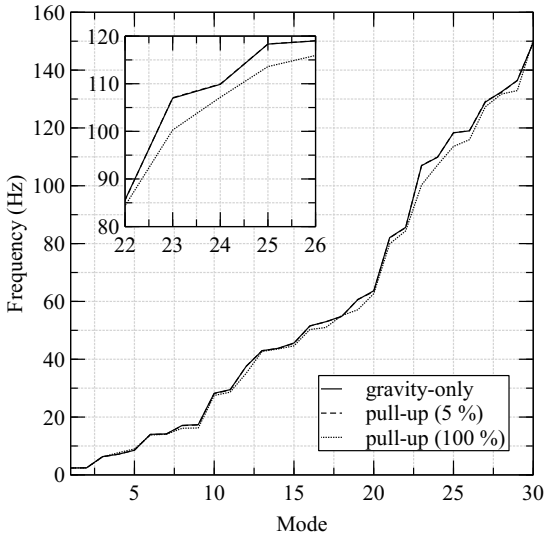

Figure 3.30: Elastic modal frequencies for three pre-loaded configurations of the JWSC.

Because the experimental modal analysis was performed at lower frequencies, these frequency changes identified at higher frequencies were not of concern for the aircraft's modal characterization.

The first set of tests was performed on configuration C1 (aft wing removed) by roving impact. This aircraft configuration was fixed to a vibration-isolated table with a rig similar to that used for static testing. A single accelerometer was used as a single

reference for each test. This accelerometer was placed in a stiff area of the tail to avoid noisy vibrations from the light wing skins to affect the quality of the measurements.

A total of 21 points were impacted, resulting in 21 FRFs. At first, the operational displacement shapes (ODSs) were investigated. The aircraft FE model was animated by directly sweeping the raw data at the frequency range of interest before curve fitting in order to get a sense of which peaks represented a resonance motion. The complex mode indicator function (CMIF) was used to identify the normal modes in the FRF [196]. A global polynomial curve fit was then performed, followed by a mode extraction using the quadrature method for the single reference data. The resulting modal parameters are presented in table 3.7a.

The second set of tests was performed on the aft wing of the aircraft (configuration C2). Given that both tail halves were expected to behave identically in isolation, only one half was tested. The half-tail test article was placed upright and cantilevered from the ceiling using a stiff aluminum fixture. The remaining steps followed the same procedure as the first set of tests for configuration C1. The same hardware was used to perform a roving impact test.

As a result of these tests, 8 points were impacted in single reference testing. Even though several runs were performed, the results turned out to be particularly noisy. In this case, animating the FE model directly, i.e., analyzing the ODS of the model, helped eliminate peaks that were not representative of resonance shapes. Once again, the global polynomial method was used to curve-fit the data, and the resulting modal parameters for this set of tests are presented in table 3.7b.

Mode	**Frequency** (Hz)	**Damping** (%)
1	2.524	1.90
2	7.328	1.60
3	12.99	3.31
4	15.10	0.30
5	45.44	0.32

(a) Aft wing removed

Mode	**Frequency** (Hz)	**Damping** (%)
1	0.884	0.0264
2	5.972	0.005 16
3	10.73	0.0433
4	17.33	0.828
5	33.16	0.702

(b) Aft wing only

Table 3.7: Modal parameters extracted from impact testing FRF results of the flexible JWSC with the aft wing removed (left) and aft wing only (right).

The third and last set of tests was performed on the full aircraft configuration (C3) and included impact and shaker tests. These tests were performed using multi-reference

modal analysis. The aircraft fuselage was fixed to a bench table using the same fixture previously used in configuration C1. An attempt at characterizing the dynamics of the aircraft was also conducted by simulating free-free boundary conditions. Different methods were tested to recreate these boundary conditions using foam, air balloons, and bungees. The best results were obtained when the aircraft was hung by elastic bungee ropes.

The mode shapes of the full aircraft are more complicated than those of the previous configurations. There is a significant coupling between the front and aft wings as they vibrate. The elasticity of these components promotes the genesis of a multitude of shapes that present complicated motion. It was decided that the first four modes would be targeted to later use as data for the FE model update.

Using eight references and eight accelerometers provided a total of 64 FRFs. At first, the CMIF indicator function was applied, followed by a multi-reference global curve-fit based on the rational fraction polynomial (RFP) method. This method directly curve-fits the empirical data to a rational fraction where the numerator and denominator polynomials are determined and compared to the modal superposition equation. The residuals are then transformed into mode shapes, exploiting the orthogonality of the mode shapes [181]. The results from the curve fit for fixed boundary conditions are presented in table 3.8a.

With the intent of increasing the resolution in the identification of the mode shapes that were obtained with impact tests, shaker tests were performed on the full aircraft article as they allow for a higher signal-to-noise ratio. A total of 17 accelerometers were used, which gave a higher resolution to the acquired data. With the additional accelerometers, the number of targeted modes was increased from four to eight modes.

A chirp signal was used to excite the aircraft structure. An initial chirp ramp control was introduced, allowing the amplitude to grow slowly and steadily at low frequencies, where the shakers do not perform very well. In addition, a logarithmic frequency spacing of the signal promoted better coherence in the low frequencies of the measured FRF. The frequency range used for the chirp was between 2 Hz to 60 Hz.

Following the same procedure as for the impact tests, the CMIF indicator was used, followed by a multi-reference global curve-fit using the RFP method. The results from the curve fit for free boundary conditions are presented in table 3.8b.

Mode	Frequency (Hz)	Damping (%)
1	2.098	0.0275
2	14.698	0.146
3	15.205	0.0243
4	17.946	0.135

(a) Fixed fuselage

Mode	Frequency (Hz)	Damping (%)
1	3.051	0.223
2	4.946	0.0623
3	5.981	0.176
4	13.775	0.0695

(b) Bungee-suspended aircraft

Table 3.8: Modal parameters extracted from impact testing FRF results with a cantilever-wing boundary condition (left) and shaker testing FRF results with a bungee-suspended-aircraft boundary condition (right) of the flexible fully-assembled JWSC configuration.

3.4.4 Model Update and Comparison

The results obtained from the model updating process of the flexible JWSC's NASTRAN model are summarized in terms of elastic modal frequencies in table 3.9 for configurations C1 and C2 and table 3.10 for configuration C3, for fixed and free boundary conditions.

Mode	EMA (Hz)	NASTRAN (Hz)
1	2.524	2.159
2	7.328	7.015
3	12.99	14.00
4	15.10	14.09
5	45.44	46.34

(a) Aft wing removed

Mode	EMA (Hz)	NASTRAN (Hz)
1	0.884	0.884
2	5.972	5.936
3	10.73	11.151
4	17.33	18.273
5	33.16	35.935

(b) Aft wing only

Table 3.9: Comparison of elastic modal frequencies between impact testing EMA and updated NASTRAN model of the flexible JWSC with aft wing removed (left) and aft wing only (right).

The frequencies were compared to the ones obtained experimentally from GVTs. It is possible to see that the error between the frequencies obtained from NASTRAN model and EMA was in general below than 10 %, except for mode 1 in table 3.9a and mode 2 in table 3.10b where the error was higher (14.5 % and 21.6 %, respectively). A MAC analysis was carried out as part of the update process and is shown in fig. 3.31 for

Mode	EMA (Hz)	NASTRAN (Hz)	ASWING (Hz)
1	2.098	2.172	2.235
2	14.698	13.581	13.888
3	15.205	13.935	13.983
4	17.946	17.340	18.078

(a) Cantilever wing

Mode	EMA (Hz)	NASTRAN (Hz)	ASWING (Hz)
1	3.051	2.601	2.917
2	4.946	4.006	4.291
3	5.981	6.457	7.299
4	13.775	13.69	11.847

(b) Bungee-suspended aircraft

Table 3.10: Comparison of elastic modal frequencies between impact testing EMA with a cantilever-wing boundary condition (left), shaker testing EMA with a bungee-suspended-aircraft boundary condition (right), and updated NASTRAN and ASWING models of the flexible fully-assembled JWSC configuration.

the three configurations (C1, C2, and C3). The comparison showed good consistency between NASTRAN and EMA mode shapes. Mode shapes of the updated full aircraft model are shown in fig. 3.32 for free boundary conditions.

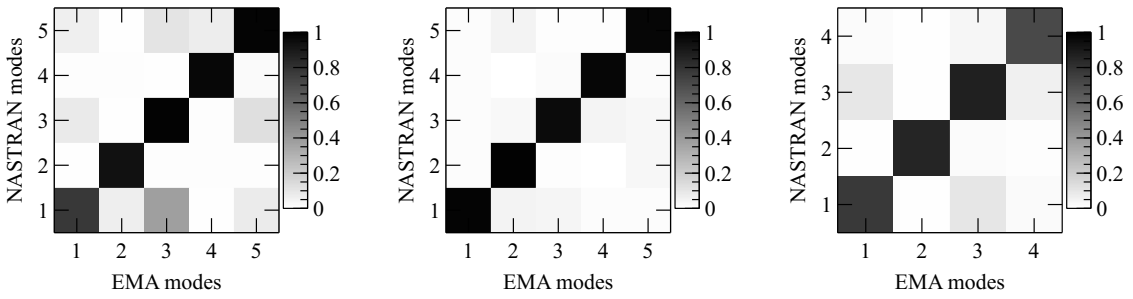

(a) Aft wing only (b) Aft wing removed (c) Full assembly

Figure 3.31: MAC analysis comparing elastic mode shapes of the JWSC between EMA and NASTRAN for aft wing only (left), with aft wing removed (center), and full assembly (right).

The updated NASTRAN model properties were transferred to the ASWING model, and a comparison between the two was carried out for the full aircraft model in terms of elastic modal frequencies. In order to perform an elastic modal analysis in ASWING, a zero-speed aeroelastic modal analysis was set up, ensuring the resultant modes were purely elastic. These results are shown in table 3.10 and show good agreement between the two models for low frequencies and a more significant discrepancy for

higher frequencies.

Figure 3.32: Elastic mode shapes of the flexible JWSC for free boundary conditions.

3.4.5 Aerodynamics and Flight Dynamics

The aerodynamics of the JWSC were compared between AVL and a stiff ASWING model. The comparison considered two flight conditions: a $1g$ level-flight trim and a $2.5g$ pull-up flight conditions.

The lift distribution of both models is shown in fig. 3.33 for the two flight conditions. Even though the lift distribution is similar between models, some discrepancies are observed in the aft wing. AVL predicts a higher C_l at the front wing for a level-flight condition and slightly higher C_l at the inboard aft wing for the pull-up conditions.

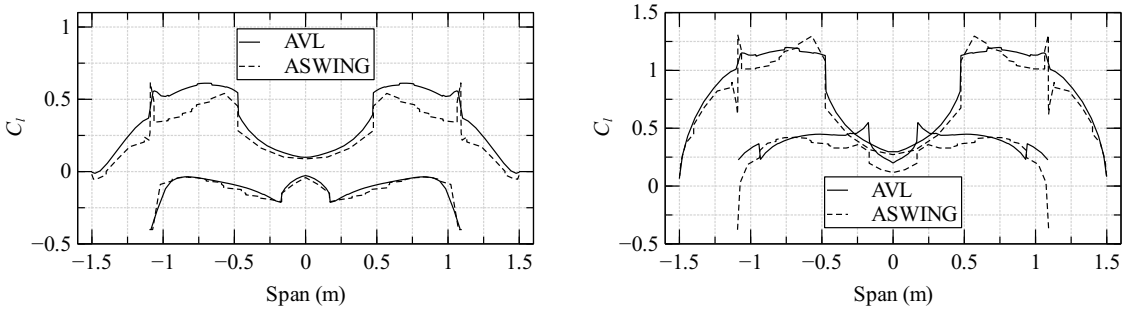

(a) $1g$ level-flight trim

(b) $2.5g$ pull-up

Figure 3.33: Comparison of JWSC aerodynamics between AVL and ASWING for $1g$ level-flight trim (left) and $2.5g$ pull-up (right) flight conditions.

The lift distribution obtained from AVL also appears to be smoother than ASWING. At the front-aft wing intersection, some instabilities are observed in the value of C_l obtained from ASWING, which could be due to singular velocity values originating from the proximity of the front wing wake with a downstream aft wing. ASWING attempts to overcome singular velocity issues in the solution process by defining a vortex core radius. However, the front and aft wing structural beams were assigned a zero vortex core radius, ensuring a more accurate prediction of the near-field effects between the two structures when mutual vortex lattice influences are computed in the solution process.

The flight-dynamic modes of the rigid JWSC were calculated for level-flight conditions using both AVL and a stiffened ASWING model at different airspeeds. The root loci of the modes are shown in fig. 3.34 for both models. All the flight-dynamic modes—phugoid (P), short-period (SP), roll (R), and Dutch-roll (DR) modes—show good agreement between the two models.

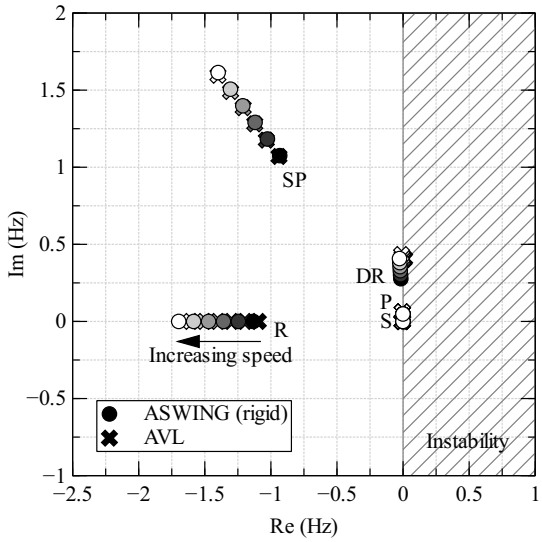

Figure 3.34: Root loci of flight-dynamic modes for the rigid JWSC obtained from an AVL and rigid ASWING model, for airspeeds between 20 and 30 m/s.

3.4.6 Aeroelastic Characterization and Preliminary Flight Tests

The internal structure of the flexible JWSC had to be designed to exhibit nonlinear behavior of the aft wing during a high g loading maneuver while maintaining approximately linear behavior at $1g$ steady level flight. The aircraft should also be safe to operate despite the nonlinear deformation of the aft wing.

A designs of experiments (DOEs) was conducted to assess the feasibility of a flexible JWSC design until a configuration for the internal wing structure was found that satisfied the desired level of nonlinear behavior in the aft wing while guaranteeing flight safety and manufacturability.

Several design objectives were defined, each measuring a feature that was sought to be accomplished in the flexible design. These objectives are summarized in table 3.11. An objective function was defined that took into account all the design objectives.

Stability, operational, structural, experimental, and manufacturability constraints were also defined and are summarized in table 3.12.

Objective	Description
	Front wing
O1 and O2	Difference between linear and nonlinear strain at two spanwise locations
O3	Difference between linear and nonlinear spanwise twist angle
O4	Difference between linear and nonlinear spanwise displacement
O5	Difference between linear and nonlinear spanwise lift distribution
	Aft wing
O6 and O7	Difference between linear and nonlinear strain at two spanwise locations
O8	Difference between linear and nonlinear spanwise twist angle
O9	Difference between linear and nonlinear spanwise displacement
O10	Difference between linear and nonlinear spanwise lift distribution

Table 3.11: Objectives defined in the DOE problem of finding flexible JWSC design candidates.

The carbon fiber spars of the rigid JWSC were not good candidates for bonding strain gauges, in addition to being too complex to modify and achieve the desired level of wing flexibility. Therefore, they were replaced with aluminum ones, and their cross-section was modified until the desired level of flexibility was achieved. The design variables of the experiment focused on the geometric properties of the front and aft wings' spar cross-sections. Table 3.13 lists the chosen design variables.

A rectangular cross-section was chosen for the front wing spar because of its ease of manufacturing. An I-beam cross-section was chosen for the aft wing, oriented in a way to provide the highest in-plane bending stiffness possible. This choice was made to open up the design space for the aft wing, allowing for higher out-of-plane deflections while keeping the wing relatively stiff in in-plane bending. Two design candidates were chosen from the DOEs after more than 2000 iterations. Each design candidate presented a different set of wing spar properties, summarized in table 3.13.

Design candidate 1 (DC1) was selected as it showed a slightly lighter aft wing and much higher safety margins than design candidate 2 (DC2). Good nonlinear twist and strain behavior of the aft wing was observed in DC1. This design also presented a suitable spar geometry for strain gauge placement. Additionally, DC1 showed a figure

Constraint	Description
	Stability limits
CS1	Stability of aeroelastic roots at never-exceed speed V_{NE}
CS2	Stability derivatives deviation from baseline rigid aircraft
CS3	Control surface deflection limits
	Structural limits
CSL1	Maximum stress during launch maneuver
CSL2	Maximum stress during a 2.5g pull-up maneuver
	Operational limits
COL1	Maximum roll rate during transient maneuver
COL2	Maximum pitch rate during transient maneuver
COL3	Minimum and maximum pitch angle limits
COL4	Maximum roll angle allowed
COL5	MTOW
COL6	Maximum wing tip deflection and twist angle in trimmed level flight
	Manufacturability limits
CM1	Overall dimensions of front and aft wing spar cross-sections

Table 3.12: Constraints used in the DOE problem of finding flexible JWSC design candidates.

of merit of 3059.4, while design candidate 2 (DC2) showed a figure of merit of 2112.2. The linear and nonlinear aeroelastic response to a 2.5g pull-up maneuver for the two design candidates is shown in fig. 3.35.

After selecting DC1 as the design to be manufactured, an ASWING model was built closely following its NASTRAN model. A 2.5g pull-up maneuver was set up in ASWING and in the nonlinear NASTRAN–AVL framework and the results compared. The comparison is shown in fig. 3.36. It is possible to observe that the two models produce similar deflections with some error close to the connection point of the front and aft wings. The two deformed aeroelastic models are shown in fig. 3.37.

Stability and control derivatives of the JWSC were calculated to configure the autopilot for flight. Flight-dynamic modes of the rigid variant of the JWSC served as

Design variable	Description	DC1	DC2
	Front wing		
DV1	Spar height (mm)	4.45	4.75
DV2	Spar width (mm)	28.48	30.4
DV3	Spar twist angle (°)	−10.0	−7.5
	Aft wing		
DV4	Spar flange thickness (mm)	3.97	8.5
DV5	Spar flange width (mm)	7.89	3.0
DV6	Spar web thickness (mm)	1.95	1.95
DV7	Spar web height (mm)	25.0	17.5
DV8	Spar twist angle (°)	0.0	0.0

Table 3.13: Design variables defined in the DOE problem of finding flexible JWSC design candidates. Wing spar properties for two flexible wing designs are also shown.

a reference for comparison with the flexible JWSC aeroelastic modes. The flexible JWSC stability and control derivatives were determined using ASWING. A stiffened ASWING model was used to calculate the derivatives of the rigid variant of the JWSC. Table 3.14 lists the stability and control derivatives of both models. All derivatives were obtained at trimmed level-flight conditions.

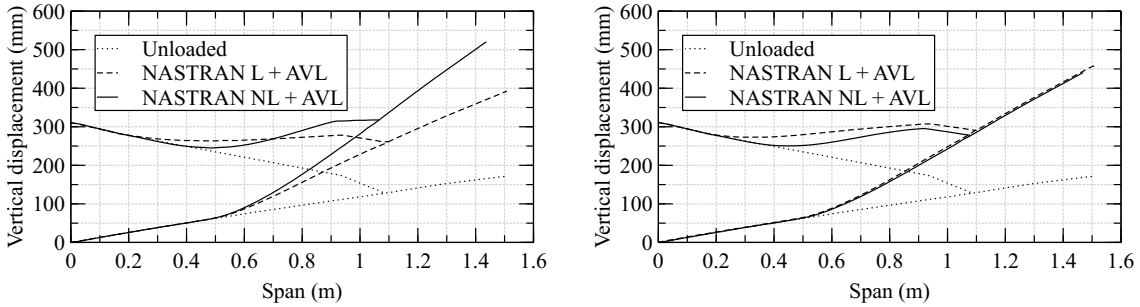

(a) Design candidate 1

(b) Design candidate 2

Figure 3.35: Linear and nonlinear aeroelastic response to a 2.5g pull-up maneuver for two different design candidates of the flexible JWSC.

A comparison between the rigid and flexible derivatives reveals a decrease in C_{L_α}, C_{m_α}, and C_{m_q} with the increase in flexibility. This could be justified by the smaller

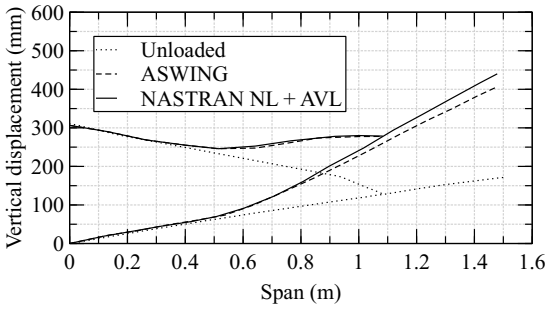

Figure 3.36: Comparison of aeroelastic response of the flexible JWSC to a 2.5g pull-up maneuver between the nonlinear NASTRAN-AVL framework and ASWING.

projected horizontal wing surface area due to a higher wing deflection required to trim the flexible aircraft in level-flight conditions, reducing the effective wing aspect ratio. In terms of lateral/directional derivatives, there is an increase in C_{Y_β} and C_{l_β}, and a decrease in C_{n_β}, as flexibility increases. The increase in the side force coefficient C_{Y_β} is a consequence of the higher vertical wing surface area component, which appears to decrease the C_{n_β} coefficient (destabilizing) but causes an increase in C_{l_β} (stabilizing) due to a higher wing dihedral. The cross-coupling terms in table 3.14 are zero for the rigid model but non-zero for the flexible ASWING model.

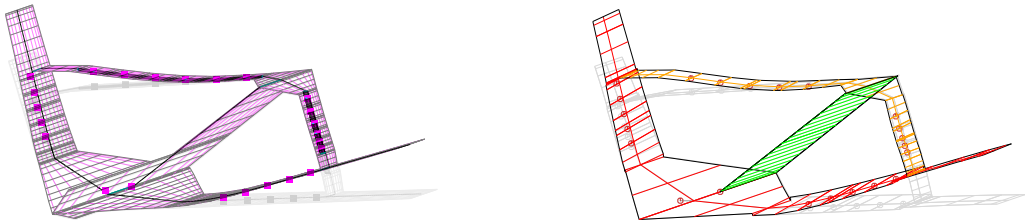

(a) Coupled AVL–NASTRAN model (b) ASWING model

Figure 3.37: Deformed coupled AVL–NASTRAN (left) and ASWING (right) aeroelastic models of the flexible JWSC.

The root loci of the flexible aircraft aeroelastic modes can be seen in fig. 3.38, for a range of airspeeds between 20 and 30 m/s, within the flight envelope of the aircraft. All aeroelastic roots damp out as speed increases, and no flutter modes are observable in this speed range. The absence of aeroelastic instabilities in this speed range agrees with what was expected from the design candidate chosen.

A preliminary flight test campaign was carried out for the rigid JWSC with the goal of establishing the controllability and handling qualities of the airframe.

A flight test was selected from the flight test campaign of the rigid variant of the

Derivative	Rigid JWSC	Flexible JWSC
C_{L_α}	9.851	8.298
C_{m_α}	−13.444	−10.586
C_{Y_β}	−0.395	−0.476
C_{l_β}	−0.126	−0.176
C_{n_β}	0.052	0.049
C_{l_p}	−0.887	−0.538
C_{m_p}	–	−0.016
C_{n_p}	−0.111	−0.056
C_{l_q}	–	−0.015
C_{m_q}	−144.802	−135.384
C_{n_q}	–	−0.002
C_{l_r}	0.182	0.133
C_{m_r}	–	−0.003
C_{n_r}	−0.042	−0.0456
$C_{l_{\delta_\mathrm{a}}}$	0.231	0.127
$C_{m_{\delta_\mathrm{e}}}$	−3.889	−4.008
$C_{n_{\delta_\mathrm{r}}}$	0.006	0.005

Table 3.14: Stability and control derivatives of the rigid JWSC (obtained from a stiff ASWING model), and the flexible JWSC (obtained from the flexible ASWING model).

JWSC. The data recorded during this flight is shown in fig. 3.39 in terms of altitude, ground speed, and GPS trajectory. The aircraft flight trajectory followed the racetrack pattern shown in fig. 3.39c. The aircraft was launched from a pneumatic launcher and completed a successful belly landing, with a total flight time of 12 min, 40 s. A flight test of the flexible JWSC was also performed but resulted in a crash and loss of one set of flexible wings, aircraft fuselage, and some avionics. The aircraft failed immediately after launch, going into a spiral descent and crashing into the ground. No useful flight test data was recorded, and so no flight test results are shown here for the flexible aircraft. The reason for this crash was most likely related to a faulty actuator.

Open-loop time-marching simulations were carried out in ASWING for the flexible

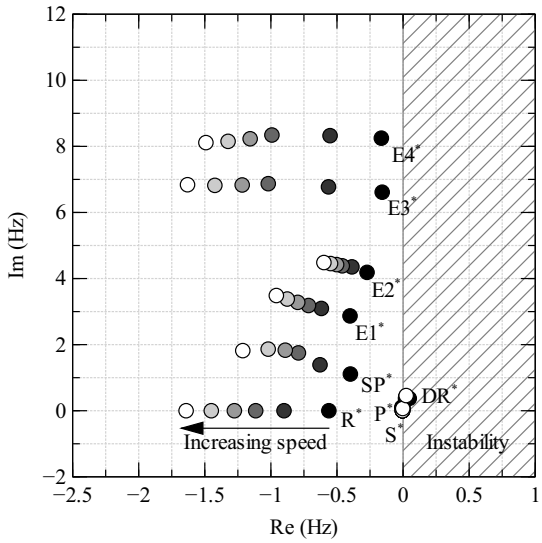

Figure 3.38: Root loci of aeroelastic modes for the flexible JWSC obtained from its ASWING model, for airspeeds between 20 and 30 m/s.

JWSC where the elevators and ailerons were commanded with doublet signals to excite the aircraft longitudinal and lateral/directional dynamics. The aircraft was trimmed prior to initiating the time-domain analysis in ASWING.

The results of a simulated ASWING response to an elevator doublet command are shown in fig. 3.40 for the angle of attack α, TAS, x-acceleration, z-acceleration, pitch rate q, and pitch angle θ, for both rigid and flexible JWSC variants.

The response to a simulated aileron doublet command was also assessed to understand the effects of the added flexibility on the lateral/directional dynamics of the aircraft. The results are shown in fig. 3.41 for the angle of attack α and sideslip β, angular rates (p, q, r), and attitude angles (ϕ, θ, ψ), for both rigid and flexible JWSC variants.

The results suggest that the added flexibility does not appear to affect the longitudinal dynamics of the aircraft. On the other hand, the wing deflection appears to affect the lateral/directional response of the aircraft. In fact, without any closed-loop stability augmentation system, the aircraft response is unstable for the aileron perturbation. Different magnitude doublet input commands were tested, but the aircraft response followed the same trend, the only difference being a change in the magnitude of oscillation of the different states.

A comparison of the wing displacement between rigid and flexible aircraft configurations for the two control surface input commands is shown in fig. 3.42. On

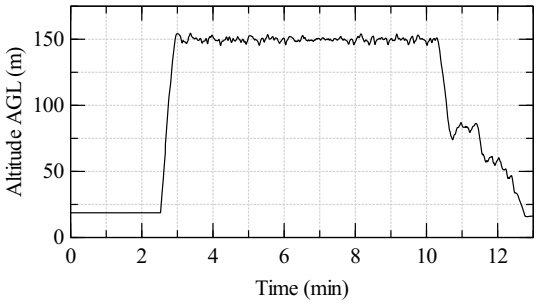

(a) Altitude AGL

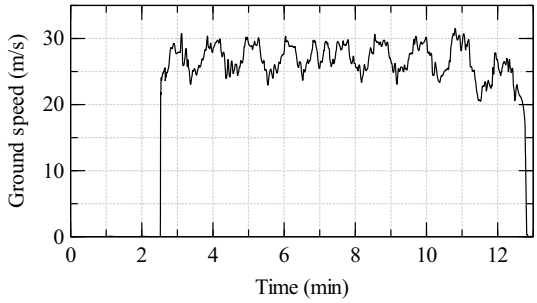

(b) Ground speed

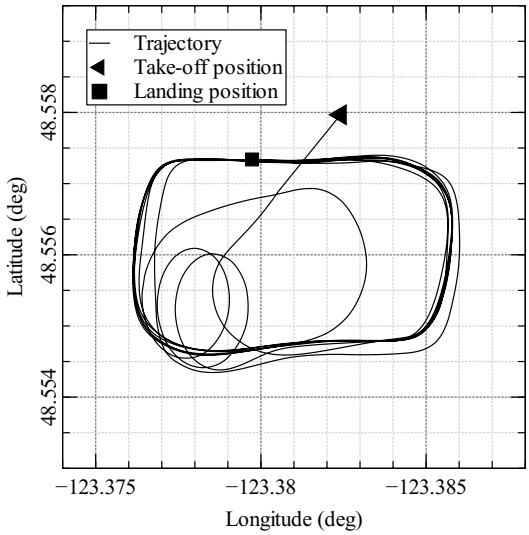

(c) GPS trajectory

Figure 3.39: Data recorded from the autopilot during a flight test of the rigid JWSC.

the left, the wing displacement at two different points—front wing tip and aft wing midspan points—is shown. These two points were selected because they show each wing's maximum deformation amplitude. On the right, the figure shows the spanwise

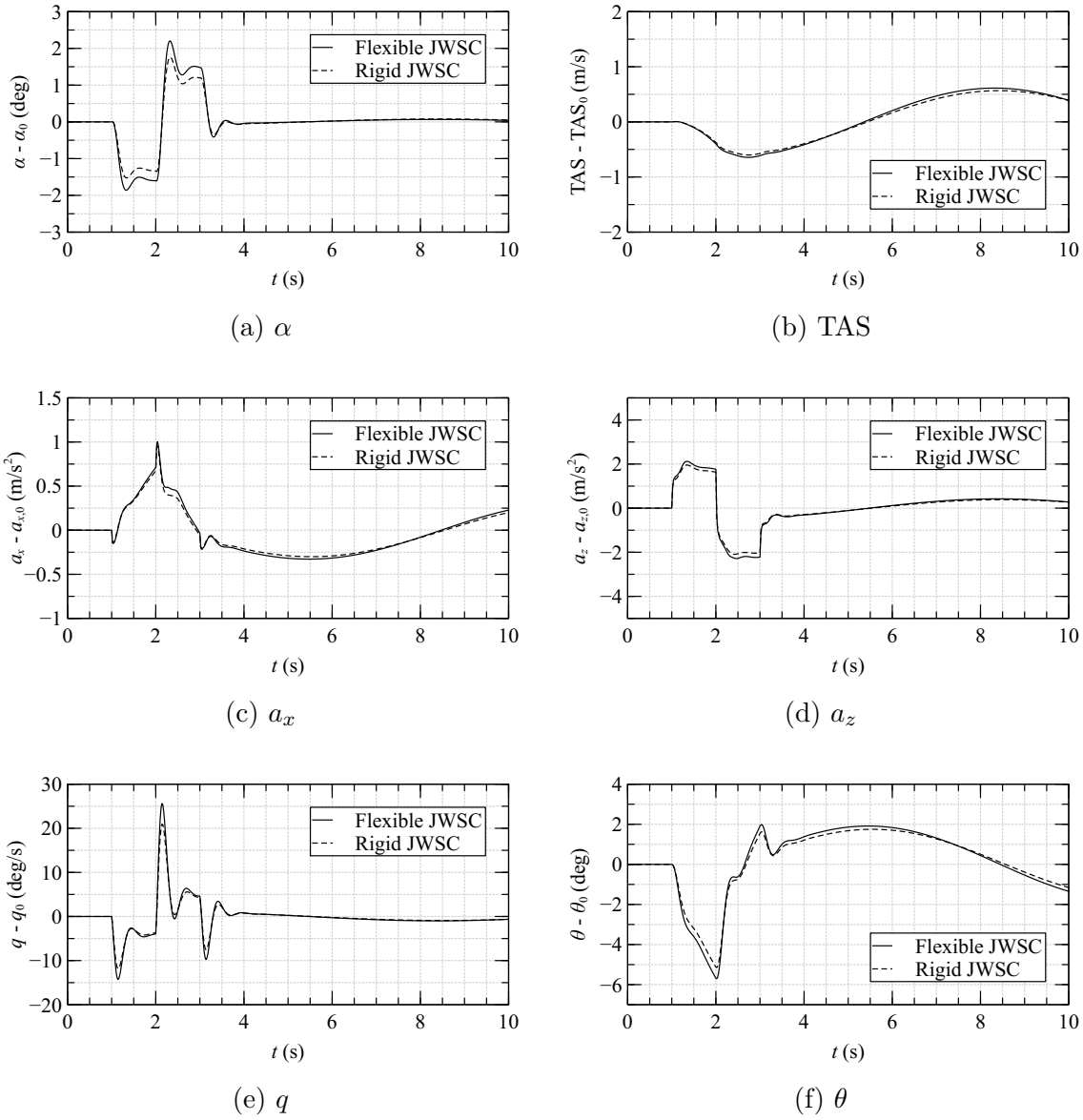

(a) α (b) TAS

(c) a_x (d) a_z

(e) q (f) θ

Figure 3.40: Simulated response of the flexible JWSC to an elevator doublet command, for angle of attack α, TAS, x-acceleration a_x, z-acceleration a_z, pitch rate q, and pitch angle θ.

wing displacement at three selected time instants, where different front and aft wing deformation behavior is observed as the wing responds to the input commands.

It can be seen that the aircraft response to an aileron doublet command is much more pronounced than to a symmetric elevator input with the same amplitude. This difference was already evident from figs. 3.40 and 3.41.

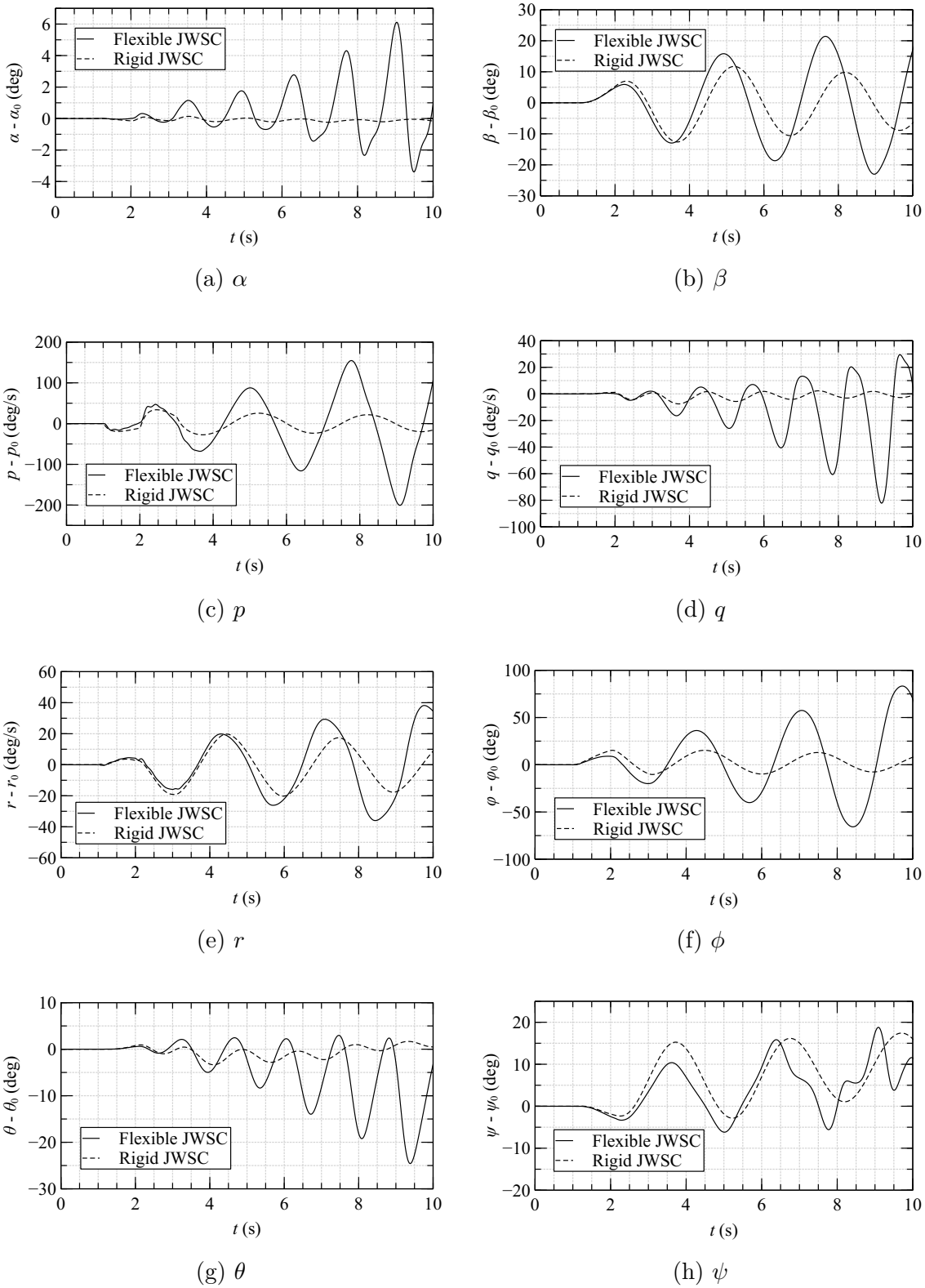

(a) α (b) β

(c) p (d) q

(e) r (f) ϕ

(g) θ (h) ψ

Figure 3.41: Simulated response of the flexible JWSC to an aileron doublet command, for angle of attack and sideslip α, β, roll, pitch, and yaw rates p, q, r, and roll, pitch, and yaw angles ϕ, θ, ψ.

It is also interesting to note the bucking effect being captured at the aft wing in fig. 3.42d. For example, at $t = 6.6\,\text{s}$, both front wing tip and aft wing midspan points deflect upward, while at $t = 7.6\,\text{s}$, the front wing bends upwards while the aft wing bows in the opposite direction.

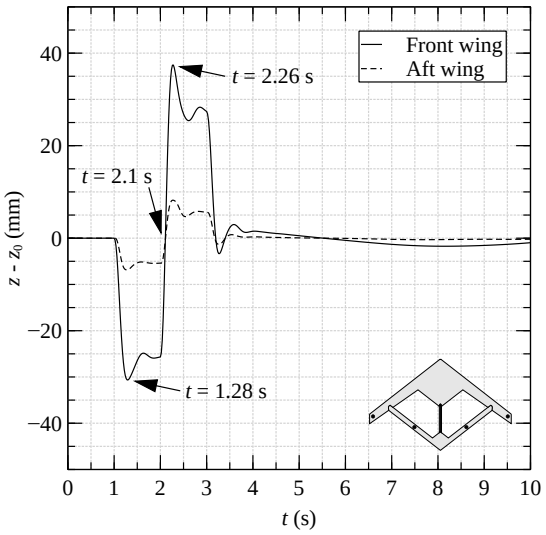

(a) Front wingtip and aft midpoint wing deflection in response to elevator doublet

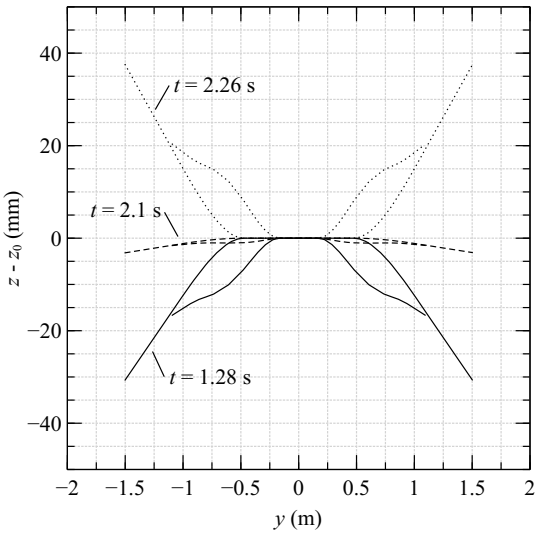

(b) Front and aft spanwise wing deflection in response to elevator doublet

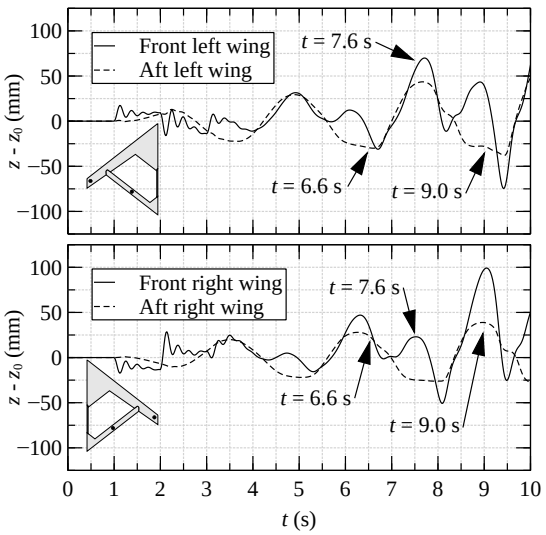

(c) Front wingtip and aft midpoint wing deflection in response to aileron doublet

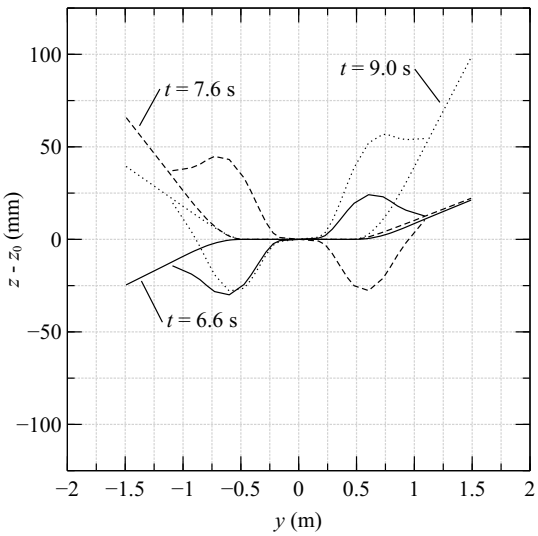

(d) Front and aft spanwise wing deflection in response to aileron doublet

Figure 3.42: Aeroelastic ASWING simulation of front wingtip and aft midpoint wing deflection (left) and spanwise wing deflection at three time instants (right) in response to elevator and aileron doublet commands, for the flexible JWSC.

3.5 Concluding Remarks

This work describes the design, sizing, numerical modeling, ground testing, and validation of an aeroelastically-tuned joined-wing UAV platform with flexible front and aft wings based on the Boeing SensorCraft concept.

Structural, aerodynamic, and aeroelastic models of the aircraft were developed in NASTRAN, AVL, and ASWING, respectively. A higher-fidelity nonlinear framework coupling NASTRAN and AVL was developed to design the internal aircraft structure.

The flexible joined-wing platform was characterized using bifilar pendulum tests, static load tests, and ground vibration tests. Numerical studies of the static aeroelastic deformation, lift distribution, variations of stability derivatives, and aeroelastic roots for the flexible aircraft have been presented.

The static load tests presented good agreement with the NASTRAN and ASWING models. GVTs were conducted with two excitation methods, shaker and impact tests. It was found that higher frequency modes were more challenging to obtain and that impact testing was more versatile than the shaker testing method. Results from GVTs were used to update the finite element models of the flexible aircraft.

Time-marching aeroelastic simulations were carried out in ASWING in response to elevator and aileron doublet maneuver commands for the rigid and flexible variants of the aircraft. It was found that while the aircraft response to an elevator doublet command barely exhibited any difference with the added wing flexibility, the aileron doublet command caused the aircraft to respond in an unstable manner with large deformations of both front and aft wings.

Pre-flight ground testing was also conducted, which included SIL and HIL simulations, in order to approximate acceptable controller gains for flight testing, as well as to test maximum amplitudes and test duration of maneuver commands. Preliminary flight tests were carried out for the rigid variant of the aircraft in preparation for a future and more extensive flight campaign for the flexible aircraft.

This work provides insights into the aeroelastic behavior of flexible joined-wing aircraft configurations. It reinforces the importance of accounting for geometric nonlinearities in the structural analysis due to the buckling that can occur in the aft wing. Finally, this work also illustrates the feasibility of using flexible scaled flight test demonstrators as cost-effective platforms for testing the nonlinear aeroelastic behavior of joined-wing configurations.

Chapter 4

A Framework for Medium-Fidelity Nonlinear Aeroelastic Analysis using Absolute Nodal Coordinates and the Fast Multipole Method

The work presented in this chapter discusses the development of an aeroelastic framework for the dynamic aeroelastic analysis of flexible aircraft, based on a three-dimensional accelerated unsteady panel method with convected wakes and a flexible multibody dynamics formulation based on absolute nodal coordinates that accounts for structural geometric nonlinearities. Multibody dynamics allows for the modeling of kinematic nonlinearities, making it an effective approach for modeling the aeroelasticity of flexible aircraft that may exhibit structural nonlinear effects in flight. This framework is used to study the aerodynamic and dynamic aeroelastic response of HARW and joined-wing aircraft configurations and the results are compared with those obtained from other computational models.

This chapter is based on a journal publication currently under preparation.

Abstract

Novel aircraft configurations with high aspect-ratio wings and joined-wing designs cannot be studied using conventional linear aeroelastic analysis methods due to the large deformations shown when they undergo flexible motion.

Due to their large wing span, high aspect-ratio wings may see increased bending moment and structural weight. Lightweight wing designs are thus necessary to achieve effective performance benefits, which leads to very flexible structures where geometric nonlinearities cannot be neglected. The increased flexibility may also cause coupling between structural dynamics and flight dynamics modes, leading to undesirable aeroelastic effects. Joined-wing aircraft configurations have the potential to enhance aerodynamic efficiency, reduce structural weight, and improve sensing capabilities. However, their design is prone to nonlinear geometric behavior, such as buckling of the aft wing.

Current aeroelastic computational codes are relatively new, and their ability to accurately predict the nonlinear aeroelastic performance of novel aircraft configurations requires extensive validation. Furthermore, these codes employ low-fidelity aerodynamic and structural formulations to speed up calculations.

In an effort to improve on the current available aeroelastic modeling tools, a framework has been created for analyzing the dynamic aeroelasticity of flexible aircraft, incorporating a flexible multibody dynamics formulation based on absolute nodal coordinates that accounts for structural geometric nonlinearities. Multibody dynamics allows for the modeling of kinematic nonlinearities, making it an effective approach for modeling the aeroelasticity of flexible aircraft that may exhibit structural nonlinear effects in flight.

The flexible multibody dynamics framework makes use of a three-dimensional FMM-accelerated unsteady panel method with convected wakes and models the wing as a series of beam elements based on ANCF. Although ANCF-based flexible multibody dynamics has been widely used for analyzing various flexible structures, their application to HARW and joined-wing aircraft is still limited. This framework has been applied to study the aerodynamic and the dynamic aeroelastic response of HARW and joined-wing aircraft models. Aerodynamic and time-depended aeroelastic results have been compared with those obtained from AVL and ASWING computational models.

4.1 Introduction

The work presented in this chapter is concerned with the development of a medium-fidelity aeroelastic tool using an accelerated low-order panel method and a flexible multibody dynamics formulation based on absolute coordinates. The main objective of this work is to propose a versatile framework that can be applied to the time-domain analysis of aeroelastic models based on flexible multibody dynamics and unsteady aerodynamics. To this end, a framework coupling a three-dimensional unsteady panel method with a flexible multibody dynamics formulation based on absolute coordinates is developed from the ground up. A FMM formulation was employed in an effort to reduce the computational time associated with the panel method solver.

The major downside of the panel method is that it requires the solution of a dense system of linear equations. Due to the density of this system, computational and memory requirements scale, in the best case scenario, with the size of the system, or $\mathcal{O}(N^2)$, where N is the number of elements. In comparison to finite element methods (FEMs), finite volume methods (FVMs), or finite difference methods (FDMs), these methods require the solution of a spare linear system, allowing solutions to be found in $\mathcal{O}(N)$ time, where N is now the total number of DOFs. Using the FMM, the time complexity required by the boundary element method (BEM) can be reduced from $\mathcal{O}(N^2)$ to $\mathcal{O}(N)$. While this modification adds complexity to the BEM, it makes the simulation of larger problems feasible.

To model the aircraft flight mechanics including unsteady aeroelastic effects, MBD is a convenient tool due to its capability of simulating multiphysics systems composed of rigid and flexible bodies with arbitrary types of nonlinearities dominated by large rigid-body motion [100, 101]. This approach allows for an efficient representation of both elastic motion and arbitrary rotations, making it ideal for multi-physics simulations that include nonlinearities. It allows for direct modeling of structural dynamics, servo-systems, controls, and nonlinearities such as backlash, free-play, friction, and generic nonlinearities all within a single framework.

Most of the work in the literature has employed FFRFs, corotational formulations, or GEBFs to model aeroeaslticity using a MBD framework. Few studies have focused on modeling aeroelasticity using a multibody dynamics formulation based on the ANCF. The ANCF uses global position and gradient coordinates and is designed for large deformation analysis of beam, plate, and shell elements in multibody applications [197]. The formulation leads to a singularity-free description in large rotation problems,

simplifying the description of the equations of motion. The ANCF does not involve tangent stiffness matrices and leads to a constant mass matrix, while the elastic forces are nonlinear functions of the element coordinates.

Examples where ANCF has been used to study the aeroelasticity of flexible aircraft structures includes the work of Otsuka and Makihara [121, 122] and Otsuka et al. [123, 124]. In their work, they employed a multibody dynamics framework based on geometrically nonlinear ANCF beams to study morphing deployable wings expected to be used for Mars exploration. They simulated the rigid-body rotation of the wing around the kinematic constraints as induced by the aeroelasticity.

To couple aerodynamics with structural dynamics, different FSI strategies have been successfully employed in the past. Fluid and structural domains can be coupled in a monolithic manner, where the two disciplines are solved simultaneously. In this case, a multi-physics solver handles a single system of equations describing fluid, solid, and their coupling. These monolithic solvers must be explicitly designed for the problem at hand, but usually yield good numerical stability of the calculations [198]. In contrast, partitioned approaches make use of existing single-physics solvers to handle each discipline separately. The FSI problem is split into a fluid and structural problem, which are treated independently by their respective solvers. A third component, the coupling component, handles the interaction aspects. An advantage of this approach is that existing well-established solvers for both fluid and solid problems can be used. The programming efforts are lower for partitioned methods since only the coupling of the existing solvers has to be implemented rather than the solvers themselves [199, 200].

The transfer of information between structure and fluid can be carried out using RBFs interpolation. This is a mathematical tool to allow interpolation and extrapolation of scalar values everywhere in space. The resulting field is retrieved on a distance basis through the solution of a linear system of equations [201]. A single solution can be performed for a set of source points, once, to compute the coefficients of the linear system that can be used later to directly retrieve interpolated or extrapolated values elsewhere in the target space as the summation of their radial contribution.

In this work, a FMM-accelerated panel method was coupled with a ANCF-based multibody dynamics formulation in a unified aeroelatic framework to study the unsteady aeroelastic response of flexible aircraft configurations. A partioned method was employed to coupled the two formulations and the transfer of information was carried out by means of a RBF interpolation. To benchmark the developed framework,

the aerodynamics, as well as the unsteady aeroelastic response of two flexible aircraft models was studied. The first model was the QT1 aircraft, a flexible HARW UAV platform, and the second was a flexible reduced-scale version of the Boeing JWSC concept. The aerodynamics of the FMM-accelerated panel method were first compared with ASWING and AVL models of the two aircraft. Next, time-marching aeroelastic simulations of the aircraft wings were set up using the proposed framework and compared against ASWING in response to a wingtip impulse command.

The present work is organized as follows: In section 4.2, the three-dimensional unsteady panel method formulation is presented, including the unsteady wake convection employed and an automatic trailing edge detection algorithm that was developed as part of this work. This section also formulates and describes the implementation of the FMM-accelerated panel method. The flexible multibody dynamics formulation is the focus of section 4.3. In section 4.4, fluid-structure interaction strategies are discussed, including the chosen solver coupling strategy and the implementation of mesh interpolation based on a RBFs formulation. The overall design and computer implementation of the developed framework is described in section 4.5. Section 4.6 presents results on the application of the framework to model the aerodynamics and aeroelasticity of a HARW and a joined-wing reduced-scale UAV models. The aerodynamics of the two aircraft are first presented and compared with previously-obtained results, followed by a benchmark of the FMM-accelerated panel method. Dynamic aeroelastic results are also presented for the two aircraft models. Finally, section 4.7 summarizes the findings and conclusions of the study. An overview of the steps taken in this work is illustrated in fig. 4.1.

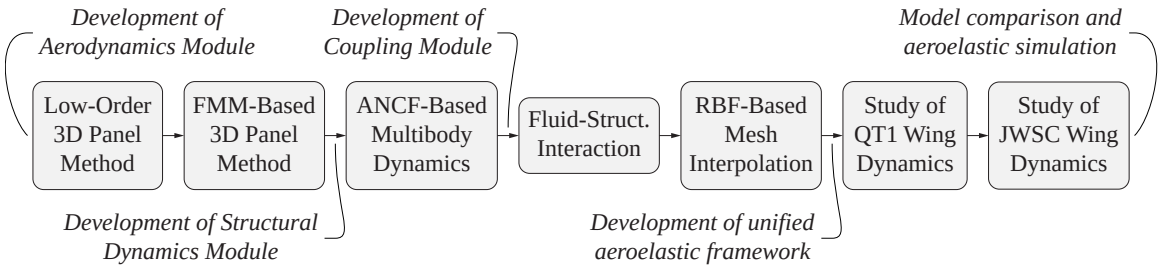

Figure 4.1: Timeline of the different tasks executed in chapter 4.

4.2 Aerodynamics

The aerodynamic formulation implemented in this work is based on potential fluid flow. A three-dimensional unsteady panel method implements the potential fluid equations and allows for the modeling of complex geometries. The shed vorticity from lifting surfaces is modeled with convected wakes. A trailing edge detection algorithm is implemented to automatically shed wake panels at trailing edges of lifting surfaces. Finally, a FMM-based panel method formulation is implemented to reduce the overall computational complexity of the problem.

4.2.1 Low-Order Panel Method

BEMs were developed in the 1960s to solve numerical problems on the boundary of a given region of interest. This boundary may either be a surface or curve in a three-dimensional space, or a curve in a two-dimensional space. By seeking solutions on the boundary, rather than the entire volume or area, the BEM reduces the problem's dimensionality by one dimension. This, in turn, allows for a more efficient computation and solution of the problem.

A three-dimensional unsteady low-order panel method was developed as part of this work. The method is based on the constant-strength combined source and doublet method presented in [165]. The fluid is assumed to be inviscid, irrotational, and incompressible over the entire flow field. As a result, conservation of mass, or continuity

$$\frac{\partial \rho}{\partial t} + \nabla \cdot (\rho \mathbf{q}) = 0, \tag{4.1}$$

reduces to a velocity potential that satisfies the Laplace equation

$$\nabla^2 \Phi = 0, \tag{4.2}$$

where $\mathbf{q}$ is the flow velocity field and Φ is the velocity potential.

Two boundary conditions are used when solving eq. (4.2). The first requires the normal component of velocity to be zero on the surfaces of the body

$$(\nabla \Phi + \mathbf{v}) \cdot \mathbf{n} = 0, \tag{4.3}$$

where $\mathbf{n}$ is the surface outward normal vector and $\mathbf{v}$ is the surface velocity, both in

global inertial coordinates. The second boundary condition requires that the flow disturbances due to the body's motion through the fluid decay far from the surface ($r \to \infty$), such that

$$\lim_{r\to\infty} \nabla\Phi = 0, \tag{4.4}$$

with r being the distance to a point far from the surface, measured in the inertial frame of reference.

This mathematical problem is described schematically in fig. 4.2. Laplace's equation for the velocity potential, eq. (4.2), must be solved for any body j with boundary $S_{b,j}$ enclosed in a volume Ω with boundary $\partial\Omega$. The boundary conditions in eq. (4.3) and eq. (4.4) are applied to boundaries $S_{b,j}$ and S_∞ of the domain, respectively.

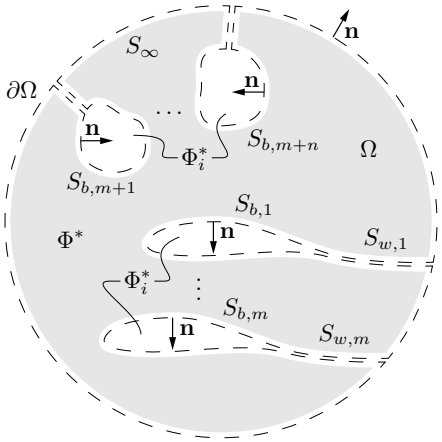

Figure 4.2: Potential flow problem.

We are interested in finding solutions to eq. (4.2), which is a differential equation of the form

$$Lu(\mathbf{x}) = 0, \tag{4.5}$$

where $L = L(\mathbf{x})$ is a linear differential operator defined in $\mathbb{R}^n$.

The Green's function $G(P, Q)$ of a linear differential operator $L = L(\mathbf{x})$ at a source point $P = P(\mathbf{x})$ is any solution of

$$LG(P, Q) = \delta(P, Q), \tag{4.6}$$

where $\delta(P, Q) = \delta(Q - P)$ is the Dirac delta function and $Q = Q(\mathbf{x})$ is a field or target point.

Green's functions can be thought of as the function space analogs of the matrix inverse. They act like the inverse of a differential operator for specific boundary

conditions. That means we can use them to solve boundary value problems with just one fundamental solution.

The Dirac delta is not a function in the traditional sense but rather commonly defined as a distribution. It has a sifting property that picks out, under integration, the value of some other function at the point the delta function is acting

$$\langle f(Q), \delta(P,Q)\rangle = f(P). \tag{4.7}$$

The derivation of the boundary integral equation that is equivalent to eq. (4.2) begins by noting that

$$\langle f(\mathbf{x}), \nabla^2\Phi(\mathbf{x})\rangle = 0, \tag{4.8}$$

for any sufficiently well behaved function $f(\mathbf{x})$ defined in the volume.

Integrating the previous equation by parts, i.e., applying the divergence theorem, we obtain

$$\int_\Omega \Phi(\mathbf{x})\nabla^2\Phi(\mathbf{x})dV = \int_{\partial\Omega}\left[\Phi(Q)\frac{\partial G}{\partial \mathbf{n}}(P,Q) - G(P,Q)\frac{\partial \Phi}{\partial \mathbf{n}}(Q)\right]dS. \tag{4.9}$$

In order to eliminate the volume integral, we wish to choose $f(\mathbf{x})$ so that it also satisfies eq. (4.2). Such functions are the so-called free-space Green's functions that physically correspond to the potential at the field point Q given a point charge at P. These functions satisfy a simpler problem given by

$$\nabla^2 G(P,Q) = \delta(P,Q). \tag{4.10}$$

Thus, $G(P,Q)$ is also called the point source potential, and for each fixed P, it satisfies eq. (4.2) as a function of Q, for $Q \neq P$.

The Green's functions G and $\frac{dG}{d\mathbf{n}}$ in eq. (4.9) are both known quantities and, for a three-dimensional problem, are given as

$$G = \frac{1}{4\pi r}, \qquad \frac{\partial G}{\partial \mathbf{n}} = -\frac{1}{4\pi}\frac{\mathbf{n}\cdot\mathbf{R}}{r^3}, \tag{4.11}$$

where $\mathbf{R}$ is the vector between the source point P and the field point Q, and $r = \|\mathbf{R}\|$.

The Green's functions are singular when $Q = P$ and, as a consequence, for $P \in \Omega \cup \partial\Omega$, the use of the divergence theorem in eq. (4.9) is not permissible. However,

for $P = P_E$ exterior to Ω, i.e., $P \notin \Omega \cup \partial\Omega$ we obtain the exterior integral equation

$$\int_{\partial\Omega} \left[\Phi(Q) \frac{\partial G}{\partial \mathbf{n}}(P_E, Q) - G(P_E, Q) \frac{\partial \Phi}{\partial \mathbf{n}}(Q) \right] dS = 0. \tag{4.12}$$

An interior equation for $P_I \in \Omega$ can also be derived as

$$\Phi(P_I) + \int_{\partial\Omega} \left[\Phi(Q) \frac{\partial G}{\partial \mathbf{n}}(P_I, Q) - G(P_I, Q) \frac{\partial \Phi}{\partial \mathbf{n}}(Q) \right] dS = 0. \tag{4.13}$$

A boundary-only equation, allowing $P \in \partial\Omega$, can also be derived for a smooth surface [202]. The three statements can be combined in a single equation as

$$\varepsilon(P)\Phi(P) = \int_{\partial\Omega} \left[\Phi(Q) \frac{\partial G}{\partial \mathbf{n}}(P, Q) - G(P, Q) \frac{\partial \Phi}{\partial \mathbf{n}}(Q) \right] dS, \tag{4.14}$$

where $\varepsilon(P)$ is the free term coefficient, which depends on the position of point P and is defined as

$$\varepsilon(P) = \begin{cases} 1, & P \in \Omega \\ \frac{1}{2}, & P \in \partial\Omega \\ 0, & P \notin \Omega \cup \partial\Omega. \end{cases} \tag{4.15}$$

However, $G(P, Q)$ and $\frac{\partial G}{\partial \mathbf{n}}(P, Q)$ are singular when $P = Q$. Even though the former is only weakly singular, and thus this integral exists for $P \in \partial\Omega$, the singularly in the latter function is worse, making this statement difficult to implement in reality. A more practical approach involves using one of the other statements and placing the source points only slightly outside or inside the domain to avoid the singularities in Green's functions [165].

Choosing to proceed with the interior limit, eq. (4.13) can now be applied to the potential flow problem illustrated in fig. 4.2 to yield

$$\Phi(P_I) + \int_{S_b} \Phi(Q) \frac{\partial G}{\partial \mathbf{n}}(P_I, Q) dS - \int_{S_b + S_w} G(P_I, Q) \frac{\partial \Phi}{\partial \mathbf{n}}(Q) dS + \Phi_\infty = 0, \tag{4.16}$$

where $S_b = S_{b,1} \cup \ldots \cup S_{b,m+n}$, $S_w = S_{w,1} \cup \ldots \cup S_{w,m}$, and

$$\Phi_\infty = \int_{S_\infty} \left[\Phi(Q) \frac{\partial G}{\partial \mathbf{n}}(P_E, Q) - G(P_E, Q) \frac{\partial \Phi}{\partial \mathbf{n}}(Q) \right] dS,$$

is the contribution of S_∞ to the velocity potential, which can be selected as a constant

if an inertial frame is used where the bodies move through a stationary fluid [165]. Alternatively, the exterior limit equation could have been chosen instead.

For an enclosed boundary (e.g., S_b), it can be shown that the interior potential inside the body will not change in the absence of internal singularities, that is $\Phi(P_I) = \text{const.}$. Different values can be set for the inner potential. One possible choice is to set $\Phi(P_I) = \Phi_\infty$, which avoids large strength distributions on the surface S_b. In this case, eq. (4.16) reduces to

$$\int_{S_b} \Phi(Q) \frac{\partial G}{\partial \mathbf{n}}(P_E, Q) dS - \int_{S_b+S_w} G(P_E, Q) \frac{\partial \Phi}{\partial \mathbf{n}}(Q) dS = 0. \tag{4.17}$$

The discretized form of this equation is expressed for a given point P_i as

$$\sum_{j=1}^{N} \int_{\partial\Omega_j} \Phi(Q) \frac{\partial G}{\partial \mathbf{n}}(P_i, Q) dS_j - \sum_{j=1}^{N} \int_{\partial\Omega_j} G(P_i, Q) \frac{\partial \Phi}{\partial \mathbf{n}}(Q) dS_j = 0, \tag{4.18}$$

where $\partial\Omega_j$ is the segment j of the boundary over which integration is carried out, and P_i is a source point on the i-th element. For the low order panel method, the values of Φ and $\frac{\partial \Phi}{\partial \mathbf{n}}$ are constant on each element, so they can be moved outside the integral

$$\sum_{j=1}^{N} \left(\int_{\partial\Omega_j} \frac{\partial G}{\partial \mathbf{n}}(P_i, Q) dS_j \right) \Phi^j(Q) = \sum_{j=1}^{N} \left(\int_{\partial\Omega_j} G(P_i, Q) dS_j \right) \Psi^j(Q), \tag{4.19}$$

where $\Psi^j = \left(\frac{\partial \Phi}{\partial \mathbf{n}}\right)^j$. The values of Φ and Ψ are typically referred to as doublet and source values, respectively.

The integrals involved in eq. (4.19) relate the source point P_i, where the fundamental solution is applied, to the field point Q_j $(j = 1, \ldots, N)$, and are called the influence coefficients, as their values express the contribution of the nodal values Φ^j and Ψ^j to the solution at point i. These coefficients are denoted by H^i_j and G^i_j, which are defined as

$$H^i_j = \int_{\partial\Omega_j} \frac{\partial G}{\partial \mathbf{n}}(P_i, Q)\, dS_j, \qquad G^i_j = \int_{\partial\Omega_j} G(P_i, Q)\, dS_j, \tag{4.20}$$

where the integration can be performed analytically or numerically. Analytical solutions of the integrals for constant quadrilateral panels can be found in the literature [165]. Numerical solutions usually require the use of Gaussian quadrature to evaluate the integrals.

The previous coefficients can be used to write eq. (4.19) in a more succinct form

$$H_j^i \Phi^j = G_j^i \Psi^j. \tag{4.21}$$

The previous formulation does not uniquely describe a solution since a large number of doublet Φ and source Ψ values will satisfy a given set of boundary conditions. Therefore, a choice has to be made in order to select a desirable combination of such singularity elements [165]. Neumann boundary conditions of the form $\Psi = 0$ can be chosen, which directly satisfy eq. (4.2). This is called the direct formulation or the Neumann problem. Alternatively, Dirichlet boundary conditions of the form $\Phi = c$, where c is a constant, can be applied instead. This results in an indirect formulation or the Dirichlet problem.

For a three-dimensional lifting problem, there is a need to model a wake, since the bound vorticity needs to be continued beyond the wing. For the wing to have circulation at a given spanwise location, a discontinuity in the velocity potential near the trailing edge must exist such that $\Phi_2 - \Phi_1 = \Gamma$, where Φ_2 and Φ_1 are velocity potential values immediately above and below the wake surface, respectively, and Γ is the circulation. For a given lifting body j, two additional conditions need to be specified on the wake surface $S_{w,j}$. The first condition is to set the wake strength at the trailing edge, and the second is to set its shape and location in space.

The Kutta condition states that the flow must leave the sharp trailing edge of a wing smoothly, and the velocity there is finite. This can be interpreted as the flow leaving the trailing edge at a median angle $\frac{\delta_{\text{TE}}}{2}$, i.e., along the bisector line. Also, since the trailing-edge angle is finite, the upper and lower normal component of the velocity must vanish, which is only possible if this is a stagnation point, i.e., $\Delta C_p = 0$ at the trailing edge. If the circulation is modeled by a vortex distribution, this can be expressed as $\Phi_u - \Phi_l = \Phi_w$ (see fig. 4.3a).

To specify the time-dependent boundary conditions, the solution of eq. (4.21) begins by considering that at $t = 0$, no wake is shed from any lifting surface. In this case, the right-hand side of eq. (4.21) can be easily determined from the specified zero normal flow boundary conditions

$$\text{RHS}^i = G_j^i \left(\Psi^j\right)_b, \tag{4.22}$$

where Ψ_b are the source values on the lifting surfaces given by the zero normal flow

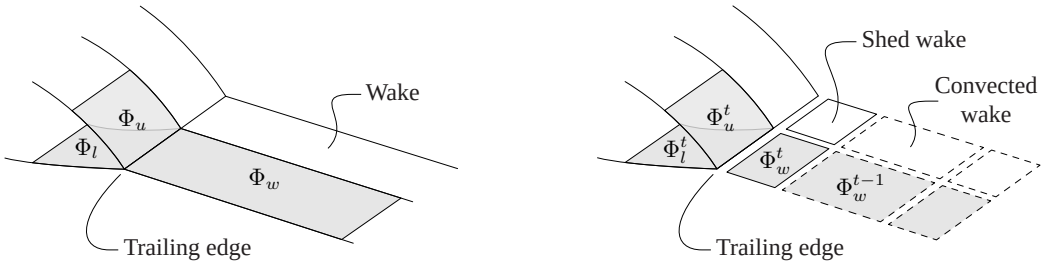

(a) Fixed wake (b) Convected wake

Figure 4.3: Schematic illustration of the Kutta condition at a wing's trailing edge showing the relation between trailing edge upper and lower panel doublet strength and the corresponding wake doublet strength for a steady-state fixed wake (left) and an unsteady convected wake (right).

boundary condition.

For subsequent time steps, wing motion occurs due to rigid-body motion and deformation, and each trailing-edge segment sheds a wake panel with a vortex strength given from the previous time step as $\Phi_w^t = \Phi_u^{t-1} - \Phi_l^{t-1}$. The local wing trailing-edge velocity determines the geometry of the wake panel: a slow-moving wing generates long wake panels, while a fast-moving wing generates short wake panels. Note that during the second time step, there will be only one row of wake panels. Each time step adds a row of wake panels to the analysis.

The influence of any previously shed wake must be taken into account when solving eq. (4.21). Since the strength of any previously-shed wake is known, this influence can be accounted for with a redefined right-hand side vector

$$\mathrm{RHS}^i = H_k^i \left(\Phi^k\right)_w + G_j^i \left(\Psi^j\right)_b , \tag{4.23}$$

where Φ_w are the known shed wake doublet values.

At every time step, the system of equations can be solved for the unknown doublet distribution as

$$\Phi^i = \left(H_j^i\right)^{-1} \mathrm{RHS}^j . \tag{4.24}$$

Since the wake is force-free, each wake panel must move with the local stream velocity—this is known as wake roll-up. The local velocity is a result of the kinematic motion of the wing and the velocity components induced by the wake and body vorticity. This velocity can be calculated since the strength of all the singularity elements in the field is known at this point of the calculation. This process repeats for

subsequent time steps until the desired simulation time is reached.

4.2.2 Compressibility Correction

The effect of low-speed compressibility can be easily incorporated into this aerodynamic formulation. The Prandtl-Glauert transformation [203] can be used to include the correction for compressibility. According to this transformation, the pressure coefficient C_p in a compressible flow can be derived from the pressure coefficient C_{p_0} in an incompressible flow as

$$C_p = \frac{C_{p_0}}{\beta}. \tag{4.25}$$

Other corrections can also be used [204], such as the Karman-Tsien transformation

$$C_p = \frac{C_{p_0}}{\beta + \dfrac{M_\infty^2}{1+\beta}\dfrac{C_{p_0}}{2}}, \tag{4.26}$$

or Laitone's transformation

$$C_p = \frac{C_{p_0}}{\beta + \dfrac{M_\infty^2\left(1+\frac{\gamma-1}{2}M_\infty^2\right)}{\beta}\dfrac{C_{p_0}}{2}}, \tag{4.27}$$

In the previous equations, $\beta = \sqrt{1-M_\infty^2}$ and M_∞ is the free stream Mach number.

4.2.3 Unsteady Wake Convection

The unsteady panel method formulation solves aerodynamic loads in the time domain and gives the wake position as part of the solution. The Kutta condition is imposed by shedding vorticity from the trailing edges into the wake [165, 203]. In the procedure presented above for steady aerodynamics, the wake's shape is unknown and needs to be prescribed. For the case of unsteady aerodynamics, the procedure needs to be modified to include the time-dependency of doublet vortices and source strength quantities. The unsteady wake is formed by convecting the vortex ring elements with the local velocity while holding the circulations around them constant. The shedding-convecting process generates the vortex lattice that represents the wake as part of the solution.

The zero normal force boundary condition has to be enforced at each time step as

the surface moves. Additionally, a new row of wake panels is shed at each time step. The newest wake panel is bounded at one end by the lifting surface trailing edge, and the other end is placed in the interval covered by the trailing edge during the last time step. It is usually placed closer to the trailing edge within 20 % to 30 % of the traveled distance [165]. The wake shedding procedure is described schematically in fig. 4.3b.

The wake panels are force-free and travel according to the local flow velocity. The local flow velocity results from the surface's motion, including rigid-body and elastic deformations, and the velocity induced by the panels. The flow velocity at each wake panel corner point is calculated and used to displace the corner points to their new location. The remaining steps mentioned in the steady state procedure remain unchanged.

Aerodynamic loads are determined by finding the pressure on the surface representing the wing according to the unsteady Bernoulli's equation [203]. The unsteady pressure coefficient at each panel is now given by

$$C_p = 1 - \frac{\mathbf{v}^{\mathrm{T}}\mathbf{v}}{\mathbf{v}_{\mathrm{ref}}^{\mathrm{T}}\mathbf{v}_{\mathrm{ref}}} - \frac{2}{\mathbf{v}_{\mathrm{ref}}^{\mathrm{T}}\mathbf{v}_{\mathrm{ref}}}\frac{\partial \Phi}{\partial t}. \tag{4.28}$$

4.2.4 Trailing Edge Detection

The trailing edge of a lifting surface is the line from which a wake is shed. It models the thin vortex layer that leaves a lifting surface when the boundary layer is still attached. In this work, the trailing edge is identified geometrically according to a set of parameters.

For parametrically generated surface meshes, the trailing edge is easily identifiable at the connection of upper and lower airfoil sections. A parametric mesh can be easily generated from imported airfoil coordinates, which are typically provided as an ordered list of points. This inherent order allows for trivial detection of the airfoil trailing edge point—usually the first or last point of this list. The trailing edge of a lifting surface can be constructed by traversing all the airfoil sections used to define the surface and connecting the trailing edge points of every section.

The process is more involved for unstructured surface meshes since the mesh entities are not necessarily ordered in memory. Algorithm 1 describes an automatic trailing edge detection algorithm that can be used with unstructured meshes.

In this case, one needs to use the topological mesh information (or connectivity) to look for trailing edges. For closed surface meshes, a sharp edge can be defined

Algorithm 1 Automatic trailing edge detection for an unstructured surface mesh $\mathcal{T}$ given a threshold angle θ_{te}.

```
1  function FindAllTrailingEdges(T, θ_te)
2      Create empty list L of trailing edges
3      for all t_i ∈ T do                          Traverse all elements of the mesh
4          for all t_j ∼ t_i do                    Traverse all adjacent elements of t_i
5              n_i ← unit normal of element t_i
6              n_j ← unit normal of element t_j
7              θ ← arccos(n_i · n_j) angle between unit normals
8              if θ ≥ θ_te then                    Adjacent elements form a sharp edge
9                  b_ij ← n_i + n_j unit bisector between unit normals
10                 γ ← b_ij · u_∞/(‖b_ij‖‖u_∞‖) dot product between bisector and flow
                   velocity vectors
11                 if γ > 0 then                   Adjacent elements form a trailing edge
12                     e_ij ← edge between elements t_i and t_j
13                     Insert e_ij into L
14                 end if
15             end if
16         end for
17     end for
18 end function
```

as the edge between two adjacent faces with a sharp angle. The angle between two adjacent faces can be calculated by first calculating the normal of each face and then the angle between the normals. If this angle exceeds a given threshold, the edge can be considered a sharp edge.

Since a sharp edge is not necessarily a trailing edge, the trailing edge detection algorithm should be robust enough to distinguish between sharp and trailing edges. For example, a fuselage body must not generate lift and should have no trailing edge to shed wakes from, but it might have sharp corners. A trailing edge can be distinguished from a sharp edge by calculating the bisector between the two adjacent faces that define the edge. If the bisector points in the same direction as the external flow, the sharp edge is considered to be a trailing edge. Otherwise, the edge is ignored. An example of the trailing edge detection algorithm applied to a surface mesh is shown in fig. 4.4.

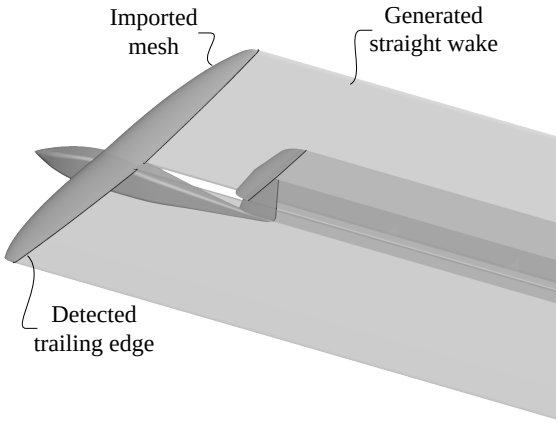

Figure 4.4: Example of detected trailing edge (thick solid lines) and automatically generated fixed wake shed from trailing edge segments for the QT1 aircraft.

4.2.5 Fast Multipole Method

The major downside of the BEM is that it requires the solution of a dense system of linear equations, $\mathbf{Ax} = \mathbf{b}$, where $\mathbf{A} \in \mathbb{R}^{N \times N}$ and N is the number of discretized elements. Due to the density of A, computational work and memory requirements for this solution scale, in the best case scenario, with the size of the matrix, or in asymptotic notation, $\mathcal{O}(N^2)$ time for an iterative solver and $\mathcal{O}(N^3)$ for exact solution methods, such as Gauss elimination.

In comparison to FEMs, FVMs, or FDMs, these methods require the solution of a sparse linear system, allowing solutions to be found in $\mathcal{O}(N)$ time, where N is now the total number of DOFs, which is, in general, significantly larger than the number of discretized elements in BEM problems.

Evaluating large particle fields that decay in space has been a significant computational problem in many disciplines, such as molecular dynamics [205], astrophysics simulations [206] and vortex methods for computational fluids [207]. Evaluating these fields requires the solution of an N-body problem, i.e., the summation of contributions from N particles as seen in eq. (4.21). However, due to the $\mathcal{O}(n^2)$ computational complexity of directly performing this evaluation, simulations beyond a certain size were impossible.

Two major categories of fast summation methods have been discussed in the literature. One is the so-called treecode method [206, 208–211], and the other is the FMM [212, 213]. Both of these algorithms rely on adaptively decomposing the space hierarchically into clusters, usually in the form of a quadtree in two-dimensional

problems or an octree in three-dimensional problems, as schematically illustrated in fig. 4.5 in two dimensions, and approximating the particles contained within each cluster with a multipole expansion which only converges far from the cluster center.

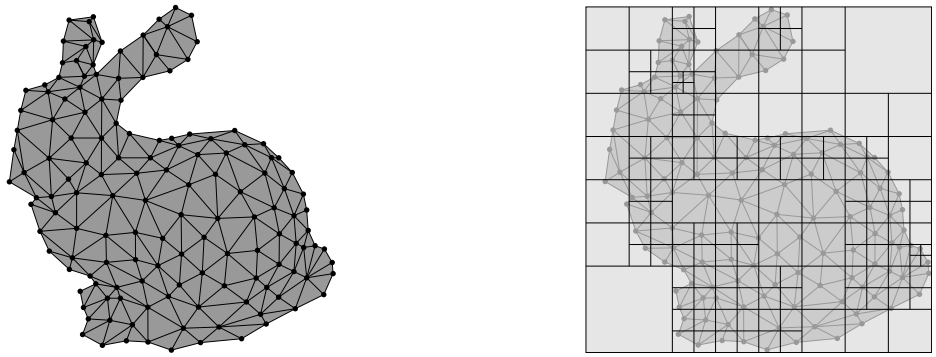

(a) Two-dimensional mesh (b) Adaptive quadtree in two dimensions

Figure 4.5: Schematic illustration of hierarchical spatial decomposition of a two-dimensional mesh (left) into an adaptive quadtree (right).

The multipoles are shifted and accumulated up the tree from child to parent clusters until every cluster holds an expansion representing all sources contained by itself and its children.

The tree structure is then traversed upward, directly summing the influences of near clusters (particle-particle) and evaluating the multipole approximations of distant clusters (cluster-particle). The influence of a source cell (cluster of particles) on a target particle is obtained through multipole expansion if the distance between them is larger than a critical distance. Otherwise, the influence is calculated by direct interaction. This approach gives a computational complexity of $\mathcal{O}(N \log N)$.

The FMM—named one of the top 10 scientific algorithms of the 20^{th} century [214]—extends treecode methods by adding local expansions which converge within a short distance of the expansion center. Instead of directly evaluating the multipole expansions of far clusters, the multipoles are translated and converted into local expansions in a downward pass of the tree (cluster-cluster) before being translated to the lowest nodes of the tree and evaluated against target points. This modification allows the FMM to reduce the time complexity of the problem to $\mathcal{O}(N)$, at the cost of higher complexity of implementation and higher memory requirements. A graphical representation of the FMM algorithm is shown in fig. 4.6b and contrasted against a direct (particle-particle) interaction method fig. 4.6a.

BEM problems involving Laplace and Stokes equations have been accelerated using

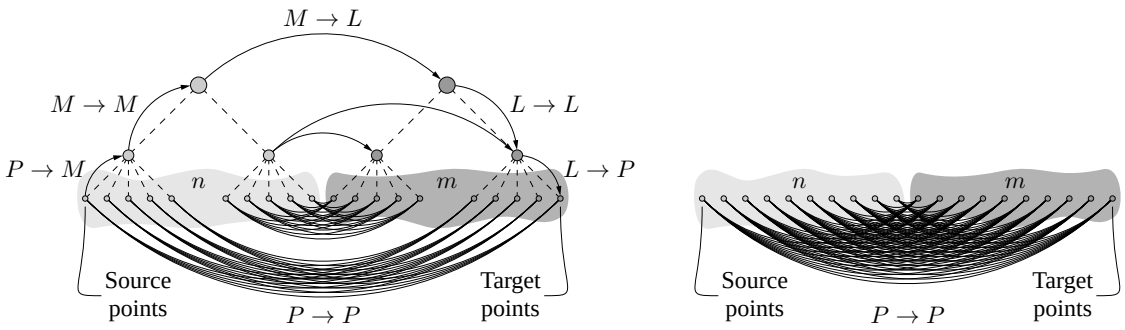

(a) FMM interaction (b) Direct interaction

Figure 4.6: FMM (left) and direct (right) approaches for solving an N-body interaction problem.

the FMM [215, 216]. Using the FMM within an iterative solution of the BEM linear system reduced the time complexity from $\mathcal{O}(N^2)$ to $\mathcal{O}(N)$. While this modification adds complexity to the BEM, it makes the simulation of larger problems feasible.

Seven operators form the standard FMM, each performing a distinct operation: directly evaluating the influence of one particle on another, creating a multipole expansion, and translating series expansions up, down, and across the tree.

In three dimensions, multipole expansions are expressed in terms of spherical harmonics. The spherical harmonics have a degree n and order m and are defined by the following formula

$$Y_n^m(\theta, \phi) = \sqrt{\frac{(n - |m|)!}{(n + |m|)!}} P_n^{|m|} \cos(\theta) e^{im\phi}, \tag{4.29}$$

where P_n^m are the associated Legendre functions and (θ, ϕ) are the polar and azimuthal angle components of a (r, θ, ϕ) spherical coordinate system, respectively.

The particle-to-multipole operator ($P \to M$) generates a multipole expansion about the center of a cluster or box of all source particles contained within that cluster.

A truncated multipole expansion of order p about a box origin representing a collection of k charges c (sources or doublets) located at spherical coordinates (r_i, θ_i, ϕ_i), for $i = 1, \ldots, k$ with respect to the box centroid, is defined by

$$\Phi(r, \theta, \phi) = \sum_{n=0}^{p} \sum_{m=-n}^{n} \frac{M_n^m}{r^{n+1}} Y_n^m(\theta, \phi), \tag{4.30}$$

where (r, θ, ϕ) are the spherical coordinates of the point where the multipole expansion is evaluated, and M_n^m are the multipole coefficients of the multipole expansion. The multipole coefficients for a collection of k charges c (sources or doubles) are given by

$$M_n^m = \sum_{i=1}^{k} r_i^n Y_n^{-m}(\theta_i, \phi_i) c_i. \tag{4.31}$$

In the multipole-to-multipole translation step ($M \to M$) of the algorithm, multipole expansions of child boxes must be transferred or translated to the centroid of their parent box. If (r, θ, ϕ) are the spherical coordinates of the parent box's centroid with respect to the child box's centroid, then the multipole coefficients M_n^m of the parent box are given by the following multipole translation formula

$$\widetilde{M}_j^k = \sum_{n=0}^{j} \sum_{m=-n}^{n} \frac{M_{j-n}^{k-m} i^{|k|-|m|-|k-m|} A_n^m A_{j-n}^{k-m} r^n Y_n^{-m}(\theta, \phi)}{(-1)^n A_j^k}, \tag{4.32}$$

with A_n^m defined as

$$A_n^m = \frac{(-1)^n}{\sqrt{(n-m)!(n+m)!}}.$$

In the multipole-to-local translation step ($M \to L$), a multipole expansion is converted into a local expansion about a well-separated box center. If M_n^m are the multipole expansion coefficients of a box in the box's interaction list with respect to the box's centroid and (r, θ, ϕ) are the spherical coordinates of the center point of the box, then the corresponding local expansion coefficients about the center of the box are given by

$$L_j^k = \sum_{n=0}^{p} \sum_{m=-n}^{n} \frac{\widetilde{M}_n^m i^{|k-m|-|k|-|m|} A_n^m A_j^k Y_{j+n}^{m-k}(\theta, \phi)}{(-1)^n A_{j+n}^{m-k} r^{j+n+1}}. \tag{4.33}$$

The local-to-local translation step $L \to L$ translates a local expansion to a different center. If L_m^n are the coefficients of the parent box's local expansion and (r, θ, ϕ) are the spherical coordinates of a child box's centroid with respect to its parent's centroid, then the corresponding local expansion coefficients about the child box's center are

$$\widetilde{L}_j^k = \sum_{n=j}^{p} \sum_{m=-n}^{n} \frac{L_n^m A_{n-j}^{m-k} A_j^k Y_{n-j}^{m-k}(\theta, \phi) r^{n-j}}{(-1)^{n+j} A_n^m}. \tag{4.34}$$

In the local-to-particle step ($L \to P$), local expansions are evaluated at well-

separated target particles. The potential resulting from the evaluation of the local expansion at spherical coordinates (r, θ, ϕ) with respect to a box's centroid is determined as

$$\Phi(r, \theta, \phi) = \sum_{j=0}^{p} \sum_{k=-j}^{j} \widetilde{L}_j^k Y_j^k(\theta, \phi) r^j, \tag{4.35}$$

where L_j^k are the local expansion coefficients representing the potentials of all cells that are far from the box. There will be two sets of L_j^k coefficients per childless box, corresponding to the contributions from the source and doublet charges.

Finally, for particles that are not well separated, the particle-to-particle operator $(P \rightarrow P)$ calculates the interactions between source and target points in a direct manner. This method has a time complexity of $\mathcal{O}(N^2)$.

There are four distinct phases in the FMM: the hierarchical domain decomposition, the upward tree evaluation phase, the interaction phase, and the downward tree evaluation pass. Each of these phases is described below.

In the domain decomposition phase (algorithm 2), a bounding box is generated, spanning all the elements in three-dimensional space.

Algorithm 2 Domain decomposition phase of the FMM

```
1  function PartitionDomain(P, n_div)
2      Create empty source cell tree S with maximum number of divisions n_div
3      s_i ← root cell of S
4      for all p̄_i ∈ P do          Traverse all cell centroids p̄_i in source mesh P
5          Insert(s_i, p̄_i)
6      end for
7  end function

8  function Insert(s_i, p̄_i)
9      if s_i can be further subdivided then
10         s_c ← child octant of s_i that contains p̄_i
11         Insert(s_c, p̄_i)
12     else                                                    Reached n_div
13         Insert p̄_i into s_i
14     end if
15 end function
```

The box is recursively divided into eight boxes until there is no more than a specified maximum number of elements $N_{\max}$ in a box. Boxes with no elements in them are deleted. Links between cells and their parents and parents and children are

created at this point for fast traversal later. The computational cost of the domain decomposition can range from $\mathcal{O}(N \log N)$ to $\mathcal{O}(N)$, depending on the homogeneity of the element distribution, where N is the number of elements in the domain.

The upward tree evaluation (algorithm 3) is composed of two steps: the multipole generation ($P \to M$) and the multipole-to-multipole ($M \to M$) translation. In the multipole generation step, multipole expansion coefficients are computed due to all sources and doublets in each childless or leaf box of the spatial tree. This process results in two expansion coefficients for each box, corresponding to the source and doublet potentials. The complexity of the multipole generation step is $\mathcal{O}(Np^2)$, where p is the order of the multipole expansion. The multipole-to-multipole translation is the recursive translation of the multipole coefficients up the tree, starting with the leaf boxes. The computational complexity of this step is $\mathcal{O}(Np^4)$.

Algorithm 3 Upward evaluation phase of the FMM for kernel $\mathcal{K}$ and source cell tree $\mathcal{S}$.

```
1  function EvaluateUpward(K, S)
2      for all s_i ∈ S do                          Post-order traversal of the tree
3          if s_i is a leaf cell then
4              P_i ← set of points contained in s_i
5              C_i ← set of charges contained in s_i
6              p̄_i ← center point of cell s_i
7              m_i ← GenerateMultipole(K, P_i, C_i, p̄_i, ) Create multipole expan-
                   sion (P → M) at leaf cells
8          end if
9          s_p ← parent cell of s_i
10         r_ip ← translation vector between center points of cells s_i and s_p
11         m_i ← multipole expansion of cell s_i
12         m_p ← TranslateMultipole(K, r_ip, m_i) Translate multipole expansion
               (M → M) up the tree
13     end for
14 end function
```

In the interaction phase (algorithm 4), both long and short-range interactions are calculated based on interacting source and target clusters against each other. If the distance between two cluster centers is less than some specified acceptance criteria, which is also a function of the cluster size, then direct particle-particle ($P \to P$) evaluation is used, with a complexity cost of $\mathcal{O}(N)$. Otherwise, cluster-cluster multipole translation ($M \to L$) operators are evaluated. This step has a complexity that scales as $\mathcal{O}(Np^4)$.

Algorithm 4 Interaction phase of the FMM for kernel $\mathcal{K}$ across source and target cell trees $\mathcal{S}$ and $\mathcal{T}$, respectively.

function EvaluateAcross($\mathcal{K}, \mathcal{S}, \mathcal{T}$)
  $s_r, t_r \leftarrow$ root cells of $\mathcal{S}$ and $\mathcal{T}$, respectively
  Create queue Q of pairs of source and target cells
  Initialize Q with (s_r, t_r)
  while Q is not empty **do** *Queue-based level-order traversal of the tree*
    $s_i, t_j \leftarrow$ pop source and target cells, respectively, from the front of Q
    if s_i is a leaf cell **then**
      if t_j is a leaf cell **then** *Both s_i and t_j are leaf cells*
        $\mathcal{P}_i \leftarrow$ set of points contained in s_i
        $\mathcal{C}_i \leftarrow$ set of charges contained in s_i
        $\mathcal{P}_j \leftarrow$ set of points contained in t_j
        $\mathcal{R}_j \leftarrow$ DirectEval($\mathcal{K}, \mathcal{P}_i, \mathcal{C}_i, \mathcal{P}_j$) *Perform direct evaluation ($P \rightarrow P$)*
      else *s_i is a leaf cell but t_j is not*
        for all $t_c \in$ children of t_j **do**
          Interact($\mathcal{K}, s_i, t_c, Q$)
        end for
      end if
    else if t_j is a leaf cell **then** *t_j is a leaf cell but s_i is not*
      for all $s_c \in$ children of s_i **do**
        Interact($\mathcal{K}, s_c, t_j, Q$)
      end for
    else *Neither s_i or t_j are leaf cells*
      Interact($\mathcal{K}, s_i, t_j, Q$)
    end if
  end while
end function

function Interact($\mathcal{K}, s_i, t_j, Q$)
  if AcceptMultipole(s_i, t_j) **then** *Long-range interaction*
    $r_{ij} \leftarrow$ translation vector between center points of cells s_i and t_j
    $m_i \leftarrow$ multipole expansion of cell s_i
    $l_j \leftarrow$ TranslateMultipoleLocal($\mathcal{K}, r_{ij}, m_i$) *Translate multipole expansion ($M \rightarrow L$)*
  else *Not accepted, defer for splitting*
    Push (s_i, t_j) into Q
  end if
end function

The downward tree evaluation phase (algorithm 5) is composed of two steps: the local-to-local translation ($L \to L$) and the local expansion evaluation ($L \to P$). The local-to-local translation is a recursive translation of local expansions down the tree from each box to its children. The complexity of this operation scales as $\mathcal{O}(Np^4)$. Finally, the local expansion evaluation occurs at the leaf nodes, where the local expansion coefficients are evaluated at all target points within each relevant cluster.

Algorithm 5 Downward evaluation phase of the FMM for kernel $\mathcal{K}$ and target cell tree $\mathcal{T}$.

function EvaluateDownward($\mathcal{K}, \mathcal{T}$)
  for all $t_i \in \mathcal{T}$ **do** *Pre-order traversal of the tree*
    $t_p \leftarrow$ parent cell of t_i
    $r_{pi} \leftarrow$ translation vector between center points of cells t_p and t_i
    $l_p \leftarrow$ local expansion of cell t_p
    $l_i \leftarrow$ TranslateLocal($\mathcal{K}, r_{pi}, l_p$) *Translate local expansion ($L \to L$) down the tree*
    if t_i is a leaf cell **then**
      $l_i \leftarrow$ local expansion of cell t_i
      $\bar{p}_i \leftarrow$ center point of cell t_i
      $\mathcal{P}_i \leftarrow$ set of points contained in t_i
      $\mathcal{R}_i \leftarrow$ ExpandLocal($\mathcal{K}, l_i, \bar{p}_i, \mathcal{P}_i$) *Evaluate local expansion ($L \to P$) at leaf cells*
    end if
  end for
end function

4.3 Flexible Multibody Dynamics

A system of flexible bodies may consist of several connected elastic and rigid components. The connections between components can be joints and force elements such as springs, actuators, and dampers, as illustrated in figure fig. 4.7.

Deformation can significantly affect some dynamic systems, including robotic systems, precision machines, ground vehicles, space vehicles, structures, and mechanisms, and needs to be considered in the dynamic modeling of such systems [197]. An initial approach to describe the kinematics of the motion of deformable bodies consisted in treating deformable bodies by building on the methodologies developed for rigid body dynamics.

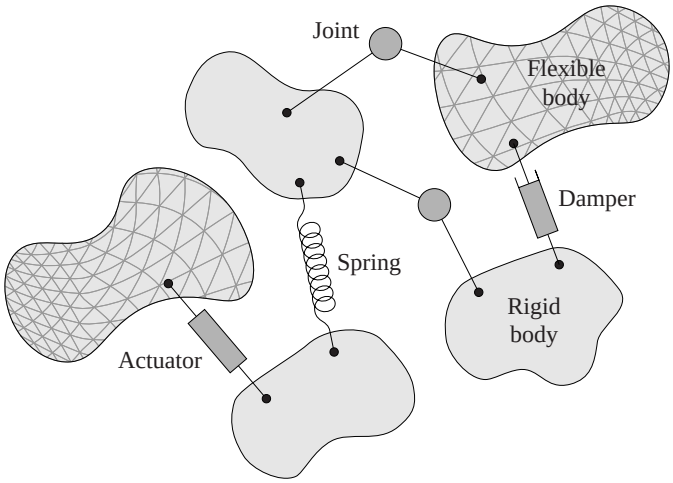

Figure 4.7: Flexible multibody dynamics system.

The analysis of constrained deformable bodies subjected to large displacements, including rigid body motion and elastic deformation, is the subject of study of flexible multibody dynamics theory. Although the elastic deformation within a single body can often be considered small, the large rigid body rotations between different bodies make the problem geometrically nonlinear.

The kinematics of a body can be described by the motion of a set of coordinate frames, each frame being attached to a material point on the body. Kinematic constraints introduce connections between bodies and relate the motions of the coordinate frames of interface points located at different bodies.

Three commonly used formulations can be used to describe the behavior of flexible multibody systems: inertial frame formulations, corotational frame formulations, and floating frame formulations. These formulations differ in the way they describe a body's elastic behavior. Thus, there are essential differences in the choice of degrees of freedom and how kinematic constraints between bodies are enforced. Figure 4.8 illustrates each formulation. A comprehensive overview of these formulations can be found in [217].

4.3.1 Corotational Frame Formulation

The corotational frame formulation can be thought of as the geometrically nonlinear extension of a linear finite element formulation [218, 219]. This frame describes an element's large rigid body motion with respect to the inertial frame. Small elastic deformations within the element are superimposed using a linear finite element formu-

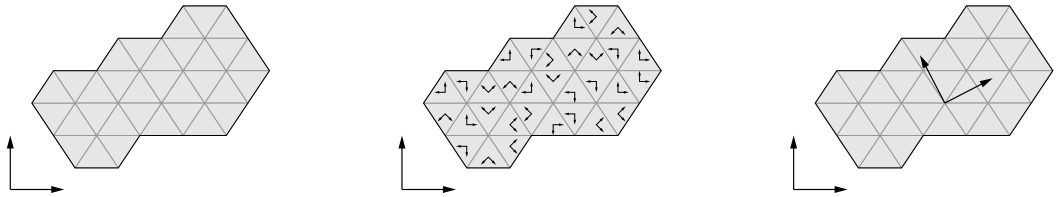

(a) Inertial frame formulation (b) Corotational frame formulation (c) Floating frame formulation

Figure 4.8: Representation of a flexible body using an inertial frame formulation expressed in absolute coordinates (left), a corotational formulation using a local frame for each element (center), and a floating frame formulation using a local frame for each body (right).

lation based on the Cauchy strain. The formulation can still describe geometrically nonlinear elastic deformations within a single body because each element is given its own corotational frame, provided that the small strain assumption within an element holds.

The corotational frame formulation uses absolute nodal coordinates as degrees of freedom. In order to arrive at this formulation, a unique kinematic relation must be established that expresses the coordinates of an element's corotational frame in terms of the element's absolute nodal coordinates. This relation is commonly established by locating the corotational frame at one of the element's nodes or by expressing the corotational frame coordinates as a weighted average of the element's nodal coordinates. Alternatively, it is possible to define the orientation of each corotational frame by enforcing zero elastic deformation at its location [220].

An advantage of the corotational technique is that it allows the use of standard linear formulations with respect to the rotating coordinate system, with the geometric nonlinearities incorporated via the system's rotation. An advantage of this approach is that it is possible to solve nonlinear problems using the best available linear elements, thereby exploiting the considerable research effort dedicated to the latter. A drawback of this formulation is that it does not distinguish between rigid and flexible bodies. That is, rigid bodies are modeled as flexible bodies with a large stiffness, resulting in a less efficient formulation for multibody systems that contain both rigid and flexible bodies.

4.3.2 Floating Frame of Reference Formulation

The FFRF can be interpreted as the flexible extension of a rigid multibody formulation and is the most widely used method to simulate systems of flexible bodies. In this formulation, one set of coordinates in a floating frame describes a body's large rigid body motion with respect to the inertial frame. The second set of coordinates describes the deformation of the body with respect to the floating frame, as shown in 4.9.

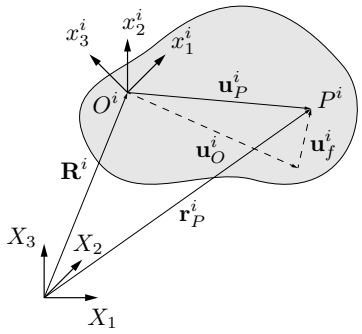

Figure 4.9: Floating frame of reference.

Mass and stiffness matrices are typically obtained from a linear finite element model. The degrees of freedom thus consist of the absolute coordinates of the floating frame and a set of local generalized coordinates used to describe the body's local elastic behavior. Because the absolute interface coordinates are not part of the degrees of freedom, the kinematic constraints are typically highly nonlinear equations in terms of many degrees of freedom.

In the FFRF, the global position of an arbitrary point P of a deformable body i can be written as

$$\mathbf{r}_P^i = \mathbf{R}^i + \mathbf{A}^i \left(\mathbf{u}_o^i + \mathbf{u}_f^i \right), \tag{4.36}$$

where $\mathbf{u}_o^i$ is the position of point P in the undeformed state, $\mathbf{u}_f^i$ is the deformation vector, and $\mathbf{A}^i$ is the transformation matrix that defines the orientation of the body coordinate system with respect to the global inertial coordinate system.

The kinematic description used in equation 4.36 leads to exact modeling of the rigid body dynamics when the deformation is equal to zero [197]. Additionally, it does not imply any separation between the rigid body motion and the elastic deformation of the flexible body since any coordinate system can be selected as the body coordinate system. The selection of the deformable body coordinate system is one of the fundamental problems when using the FFRF.

In the case of rigid body dynamics, using a centroidal body coordinate system simplifies the dynamic equations by decoupling the rigid body's translational and rotational motion. Deformable body coordinate systems that satisfy the mean axis conditions are frequently chosen. These conditions are obtained by minimizing the relative kinetic energy with respect to a point stationed on the body. The use of the mean axis conditions minimizes the coupling between the reference motion and the elastic deformation.

The FFRF is suitable for problems characterized by large reference motions, that is, rigid body translations and rotations, but small flexible deformations and strains, which is the case for a wide range of engineering problems. Large reference motions of deformable bodies are described with translations and rotations of the reference coordinate system, leading to a highly nonlinear description of inertial forces that exhibit strong coupling between the reference and elastic coordinates.

The deformation of the bodies can be described using conventional finite elements or modal reduction techniques [100, 197, 221]. In the modal reduction approach, body flexibility is defined with assumed forms of deformation obtained from an eigenvalue analysis of a finite element model. Large deformation problems can also be studied using this formulation. However, an incremental solution procedure needs to be implemented, making it computationally inefficient.

4.3.3 Inertial Frame Formulation

The inertial frame formulation is a standard nonlinear finite element formulation [222] in which elastic deformations are described using the nonlinear Green-Lagrange strain definition, which describes large rigid body rotations correctly. In this formulation, each body is discretized using a set of global interpolation functions. The degrees of freedom are the absolute positions and orientations of the coordinate frames located at the nodes of the finite element mesh. Constraints between bodies can be enforced by directly equating the appropriate degrees of freedom of the nodes that both bodies have in common at a particular interface point.

The GEBF is a commonly used example of an inertial frame formulation [223]. This formulation is suitable for multibody applications in which large deformations, i.e., large displacements and rotations and possibly large strains, need to be considered. When the theory is applied to practical applications, the element can be described in a total Lagrangian approach.

The beam element equations are directly derived from a three-dimensional nonlinear theory, with a complete account of finite rotations. These rotations can be parametrized with a rotational vector, an axis-angle representation of the rotation, which does not introduce any singularity in representing rotations of any magnitude and has a minimal set of parameters [224]. The finite elements based on GEBF are discretized using position and rotational nodal coordinates. This discretization leads to a constant description of the mass matrix for two-dimensional elements. However, in three-dimensional cases, discretization leads the mass matrix to no longer be constant, regardless of the choice of rotational coordinates.

The ANCF is a nonlinear finite element approach that is based on the use of global position and gradient coordinates. The formulation is designed for large deformation analysis of beam, plate, and shell elements in multibody applications [197]. The kinematics description of an element does not include the rotational degrees of freedom. Instead, position vector gradients, that is, partial derivatives of the position vector, are used to describe the cross-section orientations and deformations.

All nodal coordinates are described in an inertial frame allowing for the usage of the total Lagrangian approach, such as in the case of GEBF. Using this set of generalized coordinates leads to a singularity-free description in large rotation problems. This simplifies the description of the equations of motion. Additionally, general continuum mechanics material models can be implemented using this formulation. The ANCF does not involve tangent stiffness matrices and leads to a constant mass matrix, while the elastic forces are nonlinear functions of the element coordinates.

4.3.4 Beam Element Kinematics

Figure 4.10 presents a diagram of a two-noded fully-parameterized three-dimensional beam element based on the ANCF, as introduced by Shabana and Yakoub [225, 226]. A fully-parameterized element implies that the full deformation gradient is represented with the chosen nodal coordinates, i.e., the element employs all three position vector gradients at each node location, leading to a total of 24 degrees of freedom for the two-noded element.

In the ANCF, the global position vector $\mathbf{r}$ is defined in terms of local element coordinates as

$$\mathbf{r}(\mathbf{x}, t) = \mathbf{S}(\mathbf{x})\,\mathbf{e}(t), \tag{4.37}$$

where $\mathbf{x} = [x_1 \quad x_2 \quad x_3]^{\mathrm{T}}$ is the position vector in the local (straight) element frame,

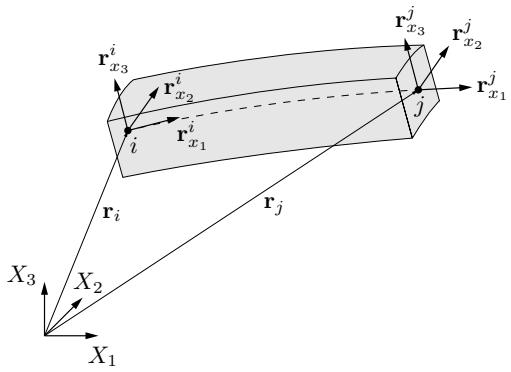

Figure 4.10: Two-noded fully parametrized beam element.

$\mathbf{r} = [r_1 \quad r_2 \quad r_3]^{\mathrm{T}}$ is the current position vector in the global frame, $\mathbf{S}$ is the global shape function matrix, and $\mathbf{e}$ is the vector of time-dependent nodal coordinates, or DOFs. The ANCF leads to isoparametric beam elements in both cases of gradient deficient and shear deformable elements. The global velocity of an arbitrary point of the beam can be written as

$$\dot{\mathbf{r}}(\mathbf{x}, t) = \mathbf{S}(\mathbf{x})\, \dot{\mathbf{e}}(t). \tag{4.38}$$

In the three-dimensional analysis of beams, plates, and shells, twelve coordinates are used for each finite element node for the case of fully parametric elements [225, 226]. The vector of nodal coordinates consists of three position DOFs and nine components of the position vector gradients. For a node j on an element, the twelve-dimensional vector of nodal coordinates is written as

$$\mathbf{e}^j = \left[\mathbf{r}^{j^{\mathrm{T}}} \quad \mathbf{r}^{j^{\mathrm{T}}}_{x_1} \quad \mathbf{r}^{j^{\mathrm{T}}}_{x_2} \quad \mathbf{r}^{j^{\mathrm{T}}}_{x_3}\right]^{\mathrm{T}}. \tag{4.39}$$

In this equation, the vector $\mathbf{r}^j$ defines the global position vector of node j and the vectors $\mathbf{r}^j_{x_1} = \frac{\partial \mathbf{r}}{\partial x_1}$, $\mathbf{r}^j_{x_2} = \frac{\partial \mathbf{r}}{\partial x_2}$, and $\mathbf{r}^j_{x_3} = \frac{\partial \mathbf{r}}{\partial x_3}$ define the position vector gradients of node j. A physical interpretation of the slope coordinates is depicted in fig. 4.11.

For the case of the two-noded fully parametrized beam element depicted in fig. 4.10 there are 24 nodal coordinates given by the vector

$$\mathbf{e} = \left[\mathbf{e}^{1^{\mathrm{T}}} \quad \mathbf{e}^{2^{\mathrm{T}}}\right]^{\mathrm{T}}. \tag{4.40}$$

The element shape function matrix $\mathbf{S}$ is defined as

$$\mathbf{S} = \left[S_1\mathbf{I} \quad S_2\mathbf{I} \quad S_3\mathbf{I} \quad S_4\mathbf{I} \quad S_5\mathbf{I} \quad S_6\mathbf{I} \quad S_7\mathbf{I} \quad S_8\mathbf{I}\right], \tag{4.41}$$

where $\mathbf{I}$ is a 3×3 identity matrix, and

$$S_1 = 1 - 3\xi^2 + 2\xi^3, \quad S_2 = l(\xi - 2\xi^2 + \xi^3), \quad S_3 = l(\eta - \xi\eta), \quad S_4 = l(\zeta - \xi\zeta),$$
$$S_5 = 3\xi^2 - 2\xi^3, \quad S_6 = l(-\xi^2 + \xi^3), \quad S_7 = l\xi\eta, \quad S_8 = l\xi\zeta,$$

where the non-dimensional quantities ξ, η, and ζ are defined as

$$\xi = \frac{x_1}{l}, \quad \eta = \frac{x_2}{l}, \quad \zeta = \frac{x_3}{l},$$

and l is the length of the beam element in the undeformed configuration. It can be demonstrated that the shape functions of equation eq. (4.41) can describe an arbitrary rigid body motion including large translation and finite rotations [100].

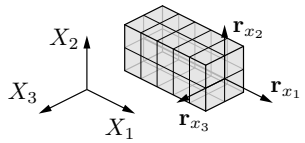

(a) $\mathbf{r}_{x_1} = [1\ 0\ 0]^{\mathrm{T}}$, $\mathbf{r}_{x_2} = [0\ 1\ 0]^{\mathrm{T}}$, $\mathbf{r}_{x_3} = [0\ 0\ 1]^{\mathrm{T}}$

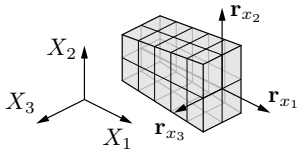

(b) $\mathbf{r}_{x_1} = [1\ 0\ 0]^{\mathrm{T}}$, $\mathbf{r}_{x_2} = [0\ 1.5\ 0]^{\mathrm{T}}$, $\mathbf{r}_{x_3} = [0\ 0\ 1]^{\mathrm{T}}$

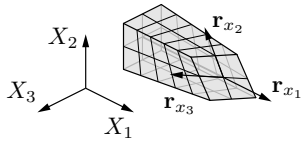

(c) $\mathbf{r}_{x_1} = [1\ 0\ 0]^{\mathrm{T}}$, $\mathbf{r}_{x_2} = [0\ 1\ 0.5]^{\mathrm{T}}$, $\mathbf{r}_{x_3} = [0\ 0.5\ 1]^{\mathrm{T}}$

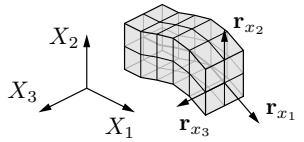

(d) $\mathbf{r}_{x_1} = [1\ -1\ 0]^{\mathrm{T}}$, $\mathbf{r}_{x_2} = [0\ 1\ 0]^{\mathrm{T}}$, $\mathbf{r}_{x_3} = [0\ 0\ 1]^{\mathrm{T}}$

Figure 4.11: Physical interpretation of the slope coordinates in the ANCF (adapted from [227]).

4.3.5 Formulation of the Elastic Forces

The strain tensor $\boldsymbol{\varepsilon}_m$ can be obtained by employing the Cauchy-Green formula [228] as follows

$$\boldsymbol{\varepsilon}_m = \frac{1}{2}(\mathbf{J}^{\mathrm{T}}\mathbf{J} - \mathbf{I}), \tag{4.42}$$

where the subscript m indicates the matrix form of the Lagrangian strains and $\mathbf{I}$ is a 3×3 identity matrix.

The deformation gradient $\mathbf{J}$ describes how a line element in the reference configuration maps into a line element in the current configuration. In the ANCF, the

deformation gradient can be defined via the matrix of position vector gradients as

$$\mathbf{J} = \frac{\partial \mathbf{r}}{\partial \mathbf{r}_0} = \frac{\partial \mathbf{r}}{\partial \mathbf{x}} \left(\frac{\partial \mathbf{r}_0}{\partial \mathbf{x}} \right)^{-1} = \mathbf{J}_e \mathbf{J}_0^{-1}, \tag{4.43}$$

where $\mathbf{J}_e$ is the matrix of position vector gradients in the current configuration computed with respect to the straight configuration and $\mathbf{J}_0$ is the matrix of position vector gradients in the reference configuration computed with respect to the straight configuration as shown in fig. 4.12. In case of a straight and undistorted reference configuration, $\mathbf{J}_0$ simplifies to the identity matrix $\mathbf{I}$.

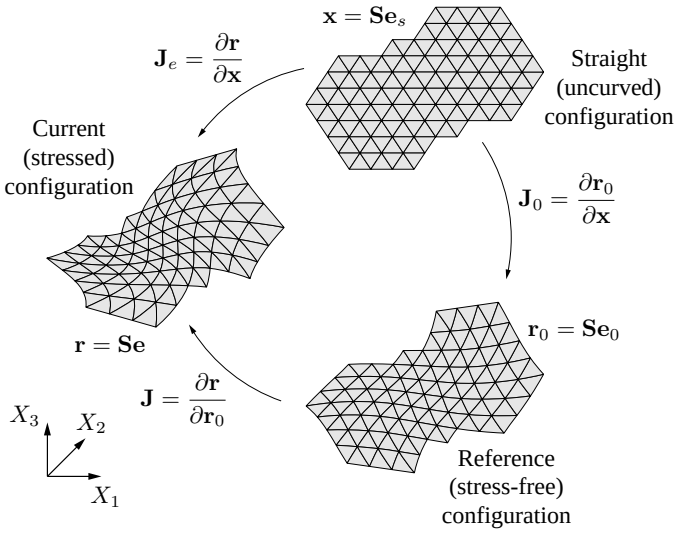

Figure 4.12: General configurations of a continuum body.

In the ANCF, the vector of global positions in the reference (stress-free) configuration $\mathbf{r}_0$ can simply be written as

$$\mathbf{r}_0(\mathbf{x}) = \mathbf{S}(\mathbf{x})\, \mathbf{e}_0, \tag{4.44}$$

where $\mathbf{e}_0$ is the vector of nodal coordinates in the same configuration. Note that this configuration is not required to be straight. Finally, the position vector in the straight (uncurved) configuration $\mathbf{x}$ can be expressed in terms of the vector of nodal coordinates in the same configuration $\mathbf{e}_s$ as

$$\mathbf{x} = \mathbf{S}(\mathbf{x})\, \mathbf{e}_s. \tag{4.45}$$

The strain tensor of eq. (4.42) can be expressed in terms of $\mathbf{J}_e$ and $\mathbf{J}_0$ as

$$\boldsymbol{\varepsilon}_m = \frac{1}{2}(\mathbf{J}_0^{-\mathrm{T}}\mathbf{J}_e^{\mathrm{T}}\mathbf{J}_e\mathbf{J}_0^{-1} - \mathbf{I}). \tag{4.46}$$

Using eqs. (4.37) and (4.44), the deformation gradient $\mathbf{J}$ in eq. (4.43) can be written in terms of the element shape functions and the vector of nodal coordinates as

$$\mathbf{J} = \frac{\partial \mathbf{S}}{\partial \mathbf{x}}\mathbf{e}\left(\frac{\partial \mathbf{S}}{\partial \mathbf{x}}\mathbf{e}_0\right)^{-1} = \begin{bmatrix} \mathbf{S}_{1,x_1}\mathbf{e} & \mathbf{S}_{1,x_2}\mathbf{e} & \mathbf{S}_{1,x_3}\mathbf{e} \\ \mathbf{S}_{2,x_1}\mathbf{e} & \mathbf{S}_{2,x_2}\mathbf{e} & \mathbf{S}_{2,x_3}\mathbf{e} \\ \mathbf{S}_{3,x_1}\mathbf{e} & \mathbf{S}_{3,x_2}\mathbf{e} & \mathbf{S}_{3,x_3}\mathbf{e} \end{bmatrix} \begin{bmatrix} \mathbf{S}_{1,x_1}\mathbf{e}_0 & \mathbf{S}_{1,x_2}\mathbf{e}_0 & \mathbf{S}_{1,x_3}\mathbf{e}_0 \\ \mathbf{S}_{2,x_1}\mathbf{e}_0 & \mathbf{S}_{2,x_2}\mathbf{e}_0 & \mathbf{S}_{2,x_3}\mathbf{e}_0 \\ \mathbf{S}_{3,x_1}\mathbf{e}_0 & \mathbf{S}_{3,x_2}\mathbf{e}_0 & \mathbf{S}_{3,x_3}\mathbf{e}_0 \end{bmatrix}^{-1}, \tag{4.47}$$

where $\mathbf{S}_{i,x_j} = \frac{\partial \mathbf{S}_i}{\partial x_j}$ and $\mathbf{S}_i$ is the i-th row of the shape function matrix. Note that because $\mathbf{J}_0$ does not change with time, the matrix inversion in the previous equation only needs to be computed once.

The strain tensor in eq. (4.46) can also be written in terms of the element shape functions and the vector of nodal coordinates, and cast into a strain vector form

$$\begin{aligned} \boldsymbol{\varepsilon} &= \begin{bmatrix} \varepsilon_{11} & \varepsilon_{22} & \varepsilon_{33} & \varepsilon_{12} & \varepsilon_{13} & \varepsilon_{23} \end{bmatrix}^{\mathrm{T}} \\ &= \frac{1}{2}\begin{bmatrix} (\mathbf{r}_{X_1}^{\mathrm{T}}\mathbf{r}_{X_1} - 1) & (\mathbf{r}_{X_2}^{\mathrm{T}}\mathbf{r}_{X_2} - 1) & (\mathbf{r}_{X_3}^{\mathrm{T}}\mathbf{r}_{X_3} - 1) & \mathbf{r}_{X_1}^{\mathrm{T}}\mathbf{r}_{X_2} & \mathbf{r}_{X_1}^{\mathrm{T}}\mathbf{r}_{X_3} & \mathbf{r}_{X_2}^{\mathrm{T}}\mathbf{r}_{X_3} \end{bmatrix}^{\mathrm{T}}. \end{aligned} \tag{4.48}$$

4.3.6 Equations of Motion

All existing finite element formulations for the large deformation and rotation analysis of beams, plates, and shells that include information about the nodal rotations lead to a nonlinear mass matrix in a three-dimensional analysis [226, 229]. In the ANCF, the mass matrix of the element can be simply obtained from the kinetic energy equation

$$T = \frac{1}{2}\int_{V_0} \rho \dot{\mathbf{r}}^{\mathrm{T}}\dot{\mathbf{r}}\, dV_0, \tag{4.49}$$

where ρ is the mass density of the element, V_0 is the volume of the reference (stress-free) configuration, and $\dot{\mathbf{r}}$ is the absolute velocity vector given by equation eq. (4.38). If element is initially curved, a relation between volumes in the uncurved reference and

initially curved configuration can be defined using the transformation

$$V_0 = |\mathbf{J}_0| \, V_e, \tag{4.50}$$

where V_e is the element volume in the straight (uncurved) configuration. Substituting eq. (4.38) into eq. (4.49) yields the following expression for the kinetic energy

$$T = \frac{1}{2}\dot{\mathbf{e}}^{\mathrm{T}}\mathbf{M}\dot{\mathbf{e}}, \tag{4.51}$$

where $\mathbf{M}$ is the mass matrix and is defined as

$$\mathbf{M} = \int_{V_0} \rho \mathbf{S}^T \mathbf{S} \, dV_0 = \int_{V_e} \rho \mathbf{S}^T \mathbf{S} \, |\mathbf{J}_0| \, dV_e. \tag{4.52}$$

The mass matrix is constant since it only depends on the density and dimensions of the element. While the models employed can account for the effects of rotary inertia and shear deformation, the mass matrix obtained using the ANCF remains constant [230]. As a result of having a constant mass matrix, the centrifugal and Coriolis inertia forces are equal to zero. Having a constant mass matrix also allows for the development of efficient algorithms for solving the nonlinear equations of motion of multibody systems [231–234].

Using a global coordinate system to define the nodal coordinates leads to a simple expression for the inertia forces and a nonlinear expression for the elastic forces. Two different methods can be used when the elastic forces are derived [100]. One method introduces a local element coordinate system that describes the element deformation. This method is a structural mechanics approach and allows for the use of classical beam and plate theories. By employing the local element coordinate system, the ANCF can be used in a straightforward manner to express the strain-displacement relations in terms of the absolute element coordinates.

Another method for evaluating the elastic forces is using a continuum mechanics approach that does not require a local element coordinate system [230]. By employing a continuum mechanics approach, all elastic nonlinearities must be considered in order to achieve zero strain under an arbitrary rigid body motion. The elastic forces of the element can be derived using the following expression for the strain energy

$$U = \frac{1}{2}\int_{V_0} \boldsymbol{\varepsilon}^{\mathrm{T}}\mathbf{E}\boldsymbol{\varepsilon} \, dV_0 = \frac{1}{2}\int_{V_e} \boldsymbol{\varepsilon}^{\mathrm{T}}\mathbf{E}\boldsymbol{\varepsilon} \, |\mathbf{J}_0| \, dV_e, \tag{4.53}$$

where $\mathbf{E}$ is the matrix of elastic coefficients, and $\boldsymbol{\varepsilon}$ is the vector form of the strain tensor ε_m.

The elastic forces of the element $\mathbf{Q}_k$ can be obtained by differentiating the strain energy once with respect to the vector of nodal coordinates $\mathbf{e}$, that is

$$\mathbf{Q}_k = \left(\frac{\partial U}{\partial \mathbf{e}} \right)^{\mathrm{T}}. \tag{4.54}$$

Finally, the equations of motion for the finite element can be written in a matrix form as follows [100]

$$\mathbf{M}\ddot{\mathbf{e}} + \mathbf{Q}_k = \mathbf{Q}_e, \tag{4.55}$$

where $\mathbf{Q}_e$ is the vector of the generalized external nodal forces. The preceding equation can be written in a simplified form as

$$\mathbf{M}\ddot{\mathbf{e}} = \mathbf{Q}, \tag{4.56}$$

where the force vector $\mathbf{Q}$ is defined as

$$\mathbf{Q} = \mathbf{Q}_e - \mathbf{Q}_k. \tag{4.57}$$

Since the mass matrix is constant, the equations of motion can be efficiently solved for the accelerations using the following equation

$$\ddot{\mathbf{e}} = \mathbf{M}^{-1}\mathbf{Q}. \tag{4.58}$$

4.3.7 Definition of the Beam Cross Section

In Euler-Bernoulli beam theory, the cross section of a beam is assumed to remain rigid and perpendicular to the centerline. Therefore, the cross-section normal can be defined by the tangent vector $\frac{\partial \mathbf{r}}{\partial x}$.

For a fully-parametrized ANCF beam, i.e., a beam with a complete set of position vector gradients, the beam cross section does not, in general, remain perpendicular to the centerline, as illustrated in fig. 4.11. Therefore, the cross section is not defined by the vector $\frac{\partial \mathbf{r}}{\partial x}$ tangent to the centerline.

Shabana and Yakoub [225] showed that an arbitrary vector drawn on the cross

section $\mathbf{r}_s$ can be expressed as a linear combination of the two vectors $\frac{\partial \mathbf{r}}{\partial y}$ and $\frac{\partial \mathbf{r}}{\partial z}$ as

$$\mathbf{r}_s = y\frac{\partial \mathbf{r}}{\partial y} + z\frac{\partial \mathbf{r}}{\partial z}. \tag{4.59}$$

Through an orthogonalization process, Shabana and Yakoub present the three vectors that form an orthogonal triad for the beam cross section

$$\mathbf{n}_s = \frac{\mathbf{r}_y}{\|\mathbf{r}_y\|}, \qquad \mathbf{b}_s = \frac{\mathbf{r}_z - h\mathbf{r}_y}{\|\mathbf{r}_z - h\mathbf{r}_y\|}, \qquad \mathbf{t}_s = \mathbf{n}_s \times \mathbf{b}_s, \tag{4.60}$$

where

$$h = \frac{\mathbf{r}_z^{\mathrm{T}}\mathbf{r}_y}{\|\mathbf{r}_y\|^2}.$$

The vectors $\mathbf{t}_s$, $\mathbf{n}_s$, and $\mathbf{b}_s$ constitute a right-handed orthonormal set, which completely defines the orientation of the beam cross-section. A rotation matrix representing the orientation of the beam cross-section can be constructed as

$$\mathbf{R}_B^W = \begin{bmatrix} \mathbf{n}_s & \mathbf{b}_s & \mathbf{t}_s \end{bmatrix}^{\mathrm{T}}, \tag{4.61}$$

where the subscript B refers to the beam cross-section frame, and the superscript W to the fixed world frame, and so this rotation matrix describes the rotation from the beam cross-section frame to the fixed world frame.

4.3.8 Solution of the Multibody Equations

The Newmark method provides a solution for the structural dynamics equations of motion, which has the following standard form

$$\mathbf{M}\ddot{\mathbf{q}} + \mathbf{C}\dot{\mathbf{q}} + \mathbf{K}\mathbf{q} = \mathbf{F}(t), \tag{4.62}$$

where $\mathbf{q}$, $\dot{\mathbf{q}}$, and $\ddot{\mathbf{q}}$ are the vectors of generalized position coordinates, velocities and accelerations, respectively, $\mathbf{M}$, $\mathbf{C}$, and $\mathbf{K}$ are the symmetric mass, damping and stiffness matrices, respectively, and $\mathbf{F}(t)$ is the external force vector.

The Newmark method introduces two equations that relate the position and the velocity vectors to the acceleration vector based on a Taylor series expansion. The position vector $\mathbf{q}_{n+1}$ and velocity vector $\dot{\mathbf{q}}_{n+1}$ at time t_{n+1} can be written using a

Taylor series expansion as

$$\mathbf{q}_{n+1} = \mathbf{q}_n + h\dot{\mathbf{q}}_n + \frac{h^2}{2}\ddot{\mathbf{q}}_n + \beta h^3 \dddot{\mathbf{q}}_m, \tag{4.63}$$

$$\dot{\mathbf{q}}_{n+1} = \dot{\mathbf{q}}_n + h\ddot{\mathbf{q}}_n + \gamma h^2 \dddot{\mathbf{q}}_m, \tag{4.64}$$

where $h = t_{n+1} - t_n$ is the time step, m is a state somewhere between states n and $n+1$, β and γ are two assumed parameters that control the stability of the method, and the term $\dddot{\mathbf{q}}_m$ is approximated as

$$\dddot{\mathbf{q}}_m = \frac{\ddot{\mathbf{q}}_{n+1} - \ddot{\mathbf{q}}_n}{h}. \tag{4.65}$$

Substituting eq. (4.65) into eqs. (4.63) and (4.64) leads to the Newmark equations

$$\mathbf{q}_{n+1} = \mathbf{q}_n + h\dot{\mathbf{q}}_n + \frac{h^2}{2}\left[(1-2\beta)\ddot{\mathbf{q}}_n + 2\beta\ddot{\mathbf{q}}_{n+1}\right], \tag{4.66}$$

$$\dot{\mathbf{q}}_{n+1} = \dot{\mathbf{q}}_n + h\left[(1-\gamma)\ddot{\mathbf{q}}_n + \gamma\ddot{\mathbf{q}}_{n+1}\right]. \tag{4.67}$$

The previous equations can be used in eq. (4.62) to determine the vector of accelerations $\ddot{\mathbf{q}}_{n+1}$ as

$$\ddot{\mathbf{q}}_{n+1} = \mathbf{M}^{-1}\left[\mathbf{F}(t_{n+1}) - \mathbf{C}\dot{\mathbf{q}}_{n+1} - \mathbf{K}\mathbf{q}_{n+1}\right] \tag{4.68}$$

The stability of the solution depends on the choice of values for the two parameters γ and β. These parameters should satisfy the following relations in order to have a stable solution

$$\gamma \geq \frac{1}{2}, \qquad \beta \geq \frac{\left(\gamma + \frac{1}{2}\right)^2}{4}. \tag{4.69}$$

The main drawback of the Newmark method is that it is not capable of eliminating spurious high frequencies while being stable and second-order convergence at the same time [233].

The Hilber-Hughes-Taylor (HHT) method is an improvement over the Newmark method and has the ability to eliminate undesirable high frequency oscillations, while remaining stable and second-order convergent [235]. This method is obtained by replacing eq. (4.68) with

$$\ddot{\mathbf{q}}_{n+1} = \mathbf{M}^{-1}\left[\mathbf{F}(\tau_{n+1}) - (1+\alpha)\mathbf{C}\dot{\mathbf{q}}_{n+1} + \alpha\mathbf{C}\dot{\mathbf{q}}_n - (1+\alpha)\mathbf{K}\mathbf{q}_{n+1} + \alpha\mathbf{K}\mathbf{q}_n\right], \tag{4.70}$$

where α is an assumed parameter that controls the amount of numerical damping in the system and $\tau_{n+1} = t_n + (1+\alpha)h$.

The stability of the solution depends on the choice of values for the parameters α, γ, and β. In order to obtain a stable solution these parameters should satisfy the following relations

$$-0.3 \leq \alpha \leq 0, \qquad \gamma = \frac{1}{2} - \alpha, \qquad \beta = \frac{(1-\alpha)^2}{4}. \tag{4.71}$$

The smaller the value of α, the more numerical damping is added to the system.

When dealing with a multibody system subject to kinematic constraints, the resulting equations of motion can be written in the following form [100]

$$\mathbf{M}\ddot{\mathbf{q}} + \mathbf{C}_\mathbf{q}^\mathrm{T}\boldsymbol{\lambda} = \mathbf{Q}, \tag{4.72}$$

$$\mathbf{C}(\mathbf{q}, t) = \mathbf{0}, \tag{4.73}$$

where $\mathbf{M}$ is the system mass matrix, $\mathbf{q}$ is the vector of generalized coordinates, $\mathbf{C}$ is the vector of generalized constraints, $\boldsymbol{\lambda}$ is the vector of Lagrange multipliers, $\mathbf{Q}$ is the vector of all generalized forces, including external $\mathbf{Q}_e$ and elastic $\mathbf{Q}_k$ forces, and $\mathbf{C}_\mathbf{q}$ is the Jacobian matrix of the constraint equations.

Negrut et al. [236] investigated an HHT-based algorithm for Index 3 DAEs of multibody systems, such as the system of eqs. (4.72) and (4.73). In their work, they proposed the implicit HHT-I3 method that uses the HHT method with eqs. (4.72) and (4.73). The nonlinear algebraic equations are solved simultaneously with the nonlinear constraint equations at the position level to determine the state of the system.

Applying eq. (4.70) to eq. (4.72) at time step t_{n+1} we obtain

$$(\mathbf{M}\ddot{\mathbf{q}})_{n+1} = \mathbf{H}(\tau_{n+1}), \tag{4.74}$$

where $\mathbf{H} = \mathbf{Q} - \mathbf{C}_\mathbf{q}^\mathrm{T}\boldsymbol{\lambda}$ represents the generalized forces including the constraint forces.

A Taylor series expansion is used to write

$$\mathbf{H}(\tau_{n+1}) = \mathbf{H}(t_n) + (1+\alpha)h\dot{\mathbf{H}}(t_m), \tag{4.75}$$

where t_m is a time between t_n and τ_{n+1}, and $\dot{\mathbf{H}}(t_m)$ can be approximated as

$$\dot{\mathbf{H}}(t_m) = \frac{\mathbf{H}(t_{n+1}) - \mathbf{H}(t_n)}{h}. \tag{4.76}$$

The previous equation can be used in eq. (4.75) and the result substituted into eq. (4.74) to yield

$$(\mathbf{M}\ddot{\mathbf{q}})_{n+1} = (1+\alpha)\mathbf{H}(t_{n+1}) - \alpha\mathbf{H}(t_n). \tag{4.77}$$

Since $\mathbf{H} = \mathbf{Q} - \mathbf{C}_\mathbf{q}^\mathrm{T}\boldsymbol{\lambda}$, the previous equation can be written as

$$(\mathbf{M}\ddot{\mathbf{q}})_{n+1} + (1+\alpha)\left(\mathbf{C}_\mathbf{q}^\mathrm{T}\boldsymbol{\lambda} - \mathbf{Q}\right)_{n+1} - \alpha\left(\mathbf{C}_\mathbf{q}^\mathrm{T}\boldsymbol{\lambda} - \mathbf{Q}\right)_n = \mathbf{0}. \tag{4.78}$$

The constraints are satisfied at t_{n+1}, therefore eq. (4.73) can be used to write

$$\mathbf{C}(\mathbf{q}_{n+1}, t_{n+1}) = \mathbf{0}. \tag{4.79}$$

Equations (4.63) and (4.64) can be used to write the previous two equations as functions of $\ddot{\mathbf{q}}_{n+1}$ and $\boldsymbol{\lambda}_{n+1}$ only. The result is a set of nonlinear algebraic equations that can be solved for $\ddot{\mathbf{q}}_{n+1}$ and $\boldsymbol{\lambda}_{n+1}$ using an iterative Newton–Raphson method. The iterative method requires constructing and solving the following system of equations at iteration k

$$\begin{bmatrix} \dfrac{\partial \mathbf{F}_1}{\partial \ddot{\mathbf{q}}_{n+1}} & \dfrac{\partial \mathbf{F}_1}{\partial \boldsymbol{\lambda}_{n+1}} \\ \dfrac{\partial \mathbf{F}_2}{\partial \ddot{\mathbf{q}}_{n+1}} & \dfrac{\partial \mathbf{F}_2}{\partial \boldsymbol{\lambda}_{n+1}} \end{bmatrix}^{(k)} \begin{bmatrix} \Delta\ddot{\mathbf{q}}_{n+1} \\ \Delta\boldsymbol{\lambda}_{n+1} \end{bmatrix}^{(k)} = -\begin{bmatrix} \mathbf{F}_1 \\ \mathbf{F}_2 \end{bmatrix}^{(k)}, \tag{4.80}$$

where Δ indicates Newton differences, and $\mathbf{F}_1$ and $\mathbf{F}_2$ are defined as

$$\mathbf{F}_1 = \frac{1}{1+\alpha}(\mathbf{M}\ddot{\mathbf{q}})_{n+1} + \left(\mathbf{C}_\mathbf{q}^\mathrm{T}\boldsymbol{\lambda} - \mathbf{Q}\right)_{n+1} - \frac{\alpha}{1+\alpha}\left(\mathbf{C}_\mathbf{q}^\mathrm{T}\boldsymbol{\lambda} - \mathbf{Q}\right)_n, \tag{4.81}$$

$$\mathbf{F}_2 = \frac{1}{\beta h^2}\mathbf{C}(\mathbf{q}_{n+1}, t_{n+1}). \tag{4.82}$$

4.4 Fluid-Structure Interaction

FSI problems are concerned with modeling the interaction between fluid and solid domains within a given computational problem. Different methods exist to handle the coupling of the two disciplines depending on the complexity of the problem at

hand. This section outlines the different coupling strategies considered and describes the RBF interpolation method used to transfer information between the fluid and structural domains.

4.4.1 Coupling Strategies

Fluid and structural domains can be coupled in a monolithic manner, where the two disciplines are solved simultaneously. In this case, a multi-physics solver handles a single system of equations describing fluid, solid, and their coupling. Figure 4.13a depicts this strategy schematically. Such monolithic solvers must be explicitly designed for the problem at hand. Simultaneously treating both flow and structural equations within the same system of equations often results in good numerical stability of the calculations [198].

Furthermore, monolithic approaches solve the system of equations exactly, meaning that this approach introduces no errors in the coupling process other than those inherent to numerical techniques. However, these solvers must be developed on a problem-by-problem basis. In general, the development of such solvers from scratch requires substantial work and is often cumbersome [199, 200].

In contrast, partitioned approaches make use of existing single-physics solvers to handle each discipline separately. The FSI problem is split into a fluid and structural problem, which are treated independently by their respective solvers. At the same time, a third component, the coupling component, handles the interaction aspects. It addresses the transfer of kinetic information—forces, or stresses—calculated by the fluid solver at the wet surface to the solid component and the exchange of kinematic information—displacements, or velocities—computed by the structural solver at the interface to the fluid solver in return. A schematic of this process is shown in fig. 4.13b.

An advantage of partitioned approaches is that existing well-established solvers for both fluid and solid problems can be used. These solvers can range from commercial to academic and open-source codes. Compared to a monolithic approach, the programming efforts are lower for partitioned methods since only the coupling of the existing solvers has to be implemented rather than the solvers themselves. Nevertheless, these advanced solvers can only be of good use for FSI simulations if the coupling procedure is sufficiently precise [199, 200].

Partitioned strategies for solving FSI problems can be subclassed according to their strength of preserving the overall system stability. Weak or explicit schemes

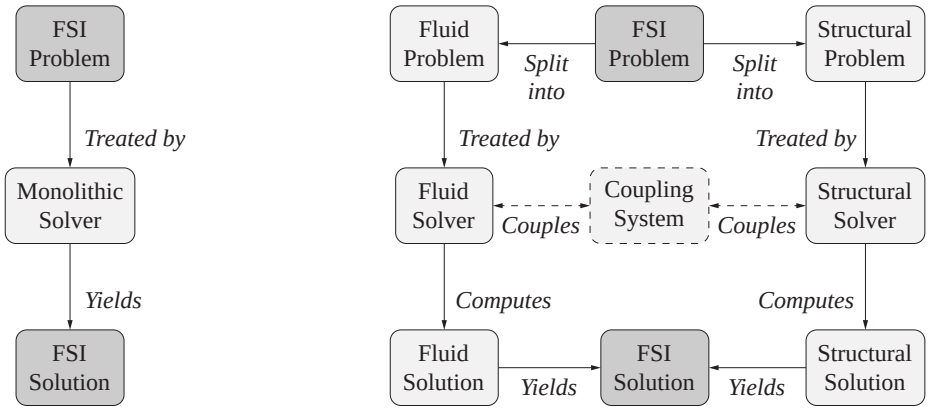

(a) Monolithic strategy (b) Partitioned strategy

Figure 4.13: Monolithic (left) and partitioned (right) coupling strategies used in fluid-structure interaction.

transfer information between solvers a fixed number of times, often once per time step. In general, this is insufficient to regain the monolithic, or exact, solution of the FSI problem as the coupling conditions are not enforced within each time step. Thus, no balance between fluid and structural domains with respect to energy, forces, and displacements at the interface can be guaranteed [199]. Generally, the more loosely coupled a system is, the less stable the overall method becomes. However, this coupling strategy can still yield good results if the interaction between fluid and solid is relatively weak. For instance, in aeroelastic simulations, where small displacements of the structure appear within single time steps, the flow field is influenced by the structural displacements only to a small extent [199, 237].

On the other hand, strong or implicit schemes require subiterations, possibly resulting in multiple invocations of both fluid and structural solvers and data exchanges between them per time step. Acceleration techniques are necessary to guarantee convergence of the underlying system of equations. The interface coupling conditions are enforced each time step up to some convergence criteria. If convergence is not achieved, another subiteration within the same time step is computed. Therefore, the solution can approximate the monolithic solution to an arbitrary accuracy depending on the chosen convergence criteria. Such a method is generally applied to FSI problems for which explicit procedures fail due to the dominant interaction of the two domains.

Even though there is a significant variety of weak and strong schemes for coupling time-dependent partitioned solvers, the basic schemes come down to a few. Note that time-dependent systems can be solved internally using an implicit time-stepping

method but be coupled with other systems by an explicit coupling scheme, or vice-versa.

In a basic weak coupling scheme with a staggered solution procedure, the solution process starts at time t_n with solver B sending its initial interface values to solver A. Solver A computes its next time step t_{n+1} and sends the obtained interface values b_{n+1} to solver B, which in turn advances to the next time step [238]. This process is illustrated in fig. 4.14a. As noted in [198, 239], this scheme has the disadvantage that it is only frst-order time-accurate, even when the underlying fluid and structural solvers are second-order time-accurate.

If accuracy or numerical stability require it, predictor–corrector iterations can be added within each cycle of a staggered scheme, in which case the overall partitioned procedure becomes a strongly coupled solution algorithm [240]. In a weak coupling scheme with a staggered solution procedure and predictor–corrector iterations (fig. 4.14b), the process begins with solver B, which computes a prediction a^p_{n+1} for the values of the next time step and sends them to solver A. Solver A computes its next time step t_{n+1} and sends the obtained solution values b_{n+1} to solver B, which in turn computes its next time step [241, 242].

Figure 4.14c illustrates a strong coupling scheme with interface iterations. In this scheme, the solution process starts with solver A (but could equally start with solver B) at time t_n. Solver A computes a first prediction b^1_{n+1} for solver B's interface values of the next time step and sends it to solver B. Solver B uses the obtained prediction to compute itself a prediction a^1_{n+1} for solver A's interface values and returns it to solver A. This procedure continues with both solvers always using the most current interface values until convergence of the values is achieved. Then, solvers A and B can advance simultaneously to time step t_{n+1} [243].

Given a set of interface values from a previous time step, a solver can compute solutions from non-coupled time steps before transferring new interface values to another solver. This technique is called subcycling and can be combined with any of the previously discussed coupling schemes [240]. For example, the basic weak coupling scheme with a staggered solution procedure can be enhanced with subcycling resulting in the scheme shown in fig. 4.14b. The solution follows the same process as described earlier, with the only difference being in solver B. When advancing to the next time step, this solver computes non-coupled time steps (indicated by gray-filled circles), using the interface values obtained by A at time t_n until it reaches time t_{n+1}. Only then a new interface iteration starts.

With the goal of minimizing the complexity of the coupling process, the weak

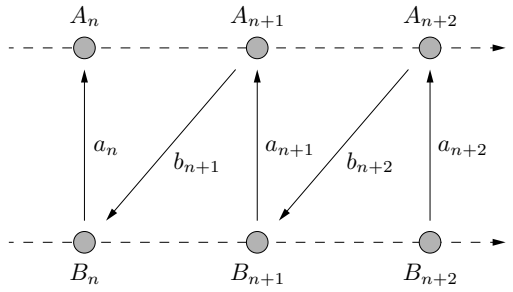

(a) Weak coupling scheme with staggered solution procedure.

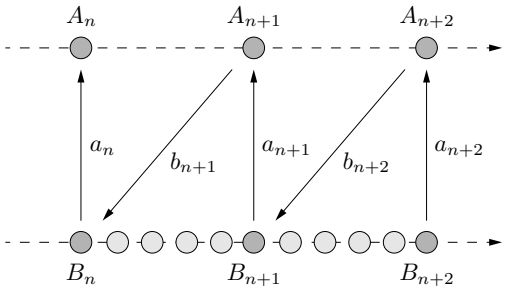

(b) Weak coupling scheme with subcycling.

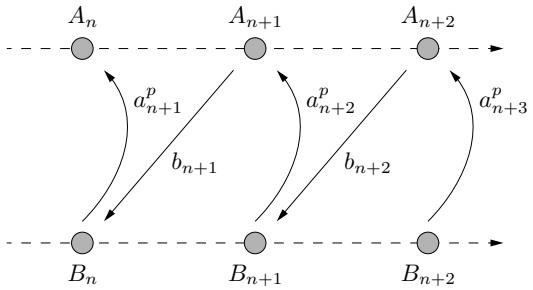

(c) Weak coupling scheme with staggered solution procedure and predictor–corrector iterations.

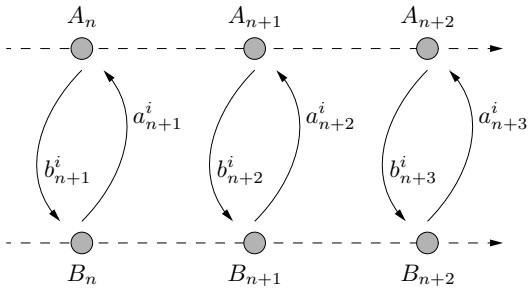

(d) Strong coupling scheme with interface subiterations.

Figure 4.14: Different partitioned coupling schemes used in fluid-structure interaction.

coupling scheme with subcycling of fig. 4.14b was implemented in this framework. In aeroelastic applications, this scheme has been shown to yield good results despite being a weak scheme [199, 237]. This is because structural displacements are small within a single time step, causing the structural displacements to influence the flow field only to a small extent. Subcycling was implemented in the aerodynamics solver where smaller time steps were used. For the structural dynamics solver, larger time steps were employed. Transfer of information occurred at the end of each structural time step.

4.4.2 Radial Basis Function Interpolation

RBFs are a mathematical tool to allow interpolation and extrapolation of scalar values everywhere in space. The resulting field is retrieved on a distance basis, and its calculation entails the solution of a linear system of order equal to the number of source points [201]. A single solution can be performed for a set of source points, once, to compute the coefficients of the linear system that can be used later to directly retrieve

interpolated or extrapolated values elsewhere in the target space as the summation of their radial contribution. The interpolation function S can be approximated by a sum of basis functions

$$S(Q) = \sum_{i=1}^{N} w_i \Psi(P_i, Q), \tag{4.83}$$

where w_i are unknown coefficients, $P_i = (x_P, y_P, z_P)_i$ are the points at which the scalar values are known (source points), $Q = (x_Q, y_Q, z_Q)$ the point where the value is to be determined (target point), N the number of source points, and Ψ a given radial basis function.

For any target point Q, the interpolant $S(Q)$ depends on the radial contribution of each source point P_i, function of the Euclidean norm between source and target points $\|Q - P_i\|$. This is illustrated in fig. 4.15.

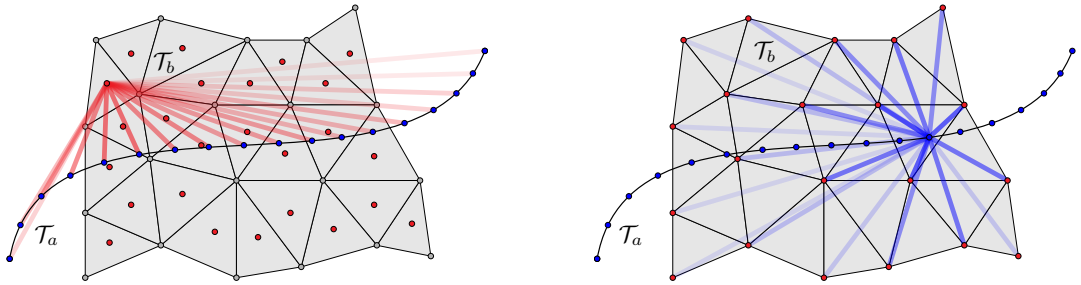

(a) Fluid to structure (b) Structure to fluid

Figure 4.15: Illustration of information transfer from fluid mesh to structural mesh (left), and information transfer from structural mesh to fluid mesh (right). Structural nodes are represented in blue. Fluid nodes and element center points are represented in red.

The symmetric distance matrix $\mathbf{M}$ in which all the mutual distances are computed is defined as

$$\mathbf{M}_{ij} = \Psi(P_j, P_i). \tag{4.84}$$

To guarantee solvability for the w_i coefficients, $\mathbf{M}$ should be positive definite, which depends on the positive-definiteness of the radial basis function Ψ. Equation (4.83) can be optionally enriched with a linear polynomial term H^1 to impart the positive definite property to the radial basis function [118]. This polynomial can be written as

$$H^1(Q) = \beta_1 + \beta_2 x_Q + \beta_3 y_Q + \beta_4 z_Q, \tag{4.85}$$

and so eq. (4.83) can be expanded to yield

$$S(Q) = \sum_{i=1}^{N} w_i \Psi(P_i, Q) + H^1(Q) = \sum_{i=1}^{N} w_i \Psi(P_i, Q) + \beta_1 + \beta_2 x_Q + \beta_3 y_Q + \beta_4 z_Q, \quad (4.86)$$

which forms a system of linear equations with w_i and β_j $(j = 1, \ldots, 4)$ as unknowns.

The coefficients w_i and the polynomial terms β_j are determined by enforcing that the RBF gives the exact prescribed value g_i at each source point P_i, and that polynomial term satisfies the orthogonality conditions

$$S(P_i) = \mathbf{g}_i, \quad (4.87)$$

with $\mathbf{g}_i$ containing the discrete known values in the source space, and the additional requirements

$$\sum_{i=1}^{N} w_i H^m(P_i) = 0, \quad (4.88)$$

for all polynomials H^m with a degree m less than or equal to that of polynomial H^1 [244].

As a result of the interpolation, the RBF coefficients w_i and polynomial terms β_j are obtained. Depending on the chosen RBF kernel, the order of H varies. As shown in [245], if the RBF is conditionally positive definite, a unique interpolant exists. The values of coefficients w_i and β_j can be obtained by solving the system

$$\begin{bmatrix} \mathbf{M}_{P,P} & \mathbf{H}_P \\ \mathbf{H}_P^{\mathrm{T}} & \mathbf{0} \end{bmatrix} \begin{bmatrix} \mathbf{w} \\ \boldsymbol{\beta} \end{bmatrix} = \begin{bmatrix} \mathbf{g} \\ \mathbf{0} \end{bmatrix}, \quad (4.89)$$

where $\mathbf{M}$ is the distance matrix of eq. (4.84) and $\mathbf{H}$ is the matrix required by the polynomial interpolation in the form

$$\mathbf{H} = \begin{bmatrix} 1 & x_{P_1} & y_{P_1} & z_{P_1} \\ 1 & x_{P_2} & y_{P_2} & z_{P_2} \\ \vdots & \vdots & \vdots & \vdots \\ 1 & x_{P_N} & y_{P_N} & z_{P_N} \end{bmatrix}. \quad (4.90)$$

The behavior of the interpolation between source and target points is dependent on the type of basis function used. RBFs can be categorized based on the sphere of

influence of each source point. Globally supported functions influence the interpolation everywhere, including at large distances, and their influence is based on the Euclidean norm. Compactly supported functions, such as Wendland's functions, only influence the interpolation within a given support radius. Using compactly supported functions results in a sparse matrix $\mathbf{M}_{P,P}$, which is helpful in its inversion through the use of sparse linear solvers [118].

The RBF interpolation presented above can only be applied to scalar values. In order to interpolate vector fields, a system can be formed to calculate for each point the components of the field. As an example, for mesh morphing in three-dimensional problems, a system can be employed to calculate the displacement field $\mathbf{u} = (u, v, w)$ as

$$\begin{aligned} u(Q) &= \sum_{i=1}^{N} w_i^x \Psi(P_i, Q) + \beta_1^x + \beta_2^x x_Q + \beta_3^x y_Q + \beta_4^x z_Q \\ v(Q) &= \sum_{i=1}^{N} w_i^y \Psi(P_i, Q) + \beta_1^y + \beta_2^y x_Q + \beta_3^y y_Q + \beta_4^y z_Q \\ w(Q) &= \sum_{i=1}^{N} w_i^z \Psi(P_i, Q) + \beta_1^z + \beta_2^z x_Q + \beta_3^z y_Q + \beta_4^z z_Q. \end{aligned} \tag{4.91}$$

4.5 Framework Overview

This work aimed at developing an extensible, scalable, and composable program for the simulation of time-depended aeroelastic problems. Due to the expected high computational cost associated with a time-dependent numerical analysis, C++ was chosen as the language of choice due to its solid reputation for being a performant language with minimal runtime while being multi-paradigm, designed to fit many use cases, and allowing for high levels of abstraction [246].

The framework was developed using features of the modern standards of the language, including C++17 and C++20 [247]. It takes advantage of the object-oriented nature of C++ to enable modularity and encapsulation of code, creating a clear separation of concerns and ensuring that changes to the inner functionality of parts of the code do not affect the functionality of other parts. Objects can also be reused in different parts of the code, reducing code duplication and allowing for better scalability where the program can be expanded as needed by adding new objects or extending existing ones. An object-oriented design also allows for better abstraction, where

complexity can be reduced by hiding implementation details within class definitions [248].

The framework is split into different modules, each responsible for a particular aspect of the simulation process. An overview of the flow of information during a coupled aeroelastic simulation is shown in fig. 4.16.

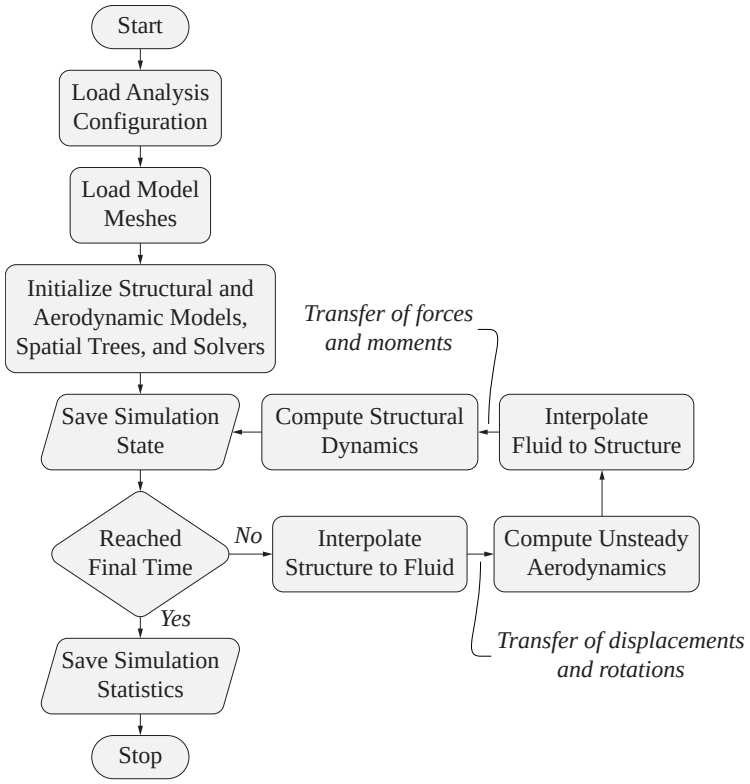

Figure 4.16: Flow of information during a weakly-coupled aeroelastic simulation.

The framework allows for meshes to be loaded from external files. A configuration file is used to define simulation parameters, such as simulation time, solver and integrator types, number of iterations, coupling schemes, and other parameters.

4.5.1 Mesh Representations

An important aspect of the developed framework is its ability to represent unstructured surface meshes. There are different ways of representing surface meshes in a computer program. Simple structured meshes can sometimes be represented with a list of vertices. In such cases, connectivity information can be retrieved implicitly and does not require explicit storage. Such meshes are referred to as vertex-vertex (VV) meshes as they represent an object as a set of vertices connected to other vertices (fig. 4.17a).

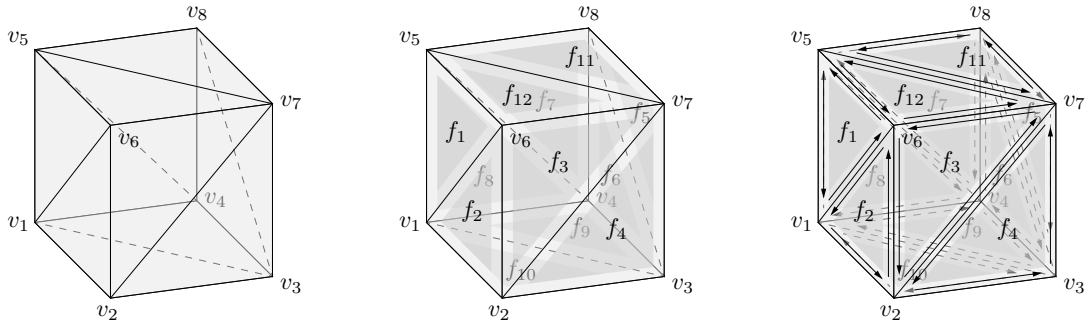

(a) VV mesh (b) FV mesh (c) DCEL mesh

Figure 4.17: Example of VV, FV, and DCEL mesh representations, showing the different entities stored as part of the mesh implementation.

This is the simplest kind of representation, but not widely used since face, and edge information is implicit. In order to generate a list of faces for processing, it is necessary to process vertex data, which can be slow for large meshes. In addition, operations on edges and faces are not easily accomplished. However, VV meshes benefit from small storage space. An example of a data structure used to represent a vertex in a VV mesh is given in listing 4.1.

Listing 4.1 Example vertex data structure used in a VV mesh representation.

```
1 template<typename V>
2 struct vertex {
3   V value; // Vertex value (e.g., position or displacement)
4 };
```

For unstructured meshes, however, a list of vertices is sometimes not sufficient since the vertex order alone in a vertex list cannot implicitly determine vertex connectivity. Traversing the faces of an unstructured mesh stored as a list of vertices requires substantial processing and is unfeasible for large meshes.

Unstructured meshes benefit greatly from storing not only a list of vertices but also connectivity information. The type of connectivity information stored gives rise to different data structures that can be implemented. Two common mesh data structures that store some level of connectivity information are the face-vertex (FV) mesh and the doubly-connected edge list (DCEL). The latter is also known as a half-edge data structure. Each has its own advantages and disadvantages.

The FV mesh data structure is simple and intuitive to implement. It typically consists of an ordered array of vertices and a list of faces (fig. 4.17b). Each face is

a list of pointers to, or indices of, the vertices that form its boundary. In this data structure, edges are implicitly given from the sequence of vertices around the face. Examples of data structures used to represent vertices and faces in a FV mesh are given in listing 4.2.

Listing 4.2 Example vertex and face data structures used in a FV mesh representation.

```
1  template<typename V>
2  struct vertex {
3    V value; // Vertex value (e.g., position or displacement)
4  };
5
6  template<typename V, typename F>
7  struct face {
8    std::array<vertex<V>*, 3> vertices; // Pointers to vertices
         surrounding this face
9    F value; // Face value (e.g., unit normal or aerodynamic
         pressure)
10 };
```

One of the advantages of this data structure is how easy it is to populate. In addition, it makes no assumptions about the structure of the data. In some cases, this is desirable and can support arbitrary arrangements of polygons. However, it encodes very little information about the structure of the mesh, which makes traversals and mesh modifications slow. For static meshes that do not require connectivity to be processed, the FV mesh is an excellent structure.

The DCEL, or half-edge, mesh data structure encodes more information than the FV mesh. Unlike the FV mesh, a DCEL makes a strong assumption about the mesh—the mesh must be manifold. For a mesh to be manifold, two conditions must hold. First, the adjacent faces around a vertex must be given in an order such that their vertices, other than the common vertex, form a chain. Second, each edge must be shared by no more than two faces. While these conditions may seem restrictive, they are a necessary, although not sufficient, condition for a mesh to represent the boundary of a volume.

A DCEL consists of a list of half-edges, vertices, edges, and faces (fig. 4.17c). Each vertex stores its position and one outgoing half-edge. Each half-edge stores the origin vertex and the destination vertex. In addition, the half-edge stores pointers, or indices, to its previous, next, and opposite half-edges. The opposite is the half-edge

along the same edge but pointing in the opposite direction. The next half-edge is the half-edge following the current half-edge around the adjacent face. The previous half-edge is the half-edge preceding the current half-edge around the adjacent face. A pointer, or index, to the associated edge is also stored. Faces can also be stored in the half-edge data structure but are optional, as they can be inferred by following half-edges around a face. If they are to be stored, a face has a pointer, or index, to an arbitrary half-edge on its boundary, and each half-edge has a pointer, or index, to its adjacent face. Because the half-edges around a face form an order, the orientation of a face can be inferred. The nature of the DCEL data structure is such that traversing the mesh is the same as traversing a graph data structure of its edges. Examples of data structures used to represent half-edges, vertices, edges, and faces in a DCEL mesh are given in listing 4.3.

Listing 4.3 Example half-edge, vertex, edge, and face data structures used in a DCEL mesh representation.

```
1  template<typename V, typename E, typename F>
2  struct halfedge {
3    halfedge* next; // Pointer to the next half-edge in the chain of
         half-edges
4    halfedge* previous; // Pointer to the previous half-edge in the
       chain of half-edges
5    halfedge* opposite; // Pointer to the opposite half-edge
6    vertex<V, E, F>* vertex; // Pointer to the origin vertex
7    edge<V, E, F>* edge; // Pointer to the edge this half-edge
       represents
8    face<V, E, F>* face; // Pointer to the face enclosed by the
       chain of half-edges
9  };
10
11 template<typename V, typename E, typename F>
12 struct vertex {
13   halfedge<V, E, F>* halfedge; // Pointer to the half-edge
       originating from this vertex
14   V value; // Vertex value (e.g., position or displacement)
15 };
16
17 template<typename V, typename E, typename F>
18 struct edge {
19   halfedge<V, E, F>* halfedge; // Pointer to the half-edge
       associated with this half-edge
```

```
20   E value; // Edge value (e.g., trailing edge marker)
21 };
22
23 template<typename V, typename E, typename F>
24 struct face {
25   halfedge<V, E, F>* halfedge; // Pointer to one half-edge
         surrounding this face
26   F value; // Face value (e.g., unit normal or aerodynamic
         pressure)
27 };
```

4.5.2 Spatial Domain Decomposition

Spatial domain partitioning was implemented as part of the framework in the form of octree and point cloud data structures. This was important in order to implement the FMM-based panel method. An octree is a tree data structure where each internal node has eight children. Non-empty leaf nodes of an octree contain one or more points that fall within the same spatial subdivision. Octrees are a useful description of three-dimensional space and can be used to quickly find nearby points.

Octrees are commonly used for spatial partitioning of three-dimensional data points in space, also known as a point cloud. The points may represent a three-dimensional shape or object. Point clouds were used to represent the set of mesh cell centroids in space.

Examples of domain partitioning using an octree are shown in fig. 4.18, for a unit sphere and in fig. 4.19 for the QT1 aircraft.

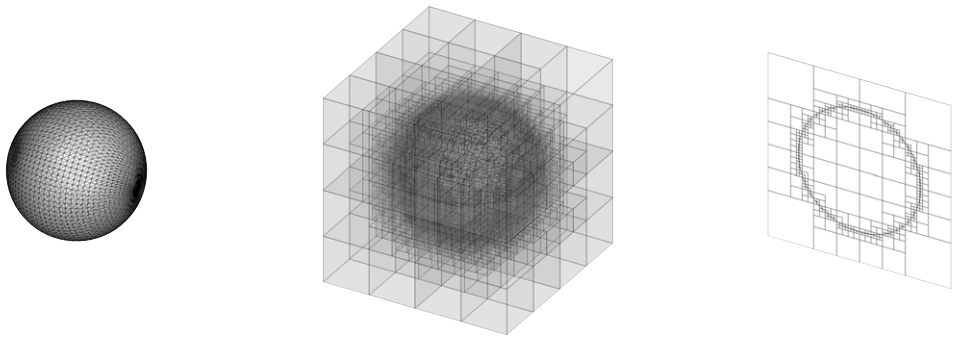

(a) Unstructured mesh (b) Spatial partitioning (c) Slice of partitioning

Figure 4.18: Representation of a unit sphere using an unstructured mesh (left), its spatial partitioning using an octree (center), and a slice of this partitioning (right).

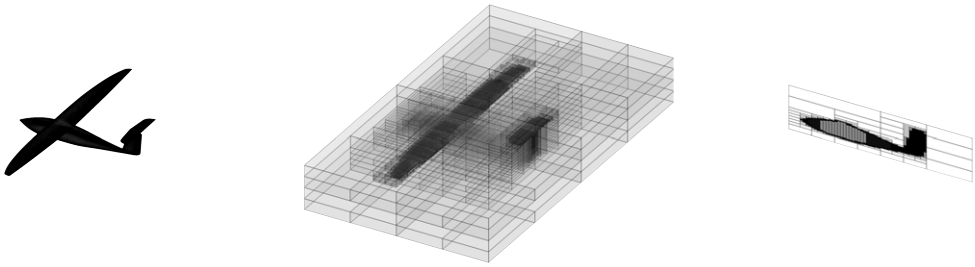

(a) Unstructured mesh (b) Spatial partitioning (c) Slice of partitioning

Figure 4.19: Representation of the QT1 geometry using an unstructured mesh (left), its spatial partitioning using an octree (center), and a slice of this partitioning (right).

4.6 Results and Discussion

This section describes the results obtained in this work, starting with aerodynamic analyses of a HARW and a joined-wing aircraft model and comparison with AVL and ASWING results. A benchmark of the FMM-accelerated panel against its non-accelerated counterpart is also presented. Following these results, the dynamic response of the two aircraft models to an impulse load is studied.

The computational aircraft models presented in this section are based on reduced-scale UAV research platforms developed in-house, namely the QT1 aircraft—a HARW UAV designed and optimized for surveillance and reconnaissance type applications—and the JWSC—a reduced-scale version of Boeing's proposed joined-wing concept.

4.6.1 FMM-Accelerated Aerodynamics of the QT1 and JWSC Configurations

The aerodynamics of the QT1 aircraft and JWSC were compared between the developed panel method, AVL, and stiff ASWING models. Three-dimensional models of both aircraft were developed to study their aerodynamics using the developed framework.

The wing and tail of the QT1 aircraft were modeled using a structured surface mesh, while its fuselage was modeled using an unstructured mesh implemented as a DCEL (fig. 4.20). The JWSC model was implemented solely using structured meshes (fig. 4.21). For each model, an aerodynamic simulation at $1g$ level trim condition was performed and the results compared with AVL and stiff ASWING models. Spanwise lift and drag coefficients were calculated from an integration of surface pressure.

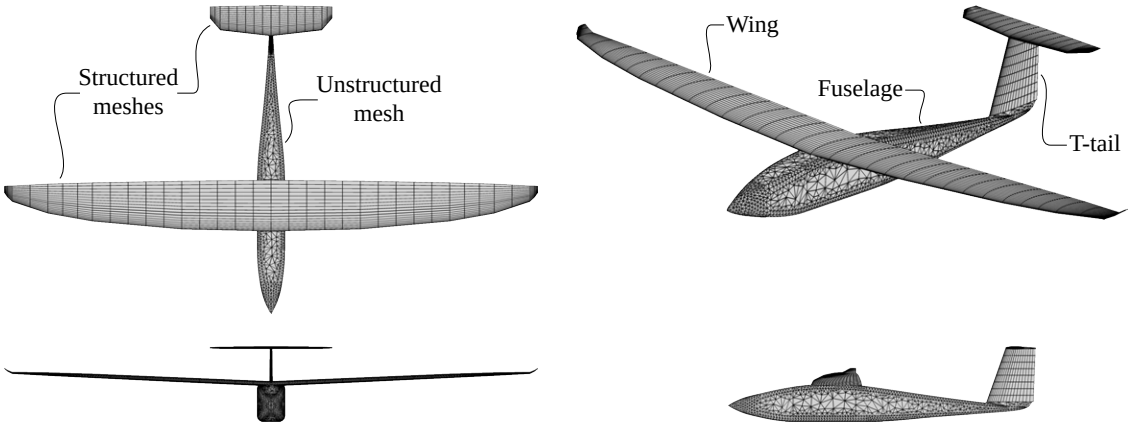

Figure 4.20: Three-dimensional aerodynamic model of the QT1 aircraft.

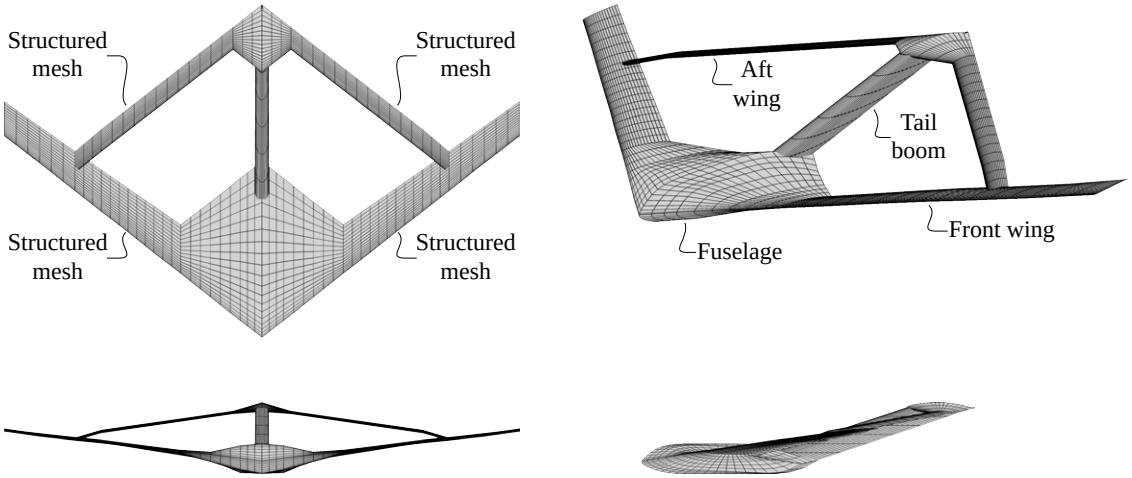

Figure 4.21: Three-dimensional aerodynamic model of the JWSC.

The lift distribution is shown in fig. 4.22a for the QT1 aircraft and in fig. 4.23a for the JWSC. For the QT1 aircraft, the lift distribution shows good agreement between models, while for the JWSC, the panel method appears to overestimate the lift distribution of the fuselage when compared to AVL and the stiff ASWING model. This could be due to the fact that the JWSC fuselage is modeled after its actual geometry in the panel method, i.e., as a solid lifting body, as opposed to a thin vortex sheet or a lifting line, which is the case for AVL and ASWING, respecrtively.

The drag distribution is shown in fig. 4.22b for the QT1 aircraft and in fig. 4.23b for the JWSC. Note that ASWING does not output the spanwise C_d distribution. The drag distribution for both aircraft shows good agreement between models, except near the fuselage where the panel method shows a larger drag distribution when compared to AVL. This could be due to the fact that the fuselage of the QT1 and JWSC aircraft

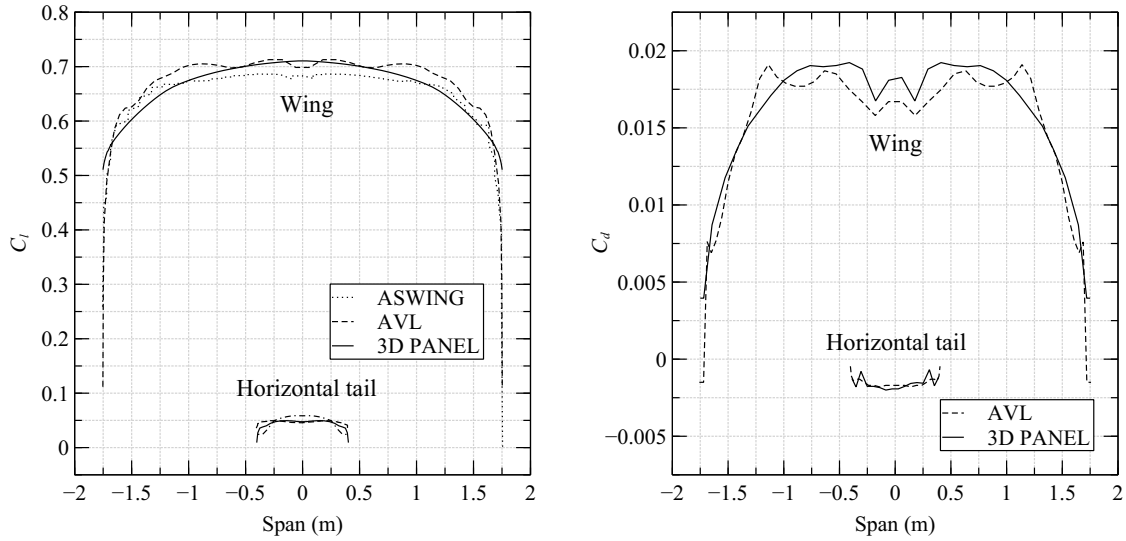

(a) Spanwise C_l distribution (b) Spanwise C_d distribution

Figure 4.22: Comparison of QT1 aerodynamics in terms of spanwise lift (left) and drag (right) distributions, between AVL, ASWING, and the developed panel method for a $1g$ level flight condition.

is modeled in AVL as a distribution of source singularities and as a thin vortex sheet, respectively, as opposed to a thick body in the panel method.

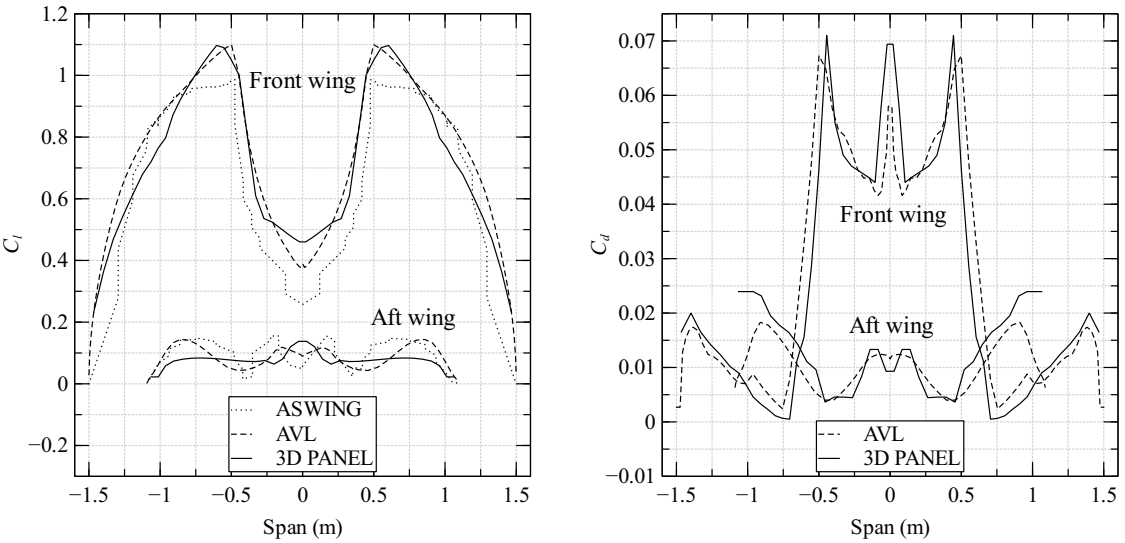

(a) Spanwise C_l distribution (b) Spanwise C_d distribution

Figure 4.23: Comparison of JWSC aerodynamics in terms of spanwise lift (left) and drag (right) distributions, between AVL, ASWING, and the developed panel method for a $1g$ level flight condition.

The pressure distribution is shown in figs. 4.24 and 4.25 for the QT1 and JWSC aircraft, respectively. These figures also show the convected wake shed from the aircraft wings at the end of an aerodynamic simulation. It is possible to see the wake roll-up effect occurring due to the shed vortices at the wingtips of both aircraft.

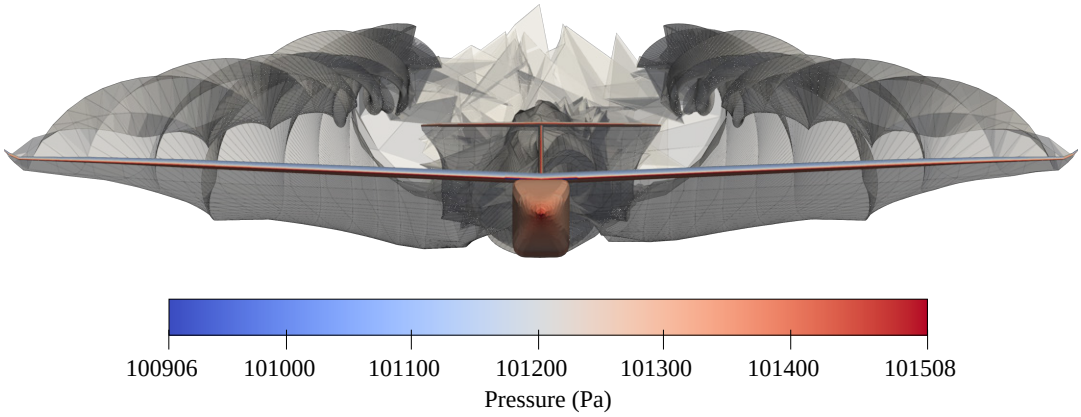

Figure 4.24: Pressure distribution and wake convection for the QT1 aircraft at the end of an aerodynamic simulation.

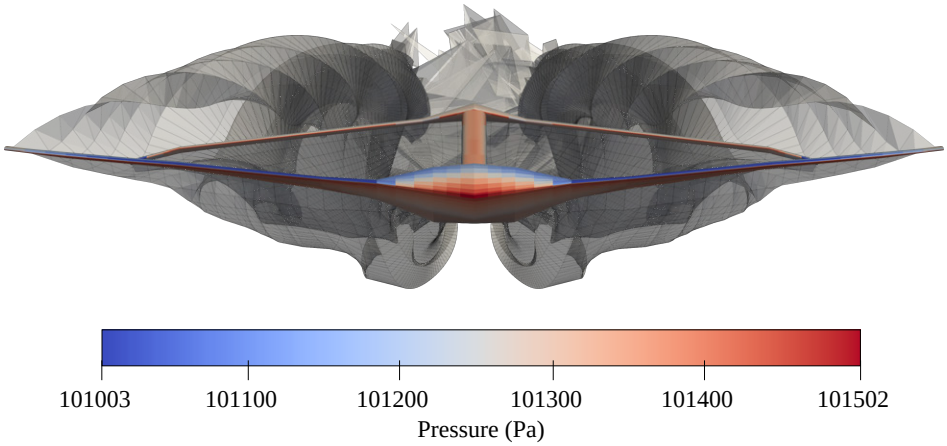

Figure 4.25: Pressure distribution and wake convection for the JWSC at the end of an aerodynamic simulation.

The FMM-accelerated version of the panel method was benchmarked against the non-accelerated version for different-size meshes. The panel method should scale with $\mathcal{O}(N^2)$, while its FMM-accelerated counterpart should scale with $\mathcal{O}(N)$. This behavior is shown in fig. 4.26, where a comparison of runtime performance between non-accelerated and FMM-accelerated Laplace potential is shown for different mesh sizes.

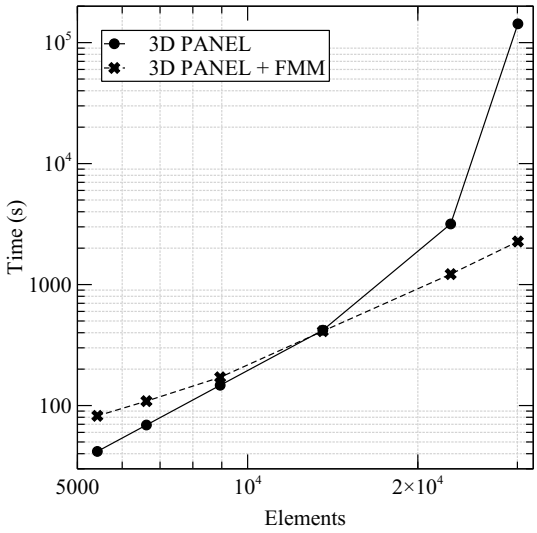

Figure 4.26: Scaling of the FMM with problem size N.

Since the number of elements was doubled from test to test, the results are presented in a log–log plot so that all data points are well distributed. The solid line shows the scaling of the Laplace potential with the number of elements N, while the dashed line shows the overall scaling of the FMM for the same potential with a multipole degree of $p = 2$.

It is possible to see that for small meshes with few elements, the FMM takes more time to run. This is due to the constant cost of performing the hierarchical decomposition and initializing all data structures needed for the FMM. Since the non-accelerated potential solver does not require these data structures, it takes the lead in terms of runtime for small meshes. As the number of elements increases, the linear scaling of the FMM becomes evident, and it is possible to see that it outperforms the non-accelerated case for $N > 13\,500$.

4.6.2 Dynamic Aeroelastic Response of the QT1 and JWSC Wings

The dynamic aeroelastic response of the QT1 and JWSC wings was studied using the developed framework. Half-wing models of each aircraft were developed and the wing was fixed at the root. An impulse load was applied to the wing tip to simulate an aileron disturbance and excite the wing dynamics.

The geometry was modeled using three-dimensional surfaces for the wings while

the spars were modeled as filament elements. The three-dimensional surface mesh of the wing was used in the developed FMM-accelerated panel method while the filament spar elements were modeled as ANCF beams. The two models are depicted in fig. 4.27.

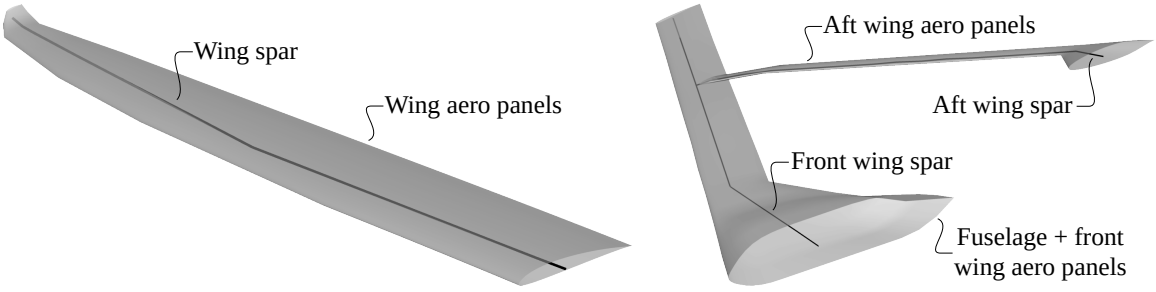

(a) QT1 wing (b) JWSC wing

Figure 4.27: Aeroelastic wing models the flexible QT1 (left) and JWSC (right) aircraft.

The natural representation of an impulse load is with a Dirac delta, but the discontinuous nature of this generalized function caused a breakdown of the simulation in most cases. Instead, a smooth approximation was chosen.

A Dirac delta can be defined in terms of a normal distribution when the variance tends to zero, such that

$$\delta(x) = \lim_{a \to 0} \frac{1}{|a|\sqrt{\pi}} e^{-\left(\frac{x}{a}\right)^2}. \tag{4.92}$$

The impulse applied at some time t_0 can then be represen3ted as

$$P(t) = P_{\max} e^{-\left(\frac{t-t_0}{a}\right)^2}, \tag{4.93}$$

which guarantees a smooth increase of the load from zero up to its maximum value $P_{\max}$ at $t = t_0$ and a smooth decrease back to zero (fig. 4.28a). The parameter a can be adjusted to control the with of the impulse. In the following results, a value of $a = 0.02$ was chosen.

To initiate the transfer of aerodynamic loads to the structure, a function of the following form was used

$$P(t) = \frac{1}{2}\left[1 - \cos\left(\pi \frac{(t - t_0)}{(t_1 - t_0)}\right)\right] P_{\max}, \tag{4.94}$$

where t_0 and t_1 are the start and end times, respectively. This allowed for a gradual increase of the aerodynamic loads transferred to the structure at the start of the simulation, from zero up to its maximum value $P_{\max}$ (fig. 4.28b), which prevented

spurious breakdowns in the simulations and increased the overall robustness. In the following results, a value of $t_0 = 0.1\,\text{s}$ was used for all simulations, while a value of $t_1 = 0.2\,\text{s}$ was used for the QT1 simulations and $t_1 = 1.0\,\text{s}$ was used for the simulations involving the JWSC wing.

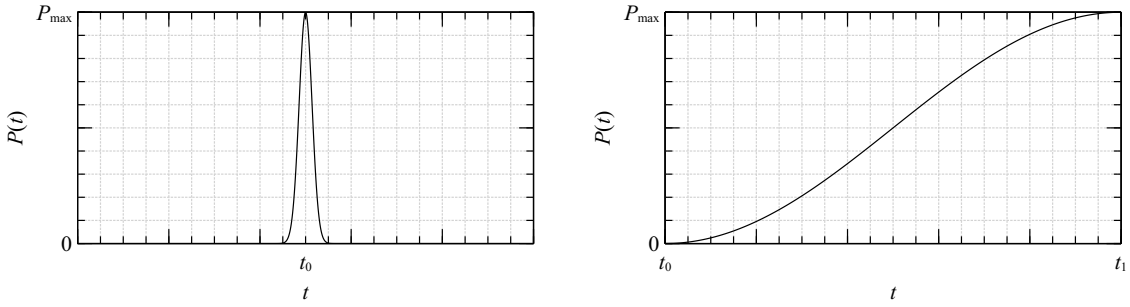

(a) Impulse load as a normal distribution.

(b) Aerodynamic loads at the start of a simulation.

Figure 4.28: Representation of an impulse load as a normal distribution (left) and evolution of aerodynamic loads transferred to the structure at the start of a simulation (right).

For all time-marching simulations, aerodynamic time steps had to be kept smaller than the time step size used in the structural dynamics solver and subcycling of the aerodynamic solver was employed. For the QT1 aircraft, structural dynamics time steps were set to 0.01 s while aerodynamic time steps were set to 0.001 s. For the JWSC simulations, the time step employed were reduced to 0.005 s for the structural dynamics solver and 0.0005 s for the aerodynamic solver. These values resulted in very long simulation times, in the order of hours or days even, but it was required in order for simulations to remain robust and not break down due to accumulation of integration error. This is a drawback of using a weak FSI coupling scheme.

The flexible QT1 wing dynamics were simulated for 10 s and a wingtip impulse was applied at the 5 s mark. For comparison, an ASWING simulation was set up for the same duration and same impulse command. The dynamic response of the wingtip is shown in fig. 4.29a while the steady-state wing deformation is shown in fig. 4.29b. The time-marching simulation started from $1g$ level-flight trim conditions.

From fig. 4.29b it is possible to see that the steady-state wing deflection seems to show good agreement between the two models. In terms of the unsteady response, fig. 4.29a shows that the developed framework takes some time to stabilize when coupling starts, hence the reason for performing a gradual transfer of loads at the

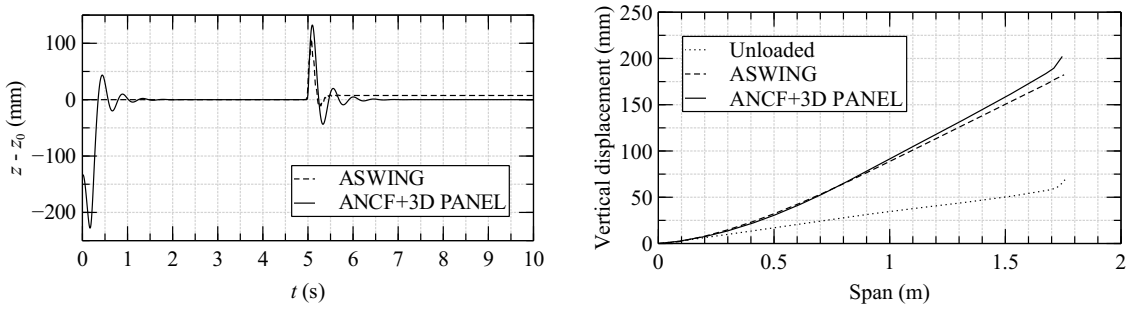

(a) Time-marching wingtip displacement

(b) Steady-state wing deformation

Figure 4.29: Comparison of aeroelastic response of the flexible QT1 wing to a wingtip impulse command between the developed aeroelastic framework and ASWING at an airspeed of 20 m/s. Unsteady wingtip deflection (left) and steady-state wing deformation (right).

beginning of the simulation. It is possible to see that the wingtip dynamic response is similar between models. However, ASWING seems to predict a more damped response than the ANCF-based simulation. This could be due to accumulation of error in the integration of the dynamics equations. It was observed that for long simulation times, the simulation began to diverge from its steady-state solution to the point where it would break down.

In a similar manner, the flexible JWSC wing dynamics were simulated for 5 s and a wingtip impulse was applied at the 3 s mark. An ASWING simulation was also set up for the same duration and same impulse command for comparison. The dynamic response of the front wing tip and aft wing midpoint is shown in fig. 4.30a. The steady-state wing deformation is shown in fig. 4.30b. The time-marching simulation started from 1g level-flight trim conditions.

Figure 4.30b shows some differences between the two solutions, especially in the predicted aft wing displacements. ASWING predicts an upward deformation of the aft wing at these trim conditions, while the developed framework predicts a downward deflection of the aft wing. The front wing also shows some discrepancies in the displacements near the wing–fuselage connection. This could be due to differences in the stiffness of the two models or it could be due to the fact that the ANCF beam formulation captures the transfer of loads between the front and aft wings differently from ASWING. The cross-section of an ANCF beam can model arbitrary deformations, including arbitrary shear deformation [225], while ASWING uses an extensional strain formulation based on beam curvatures and assumes that the cross-section of a beam

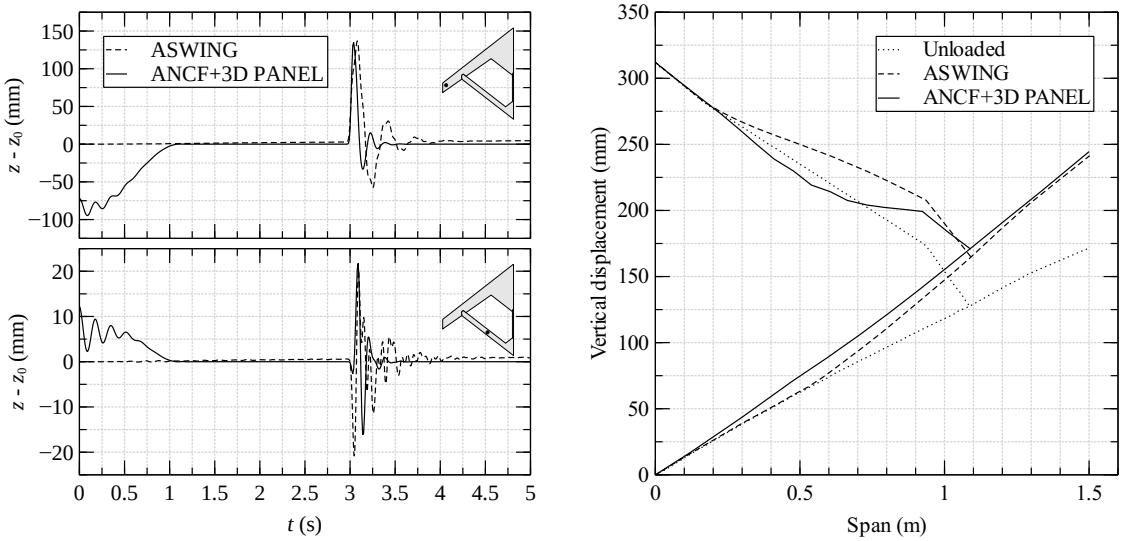

(a) Time-marching front wing tip and aft wing midpoint displacement

(b) Steady-state front and aft wing deformation

Figure 4.30: Comparison of aeroelastic response of the flexible JWSC front and aft wings to a wingtip impulse command between the developed aeroelastic framework and ASWING at an airspeed of 20 m/s. Unsteady front wing tip and aft wing midpoint deflection (left) and steady-state front and aft wing deformation (right).

cannot warp out of a plane attached to the local spanwise wing station [148].

The dynamic response is shown in fig. 4.30a for the two models. The results show that while the deflection amplitudes are comparable for the front and aft wings, the response frequencies of both models do not seem to agree. ASWING predicts a slower response for the front wing, while the aft wing response is similar in frequency but appears to exhibit spurious high frequency content as the simulation approaches steady-state conditions.

In terms of simulation runtime, the low-order methods employed in ASWING allowed for the unsteady simulations to be executed in a matter of hours or even minutes in some cases. However, it was observed that for long simulation times, the simulations would almost always eventually break down. This could be due to an accumulation of integration error over time. On the other hand, the implicit HHT-I3 method employed in the developed framework was more robust for long simulations. However, due to the more complex structural dynamics and aerodynamics formulations employed, simulations exhibited longer runtimes in the order of hours or even days. This runtime could potentially be improved if the weak FSI scheme were to be replaced with a strong coupling scheme.

4.7 Concluding Remarks

This work describes the development of a medium-fidelity aeroelastic tool using a FMM-accelerated low-order panel method and a flexible multibody dynamics formulation based on absolute coordinates. The coupling between fluid and structure was carried out using a weak coupling scheme with subcycling and the transfer of information was implemented using RBF interpolation. The developed tool was used to study the unsteady aeroelastic response of two flexible reduced-scale UAV models. The first model was the QT1 aircraft, a flexible HARW UAV platform, and the second was a reduced-scale version of Boeing's JWSC proposal.

The FMM-accelerated panel method was first benchmarked against the non-accelerated version for different-size meshes. It was observed that the FMM was able to make the computational cost scale with $\mathcal{O}(N)$ as opposed to $\mathcal{O}(N^2)$. It was shown that for small meshes with few elements, the constant set up time associated with the FMM increased the overall runtime of the problem, while for larger meshes with more elements, the linear scaling of the FMM became evident.

Aerodynamic models of the two aircraft were developed in ASWING and AVL and compared against the developed tool. The lift distribution showed good agreement between the models while the panel method predicted a larger drag coefficient near the fuselage. This could be due to the difference in how the fuselage is modeled in the different models—ASWING and AVL model non-lifting bodies as point source distributions, while the panel method models all bodies as three-dimensional surfaces after their actual geometry.

Time-marching aeroelastic simulations of the flexible QT1 and JWSC aircraft wings were carried out using the developed framework and compared against ASWING in response to a wingtip impulse command. It was found that the response of the QT1 wing tip was similar between models, with the ASWING response being more damped. The JWSC results showed some differences in terms of the response frequency of the front wing, while ASWING showed what looked like high-frequency noise for the aft wing response. The differences observed could be due to slight differences in stiffness and mass distribution between models or due to ASWING's inability to properly capture the aft wing deformation due to its simpler beam formulation.

The low-order formulation employed in ASWING allowed for time-marching simulations to be executed in a matter of hours or even minutes in some cases. However, for long simulation times, the simulations would eventually break down, which could

be due to accumulation of error in the integration of the dynamics equations. On the other hand, the developed framework employed the implicit HHT-I3 method and the simulations remained stable for long simulation times. However, due to the more complex structural dynamics and aerodynamics formulations, simulations exhibited longer runtimes in the order of hours or even days.

The developed framework expands the application range of ANCF-based flexible multibody dynamics in time-domain simulations of large elastic deformations coupled with rigid body motion that arise in next-generation aircraft.

Chapter 5

Conclusions and Future Work

This chapter wraps up this thesis by revisiting its major developments and drawing conclusions and remarks from the findings of the work. Finally, an outlook on possible future research directions is given.

5.1 Conclusions

Novel aircraft configurations are being proposed to meet the demanding environmental goals of the future of aviation. The proposed configurations range from wings with an increased aspect ratio to completely novel designs, such as joined-wing configurations. These configurations show increased aerodynamic efficiency, resulting in overall reduced fuel consumption. These benefits come at a cost of added structural complexity—longer wings require a more careful design of their internal structure, are heavier, and are subject to larger deflections—and unpredictable aeroelastic effects during flight—joined-wing aircraft are prone to buckling of the aft wing and tail boom.

On the one hand, characterizing these novel aircraft configurations in terms of their aeroelastic behavior is of extreme importance if they are to be used in future commercial aircraft designs. Due to the significant cost and risk associated with the testing of full-scale aircraft, reduced-scale flexible UAV models are an attractive alternative that can be used to understand the aeroelastic behavior of these designs during flight. On the other hand, current aeroelastic computational codes are relatively new, and their ability to accurately predict the aeroelastic performance of full-scale aircraft requires extensive validation. There is a need for experimental data sets demonstrating in-flight aircraft elastic behavior for tuning such models.

To this end, chapter 2 discusses work done on sizing, design, ground and flight testing, numerical modeling, and validation of a flexible HARW UAV platform with a wing structure designed to reach large deformations at low subsonic flight conditions. The aerodynamic, structural, and aeroelastic behavior, as well as the flight dynamics of the aircraft, were characterized and compared against computational models developed in AVL, NASTRAN, and ASWING, respectively. The aircraft was subjected to static load testing, and ground vibration testing, whose results were used to update the computational models developed. The aeroelastic behavior and flight dynamics of the aircraft were validated against flight test data collected during 3–2–1–1, frequency sweep, and doublet maneuver commands of the flexible vehicle.

It was observed that time-marching results obtained from ASWING aeroelastic simulations agreed well with the flight test data for all flight tests. Possible discrepancies in the initial conditions used to start the simulations, as well as the low-fidelity models employed by ASWING, were identified as two probable causes for some of the differences observed between the experimental and computational results. This work illustrated the feasibility of using scaled flight test demonstrators as a cost-effective platform for testing aeroservoelastic coupling in HARW aircraft designs and the importance of accurately modeling the multiple disciplines (aerodynamics, structures, and controls) involved in aeroservoelastic evaluation of HARW aircraft.

The focus of chapter 3 was on the design, sizing, numerical modeling, ground testing, and validation of an aeroelastically-tuned JWSC UAV platform with flexible front and aft wings. The flexible wing airframe was designed to exhibit geometric nonlinearities under normal flight conditions. This flexible aircraft platform was developed to investigate the nonlinear aeroelastic behavior and flight dynamics of joined-wing aircraft configurations and validation of computational models. Experimental data consisting of static load tests, ground vibration tests, and preliminary flight tests were compared with the results generated from aerodynamic, structural, and aeroelastic computational models developed in AVL, NASTRAN, and ASWING, respectively. Due to the low-fidelity formulation used in ASWING, a higher-fidelity coupled NASTRAN–AVL nonlinear framework was developed as part of this work to design the internal wing structure.

Time-marching aeroelastic simulations were carried out in ASWING in response to elevator and aileron doublet maneuver commands for rigid and flexible variants of the aircraft. It was found that while the aircraft response to an elevator doublet command barely exhibited any difference with the added wing flexibility, the aileron

doublet command caused the aircraft to respond in an unstable manner with large deformations of both front and aft wings. These results reinforce the importance of accounting for geometric nonlinearities when modeling the aeroelastic behavior of joined-wing aircraft configurations.

The computational aeroelastic results obtained in chapters 2 and 3 demonstrated that there is interest in developing higher-fidelity tools to simulate the dynamic aeroelastic behavior of flexible aircraft. High-fidelity simulations that couple CFD with structural dynamics formulations can be used, but these tend to be computationally heavy and can take days or weeks to perform a single dynamic analysis of simple aircraft geometries. An alternative is to develop medium-fidelity tools coupling unsteady panel methods with structural dynamics formulations capable of capturing geometric nonlinearities and simulating the dynamic aeroelastic behavior of complex aircraft geometries within hours or minutes.

To this end, chapter 4 outlines work done towards the development of a medium-fidelity aeroelastic tool based on a FMM-accelerated three-dimensional unsteady panel method and a ANCF-based flexible multibody dynamics formulation. The framework was benchmarked in terms of aerodynamic results and unsteady aeroelastic response to an impulse command for flexible HARW and JWSC aircraft models.

It was shown that for small meshes with few elements, the constant set up time associated with the FMM increased the overall runtime of the problem, while for larger meshes with more elements, the linear time scaling of the FMM became evident.

Aerodynamic models of the two aircraft were developed in ASWING and AVL and compared against the developed tool. The lift distribution showed good agreement between the models while the panel method predicted a larger drag coefficient near the fuselage possibly due to differences in how the fuselage is modeled in the different formulations.

Time-marching aeroelastic simulations of the flexible aircraft wings were carried out and compared against ASWING in response to a wingtip impulse command. The dynamic response of the QT1 wing tip was similar between models, with the ASWING response being more damped. The JWSC results showed some differences in terms of the response frequency of the front wing, while ASWING showed what looked like high-frequency noise for the aft wing response. The differences observed could be due to slight differences in stiffness and mass distribution between models or due to ASWING's inability to properly capture the aft wing deformation due to its simpler beam formulation.

The low-order formulation employed in ASWING allowed for time-marching simulations to be executed in a matter of hours or even minutes in some cases. However, for long simulation times, the simulations would eventually break down, which could be due to accumulation of error in the integration of the dynamics equations. On the other hand, the developed framework employed the implicit HHT-I3 method and the simulations remained stable for long simulation times. However, due to the more complex structural dynamics and aerodynamics formulations, simulations exhibited longer runtimes in the order of hours or even days.

5.2 Future Work

In developing the contributions of this thesis, three broad categories for future work have been identified. The first is on modifications to flight testing methodologies and the collection of data during flight. The second is on improvements to aeroelastic simulations. The last is on further progress towards a more complete aeroelastic framework.

5.2.1 Flight Testing and Data Collection

In chapter 2 it was shown that some of the signals collected during flight showed some degree of high-frequency noise. This could be due to the high sampling rate used by the DAQ system or interference with the many radio signals—GPS, telemetry, and video signals—used by the aircraft. This noise was eventually removed with a low-pass filter but could be improved in future flight tests by either moving any antenna away from the sensors, creating a shielding system around any sensor susceptible to interference, or simply lowering the sampling rate used by the DAQ system.

It was mentioned that the correct identification of initial conditions from the collected flight test data was very important in generating good unsteady aeroelastic simulation results. These conditions were used to trim the aircraft prior to initiating time-domain aeroelastic analysis in ASWING. During flight tests, the aircraft was commanded to follow a straight and level flight path prior to the start of a maneuver command test. However, due to external disturbances, such as wind gusts, this path was not always straight and the collected aircraft states were not completely steady before the test. Because of this, it was difficult to determine the initial conditions for the time-domain simulations. To determine the initial conditions, the collected

signals were averaged for a given time length window and these values were used as initial conditions for the simulations. However, different time length windows yielded slightly different initial conditions, which had a considerable impact on the validity of the simulated results.

This process could be improved by either simply flying the aircraft in better weather conditions or measuring wind gusts during flight tests. The former solution is difficult to execute in practice. The latter requires the measurement of gusts at the flight test location and incorporation these effects in the initial conditions used in the simulations. The measurements could be done on the aircraft and collected alongside the remaining data, or they could be performed by the GCS and recorded in tandem with the aircraft signals. The initial conditions used in the simulations could be updated with the measured gusts at the start of the maneuver command test. Another way to improve the conditions at the start of a maneuver command test is to increase the length of a flight test leg to give the autopilot more time to level and stabilize the aircraft.

In chapter 3, it was mentioned that a flight test of the flexible JWSC resulted in a crash and loss of one set of flexible wings, aircraft fuselage, and some avionics. Even though the reason for this crash was most likely a faulty actuator, it would be wise to perform future flights of this highly-flexible aircraft configuration in progressive flexibility increments, given that the open-loop simulations showed a considerable degradation of aircraft lateral stability with the flexible front and aft wings installed. Different stiffness spars could be manufactured and a flight test campaign could be designed to fly the aircraft in incremental steps of flexibility. The spars could be swapped from flight test to flight test and the stability of the aircraft could be assessed in each step.

5.2.2 Improvements to Aeroelastic Simulations

In chapter 2, discrepancies in some of the flight test data and simulated ASWING results were observed. It was mentioned that a lack of an engine model could be the reason for the observed discrepancies. Another explanation for the observed differences could be due to a lack of wind gust prediction in the simulations. If wind gusts were to be measured during flight, these could be added to the simulation as perturbations of aircraft states. Otherwise, gust models could be incorporated into the ASWING simulations. An engine model could be developed relating throttle setting to thrust

force and incorporated into the simulation as well.

Chapter 4 mentioned issues with long simulation times in the developed aeroelastic framework because of the use of very small time steps required due to the use of a weak FSI coupling scheme. One way of improving simulation time and robustness of the simulation could be to implement a strong coupling scheme. This should relax the constraints on the time step size used, at the cost of a more complex implementation. This, however, is not guaranteed to decrease simulation time, since the coupling scheme would require an iterative solver which could need more time to perform a single coupling step even with the use of larger time steps. It would, however, make the simulation more robust since it would reduce accumulated error due to coupling in each time step.

5.2.3 Progress Towards a Complete Aeroelastic Framework

In chapter 4, a medium fidelity unsteady aeroelastic framework was implemented based on an unsteady panel method and flexible multibody dynamics. However, the test cases presented did not fully realize the possible benefits of this framework. First, the models presented were of cantilever wings, not full aircraft models, and so the full aircraft dynamics were not analyzed. Second, even though time-depended unsteady simulations were performed, the maneuver command was not very dynamic in nature.

The reason for choosing to only model the wing dynamics was due to modeling complexity, computational power requirements, and simulation time constraints. It was already mentioned that some test cases took days to simulate. Simulating the entire aircraft dynamics would take even longer using the current implementation, but would show the possible benefits of using a flexible multibody dynamics approach to capture the large inertial effects present. Different maneuver commands could be tested to see their effects of the aircraft dynamics.

It was also described in chapter 4 that the developed framework implemented an unsteady convected wake with the goal of capturing interactional aerodynamics. This, however, would only be possible to observe and capture in cases where large moving lifting bodies were moving close to each other, such in the case of the blades of a rotating rotor. In fact, some test cases of rigid rotating rotors with convected wakes were developed but they were not presented in this work. It was found that, in these cases, as the wake carried the shed vorticity downstream, it would eventually become highly distorted after some time. Very small time steps were required to keep the

wake panels small, and delay their inevitable distortion. One way of avoiding this would be to model the wake as a system of wake particles, instead of a thin surface, convected with the flow downstream. A system of vortex particles is meshless, and does not require knowledge and storage of topology associated with them, eliminating the distortion problem. Topology can be inferred by searching for neighbor particles and requires storing them in a data structure that allows for fast neighbor search.

To account for viscous drag, the panel method formulation could be coupled with a boundary layer formulation. An attempt was made at this by developing a two-dimensional interactive boundary layer solver and coupling it with the three-dimensional panel method along the wing span. There are many numerical issues associated with the solution of interactive boundary layer equations and, while an implementation was tested for a steady-state case, the results were not completely satisfactory and the implemented solver was not robust enough to handle unsteady simulations.

Other improvements to the framework could be related to the implementation of different force/moment functions to model certain moving components in the aircraft. For example, propellers could be modeled as a point force/moment whose magnitude is calculated at each time step given known system states. Gust models could also be developed and incorporated as an extra step in the unsteady simulation process to better model external disturbances to the aircraft dynamics.

Bibliography

[1] J. Green. "Civil aviation and the environmental challenge". In: *The Aeronautical Journal* 107.1072 (2003), pp. 281–299. DOI: 10.1017/S0001924000013579.

[2] J. E. Penner et al. *Aviation and the Global Atmosphere*. Tech. rep. IPCC. 1999.

[3] J. Reneaux. "Overview on Drag Reduction Technologies for Civil Transport Aircraft". In: *European Congress on Computational Methods in Applied Sciences and Engineering (ECCOMAS) 2004*. 2004.

[4] J. G. Marshall and M. Imregun. "A Review of Aeroelasticity Methods with Ephasis on Turbomachinery Applications". In: *Journal of Fluids and Structures* 10.3 (1996), pp. 237–267. DOI: 10.1006/jfls.1996.0015.

[5] D. M. Schuster, D. D. Liu, and L. J. Huttsell. "Computational Aeroelasticity: Success, Progress, Challenge (Invited)". In: *AIAA Dynamics Specialists Conference*. 2003.

[6] D. M. Schuster, D. D. Liu, and L. J. Huttsell. "Computational Aeroelasticity: Success, Progress, Challenge". In: *Journal of Aircraft* 40.5 (2003), pp. 843–856. DOI: 10.2514/2.6875.

[7] R. E. Bartels and A. I. Sayma. "Computational aeroelastic modelling of airframes and turbomachinery: Progress and challenges". In: *Philosophical Transactions of the Royal Society A: Mathematical, Physical and Engineering Sciences* 365.1859 (2007), pp. 2469–2499. DOI: 10.1098/rsta.2007.2018.

[8] F. Afonso et al. "A review on non-linear aeroelasticity of high aspect-ratio wings". In: *Progress in Aerospace Sciences* 89 (2017), pp. 40–57. DOI: 10.1016/j.paerosci.2016.12.004.

[9] E. Ortega et al. "Efficient aeroelastic analysis of inflatable structures using enhanced potential flow aerodynamics". In: *Journal of Fluids and Structures* 90 (2019), pp. 230–245. DOI: 10.1016/j.jfluidstructs.2019.06.013.

[10] R. M. Ajaj et al. "Recent developments in the aeroelasticity of morphing aircraft". In: *Progress in Aerospace Sciences* 120 (2021), p. 100682. DOI: 10.1016/j.paerosci.2020.1006823.

[11] A. R. Collar. "The Expanding Domain of Aeroelasticity". In: *The Journal of the Royal Aeronautical Society* 50.428 (1946), pp. 613–636. DOI: 10.1017/S0368393100120358.

[12] P. P. Friedmann. "Renaissance of Aeroelasticity and Its Future". In: *Journal of Aircraft* 36.1 (1999), pp. 105–121. DOI: 10.1017/S0368393100120358.

[13] E. Livne. "Future of Airplane Aeroelasticity". In: *Journal of Aircraft* 40.6 (2003), pp. 1066–1092. DOI: 10.2514/2.7218.

[14] Y. Rudy, D. Liu, and P. Chen. "The State-of-the-Art of Unsteady Aerodynamics for High Performance Aircraft". In: *39th Aerospace Sciences Meeting and Exhibi (ASME)*. 2001. DOI: 10.2514/6.2001-428.

[15] E. Dowell, J. Edwards, and T. Strganac. "Nonlinear Aeroelasticity". In: *Journal of Aircraft* 40.5 (2003), pp. 857–874. DOI: 10.2514/2.6876.

[16] L. Cavagna, P. Masarati, and G. Quaranta. "Coupled Multibody/Computational Fluid Dynamics Simulation of Maneuvering Flexible Aircraft". In: *Journal of Aircraft* 48.1 (2011), pp. 92–106. DOI: 10.2514/1.C000253.

[17] L. Meirovitch and I. Tuzcu. *Integrated Approach to the Dynamics and Control of Maneuvering Flexible Aircraft*. Tech. rep. CR-2003-211748. NASA, 2003.

[18] D. E. Raveh. "Computational-fluid-dynamics-based aeroelastic analysis and structural design optimization—a researcher's perspective". In: *Computer Methods in Applied Mechanics and Engineering* 194.30 (2005), pp. 3453–3471. DOI: 10.1016/j.cma.2004.12.027.

[19] J. Richards et al. "Design of a Scaled RPV for Investigation of Gust Response of Joined-Wing Sensorcraft". In: *50th AIAA/ASME/ASCE/AHS/ASC Structures, Structural Dynamics, and Materials Conference*. 2009. DOI: 10.2514/6.2009-2218.

[20] I. H. Abbot and A. E. von Doenhoff. *Theory of Wing Sections*. Dover Publications, 1959.

[21] A. Abbas, J. de Vicente, and E. Valero. "Aerodynamic Technologies to Improve Aircraft Performance". In: *Aerospace Science and Technology* 28.1 (2013), pp. 100–132. DOI: 10.1016/j.ast.2012.10.008.

[22] D. H. Hodges and E. H. Dowell. *Nonlinear Equations of Motion for the Elastic Bending and Torsion of Twisted Nonuniform Rotor Blades*. Tech. rep. TN-D-7818. NASA, 1974.

[23] M. J. Patil, D. H. Hodges, and C. E. S. Cesnik. "Nonlinear Aeroelasticity and Flight Dynamics of High-Altitude Long-Endurance Aircraft". In: *Journal of Aircraft* 38.1 (2001), pp. 88–94. DOI: 10.2514/2.2738.

[24] M. J. Patil and D. H. Hodges. "On the Importance of Aerodynamic and Structural Geometrical Nonlinearities in Aeroelastic Behavior of High-Aspect-Ratio Wings". In: *Journal of Fluids and Structures* 19.7 (2004), pp. 905–915. DOI: 10.1016/j.jfluidstructs.2004.04.012.

[25] D. M. Tang and E. H. Dowell. "Effects of geometric structural nonlinearity on flutter and limit cycle oscillations of high-aspect-ratio wings". In: *Journal of Fluids and Structures* 19.3 (2004), pp. 291–306. DOI: 10.1016/j.jfluidstructs.2003.10.007.

[26] D. Tang and E. H. Dowell. "Experimental and Theoretical Study on Aeroelastic Response of High-Aspect-Ratio Wings". In: *AIAA Journal* 39.8 (2001), pp. 1430–1441. DOI: 10.2514/2.1484.

[27] D. Tang and E. H. Dowell. "Experimental and Theoretical Study of Gust Response for High-Aspect-Ratio Wing". In: *AIAA Journal* 40.3 (2002), pp. 419–429. DOI: 10.2514/2.1691.

[28] W. Su and C. E. S. Cesnik. "Dynamic Response of Highly Flexible Flying Wings". In: *AIAA Journal* 49.2 (2011), pp. 324–339. DOI: 10.2514/1.j050496.

[29] M. J. Patil and D. H. Hodges. "Flight Dynamics of Highly Flexible Flying Wings". In: *Journal of Aircraft* 43.6 (2006), pp. 1790–1799. DOI: 10.2514/1.17640.

[30] C. M. Shearer and C. E. S. Cesnik. "Nonlinear Flight Dynamics of Very Flexible Aircraft". In: *Journal of Aircraft* 44.5 (2007), pp. 1528–1545. DOI: 10.2514/1.27606.

[31] W. Su and C. E. S. Cesnik. "Nonlinear Aeroelasticity of a Very Flexible Blended-Wing-Body Aircraft". In: *Journal of Aircraft* 47.5 (2010), pp. 1539–1553. DOI: 10.2514/1.47317.

[32] D. Tang, A. Grasch, and E. H. Dowell. "Gust Response for Flexibly Suspended High-Aspect Ratio Wings". In: *AIAA Journal* 48.10 (2010), pp. 2430–2444. DOI: 10.2514/1.j050309.

[33] T. E. Noll et al. *Investigation of the Helios Prototype Aircraft Mishap*. Tech. rep. 2004.

[34] T. E. Noll et al. "Technical Findings, Lessons Learned, and Recommendations Resulting from the Helios Prototype Vehicle Mishap". In: *Meeting Proceedings RTO-MP-AVT-145*. 2007, pp. 3.4-1–3.4-18.

[35] Leeran Yagil, Daniella E. Raveh, and Moshe Idan. "Deformation control of highly flexible aircraft in trimmed flight and gust encounter". In: *Journal of Aircraft* 55.2 (2018), pp. 829–840. DOI: 10.2514/1.C034353.

[36] X. Wang et al. "A new deformation control approach for flexible wings using moving masses". In: *Aerospace Science and Technology* 106.106118 (2020). DOI: 10.1016/j.ast.2020.106118.

[37] X. Wang et al. "Modeling and simulation of mass-actuated flexible aircraft for roll control". In: *Aerospace Science and Technology* 107.106254 (2020). DOI: 10.1016/j.ast.2020.106254.

[38] A. Bows-Larkin et al. "Aviation and Climate Change—The Continuing Challenge". In: *Encyclopedia of Aerospace Engineering*. Wiley, 2016, pp. 1–11. DOI: 10.1002/9780470686652.eae1031.

[39] A. J. Timmis et al. "Environmental impact assessment of aviation emission reduction through the implementation of composite materials". In: *The International Journal of Life Cycle Assessment* 20 (2015), pp. 233–243. DOI: 10.1007/s11367-014-0824-0.

[40] J. Wolkovitch. "The joined wing: An overview". In: *Journal of Aircraft* 23.3 (1986), pp. 161–178. DOI: 10.2514/3.45285.

[41] M. F. Samuels. "Structural Weight Comparison of a Joined Wing and a Conventional Wing". In: *Journal of Aircraft* 19.6 (1982), pp. 485–491. DOI: 10.2514/3.57418.

[42] C. C. Rasmussen, R. A. Canfield, and M. Blair. "Joined-Wing Sensor-Craft Configuration Design". In: *Journal of Aircraft* 43.5 (2006), pp. 1470–1478. DOI: 10.2514/1.21951.

[43] C. C. Rasmussen, R. A. Canfield, and M. Blair. "Optimization process for configuration of flexible joined-wing". In: *Structural and Multidisciplinary Optimization* 37 (2009), pp. 265–277. DOI: 10.1007/s00158-008-0229-4.

[44] J. S. Letcher. "V-Wings and Diamond Ring-Wings of Minimum Induced Drag". In: *Journal of Aircraft* 9.8 (1972), pp. 605–607. DOI: 10.2514/3.5904.

[45] J. M. Kuhlman and T. J. Ku. *Numerical Optimization Techniques for Bound Circulation Distribution for Minimum Induced Drag of Non-Planar Wings: Computer Program Documentation*. Tech. rep. CR-3458. NASA, 1993.

[46] J. Richards. "An Experimental Investigation of a Joined Wing Aircraft Configuration Using Flexible, Reduced Scale Flight Test Vehicles". PhD thesis. University of Victoria, 2014.

[47] B. Smallwood, R. Canfield, and A. Terzuoli. "Structurally Integrated Antennas on a Joined-Wing Aircraft". In: *44th AIAA/ASME/ASCE/AHS/ASC Structures, Structural Dynamics, and Materials Conference*. 2003. DOI: 10.2514/6.2003-1459.

[48] I. Kroo, J. Gallman, and S. Smith. "Aerodynamic and structural studies of joined-wing aircraft". In: *Journal of Aircraft* 28.1 (1991), pp. 74–81. DOI: 10.2514/3.45994.

[49] J. W. Gallman and I. M. Kroo. "Structural optimization for joined-wing synthesis". In: *Journal of Aircraft* 33.1 (1996), pp. 214–223. DOI: 10.2514/3.46924.

[50] M. Blair and R. A. Canfield. "A Joined-Wing Structural Weight Modeling Study". In: *43rd AIAA/ASME/ASCE/AHS/ASC Structures, Structural Dynamics, and Materials Conference*. 2002. DOI: 10.2514/6.2002-1337.

[51] M. Blair, R. A. Canfield, and R. W. Roberts Jr. "Joined-Wing Aeroelastic Design with Geometric Nonlinearity". In: *Journal of Aircraft* 42.4 (2005), pp. 832–848. DOI: 10.2514/1.2199.

[52] H. Lin, J. Jhou, and R. Stearman. "Influence of Joint Fixity on the Structural Static and Dynamic Response of a Joined-Wing Aircraft Part I: Static Response". In: *SAE Transactions* 98 (1989), pp. 221–234.

[53] S. Bhasin et al. “Dynamic Nonlinear Aeroelastic Analysis of the Joined Wing Configuration”. In: *53rd AIAA/ASME/ASCE/AHS/ASC Structures, Structural Dynamics and Materials Conference*. 2012. DOI: 10.2514/6.2012-1791.

[54] L. Demasi, R. Cavallaro, and F. Bertuccelli. “Post-Critical Analysis of Joined Wings: the Concept of Snap-Divergence as a Characterization of the Instability”. In: *54th AIAA/ASME/ASCE/AHS/ASC Structures, Structural Dynamics, and Materials Conference*. 2013. DOI: 10.2514/6.2013-1559.

[55] L. Demasi, R. Cavallaro, and F. Bertuccelli. “Post-critical analysis of highly deformable Joined Wings: The concept of snap-divergence as a characterization of the instability”. In: *Journal of Fluids and Structures* 54 (2015), pp. 701–718. DOI: 10.1016/j.jfluidstructs.2015.01.009.

[56] R. Cavallaro, L. Demasi, and F. Bertuccelli. “Risks of Linear Design of Joined Wings: a Nonlinear Dynamic Perspective in the Presence of Follower Forces”. In: *54th AIAA/ASME/ASCE/AHS/ASC Structures, Structural Dynamics, and Materials Conference*. 2013. DOI: 10.2514/6.2013-1558.

[57] R. Cavallaro et al. “Risks of linear design of joined wings: a non-linear dynamic perspective in the presence of follower forces”. In: *CEAS Aeronautical Journal* 6 (2015), pp. 61–180. DOI: 10.1007/s13272-014-0136-x.

[58] R. Cavallaro and L. Demasi. “Challenges, Ideas, and Innovations of Joined-Wing Configurations: A Concept from the Past, an Opportunity for the Future”. In: *Progress in Aerospace Sciences* 87 (2016), pp. 1–93. DOI: 10.1016/j.paerosci.2016.07.002.

[59] S. Hamada and C. P. Moreno. “Development of an Unmanned Aerial Vehicle (UAV) Research Platform for Flutter Analysis”. In: *2018 AIAA Atmospheric Flight Mechanics Conference*. 2018. DOI: 10.2514/6.2018-0021.

[60] A. Hermanutz and M. Hornung. “Aeroelastic Wing Planform Design Optimization of a Flutter UAV Demonstrator”. In: *Aerospace* 7.4 (2020). DOI: 10.3390/aerospace7040045.

[61] D. F. C. Zúñiga, A. G. Souza, and L. C. S. Góes. “Flight dynamics modeling of a flexible wing unmanned aerial vehicle”. In: *Mechanical Systems and Signal Processing* 145 (2020), p. 106900. DOI: 10.1016/j.ymssp.2020.106900.

[62] H. V. de Figueiredo et al. “Aeroelastic Vibration Measurement Based on Laser and Computer Vision Technique”. In: *Experimental Techniques* 45 (2021), pp. 95–107. DOI: 10.1007/s40799-020-00399-0.

[63] J. Mieloszyk et al. “Validation of flight dynamic stability optimization constraints with flight tests”. In: *Aerospace Science and Technology* 106 (2020), p. 106193. DOI: 10.1016/j.ast.2020.106193.

[64] D. K. Schmidt. “MATLAB-Based Flight-Dynamics and Flutter Modeling of a Flexible Flying-Wing Research Drone”. In: *Journal of Aircraft* 53.4 (2015), pp. 1045–1055. DOI: 10.2514/1.c033539.

[65] D. K. Schmidt. “Stability Augmentation and Active Flutter Suppression of a Flexible Flying-Wing Drone”. In: *Journal of Guidance, Control, and Dynamics* 39.3 (2016), pp. 409–422. DOI: 10.2514/1.g001484.

[66] J. Ryan et al. “Current and Future Research in Active Control of Lightweight, Flexible Structures Using the X-56 Aircraft”. In: *52nd Aerospace Sciences Meeting*. 2014. DOI: 10.2514/6.2014-0597.

[67] D. K. Schmidt et al. “Flight-Dynamics, Flutter Analysis, and Control of an MDAO-Designed Flying-Wing Research Drone”. In: *AIAA Scitech 2019 Forum*. 2019. DOI: 10.2514/6.2019-1816.

[68] P. Stahl et al. “Mission and Aircraft Design of FLEXOP Unmanned Flying Demonstrator to Test Flutter Suppression within Visual Line of Sight”. In: *17th AIAA Aviation Technology, Integration, and Operations Conference*. 2017.

[69] V. Rozov et al. “Aeroelastic Analysis of a Flutter Demonstrator With a Very Flexible High-Aspect-Ratio Swept Wing”. In: *International Forum on Aeroelasticity and Structural Dynamics (IFASD) 2017*. 2017.

[70] C. Roessler et al. “Aircraft Design and Testing of FLEXOP Unmanned Flying Demonstrator to Test Load Alleviation and Flutter Suppression of High Aspect Ratio Flexible Wings”. In: *AIAA Scitech 2019 Forum*. 2019. DOI: 10.2514/6.2019-1813.

[71] C. E. S. Cesnik et al. “X-HALE: A Very Flexible Unmanned Aerial Vehicle for Nonlinear Aeroelastic Tests”. In: *AIAA Journal* (2012). DOI: 10.2514/1.J051392.

[72] C. E. S. Cesnik and W. Su. "Nonlinear Aeroelastic Simulation of X-HALE: a Very Flexible UAV". In: *49th AIAA Aerospace Sciences Meeting including the New Horizons Forum and Aerospace Exposition*. 2011. DOI: 10.2514/6.2011-1226.

[73] J. R. Jones and C. E. S. Cesnik. "Preliminary Flight Test Correlations of the X-HALE Aeroelastic Experiment". In: *The Aeronautical Journal* 119.1217 (2015), pp. 855–870. DOI: 10.1017/S0001924000010952.

[74] J. Richards et al. "Airworthiness Evaluation of a Scaled Joined-Wing Aircraft". In: *53rd AIAA/ASME/ASCE/AHS/ASC Structures, Structural Dynamics and Materials Conference*. 2012. DOI: 10.2514/6.2012-1721.

[75] J. Richards et al. "Design and Evaluation of Aeroelastically Tuned Joined-Wing SensorCraft Flight Test Article". In: *54th AIAA/ASME/ASCE/AHS/ASC Structures, Structural Dynamics, and Materials Conference*. 2013. DOI: 10.2514/6.2013-1786.

[76] C. Zhang et al. "Nonlinear Static Aeroelastic and Trim Analysis of Highly Flexible Joined-Wing Aircraft". In: *AIAA Journal* 56.12 (2018), pp. 4988–4999. DOI: 10.2514/1.J056804.

[77] M. Bras, S. Warwick, and A. Suleman. "Aeroelastic evaluation of a flexible high aspect ratio wing UAV: Numerical simulation and experimental flight validation". In: *Aerospace Science and Technology* 122 (2022), p. 107400. DOI: 10.1016/j.ast.2022.107400.

[78] S. Warwick et al. "Measurement of Aeroelastic Wing Deflections Using Modal Shapes and Strain Pattern Analysis". In: *AIAA Scitech 2019 Forum*. 2019. DOI: 10.2514/6.2019-1116.

[79] A. Sobron, Lundström D., and Krus P. "A Review of Current Research in Subscale Flight Testing and Analysis of its Main Practical Challenges". In: *Aerospace* 8.3 (2021). DOI: 10.3390/aerospace8030074.

[80] A. Raju Kulkarni et al. "Sub-scale flight test model design: Developments, challenges and opportunities". In: *Progress in Aerospace Sciences* 130 (2022), p. 100798. DOI: 10.1016/j.paerosci.2021.100798.

[81] S. Hernández et al. “Optimization approach for identification of dynamic parameters of localized joints of aircraft assembled structures”. In: *Aerospace Science and Technology* 69 (2017), pp. 538–549.
DOI: 10.1016/j.ast.2017.07.026.

[82] B. Peeters et al. “Modern solutions for Ground Vibration Testing of large aircraft”. In: *Proceedings of the International Modal Analysis Conference (IMAC) 26*. 2008.

[83] M. Böswald et al. “New Concepts for Ground and Flight Vibration Testing of Aircraft based on Output-Only Modal Analysis”. In: *Proceedings of the 7th International Operational Modal Analysis Conference (IOMAC)*. 2017.

[84] D. F. Voracek. *Ground Vibration and Flight Flutter Tests of the Single-Seat F-16XL Aircraft with a Modified Wing*. Tech. rep. TM-104264. NASA, 1993.

[85] X. Liu, N. A. J. Lieven, and P. J. Escamilla-Ambrosio. “Frequency response function shape-based methods for structural damage localisation”. In: *Mechanical Systems and Signal Processing* 23.4 (2009), pp. 1243–1259.
DOI: 10.1016/j.ymssp.2008.10.002.

[86] J. Simsiriwong and R. W. Sullivan. “Vibration testing of a carbon composite fuselage”. In: *International Journal of Vehicle Noise and Vibration* 6.2–4 (2010), pp. 149–162. DOI: 10.1504/IJVNV.2010.036683.

[87] W. L. Ko, W. L. Richards, and V. T. Tran. *Displacement Theories for In-Flight Deformed Shape Predictions of Aerospace Structures*. Tech. rep. TP-2007-214612. NASA, 2007.

[88] W. L. Ko, W. L. Richards, and V. T. Fleischer. *Applications of Ko Displacement Theory to the Deformed Shape Predictions of the Doubly-Tapered Ikhana Wing*. Tech. rep. TP-2009-214652. NASA, 2009.

[89] J. Bakalyar and C. Jutte. “Validation Tests of Fiber Optic Strain-Based Operational Shape and Load Measurements”. In: *53rd AIAA/ASME/ASCE/AHS/ASC Structures, Structural Dynamics and Materials Conference*. 2012.
DOI: 10.2514/6.2012-1904.

[90] H. M. Chan et al. “Fiber-optic sensing system: Overview, development and deployment in flight at NASA”. In: *2015 IEEE Avionics and Vehicle Fiber-Optics and Photonics Conference (AVFOP)*. 2015.
DOI: 10.1109/AVFOP.2015.7356646.

[91] H. M. Chan. *Fiber Optics Sensing System (FOSS) at NASA Armstrong Flight Research Center (AFRC): Summary and Recent Deployments*. Tech. rep. E-DAA-TN60829. AFRC, 2018.

[92] C. V. Jutte et al. *Deformed Shape Calculation of a Full-Scale Wing Using Fiber Optic Strain Data from a Ground Loads Test*. Tech. rep. TP-2011-215975. NASA, 2011.

[93] D. R. Gaukroger and C. J. W. Hassal. "Measurement of vibratory displacements of a rotating blade". In: *Vertica (International Journal of Rotorcraft and Powered Lift Aircraft)* 2.2 (1978), pp. 111–120.

[94] W. G. Bousman. *Estimation of Blade Airloads from Rotor Blade Bending Moments*. Tech. rep. TM-100020. NASA, 1987.

[95] G. C. Foss and E. D. Haugse. "Using Modal Test Results to Develop Strain to Displacement Transformations". In: *Proceedings of the 13th International Modal Analysis Conference (IMAC)*. Vol. 2460. 1995.

[96] P. Bogert, E. Haugse, and R. Gehrki. "Structural Shape Identification from Experimental Strains Using a Modal Transformation Technique". In: *44th AIAA/ASME/ASCE/AHS/ASC Structures, Structural Dynamics, and Materials Conference*. 2003. DOI: 10.2514/6.2003-1626.

[97] A. Skafte, M. L. Aenlle, and R. Brincker. "A general procedure for estimating dynamic displacements using strain measurements and operational modal analysis". In: *Smart Materials and Structures* 25.2 (2016), p. 025020. DOI: 10.1088/0964-1726/25/2/025020.

[98] K. Stefan. *Technology and Practical Use of Strain Gages: With Particular Consideration of Stress Analysis Using Strain Gages*. Wiley, 2017.

[99] K. O. Hill et al. "Photosensitivity in optical fiber waveguides: Application to reflection filter fabrication". In: *Applied Physics Letters* 32.10 (1978), pp. 647–649. DOI: 10.1063/1.89881.

[100] A. A. Shabana. *Dynamics of Multibody Systems*. 4th ed. Cambridge University Press, 2013.

[101] P. E. Nikravesh. *Computer-Aided Analysis of Mechanical Systems*. Prentice-Hall, 1988.

[102] W. Schiehlen. “Multibody System Dynamics: Roots and Perspectives”. In: *Multibody System Dynamics* 1.2 (1997), pp. 149–188. DOI: 10.1023/A:1009745432698.

[103] A. A. Shabana. “Flexible Multibody Dynamics: Review of Past and Recent Developments”. In: *Multibody System Dynamics* 1.2 (1997), pp. 189–222. DOI: 10.1023/A:1009773505418.

[104] J. A. Garcia. “Numerical Investigation of Nonlinear Aeroelastic Effects on Flexible High-Aspect-Ratio Wings”. In: *Journal of Aircraft* 42.4 (2005), pp. 1025–1036. DOI: 10.2514/1.6544.

[105] R. Palacios, J. Murua, and R. Cook. “Structural and Aerodynamic Models in Nonlinear Flight Dynamics of Very Flexible Aircraft”. In: *AIAA Journal* 48.11 (2010), pp. 2648–2659. DOI: 10.2514/1.J050513.

[106] A. Arena, W. Lacarbonara, and P. Marzocca. “Nonlinear Aeroelastic Formulation and Postflutter Analysis of Flexible High-Aspect-Ratio Wings”. In: *Journal of Aircraft* 50.6 (2013), pp. 1748–1764. DOI: 10.2514/1.C032145.

[107] M. Spieck, W. R. Krüger, and J. Arnold. “Multibody Simulation of the Free-Flying Elastic Aircraft”. In: *46th AIAA/ASME/ASCE/AHS/ASC Structures, Structural Dynamics and Materials Conference*. 2005. DOI: 10.2514/6.2005-2280.

[108] J. Scarlett, R. Canfield, and B. Sanders. “Multibody Dynamic Aeroelastic Simulation of a Folding Wing Aircraft”. In: *47th AIAA/ASME/ASCE/AHS/ASC Structures, Structural Dynamics, and Materials Conference*. 2006. DOI: 10.2514/6.2006-2135.

[109] W. R. Krüger and M. Spieck. “Aeroelastic Effects in Multibody Dynamics”. In: *Vehicle System Dynamics* 41.5 (2004), pp. 383–399. DOI: 10.1080/00423110412331300345.

[110] W. R. Krüger and M. Spieck. “A Multibody Approach for Modelling of the Manoeuvring Aeroelastic Aircraft During Pre-Design”. In: *25th International Congress of the Aeronautical Sciences (ICAS)*. 2006.

[111] W. R. Krüger. “Multibody Dynamics for the Coupling of Aeroelasticity and Flight Mechanics of Highly Flexible Structures”. In: *International Forum on Aeroelasticity and Structural Dynamics (IFASD) 2007*. 2007.

[112] W. R. Krüger. "A multi-body approach for modelling manoeuvring aeroelastic aircraft during preliminary design". In: *Proceedings of the Institution of Mechanical Engineers, Part G: Journal of Aerospace Engineering* 222.6 (2008), pp. 887–894. DOI: 10.1243/09544100JAERO264.

[113] Z. Zhao and G. Ren. "Multibody Dynamic Approach of Flight Dynamics and Nonlinear Aeroelasticity of Flexible Aircraft". In: *AIAA Journal* 49.1 (2011), pp. 41–54. DOI: 10.2514/1.45334.

[114] M. Castellani, J. E. Cooper, and Y. Lemmens. "Nonlinear Static Aeroelasticity of High Aspect Ratio Wing Aircraft by FEM and Multibody methods". In: *15th Dynamics Specialists Conference*. 2016. DOI: 10.2514/6.2016-1573.

[115] M. Castellani, J. E. Cooper, and Y. Lemmens. "Nonlinear Static Aeroelasticity of High-Aspect-Ratio-Wing Aircraft by Finite Element and Multibody Methods". In: *Journal of Aircraft* 54.2 (2017), pp. 548–560. DOI: 10.2514/1.C033825.

[116] M. Castellani, J. E. Cooper, and Y. Lemmens. "Flight Loads Prediction of High Aspect Ratio Wing Aircraft Using Multibody Dynamics". In: *International Journal of Aerospace Engineering* 2016 (2016), p. 4805817. DOI: 10.1155/2016/4805817.

[117] G. Li, Y. Z. Law, and R. K. Jaiman. "A novel 3D variational aeroelastic framework for flexible multibody dynamics: Application to bat-like flapping dynamics". In: *Computers & Fluids* 180 (2019), pp. 96–116. DOI: 10.1016/j.compfluid.2018.11.013.

[118] V. Joshi, R. K. Jaiman, and C. Ollivier-Gooch. "A variational flexible multibody formulation for partitioned fluid–structure interaction: Application to bat-inspired drones and unmanned air-vehicles". In: *Computers & Mathematics with Applications* 80.12 (2020), pp. 2707–2737. DOI: 10.1016/j.camwa.2020.09.020.

[119] A. Savino et al. "Coupling Mid-Fidelity Aerodynamics and Multibody Dynamics for the Aeroelastic Analysis of Rotary-Wing Vehicles". In: *Energies* 14.21 (2021), p. 6979. DOI: 10.3390/en14216979.

[120] A. Tamer. "Aeroelastic Response of Aircraft Wings to External Store Separation Using Flexible Multibody Dynamics". In: *Machines* 9.3 (2021), p. 61. DOI: 10.3390/machines9030061.

[121] K. Otsuka and K. Makihara. "Aeroelastic deployable wing simulation considering rotation hinge joint based on flexible multibody dynamics". In: *Journal of Sound and Vibration* 369 (2016), pp. 147–167. DOI: 10.1016/j.jsv.2016.01.026.

[122] K. Otsuka and K. Makihara. "Parametric Studies for the Aeroelastic Analysis of Multibody Wings". In: *Transactions of the Japan Society for Aeronautical and Space Sciences, Aerospace Technology Japan* 14.ists30 (2016), Pc_33–Pc_42. DOI: 10.2322/tastj.14.Pc_33.

[123] K. Otsuka et al. "Strain-Based Geometrically Nonlinear Beam Formulation for Multibody Dynamic Analysis". In: *AIAA Scitech 2022 Forum*. 2022. DOI: 10.2514/6.2022-0848.

[124] K. Otsuka et al. "Strain-Based Geometrically Nonlinear Beam Formulation for Rigid–Flexible Multibody Dynamic Analysis". In: *AIAA Journal* 60.8 (2022), pp. 4954–4968. DOI: 10.2514/1.J061516.

[125] J. Lee, K. Yee, and S. Oh. "Aerodynamic Characteristic Analysis of Multi-Rotors Using a Modified Free-Wake Method". In: *Transactions of The Japan Society for Aeronautical and Space Sciences* 52.177 (2009), pp. 168–179. DOI: 10.2322/tjsass.52.168.

[126] Hexagon AB. *Adams*. URL: https://hexagon.com/products/product-groups/computer-aided-engineering-software/adams (visited on 12/05/2022).

[127] Dassault Systèmes. *Simpack*. URL: https://www.3ds.com/products-services/simulia/products/simpack (visited on 12/05/2022).

[128] Institute of Engineering and Computational Mechanics, University of Stuttgart. *Neweul-M²*. URL: https://www.itm.uni-stuttgart.de/en/software/neweul-m (visited on 12/05/2022).

[129] FunctionBay, Inc. *RecurDyn*. URL: https://functionbay.com/en/page/single/2/recurdyn-overview (visited on 12/05/2022).

[130] Mechatronics, Electrical Energy and Dynamic Systems (MEED), Université Catholique de Louvain. *Robotran*. URL: https://www.robotran.be (visited on 12/05/2022).

[131] P. Masarati et al. "Open-Source Multibody Analysis Software". In: *Multibody Dynamics 2003, International Conference on Advances in Computational Multibody Dynamics*. 2003.

[132] M. A. Sherman, A. Seth, and S. L. Delp. "Simbody: multibody dynamics for biomedical research". In: *Procedia IUTAM* 2 (2021), pp. 241–261. DOI: doi.org/10.1016/j.piutam.2011.04.023.

[133] A. Tasora et al. "Chrono: An open source multi-physics dynamics engine". In: *International Conference on High Performance Computing in Science and Engineering*. 2015, pp. 19–49.

[134] M. Rickert and A. Gaschler. "Robotics Library: An Object-Oriented Approach to Robot Applications". In: *Proceedings of the IEEE/RSJ International Conference on Intelligent Robots and Systems*. 2017, pp. 733–740. DOI: 10.1109/IROS.2017.8202232.

[135] G. Gede et al. "Constrained Multibody Dynamics With Python: From Symbolic Equation Generation to Publication". In: *IDETC/CIE International Design Engineering Technical Conferences and Computers and Information in Engineering Conference*. 2013.

[136] R. H. MacNeal and C. W. McCormick. "The NASTRAN Computer Program for Structural Analysis". In: *Computers & Structures* 1.3 (1971), pp. 389–412. DOI: 10.1016/0045-7949(71)90021-6.

[137] MSC Software Corporation. *MSC Nastran 2018.2: Aeroelastic Analysis User's Guide*. 2018.

[138] P. C. Chen, D. Sarhaddi, and D. D. Liu. "ZAERO: A Unified AIC Module for Aerodynamic/Aeroelastic Design and Analysis". In: *Third Seminar on RRDPAE'98*. 1998.

[139] D. A. Peters, S. Karunamoorthy, and W. Cao. "Finite State Induced Flow Models Part I: Two-Dimensional Thin Airfoil". In: *Journal of Aircraft* 32.2 (2006), pp. 313–322. DOI: 10.2514/3.46718.

[140] D. H. Hodges. "A mixed variational formulation based on exact intrinsic equations for dynamics of moving beams". In: *International Journal of Solids and Structures* 26.11 (1990), pp. 1253–1273. DOI: 10.1016/0020-7683(90)90060-9.

[141] D. H. Hodges. "Geometrically Exact, Intrinsic Theory for Dynamics of Curved and Twisted Anisotropic Beams". In: *AIAA Journal* 41.6 (2003), pp. 1131–1137. DOI: 10.2514/2.2054.

[142] L. Cavagna, S. Ricci, and L. Riccobene. "A Fast Tool for Structural Sizing, Aeroelastic Analysis and Optimization in Aircraft Conceptual Design". In: *50th AIAA/ASME/ASCE/AHS/ASC Structures, Structural Dynamics, and Materials Conference*. 2009. DOI: 10.2514/6.2009-2571.

[143] L. Cavagna, S. Ricci, and L. Travaglini. "NeoCASS: An integrated tool for structural sizing, aeroelastic analysis and MDO at conceptual design level". In: *Progress in Aerospace Sciences* 47.8 (2011), pp. 621–635. DOI: 10.1016/j.paerosci.2011.08.006.

[144] L. Cavagna, S. Ricci, and L. Riccobene. "Structural Sizing, Aeroelastic Analysis, and Optimization in Aircraft Conceptual Design". In: *Journal of Aircraft* 48.6 (2011), pp. 1840–1855. DOI: 10.2514/1.C031072.

[145] G. L. Ghiringhelli, P. Masarati, and P. Mantegazza. "Multibody Implementation of Finite Volume C^0 Beams". In: *AIAA Journal* 38.1 (2000), pp. 131–138. DOI: 10.2514/2.933.

[146] J. M. Jonkman and M. L. Buhl Jr. *FAST User's Guide: Updated August 2005*. Tech. rep. TP-500-38230. NREL, 2005.

[147] M. Drela. "Integrated Simulation Model for Preliminary Aerodynamic, Structural, and Control-Law Design of Aircraft". In: *40th Structures, Structural Dynamics, and Materials Conference and Exhibit*. 1999. DOI: 10.2514/6.1999-1394.

[148] M. Drela. *ASWING 5.99 Technical Description: Steady Formulation*. 2015.

[149] M. Drela. *ASWING 5.99 Technical Description: Unsteady Extension*. 2015.

[150] C. E. S Cesnik and E. Brown. "Modeling of High Aspect Ratio Active Flexible Wings for Roll Control". In: *43rd AIAA/ASME/ASCE/AHS/ASC Structures, Structural Dynamics, and Materials Conference*. 2002. DOI: 10.2514/6.2002-1719.

[151] W. Su, J. Zhang, and C. E. S Cesnik. "Correlations Between UM/NAST Nonlinear Aeroelastic Simulations and Experiments of a Cantilever Slender Wing". In: *International Forum on Aeroelasticity and Structural Dynamics*. 2009.

[152] Z. Wan and C. E. S. Cesnik. "Geometrically Nonlinear Aeroelastic Scaling for Very Flexible Aircraft". In: *54th AIAA/ASME/ASCE/AHS/ASC Structures, Structural Dynamics, and Materials Conference*. 2013. DOI: 10.2514/6.2013-1894.

[153] Z. Wan and C. E. S. Cesnik. "Geometrically Nonlinear Aeroelastic Scaling for Very Flexible Aircraft". In: *AIAA Journal* 52.10 (2014), pp. 2251–2260. DOI: 10.2514/1.J052855.

[154] M. J. Johnson. "Finite-State Airloads for Deformable Airfoils on Fixed and Rotating Wings". MA thesis. Washington University in St. Louis, 1995. DOI: 10.7936/K7P26XJR.

[155] A. del Carre and R. Palacios. "Efficient Time-Domain Simulations in Nonlinear Aeroelasticity". In: *AIAA Scitech 2019 Forum*. 2019. DOI: 10.2514/6.2019-2038.

[156] A. del Carre et al. "Nonlinear Response of a Very Flexible Aircraft under Lateral Gust". In: *International Forum on Aeroelasticity and Structural Dynamics (IFASD) 2019*. 2019.

[157] A. del Carre et al. "SHARPy: A dynamic aeroelastic simulation toolbox for very flexible aircraft and wind turbines". In: *Journal of Open Source Software* 4.44 (2019), p. 1885. DOI: 10.21105/joss.01885.

[158] N. Anderson et al. "Flight-Testing of a UAV Aircraft for Autonomous Operation Using Piccolo II Autopilot". In: *AIAA Atmospheric Flight Mechanics Conference and Exhibit*. 2008. DOI: 10.2514/6.2008-6568.

[159] D. Dvorak et al. "Custom Hardware/Software Interface System for Data Fusion between a Commercial Autopilot and Multispectral Camera". In: *AIAA Infotech at Aerospace Conference and Exhibit*. 2012. DOI: 10.2514/6.2012-2501.

[160] D. N. Borys and R. Colgren. "Advances in Intelligent Autopilot Systems for Unmanned Aerial Vehicles". In: *AIAA Guidance, Navigation, and Control Conference and Exhibit*. 2005. DOI: 10.2514/6.2005-6482.

[161] R. J. Allemang. "The Modal Assurance Criterion (MAC): Twenty Years of Use and Abuse". In: *Sound and Vibration* (2003), pp. 14–21.

[162] M. Pastor, M. Binda, and T. Harčarik. "Modal Assurance Criterion". In: *Procedia Engineering* 48 (2012), pp. 543–548. DOI: 10.1016/j.proeng.2012.09.551.

[163] M. Richardson and B. Schwarz. “Modal Parameter Estimation from Operating Data”. In: *Sound and Vibration* 37 (2003), pp. 28–36.

[164] M. Drela and H. Youngren. *AVL: Aerodynamic Analysis, Trim Calculation, Dynamic Stability Analysis, Aircraft Configuration Development*. 2006.

[165] J. Katz and A. Plotkin. *Low-Speed Aerodynamics*. 2nd ed. Cambridge University Press, 2010.

[166] P. Minguet and J. Dugundji. “Experiments and Analysis for Composite Blades Under Large Deflections Part I: Static Behavior”. In: *AIAA Journal* 28.9 (1990), pp. 1573–1579. DOI: 10.2514/3.25255.

[167] P. Minguet and J. Dugundji. “Experiments and Analysis for Composite Blades Under Large Deflections Part II: Dynamic Behavior”. In: *AIAA Journal* 28.9 (1990), pp. 1580–1588. DOI: 10.2514/3.25256.

[168] M. Love et al. “Body Freedom Flutter of High Aspect Ratio Flying Wings”. In: *46th AIAA/ASME/ASCE/AHS/ASC Structures, Structural Dynamics and Materials Conference*. 2005. DOI: 10.2514/6.2005-1947.

[169] M. R. Jardin and E. R. Mueller. “Optimized Measurements of UAV Mass Moment of Inertia with a Bifilar Pendulum”. In: *AIAA Guidance, Navigation and Control Conference and Exhibit*. 2017. DOI: 10.2514/6.2007-6822.

[170] M. R. Jardin and E. R. Mueller. “Optimized Measurements of Unmanned-Air-Vehicle Mass Moment of Inertia with a Bifilar Pendulum”. In: *Journal of Aircraft* 46.3 (2009), pp. 763–775. DOI: 10.2514/1.34015.

[171] M. W. Green. *Measurement of the Moments of Inertia of Full Scale Airplanes*. Tech. rep. TN-265. NACA, 1927.

[172] M. P. Miller. *An Accurate Method of Measuring the Moments of Inertia of Airplanes*. Tech. rep. TN-351. NACA, 1930.

[173] D. Göge et al. *Ground Vibration Testing of Large Aircraft: State-of-the-Art and Future Perspectives*. Presented at International Modal Analysis Conference (IMAC) 25. 2007.

[174] B. Peeters, J. Debille, and H. Climent. “Modern Solutions for Ground Vibration Testing of Small, Medium and Large Aircraft”. In: *SAE International Journal of Aerospace* 1.1 (2009), pp. 732–742. DOI: 10.4271/2008-01-2270.

[175] P. Lubrina et al. “AIRBUS A350 XWB GVT: State-of-the-Art Techniques to Perform a Faster and Better GVT Campaign”. In: *Topics in Modal Analysis II, Volume 8*. Springer International Publishing, 2004, pp. 243–256. DOI: 10.1007/978-3-319-04774-4_24.

[176] P. Avitabile. “Why Can’t I Run a Modal Test with One Big Shaker and Just “Crank Up the Signal”?” In: *Experimental Techniques* 35.3 (2011). DOI: 10.1111/j.1747-1567.2011.00742.x.

[177] J.-N. Juang and Richard S. Pappa. “An Eigensystem Realization Algorithm for Modal Parameter Identification and Model Reduction”. In: *Journal of Guidance, Control, and Dynamics* 8.5 (1985), pp. 620–627. DOI: 10.2514/3.20031.

[178] B. Schwarz and M. Richardson. *Modal Parameter Estimation from Ambient Response Data*. Presented at International Modal Analysis Conference (IMAC) 19. 2001.

[179] B. J. Schwarz and M. H. Richardson. “Experimental Modal Analysis”. In: *Proceedings of CSI Reliability Week*. 1999.

[180] A. Brandt. *Noise and Vibration Analysis: Signal Analysis and Experimental Procedures*. Wiley, 2011.

[181] M. H. Richardson and D. L. Formenti. *Global Curve Fitting of Frequency Response Measurements using the Rational Fraction Polynomial Method*. Presented at 3rd International Modal Analysis Conference (IMAC). 1985.

[182] L. Li et al. “Structural Shape Reconstruction Through Modal Approach Using Strain Gages”. In: *Communications in Computer and Information Science*. Springer, 2014, pp. 273–281. DOI: 10.1007/978-3-662-45261-5_29.

[183] N. Tourjansky and E. Széchényi. “The Measurement of Blade Deflections: A New Implementation of the Strain Pattern Analysis”. In: *Eighteenth European Rotorcraft Forum*. 1992.

[184] M. B. Tischler and R. K. Remple. *Aircraft and Rotorcraft System Identification*. 2nd ed. American Institute of Aeronautics and Astronautics, 2012. DOI: 10.2514/4.868207.

[185] M. G. Gilbert, D. K. Schmidt, and T. A. Weisshaar. “Quadratic Synthesis of Integrated Active Controls for an Aeroelastic Forward-Swept-Wing Aircraft”. In: *Journal of Guidance Control and Dynamics* 7.2 (1984), pp. 190–196. DOI: 10.2514/3.8566.

[186] D. Lucia. "The SensorCraft Configurations: A Non-Linear AeroServoElastic Challenge for Aviation". In: *46th AIAA/ASME/ASCE/AHS/ASC Structures, Structural Dynamics and Materials Conference*. 2005. DOI: 10.2514/6.2005-1943.

[187] F. Kimler and R. Canfield. "Structural Design of Wing Twist for Pitch Control of Joined Wing SensorCraft". In: *11th AIAA/ISSMO Multidisciplinary Analysis and Optimization Conference*. 2006. DOI: 10.2514/6.2006-7134.

[188] A. P. Ricciardi et al. "High Fidelity Nonlinear Aeroelastic Analysis for Scaled Vehicle Design". In: *12th AIAA Aviation Technology, Integration, and Operations (ATIO) Conference and 14th AIAA/ISSMO Multidisciplinary Analysis and Optimization Conference*. 2012. DOI: 10.2514/6.2012-5624.

[189] A. P. Ricciardi et al. "Nonlinear Aeroelastic Scaling of a Joined Wing Aircraft". In: *53rd AIAA/ASME/ASCE/AHS/ASC Structures, Structural Dynamics and Materials Conference*. 2012. DOI: 10.2514/6.2012-1454.

[190] A. P. Ricciardi et al. "Nonlinear Aeroelastic Scaled Model Optimization Using Equivalent Static Loads". In: *54th AIAA/ASME/ASCE/AHS/ASC Structures, Structural Dynamics, and Materials Conference*. 2013. DOI: 10.2514/6.2013-1785.

[191] C. Howcroft et al. "Aeroelastic Modelling of Highly Flexible Wings". In: *15th Dynamics Specialists Conference*. 2016. DOI: 10.2514/6.2016-1798.

[192] S. Sehgal and H. Kumar. "Structural Dynamic Model Updating Techniques: A State of the Art Review". In: *Archives of Computational Methods in Engineering* 23.3 (2016), pp. 515–533. DOI: 10.1007/s11831-015-9150-3.

[193] J. D. Collins et al. "Statistical Identification of Structures". In: *AIAA Journal* 12.2 (1974), pp. 185–190. DOI: 10.2514/3.49190.

[194] R. M. Lim and D. J. Ewins. "Analytical model improvement using frequency response functions". In: *Mechanical Systems and Signal Processing* 8.4 (1994), pp. 437–458. DOI: 10.1006/mssp.1994.1032.

[195] R. M. Lin and J. Zhu. "Model updating of damped structures using FRF data". In: *Mechanical Systems and Signal Processing* 20.8 (2006), pp. 2200–2218. DOI: 10.1016/j.ymssp.2006.05.008.

[196] C. Y. Shih et al. *Complex Mode Indication Function and its Applications to Spatial Domain Parameter Estimation*. Presented at 7th International Modal Analysis Conference (IMAC). 1989.

[197] A. A. Shabana. "Definition of the Slopes and the Finite Element Absolute Nodal Coordinate Formulation". In: *Multibody System Dynamics* 1 (1997), pp. 339–348. DOI: 10.1023/A:1009740800463.

[198] S. Morton et al. "Accuracy and coupling issues of aeroelastic Navier-Stokes solutions on deforming meshes". In: *38th Structures, Structural Dynamics, and Materials Conference*. 1997. DOI: 10.2514/6.1997-1085.

[199] J. Degroote, K. Bathe, and J. Vierendeels. "Performance of a new partitioned procedure versus a monolithic procedure in fluid-structure interaction". In: *Computers & Structures* 87.11 (2009), pp. 793–801. DOI: 10.1016/j.compstruc.2008.11.013.

[200] G. Hou, J. Wang, and A. Layton. "Numerical Methods for Fluid-Structure Interaction—A Review". In: *Communications in Computational Physics* 12.2 (2012), pp. 337–377. DOI: 10.4208/cicp.291210.290411s.

[201] A. de Boer, M. S. van der Schoot, and H. Bijl. "Mesh deformation based on radial basis function interpolation". In: *Computers & Structures* 85.11 (2007), pp. 784–795. DOI: 10.1016/j.compstruc.2007.01.013.

[202] J. T. Katsikadelis. *The Boundary Element Method for Engineers and Scientists: Theory and Applications*. 2nd ed. Academic Press, 2016.

[203] J. Anderson. *Fundamentals of Aerodynamics*. 6th ed. McGraw-Hill, 2017.

[204] J. D. Anderson. *Modern Compressible Flow: With Historical Perspective*. McGraw-Hill, 2021.

[205] S. Plimpton. "Fast Parallel Algorithms for Short-Range Molecular Dynamics". In: *Journal of Computational Physics* 117.1 (1995), pp. 1–19. DOI: 10.1006/jcph.1995.1039.

[206] J. Barnes and P. Hut. "A hierarchical $O(N \log N)$ force-calculation algorithm". In: *Nature* 324 (1986), pp. 446–449. DOI: 10.1038/324446a0.

[207] R. Yokota and L. A. Barba. "FMM-based vortex method for simulation of isotropic turbulence on GPUs, compared with a spectral method". In: *Computers & Fluids* 80 (2013), pp. 17–27. DOI: 10.1016/j.compfluid.2012.08.002.

[208] J. K. Salmon and M. S. Warren. "Fast Parallel Tree Codes for Gravitational and Fluid Dynamical N-Body Problems". In: *The International Journal of Supercomputer Applications and High Performance Computing* 8.2 (1994), pp. 129–142. DOI: 10.1177/109434209400800205.

[209] M. S. Warren and J. K. Salmon. "A Parallel, Portable and Versatile Treecode". In: *7th Society for Industrial and Applied Mathematics SIAM Conference on Parallel Processing for Scientific Computing*. 1995.

[210] W. Dehnen. "A Hierarchical $O(N)$ Force Calculation Algorithm". In: *Journal of Computational Physics* 179.1 (2002), pp. 27–42. DOI: 10.1006/jcph.2002.7026.

[211] S. Pfalzner and P. Gibbon. *Many-Body Tree Methods in Physics*. Cambridge University Press, 1996.

[212] L. Greengard and V. Rokhlin. "A fast algorithm for particle simulations". In: *Journal of Computational Physics* 73.2 (1987), pp. 325–348. DOI: 10.1016/0021-9991(87)90140-9.

[213] H. Cheng, L. Greengard, and V. Rokhlin. "A Fast Adaptive Multipole Algorithm in Three Dimensions". In: *Journal of Computational Physics* 155.2 (1999), pp. 468–498. DOI: 10.1006/jcph.1999.6355.

[214] J. Dongarra and F. Sullivan. "Guest Editors Introduction to the top 10 algorithms". In: *Computing in Science & Engineering* 2.1 (2000), pp. 22–23. DOI: 10.1109/MCISE.2000.814652.

[215] K. Nabors et al. "Preconditioned, Adaptive, Multipole-Accelerated Iterative Methods for Three-Dimensional First-Kind Integral Equations of Potential Theory". In: *SIAM Journal on Scientific Computing* 15.3 (1994), pp. 713–735. DOI: 10.1137/0915046.

[216] K. Nabors et al. "A multipole direct and indirect BEM for 2D cavity flow at low Reynolds number". In: *Engineering Analysis with Boundary Elements* 19.1 (1997), pp. 17–31. DOI: 10.1016/S0955-7997(97)00021-0.

[217] T. M. Wasfy and A. K. Noor. "Computational strategies for flexible multibody systems". In: *Applied Mechanics Reviews* 56.6 (2003), pp. 553–613. DOI: 10.1115/1.1590354.

[218] C. C. Rankin and F. A. Brogan. “An Element Independent Corotational Procedure for the Treatment of Large Rotations”. In: *Journal of Pressure Vessel Technology* 108.2 (1986), pp. 165–174. DOI: 110.1115/1.3264765.

[219] M. A. Crisfield. “A consistent co-rotational formulation for non-linear, three-dimensional, beam-elements”. In: *Computer Methods in Applied Mechanics and Engineering* 81.2 (1990), pp. 131–150. DOI: 10.1016/0045-7825(90)90106-V.

[220] G. F. Moita and M. A. Crisfield. “A finite element formulation fo3 3-D continua using the co-rotational technique”. In: *International Journal for Numerical Methods in Engineering* 39.22 (1996), pp. 3775–3792. DOI: 10.1002/(SICI)1097-0207(19961130)39:22<3775::AID-NME23>3.0.CO;2-W.

[221] J. Gerstmayr, H. Sugiyama, and A. Mikkola. “Review on the Absolute Nodal Coordinate Formulation for Large Deformation Analysis of Multibody Systems”. In: *Journal of Computational and Nonlinear Dynamics* 8.3 (2013), p. 031016. DOI: 10.1115/1.4023487.

[222] R. de Borst et al. *Nonlinear Finite Element Analysis of Solids and Structures*. Wiley, 2012.

[223] M. Géradin and A. Cardona. *Flexible Multibody Dynamics: A Finite Element Approach*. Wiley, 2001.

[224] A. Cardona and M. Geradin. “A beam finite element non-linear theory with finite rotations”. In: *International Journal for Numerical Methods in Engineering* 26.11 (1988), pp. 2403–2438. DOI: 10.1002/nme.1620261105.

[225] A. A. Shabana and R. Y. Yakoub. “Three Dimensional Absolute Nodal Coordinate Formulation for Beam Elements: Theory”. In: *Journal of Mechanical Design* 123.4 (2001), pp. 606–613. DOI: 10.1115/1.1410100.

[226] R. Y. Yakoub and A. A. Shabana. “Three Dimensional Absolute Nodal Coordinate Formulation for Beam Elements: Implementation and Applications”. In: *Journal of Mechanical Design* 123.4 (2001), pp. 614–621. DOI: 10.1115/1.1410099.

[227] J. T. Sopanen and A. M. Mikkola. “Description of Elastic Forces in Absolute Nodal Coordinate Formulation”. In: *Nonlinear Dynamics* 34 (2003), pp. 53–74. DOI: 10.1023/B:NODY.0000014552.68786.bc.

[228] J. Bonet and R. D. Wood. *Nonlinear Continuum Mechanics for Finite Element Analysis*. 2nd ed. Cambridge University Press, 2008.

[229] A. M. Mikkola and A. A. Shabana. "A Non-Incremental Finite Element Procedure for the Analysis of Large Deformation of Plates and Shells in Mechanical System Applications". In: *Multibody System Dynamics* 9.3 (2003), pp. 283–309. DOI: 10.1023/A:1022950912782.

[230] M. A. Omar and A. A. Shabana. "A Two-Dimensional Shear Deformable Beam for Large Rotation and Deformation Problems". In: *Journal of Sound and Vibration* 243.3 (2001), pp. 565–576. DOI: 10.1006/jsvi.2000.3416.

[231] A. A. Shabana. "Computer Implementation of the Absolute Nodal Coordinate Formulation for Flexible Multibody Dynamics". In: *Nonlinear Dynamics* 16 (1998), pp. 293–306. DOI: 10.1023/A:1008072517368.

[232] R. Y. Yakoub and A. A. Shabana. "Use of Cholesky Coordinates and the Absolute Nodal Coordinate Formulation in the Computer Simulation of Flexible Multibody Systems". In: *Nonlinear Dynamics* 20.3 (1999), pp. 267–282. DOI: 10.1023/A:1008323106689.

[233] B Hussein, D. Negrut, and A. A. Shabana. "Implicit and explicit integration in the solution of the absolute nodal coordinate differential/algebraic equations". In: *Nonlinear Dynamics* 54.4 (2008), pp. 283–296. DOI: 10.1007/s11071-007-9328-9.

[234] B Hussein and A. A. Shabana. "Sparse matrix implicit numerical integration of the Stiff differential/algebraic equations: Implementation". In: *Nonlinear Dynamics* 65.4 (2011), pp. 369–382. DOI: 10.1007/s11071-010-9898-9.

[235] H. M. Hilber, T. J. R. Hughes, and R. L. Taylor. "Improved numerical dissipation for time integration algorithms in structural dynamics". In: *Earthquake Engineering & Structural Dynamics* 5.3 (1977), pp. 283–292. DOI: 10.1002/eqe.4290050306.

[236] D. Negrut et al. "On an Implementation of the Hilber-Hughes-Taylor Method in the Context of Index 3 Differential-Algebraic Equations of Multibody Dynamics". In: *Journal of Computational and Nonlinear Dynamics* 2.1 (2007), pp. 73–85. DOI: 10.1115/1.2389231.

[237] C. Farhat, K. G. van der Zee, and P. Geuzaine. "Provably second-order time-accurate loosely-coupled solution algorithms for transient nonlinear computational aeroelasticity". In: *Computer Methods in Applied Mechanics and Engineering* 195.17 (2006), pp. 1973–2001. DOI: 10.1016/j.cma.2004.11.031.

[238] J. T. Batina. "Unsteady Euler airfoil solutions using unstructured dynamic meshes". In: *AIAA Journal* 28.8 (1990), pp. 1381–1388. DOI: 10.2514/3.25229.

[239] S. Piperno, C. Farhat, and B. Larrouturou. "Partitioned procedures for the transient solution of coupled aroelastic problems Part I: Model problem, theory and two-dimensional application". In: *Computer Methods in Applied Mechanics and Engineering* 124.1 (1995), pp. 79–112. DOI: 10.1016/0045-7825(95)92707-9.

[240] C. Farhat and M. Lesoinne. "Two efficient staggered algorithms for the serial and parallel solution of three-dimensional nonlinear transient aeroelastic problems". In: *Computer Methods in Applied Mechanics and Engineering* 182.3 (2000), pp. 499–515. DOI: 10.1016/S0045-7825(99)00206-6.

[241] T. W. Strganac and D. T. Mook. "Numerical model of unsteady subsonic aeroelastic behavior". In: *AIAA Journal* 28.5 (1990), pp. 903–909. DOI: 10.2514/3.25137.

[242] E. Pramono and S. Weeratunga. "Aeroelastic computations for wings through direct coupling on distributed-memory MIMD parallel computers". In: *32nd Aerospace Sciences Meeting and Exhibit*. 1994. DOI: 10.2514/6.1994-95.

[243] S. Piperno, C. Farhat, and B. Larrouturou. "Partitioned procedures for the transient solution of coupled aeroelastic problems Part II: energy transfer analysis and three-dimensional applications". In: *Computer Methods in Applied Mechanics and Engineering* 190.24 (2001), pp. 3147–3170. DOI: 10.1016/S0045-7825(00)00386-8.

[244] A. Beckert and H. Wendland. "Multivariate interpolation for fluid-structure-interaction problems using radial basis functions". In: *Aerospace Science and Technology* 5.2 (2001), pp. 125–134. DOI: 10.1016/S1270-9638(00)01087-7.

[245] A. H. van Zuijlen, A. de Boer, and H. Bijl. "Higher-order time integration through smooth mesh deformation for 3D fluid–structure interaction simulations". In: *Journal of Computational Physics* 224.1 (2007), pp. 414–430. DOI: 10.1016/j.jcp.2007.03.024.

[246] B. Stroustrup. *The C++ Programming Language*. 4th ed. Addison-Wesley, 2013.

[247] S. Meyers. *Effective Modern C++*. O'Reilly, 2014.

[248] A. Alexandrescu. *Modern C++ Design*. Addison-Wesley, 2001.